Self-Assembly and Dynamics of Colloidal Dispersions in Steady and Time-Varying External Fields

Zachary M. Sherman

B.S., Cornell University (2013)

Submitted to the Department of Chemical Engineering in partial fulfillment of the requirement for the degree of

Doctor of Philosophy in Chemical Engineering

at the

MASSACHUSETTS INSTITUTE OF TECHNOLOGY

~~May 23, 2019~~ [June 2019]

Signature redacted

Author ... .

Department of Chemical Engineering

May 23, 2019

Signature redacted

Certified by ... .

James W. Swan

Texaco-Mangelsdorf Career Development Professor

Thesis Supervisor

Signature redacted

Accepted by ....

Patrick S. Doyle

Robert T. Haslam (1911) Professor

Chairman, Committee for Graduate Students

Self-Assembly and Dynamics of Colloidal Dispersions in Steady and Time-Varying External Fields

Zachary M. Sherman

Submitted to the Department of Chemical Engineering on May 23, 2019 in partial fulfillment of the requirement for the degree of Doctor of Philosophy in Chemical Engineering

Abstract

A diverse set of functional materials can be fabricated using dispersions of colloids and nanoparticles. If the dispersion is responsive to an external field, like dielectric and charged particles in an electric field or paramagnetic particles in a magnetic field, the field can be used to facilitate self-assembly and control particle transport. One promising feature of field-responsive materials is the ability to drive them out of equilibrium by varying the external field in time. Without the constraints of equilibrium thermodynamics, out-of-equilibrium dispersions display a rich array of self-assembled states with useful material and transport properties. To leverage their unique behaviors in real applications, a predictive, theoretical framework is needed to guide experimental design. In this thesis, I carry out a systematic investigation of the self-assembly and dynamics of colloidal dispersions in time-varying external fields using computer simulations, equilibrium and nonequilibrium thermodynamics, and electro-/magnetokinetic theory.

I first develop efficient computational models for simulating suspensions of polarizable colloids in external fields. The simulations are accurate enough to quantitatively reproduce experiments but fast enough to reach the large length and time scales relevant for self-assembly. I use this simulation method to construct the complete equilibrium phase diagram for polarizable particles in steady external fields and find that many-bodied, mutual polarization has a remarkably strong influence on the nature of the self-assembled states. Correctly accounting for mutual polarization enables a thermodynamic theory to compute the phase diagram that agrees well with simulations and experiments. Though the equilibrium structures are crystalline, in practice, dispersions typically arrest in kinetically-trapped, disordered or defective metastable states due to strong interparticle forces. This is a key difficulty preventing scalable fabrication of colloidal crystals. I show that cyclically toggling the external field on and off over time leads to growth of colloidal crystals at significantly faster rates and with many fewer defects than for assembly in a steady field. The toggling protocol stabilizes phases that are only metastable in steady fields, including complex, transmutable crystal structures. I use nonequilibrium thermodynamics to predict the out-of-equilibrium states in terms of the toggle parameters.

I also investigate the transport properties of dispersions of paramagnetic particles in rotating magnetic fields. Like toggled fields, rotating fields also drive dispersions out of equilibrium, and their dynamics can be tuned with the rotation frequency. I find that the rotating field greatly increases particle self-diffusivity compared to steady fields. The diffusivity attains a maximum value several times larger than the Stokes-Einstein diffusivity at intermediate rotation frequencies. I develop a simple phenomenological model for magnetophoresis through porous media in rotating fields that predicts enhanced mobility over steady fields, consistent with experiments.

Lastly, I study the nonlinear dynamics of polarizable colloids in electrolytes and report a new mode of electrokinetic transport. Above a critical external field strength, an instabilty occurs and particles spontaneously rotate about an axis orthogonal to the field, a phenomenon called Quincke rotation. If the particle is also charged, its electrophoretic motion couples to Quincke rotation and propels the particle orthogonally to the driving field, an electrohydrodynamic analogue to the Magnus effect. Typically, motion orthogonal to a field requires anisotropy in particle shape, dielectric properties, or boundaries. Here, the electrohydrodynamic Magnus (EHM) effect occurs for bulk, isotropic spheres, with the Quincke rotation instability providing broken symmetry driving orthogonal motion. In alternating-current (AC) fields, electrophoresis is suppressed, but the Magnus velocity persists over many cycles. The Magnus motion is decoupled from the field and acts as a self-propulsion, so I propose the EHM effect in AC fields as a mechanism for generating a new type of active matter. The EHM "swimmers" behave as active Brownian particles, and their long-time dynamics are diffusive, with a field-dependent effective diffusivity that is orders of magnitude larger than the Stokes-Einstein diffusivity. I also develop a continuum electrokinetic theory to describe the electrohydrodynamic Magnus effect that is in good agreement with my simulations.

Thesis Supervisor: James W. Swan
Title: Texas-Mangelsdorf Career Development Professor

Dedicated to my grandfather, Robert Etkins,
my first science teacher.

Acknowledgements

A person's graduate school experience is in large part related to which lab they join. I was incredibly fortunate to work under Professor James Swan, who has all the traits one could want in an advisor. Not surprisingly, Jim is an immensely talented scientist. I have always been astounded by his seemingly endless knowledge and ability, not just in our own field but even extending out of (what I thought was) his comfort zone. Perhaps even more important is his ability to communicate this expertise. I have always found Jim's approach to difficult topics to be particularly illuminating and appreciate his patience in helping to teach them to me. In fact, it was his teaching style in the first year graduate course "Numerical Methods" that drew me to consider working in his lab. As for this thesis work itself, it is safe to say that none of it would have been possible without Jim's constant time and guidance. I will always be grateful for the amount of time Jim spent working closely with me, helping me every step of the way. I think this was a big reason that the work progressed quickly, and I was able to generate a lot of results that I am proud of. Working with Jim has made me a much better scientist, presenter, and educator. As I continue on my academic career path, I will always see Jim as a role model for the kind of scientist and mentor I wish to be.

My thesis committee, Professors Daniel Blankschtein, Michael Strano, and Alfredo Alexander-Katz, has been a valuable resource throughout grad school. Not only was their guidance on my thesis project invaluable, but I also had the chance to take a graduate course taught by each committee member. I thank them for all of their time and effort spent helping me in the coursework and in research.

I had the great opportunity to work with four very talented undergraduate students. Helen Rosenthal was the first student I worked with, so I first have to thank her for her patience working with me as a first-time mentor. She made important contributions to our understanding of the complicated kinetics of out-of-equilibrium self-assembly pathways, which the reader will see in Chapter 3. I next would like to thank Stephon Henry-Rerrie for his work in modeling thermally-responsive gelling nanoemulsions, which helped in a collaboration with Li-Chiun Cheng and Professor Patrick Doyle. Dip Ghosh joined us from India to work on simulations of field-directed assembly. Even though we worked together for only a summer, he managed to get a huge amount done, and nearly all the simulation results in Chapter 4 are his. Finally, I have to thank Julia Pallone for her excellent work on the dynamics of dispersions in rotating magnetic fields. What started out as a small proof-of-concept side project turned into an important contribution to my thesis, getting the entirety of Chapter 6. To Helen, Stephon, Dip, and Julia, working with you all was a highlight of graduate school. Thank you so much, and without your efforts, I would not have been able to have nearly as strong of a thesis.

As someone who only does theory and simulations, one of the biggest personal challenges in my research was learning to stay "grounded" and relate my work to real-world experiments. Of course, because I do not know the first thing about experiments, I had to turn to my experimental collaborators for their expertise. I would like to thank Li-Chiun Cheng and Pat Doyle for the opportunity to collaborate with them on modeling experiments of thermally-responsive gelling nanoemulsions. I really learned a lot from working with them, especially on the experimental aspects of soft matter assembly. I would also like to thank Professor Randall Erb at Northeastern University for getting us interested in rotating magnetic fields and helping to prepare a manuscript, containing most of the information in Chapter 6.

Zsigmond Varga, Gang Wang, Andrew Fiore, and I were the first cohort of students to join the Swan lab, so we had the interesting experience of helping to build up a lab as we were trying to navigate our research. These three are exceptionally skilled scientists, and it was a true pleasure to work side by side. I greatly appreciate all the support Gang and Andrew gave me in developing the simulation software used in this thesis. Thanks to Zsigi for being a great desk neighbor, even if we never agreed on whether crystals or gels were "low-quality". To the other lab members, Sam Winslow, Kevin Silmore, Jerry Wang, Kelsey Reed, Emily Krucker, and Kyle Lennon, I really enjoyed my time working with you. I know that the Swan lab is in good hands from the future.

I have made so many friends during my time in Cambridge, but I wanted to acknowledge a few in particular, Aaron Garg, Aurora Zhang, Kameron Conforti, and Sam Winslow. You all have made going to grad school more than *just* going to grad school. I cherish all of the adventures we've had, all the Beyoncé we have listened to, and all love you've given. The past six years have felt truly special, and I cannot thank you enough.

I have to single out Carolyn Mills, one of my best friends, my co-Thermo TA, and my roommate. It has been amazing getting to share so many experiences with you. With all the craziness of grad school, you have given me a constant outlet of weird, laughs, smiles, and support. I can't imagine having a better person to go through it all with than you. I will always look up to you as a scientist and a truly good-at-heart person.

Being so far from home in Phoenix, Arizona, the precious time, support, and love from my family is invaluable. To my sister, Samantha Sherman, your success in everything you do has always inspired me. I am so proud of you. To my parents Theresa Etkins Chance and Scott Sherman, saying I would not be writing this thesis without you two would be a colossal understatement. Your unwavering support, love, and sacrifice throughout my entire life has given me so many wonderful opportunities. I owe everything I am to you, and there is no way to pay you back for everything you have done to help me achieve my dreams. I love you, and I love who you are.

And of course, I can't forget to thank the Muddy Charles Pub, where most of this thesis was written.

Contents

List of Figures

Chapter 1

Introduction

A major effort in chemical engineering is the synthesis of "designer materials", materials with physical properties tailored for a specific application. Photonic crystals with precise optical properties can serve as waveguides in photonic circuits.[1–4] Membranes with optimal conductivity are used in batteries for energy storage.[5,6] Special fluids with tunable rheological properties are used in automobile break lines, artificial joints, pumps, and vibrational dampeners.[7–11] The microscopic features of these materials give rise to their effective properties observed on the macroscopic scale. If we can design and control the microstructure, we can rationally synthesize materials with desired physical properties. For these materials to be *useful*, we need to engineer fabrication schemes that scale efficiently to produce large quantities of material at low costs.

Microstructural features can be patterned directly using top-down lithographic techniques.[12–14] Because these features are orders of magnitude smaller than the materials they make up, it takes a very long time to build macroscopic quantities of material. These top-down approaches are typically expensive and time-consuming at large scales. Bottom-up approaches, particularly self-assembly, offer a promising route to scalable synthesis of nanomaterials.[15,16] In self-assembly processes, interactions among small building blocks spontaneously drive them into larger, organized structures. As long as we can synthesize the building blocks, we get the entire structure "for free", in the sense that the *building blocks* do the work of creating the structure. Fabrication *via* self-assembly has the potential to scale well. To create macroscopic amounts of self-assembled material, we simply begin with macroscopic amounts of building blocks.

The types of materials we can form using self-assembly are determined by the types of building blocks we choose. Colloidal dispersions, made up of 1 nm to 10 µm sized particles dispersed in a fluid, offer a particularly powerful class of materials for self-assembling structures. Colloidal particles are highly engineerable, and there exist many controlled processes for synthesizing different types of particles with desired size, shape, and surface functionalization.[17] These particles interact, exerting forces on one another that arise from a variety of physical mechanisms, including van der Waals interactions, steric repulsions, electrostatics, magnetostatics, depletion attractions, hydrodynamic flows, and capillary forces.[18] Because the physical and chemical properties of the particles are tunable, so too are the interactions between the particles. This allows us to engineer different assembled structures simply by modifying the particles that make them up.

The simplest and most common self-assembly schemes, *static self-assembly* (SSA), involve no external driving force; the particle interactions are innate and the dispersion spontaneously assembles on its own.[15] Such systems are said to be *passive*. In static self-assembly, the configuration of particles in the dispersion evolves over time until it reaches a thermodynamic equilibrium state, which is stable and does not change. This equilibrium state can be anything from a disordered fluid-like configuration to a complex, ordered crystalline structure. The tools of equilibrium thermodynamics and statistical mechanics provide a generic algorithm to predict the equilibrium state from a known interparticle interaction potential.[19] This allows us to predict which interparticle potentials might lead to a particular target structure, informing us on what kinds of particles to use as building blocks. Thus, static self-assembly offers an efficient paradigm for rational design and synthesis of functional materials. The strategy is to engineer colloids that have an interparticle potential whose theoretical thermodynamic equilibrium state has the desired material properties for the application

of interest.

Static self-assembly has already been used to synthesize a diverse set of functional materials at the lab scale. However, two main engineering challenges have prevented robust, scalable fabrication of nanomaterials using SSA methods. The first challenge is the difficulty of designing and synthesizing building blocks with arbitrarily complex interparticle interactions. Simple structures like face-centered cubic (FCC), hexagonally close-packed (HCP), and body-centered cubic (BCC) have been self-assembled from particles with simple interactions. However, more complex structures require particles with increasingly complicated interactions, which may be difficult to engineer. Lattices mimicking atomic crystals have been assembled using nanoparticles with highly anisotropic attractions,[20,21] but existing methods for synthesizing these particles are not easily scalable.[22] Lattices mimicking ionic crystals have been formed with binary mixtures of charged nanoparticles, though two components with precisely controlled stoichiometry, charge, and size are needed.[23] Attractions mediated by grafted DNA offer a tunable platform to produce a variety of crystal structures, but can have high materials costs.[24–26] Complex crystals and quasicrystals can be assembled from steric repulsions, but require complicated, precisely-sculpted polyhedral particles with dozens of faces that may be challenging to synthesize.[27] There are systematic ways to concoct complicated, but isotropic, interparticle potentials whose thermodynamic equilibrium state is any target structure, but there is no guarantee that these can be realized experimentally.[28–30] Even if we can, the target structure might be particularly sensitive to small deviations from this exact potential, and such deviations are always present in real systems. For example, a modest of amount of size polydispersity can suppress crystallization[31,32] and slight shape deviations can stabilize wildly different crystal structures.[27]

The second challenge involves the kinetics of assembling the target structure. It is advantageous for the forces driving assembly to be many times larger than thermal forces to facilitate rapid structure formation. Though particles quickly aggregate, they often arrest in kinetically-trapped defective or disordered metastable states.* Defects degrade the performance of crystalline structures, and nearly-perfect crystals with essentially no defects are required for semiconductor or photonic applications.[1,33] In fact, if the defect density is too high, they provide nucleation sites for rapid structural change, and the material may catastrophically fail.[34] Because the metastable state is not *thermodynamically* stable, the material will slowly age as it converts to its equilibrium state. Its properties will change over time which is not desirable for use in a stable operation. Weaker forces can be used to promote controlled, defect-free crystallization *via* nucleation and growth, but the kinetics are necessarily slow and not scalable. The range of system parameters in which this mechanism is experimentally possible, the "crystallization slot", is usually quite narrow and not necessarily known *a priori*.[35] Particle interactions must be tuned to find the crystallization slot and then carefully controlled to remain inside, which may require sophisticated control schemes. Thus, for static self-assembly, there is an intrinsic coupling between the thermodynamic driving force and the assembly kinetics that forces a tradeoff between quality of the self-assembled microstructure and its rate of formation.[36,37]

This coupling between structure and dynamics can also be problematic when designing transport processes involving statically self-assembled structures. For example, magnetic nanoparticles have been proposed for targeted therapeutics, because they can be manipulated using magnetic fields to deliver cargo to target sites. However, strong dipolar attractions between particles results in significant aggregation during magnetophoresis and limits their mobility through dense, porous tissue, greatly reducing their efficacy.[38] Dispersions of monoclonal antibodies have been investigated for targeted immunotherapy technologies, but protein agglomeration results in large viscosities that prevent subcutaneous injection.[39–42] Additives to electrolytes within batteries to improve mechanical stability by forming percolating networks can also reduce the electrolyte's conductivity and degrade the battery's performance.[43–45]

If particle interactions can be controlled with an external stimulus, the stimulus can be used to facilitate self-assembly. Many such systems have been studied experimentally[46] including dispersions that respond to light, temperature, pH, electric field, and magnetic field, examples of which are listed in Table 1.1. If the stimulus is held steady in time, these dispersions behave like statically self-assembling systems and relax to thermodynamic equilibrium, suffering from the same problems plaguing other passive processes. If the

*Sometimes, these metastable states are the ones that are desired, like in the case of manufacturing a colloidal gel. However, this isn't *controllable*, and we cannot easily prevent these structures if we *don't* want them.

stimulus	chemistry	interaction
light	photo-sensitive ligand	van der Waals[47,48]
	photochromic solute	electrostatic[49,50]
temperature	thermally responsive polymer	bridging,[51–53] depletion[54]
	DNA functionalization	hybridization[24,55]
pH	pH-responsive ligand	electrostatic,[49,56] hydrogen-bonding[57–59]
electric field	dielectric contrast	dipolar,[60–62] dielectrophoretic[63]
magnetic field	magnetic contrast	dipolar,[10,64–68] magnetophoretic[69]
shear flow	any	entropic,[70] viscoelastic,[71] hydrodynamic[72]

Table 1.1: Examples of stimulus-chemistry pairs promoting switchable interparticle interactions in nanoparticle systems.

stimulus is varied in time, the particles experience time-dependent interactions, which drastically alter their dynamics and assembled structures. This type of assembly belongs to a class of nonequilibrium processes called *dynamic self-assembly* (DSA), where energy is supplied to a dispersion from an external source to drive the assembly of particles.[15] Such systems are said to be *active*. To reach a steady-state, assembled structures must dissipate the energy input, and are therefore not in equilibrium. Because the dispersion is driven out of equilibrium, there are no longer constraints that couple the dispersion structure and its assembly kinetics. Thus, using time-dependent external stimuli to synthesize materials *via* dynamic self-assembly can overcome the the challenges plaguing static self-assembly.

Early experiments involving assembly in time-dependent stimuli were performed by Promislow and Gast, who assembled paramagnetic colloids with dipolar interactions controlled with a strong, external magnetic field.[64,65] When the magnetic field was held steady in time, the particles arrested in a defective, metastable state. When the magnetic field was toggled on and off cyclically in time, the particles rapidly crystallized into large, well-ordered domains, even though the interparticle forces were many times larger than thermal forces. While the field was off, the particles' thermal motion helped anneal defective, arrested configurations that would have persisted for long times in steady fields. The second engineering challenge (coupling of the structure to its rate of formation) was solved, and it became possible to quickly assemble high-quality crystals using large interparticle forces. Further work by Swan, Furst, and coworkers showed that the assembled structures and their dynamics could be controlled with the toggle frequency.[67,68,73–75] If the toggle frequency was too large, particles could not diffuse sufficiently far from their original positions in the off half-cycle, and defects persisted from cycle to cycle. If the toggle frequency was too small, the particles diffused away farther than the range of the interaction in the off half-cycle and did not reaggregate when the field was turned back on. Only for intermediate frequencies were the particles able to diffuse far enough to relax defected structures without melting completely. Thus, they were able to optimize the toggling protocol to yield the fastest crystallization rates. Tang, Grover, Bevan, and coworkers designed a feedback control scheme for the toggle parameters to efficiently crystallize colloids in toggled electric fields.[76,77] A variety simulations extended toggled self-assembly to other types of particle interactions and structures, including those that are not observed with steady interactions.[78–84] The ability to form structures not available to static self-assembly is especially interesting because it suggests that toggled self-assembly may be used to overcome the engineering challenge of scalable synthesis of complicated particles. The strategy would be to use particles with simple interactions (that are easy to manufacture) and add complexity in the external time-signal (which is easy to control) to generate more complicated structures that would generally require more complicated particles if synthesis were restricted to static self-assembly.

There are many other types of time-variation in the external stimulus including varying the spatial potential landscape in time[85] and, if the external stimulus has an associated direction like a flow, electric, or magnetic field, flipping the field's polarity.[62,70,86–88] A particularly useful mode of time-variation in rotating the field orientation in two or three dimensions. This has been used to assemble structures not observed with SSA in steady fields,.[89–92] Rotating fields have proved especially promising for controlling the transport properties

of colloidal dispersions, and have been used to enhance mixing at the micron scale,[93,94] amplify signals from biochemical sensors,[95–97] propel artificial microswimmers,[98–100] assemble "conveyor-belts" to transport cargo,[101] and enhance electro- and magnetophoresis through porous media.[38,102]

Time-varying stimuli are only a subset of dynamically self-assembling systems. Another important subset consists of "active" particles that sustain some form of self-locomotion, including self-propulsion ("swimmers"),[98,103,104] self-rotation ("rotors"),[105–108] or growth.[109] This class of materials is called "active matter", and is inspired by biological systems where "particles" include bacteria, microorganisms, and motor proteins, that convert chemical energy into locomotion. Because active particles dissipate energy, they are free from the constraints of equilibrium thermodynamics and dynamically self-assemble into a rich assortment of out-of-equilibrium materials,[110] including flocks,[111,112] nematics,[109] and crystals.[113,114] These phases have useful collective transport properties and have been used to significantly increase the translational velocity of flocks of microrollers,[115] understand enhanced mixing in cells,[116,117] and transport passive cargo.[101,118]

These works demonstrate that active systems and dynamic self-assembly can overcome the engineering challenges inherent to passive systems and static self-assembly, at the expense of continually injecting energy into the assembling system. However, a major drawback is the difficulty in predicting the assembled structures and their dynamic properties. For steady interactions in static self-assembly, the tools of statistical mechanics and equilibrium thermodynamics provide a straightforward and generic (albeit intractable in many cases) algorithm to compute equilibrium states. There are numerous kinetic theories that rely on equilibrium thermodynamic quantities, including classical nucleation theory[119,120] and Cahn-Hilliard kinetics,[121,122] that describe the assembly dynamics. Fundamental transport quantities like diffusivity, viscosity, conductivity, and permittivity can be related to equilibrium fluctuations of thermodynamic quantities using Green-Kubo relations.[123] With time-varying and dissipative interactions in dynamic self-assembly, the dispersion evolves toward an out-of-equilibrium terminal state, which is not governed by the laws of equilibrium thermodynamics. There is no generic theory to predict and describe such dissipative, out-of-equilibrium states, their dynamics of formation, or their transport properties. This is problematic because it makes designing, optimizing, and scaling real DSA processes difficult. This remains a key hurdle preventing dynamic self-assembly from being utilized to reliably fabricate nanomaterials.

The goal of my thesis is to develop a predictive, theoretical framework for the assembly and dynamics of colloids in time-varying external fields. Such a framework will aid in the experimental design of dynamically self-assembling processes.

In Chapter 2, I discuss my approach to studying dynamic self-assembly of colloids using computer simulations. I first present the equations that govern the motion of colloidal particles and how hydrodynamic, Brownian, and steric forces are handled in simulations. I then derive a detailed mathematical model for the electro/magnetostatic forces in dispersions of arbitrarily shaped colloid particles, as well as an efficient numerical implementation accelerated on graphics processing units (GPUs). These latter sections are quite lengthy and technical and are not needed to understand the rest of the results in this thesis. While the interested reader is welcome to look through the details, reading only Section 2.1 and then proceeding to Chapter 3 is sufficient.

Chapter 3 investigates a simple model of dynamic self-assembly: colloids with a toggled, isotropic, short-ranged attraction facilitated through the depletion interaction. This is an important physical system in colloid science and has well-understood equilibrium phase behavior. I derive a first-principles theory of nonequilibrium thermodynamics to predict the out-of-equilibrium assembled states. The theory necessitates equality of the time average of pressure and chemical potential in coexisting phases of the dispersion, which can be evaluated using well known equations of state. I also develop phenomenological models to describe and predict the self-assembly rates. These models can be leveraged to optimize the assembly rate and the quality of the assembled microstructure, which are substantially enhanced over steady interactions.

This toggled depletion system is somewhat of a simple "toy" model. I would like to extend the results and analysis to toggled electric and magnetic fields, which have already been investigated experimentally. However, the analysis hinges on a full understanding of the equilibrium phase behavior in steady fields. This

was well-understood for the depletion system, but the complete phase diagram for field-directed assembly of dielectric and paramagnetic colloids has not been computed, even for steady electric and magnetic fields. Chapter 4 develops a complete thermodynamic description of such assemblies. I show how an important physical feature of these types of particles, mutual polarization, sculpts the free energy landscape and has a remarkably strong influence on the nature of the self assembled states. My theoretical predictions agree with the phase behavior I observe in dynamic simulations of these dispersions as well as that in experiments of field-directed structural transitions. This new model also predicts the existence of a eutectic point at which two crystalline phases and a disordered phase of nanoparticles all simultaneously coexist.

In Chapter 5, I develop computational and theoretical models for dielectric and paramagnetic particles in toggled external fields. The active process stabilizes phases that are only metastable in steady fields, including a dense fluid phase and body-centered orthorhombic crystals. The growth mechanism and terminal structure of the dispersion are easily controlled by the toggling protocol, and the toggle parameters can be used to continuously transmute between crystal structures with different lattice parameters. Results from linear irreversible thermodynamics are used to predict the dissipative terminal states of the active assembly process in terms of parameters of the toggling protocol.

Chapter 6 investigates the transport properties of dispersions of paramagnetic colloids in rotating magnetic fields, another mode of time-varying external fields. I find that self-diffusion of particles is enhanced in rotating fields compared to steady fields, and that the self-diffusivity in the plane of rotation reaches a maximum value at intermediate rotation frequencies that is larger than the Stokes-Einstein diffusivity of an isolated particle. The magnetophoretic velocity of particles through the bulk in a field gradient decreases with increasing rotation frequency, but the enhanced in-plane diffusion allows for faster magnetophoretic transport through porous materials in rotating fields. I also examine the effect of porous confinement on the transport properties in rotating fields and fine enhanced diffusion at all pore sizes. The confined and bulk values of the transport properties are leveraged in simple models of transport through tortuous porous media.

In Chapter 7, I investigate the electrokinetic transport properties of dispersions of charged colloids in electrolytes. For sufficiently strong fields, an instability occurs that causes spherical colloids to break symmetry and spontaneously rotate about an axis orthogonal to the applied field, a phenomenon named Quincke rotation. If the colloids also have a net charge, the electrophoretic motion couples to Quincke rotation and propels particles in a direction orthogonal to both the driving field and the axis of rotation, an electrohydrodynamic analogue to the Magnus effect. Typically, motion orthogonal to the field requires anisotropy in particle shape, dielectric properties, or geometry of boundaries. Here, the electrohydrodynamic Magnus (EHM) effect occurs for bulk, isotropic spherical particles, with the Quincke rotation instability providing broken symmetry driving orthogonal motion. The direction of the Magnus velocity is not changed by flipping the sign of the field, so net orthogonal motion persists in alternating-current (AC) electric fields. This orthogonal motion is decoupled from the field and acts as a type of self-propulsion, so I propose the electrohydrodynamic Magnus effect in AC fields as a mechanism to create a new type of active matter. Because the EHM effect is oberved for simple spheres, these active dispersions are inexpensive and simple to synthesize, easy to control with the external field, do not lose activity as long as the field is sustained, and do not require specific boundary geometries. I use a simple electrokinetic theory to analyze the charging dynamics, predict the Magnus velocity, and determine a critical AC frequency above which Quincke rotation and the EHM effect shuts off. The long-time dynamics are diffusive, with a diffusivity that is orders of magnitude larger than the Stokes-Einstein diffusivity due to the particles' activity.

Finally, in Chapter 8, I discuss how the results of the work of this thesis can be leveraged to design efficient assembly processes using external fields. I propose strategies for using the toggling protocol to assemble complicated crystals, including colloidal diamond. I also detail promising opportunities for rotating fields to optimize particle transport for targeted therapeutic purposes. Lastly, I suggest active matter and particle separation applications for the electrohydrodynamic Magnus effect.

Chapter 2

Dynamic Simulations of Colloidal Dispersions in Electric and Magnetic Fields

Computer simulations can augment our understanding of experimental systems by providing information that is difficult to obtain or inaccessible to experiments. At the colloidal scale, we are often interested in information at the individual particle level. Because the particles are small, $O(1\,\text{nm} - 10\,\mu\text{m})$, the relevant length and time scales are also small. Sophisticated scattering and imaging techniques are required for these high resolutions which can be expensive, time consuming, and difficult to interpret. It can also be challenging to control certain aspects of experiments, like gravity, temperature fluctuations, and vibrations, which may obscure observations or complicate their interpretation.

Simulations provide a controlled way to investigate systems at high resolutions, at the expense of using only an approximate model as a proxy for a real experiment. These "virtual experiments" help to interpret and predict experimental observations, which in turn allows more accurate computational models, and so simulations and experiments work together in a synergistic feedback loop. Because the level of approximation can greatly affect the outcome of a simulation, it is important to carefully construct models that incorporate the necessary physical mechanisms that dominate the behavior of the systems of interest. In this Chapter, we will discuss the computational models used in this thesis to simulate colloidal dispersions in external fields.

2.1 Brownian Dynamics Simulations of Colloidal Dispersions

There are numerous types of simulation methods we can choose for dispersions of colloids ranging from the highest resolution atomistic molecular dynamics to the most coarse-grained continuum models. A useful model should be simple enough to be computationally tractable, yet accurate enough to be a realistic representation of actual dispersions. In this thesis, we use a Langevin-type model which explicitly represents each colloid particle as a discrete element but treats the solvent implicitly as a Newtonian fluid continuum. That is, we do not incorporate solvent molecules explicitly but rather account for the *effect* of the solvent on the particles, which has two main contributions: deterministic hydrodynamic forces from flows in the fluid and stochastic Brownian forces from fluctuating interactions of the colloid and solvent molecules.

In our simulations, we have a monodisperse suspension of N colloid particles that are spheres of radius a and mass m dispersed in a fluid of viscosity η. The dynamics of each particle i at a position $\mathbf{x}_i(t)$ at time t are governed by the Langevin equation[124]

$$m\frac{\mathrm{d}^2\mathbf{x}_i}{\mathrm{d}t^2} = \mathbf{F}_i^H + \mathbf{F}_i^B + \mathbf{F}_i^I + \mathbf{F}_i^P \tag{2.1}$$

where $\mathbf{F}_i^H$ is the hydrodynamic force on particle i, $\mathbf{F}_i^B$ is the stochastic Brownian force, $\mathbf{F}_i^I$ is the interparticle

force arising from thermodynamic interactions among particles, and $\mathbf{F}_i^P$ is an external phoretic force exerted by a global force field.

If a steady force is suddenly applied to a colloid particle at rest, the particle accelerates to a terminal velocity over an inertial time scale $\tau_i \equiv m/\gamma$, where $\gamma \equiv 6\pi\eta a$ is the Stokes drag coefficient.[125] Because we are interested in modeling assembly and transport, we are more concerned with the time scales on which the particle actually moves. One such time scale is that for diffusion $\tau_D \equiv \gamma a^2/k_BT$, where k_BT is the thermal energy of the solvent. The Schmidt number $\mathrm{Sc} \equiv \tau_D/\tau_I = \gamma^2 a^2/mk_BT$, compares the rate of inertial relaxation to the rate of diffusion. For typical colloids of size $a \approx 1\,\mu\mathrm{m}$ and density $\approx 10^3\,\mathrm{kg/m^3}$ in water with viscosity $\eta \approx 10^{-3}\,\mathrm{Pa{\cdot}s}$ at room temperature $T \approx 293\,\mathrm{K}$, the Schmidt number is $\mathrm{Sc} \approx 10^7$, and inertial relaxation is orders of magnitude faster than particle motion. If we were to numerically integrate (2.1) directly, most of our computational effort would be spent resolving the inertial dynamics, and it would be difficult to reach diffusive and larger time scales. As long as we look on time scales larger than τ_i, there is essentially no error in assuming particles instantaneously move at their terminal velocity when they feel a force. In this case, the acceleration of the particle is always zero and the dynamics are said to be *overdamped*,

$$0 = \mathbf{F}_i^H + \mathbf{F}_i^B + \mathbf{F}_i^I + \mathbf{F}_i^P, \tag{2.2}$$

and the particles are always "force free".

2.1.1 Hydrodynamic Forces

The velocity field $\mathbf{u}(\mathbf{x})$ within the incompressible, Newtonian fluid solvent is governed by the Navier-Stokes equations

$$\rho\left(\frac{\mathrm{d}\mathbf{u}}{\mathrm{d}t} + \mathbf{u}\cdot\nabla\mathbf{u}\right) = -\nabla P + \eta\nabla^2\mathbf{u}, \quad \nabla\cdot\mathbf{u} = 0, \tag{2.3}$$

where ρ is the fluid density and $P(\mathbf{x})$ is the pressure. On the particle surfaces, the fluid satisfies no-slip boundary conditions and moves with the local surface velocity. The Reynolds number, $\mathrm{Re} \equiv \rho u a/\eta$, where u is a characteristic velocity, compares the magnitude of inertial forces to viscous force. For typical values at the colloidal scale, $\rho \approx 10^3\,\mathrm{kg/m^3}$, $u \approx 10^{-6}\,\mathrm{m/s}$, $a \approx 1\,\mu\mathrm{m}$, $\eta \approx 10^{-3}\,\mathrm{Pa{\cdot}s}$, the Reynolds number is 10^{-6} and inertial forces are small compared to viscous forces. In this case, for times larger than τ_i, the left side of the Navier-Stokes equation vanishes, and fluid motion is governed by the Stokes equations

$$\eta\nabla^2\mathbf{u} = \nabla P, \quad \nabla\cdot\mathbf{u} = 0. \tag{2.4}$$

The fluid flow in the solvent is pseudosteady, and time-dependence arises solely from the time-dependent no-slip boundary conditions as particles move around. Because this equation is linear in $\mathbf{u}$, there exists the linear relation

$$\mathbf{U}_i = \sum_j \mathbf{M}_{ij}^H \cdot \mathbf{F}_j, \tag{2.5}$$

where $\mathbf{M}_{ij}^H$ is the hydrodynamic mobility tensor coupling the nonhydrodynamic force $\mathbf{F}_j \equiv \mathbf{F}_j^B + \mathbf{F}_j^I + \mathbf{F}_j^P$ on particle j to the velocity $\mathbf{U}_i$ of particle i.[125,126] Forces on a particle generate flows in the fluid that entrain and move other particles, so motion among the particles is coupled together. This equation (2.5) for a single particle can be written in matrix/vector form for all N particles,

$$\begin{bmatrix}\mathbf{U}_1\\ \mathbf{U}_2\\ \vdots\end{bmatrix} = \begin{bmatrix}\mathbf{M}_{11} & \mathbf{M}_{12} & \cdots\\ \mathbf{M}_{21} & \mathbf{M}_{22} & \cdots\\ \vdots & \vdots & \ddots\end{bmatrix} \cdot \begin{bmatrix}\mathbf{F}_1\\ \mathbf{F}_2\\ \vdots\end{bmatrix} \quad \Rightarrow \quad \mathscr{U} = \mathscr{M}^H \cdot \mathscr{F} \tag{2.6}$$

where $\mathscr{U} \equiv [\mathbf{U}_1, \mathbf{U}_2, \ldots, \mathbf{U}_N]^T$ is a list of the N particle velocities, $\mathscr{F} \equiv [\mathbf{F}_1, \mathbf{F}_2, \ldots, \mathbf{F}_N]^T$ is a list of particle forces, $\mathscr{M}^H$ is the grand hydrodynamic mobility tensor whose ij^{th} block entries are $\mathbf{M}_{ij}^H$, and the T superscript indicates transposition.* $\mathscr{M}^H$ is determined from the solution to the Stokes equations (2.4) with

*We use script letters to denote *collections* of individual particle variables.

no-slip boundary conditions on the particle surfaces and therefore depends on the particle configuration. One approximation for $\mathbf{M}_{ij}^H$ is the Rotne-Prager-Yamakawa tensor,

$$\mathbf{M}_{ij}^H = \frac{1}{\gamma} \begin{cases} \left(\frac{3a}{4r} + \frac{a^3}{2r^3}\mathbf{I} + \left(\frac{3a}{4r} + \frac{3a^3}{2r^3}\right)\hat{\mathbf{r}}\hat{\mathbf{r}}\right) & r \geq 2a \\ \left(1 - \frac{9r}{32a}\right)\mathbf{I} + \frac{3r}{32a}\hat{\mathbf{r}}\hat{\mathbf{r}} & r < 2a \end{cases} \tag{2.7}$$

where $\mathbf{r} \equiv \mathbf{x}_i - \mathbf{x}_j$ is the center-to-center distance vector, $r \equiv |\mathbf{r}|$, and $\hat{\mathbf{r}} \equiv \mathbf{r}/r$.[127] $\mathbf{M}_{ij}^H$ can be succinctly written in periodic geometries with its Fourier-space representation

$$\mathbf{M}_{ij}^H = \frac{1}{\eta V} \sum_{\mathbf{k} \neq 0} \frac{e^{i\mathbf{k}\cdot\mathbf{r}}}{k^2} \left(\frac{\sin ka}{ka}\right)^2 \left(\mathbf{I} - \hat{\mathbf{k}}\hat{\mathbf{k}}\right) \tag{2.8}$$

where $\mathbf{k} \in [2\pi k_x/L_x, 2\pi k_y/L_y, 2\pi k_z/L_z : (k_x, k_y, k_z) \in \mathbb{Z}]^T$ is the wavevector, $k \equiv |\mathbf{k}|$, $\hat{\mathbf{k}} \equiv \mathbf{k}/k$, L_x, L_y, and L_z are the dimensions of the periodic simulation cell, and $V \equiv L_x L_y L_z$ is its volume.[128] This far-field representation of the hydrodynamic mobility tensor treats each particle as a point force plus a point quadrupole generating a Stokeslet that entrains the other particles. Because this is the dominant contribution to the hydrodynamic interactions, we neglect higher order force moments (*e.g.* torques and stresslets) for computational efficiency. These can be incorporated in more sophisticated hydrodynamic models to improve the accuracy of $\mathscr{M}^H$.[129] Lubrication forces between nearly touching particles can be included pairwise,[130,131] but are not implemented here.

Equation (2.5) can be numerically integrated over a time step Δt using a forward Euler scheme,

$$\mathbf{x}_i(t + \Delta t) = \mathbf{x}_i(t) + \mathbf{U}_i(t)\Delta t. \tag{2.9}$$

This discretized version is the one implemented in simulations. At each time step, particle forces are computed, particle velocities are calculated from 2.5, and the positions are updated using 2.9.

2.1.2 Brownian Forces

The solvent exerts stochastic, Brownian forces on the particles originating from fluctuating interactions between solvent molecules with the colloids. The statistics of the Brownian forces satisfy the fluctuation-dissipation theorem,[125]

$$\left\langle \mathscr{F}^B(t) \right\rangle = 0, \quad \left\langle \mathscr{F}^B(t)\mathscr{F}^B(t+\tau) \right\rangle = 2k_B T(\mathscr{M}^H)^{-1}\delta(\tau) \tag{2.10}$$

where δ is the Dirac δ-function and $\langle\cdot\rangle$ indicates an ensemble average over particles and time. The average Brownian force is zero, while its variance is related to the inverse of the grand hydrodynamic mobility tensor. The Brownian forces are uncorrelated in time (*i.e.* the set of forces $\mathscr{F}^B$ at one time does not affect the set of forces at a later time), but the forces are correlated between particles through their hydrodynamic interactions. The discretized version of (2.10) averages the Brownian force over a single time step Δt,

$$\left\langle \mathscr{F}^B \right\rangle = 0, \quad \left\langle \mathscr{F}^B\mathscr{F}^B \right\rangle = \frac{2k_B T(\mathscr{M}^H)^{-1}}{\Delta t}, \tag{2.11}$$

and the magnitude of the force depends on the time step.[132] Sampling these Brownian forces is generally a difficult task because it requires evaluating the square root of $\mathscr{M}^H$, but a computationally efficient "positively-split Ewald" method has been developed.[128]

2.1.3 Interparticle Forces

Interparticle forces arising from thermodynamic interactions among particles are represented as the gradient of a potential energy $U(\mathscr{X})$, which is a function of the coordinates of all particles $\mathscr{X} \equiv [\mathbf{x}_1, \mathbf{x}_2, \ldots, \mathbf{x}_N]^T$,

$$\mathbf{F}_i^I(\mathscr{X}) \equiv -\nabla_{\mathbf{x}_i} U(\mathscr{X}), \tag{2.12}$$

where the gradient is taken with respect to the position of the i^{th} particle. In some cases, the total potential energy (or at least a contribution to it) can be decomposed into a sum of pair potentials U_{ij} that depend only on the relative displacement between a pair of particles

$$U(\mathscr{X}) = \frac{1}{2}\sum_{ij} U_{ij}(\mathbf{r}), \tag{2.13}$$

where i and j run from 1 to N and the factor of $1/2$ corrects for double-counting each pair. In this case, the forces can also be decomposed into sums of pairwise forces

$$\mathbf{F}^I_{ij}(\mathbf{r}) \equiv \nabla_{\mathbf{r}} U_{ij}(\mathbf{r}). \tag{2.14}$$

In this thesis, we are concerned with solid, rigid colloids, which cannot overlap. In terms of a function, these steric interactions are represented by the hard sphere pair potential

$$U^{\text{hs}}_{ij} = \begin{cases} \infty & \text{if } r < 2a \\ 0 & \text{if } r \geq 2a \end{cases}. \tag{2.15}$$

In other words, particle overlaps are forbidden (require infinite energy), but the particles are otherwise non-interacting. Though real colloidal particles are not perfectly hard, hard-core models have been successful at reproducing generic behavior seen in many dispersions.[133,134] The hard sphere force computed by the derivative of this potential is discontinuous; it is everywhere zero except for a δ-function of infinite magnitude at contact. This type of force cannot be implemented directly in simulations. Typically, the hard potential is approximated with a soft potential of the form r^{-n}, where n is a large power. The larger n, the more accurately the soft potential approximates the hard potential, but the larger the resulting forces become as the potential diverges faster and faster.[135] Smaller time steps must be taken as n increases to prevent unphysically large steric forces, leaving this method computationally inefficient. Heyes and Melrose implemented a "potential-free" hard sphere algorithm by allowing particles to overlap over the course of a time step due to other forces and then separating them to contact at the end of the time step.[136] Because equations (2.5) and (2.9) give a relation between particle displacements and forces we can compute the effective hard sphere force that was required to separate these two hydrodynamically interacting particles to contact. Thus, the potential-free algorithm can be equivalently written in terms of a hard sphere pair potential. For the particular choice of the Rotne-Prager-Yamakawa tensor for $\mathbf{M}^H_{ij}$,[137]

$$U^{\text{hs}}_{ij} = \begin{cases} \dfrac{8\gamma a}{3\Delta t}\left(2a\ln\dfrac{2a}{r} + r - 2a\right) & \text{if } r < 2a \\ 0 & \text{if } r \geq 2a \end{cases} \tag{2.16}$$

This potential does not diverge as particles approach contact, so we do not need to worry about taking small time steps to avoid large forces.† There are no adjustable parameters, but because Δt is explicitly included in the functional form, the strength of the hard sphere potential always adjusts to bring particles exactly to contact over a single time step. This hard sphere potential reproduces all of the correct hard sphere thermodynamic and transport quantities.[138]

2.1.4 Freely Draining Model

We refer to the above method of handling hydrodynamic interactions as the "HI model". Because of the computational cost of computing the long-ranged, many-bodied hydrodynamic interactions, a common simplification is the "freely draining" (FD) model, which neglects interparticle hydrodynamic interactions so that the drag on each particle is decoupled from all of the others and equal to the Stokes drag,

$$\mathbf{M}^H_{ij} = 0, i \neq j \qquad \mathbf{M}^H_{ii} = \mathbf{I}/\gamma. \tag{2.17}$$

†Equation (2.16) does have a slow logarithmic divergence as $r \to 0$. This is only a problem if particles are nearly completely overlapped, in which case they are not behaving like hard spheres anyway (which may be due to excessively large forces, large time steps, *etc.*). This is quite different from the case of $1/r^{-n}$ potentials, where even a small amount of overlap can lead to unphysically large forces if n is large.

In this case, the discrete equations of motion take the simpler form

$$\mathbf{x}_i(t+\Delta t) = \mathbf{x}_i(t) + \frac{1}{\gamma}\mathbf{F}_i(t)\Delta t. \tag{2.18}$$

With this approximation for $\mathscr{M}^H$, the Brownian forces among particles are no longer correlated with one another,

$$\left\langle \mathscr{F}^B \right\rangle = 0, \quad \left\langle \mathscr{F}^B \mathscr{F}^B \right\rangle = \frac{2k_BT\gamma\mathbf{I}}{\Delta t}, \tag{2.19}$$

and the effective hard sphere potential takes on a different form,[137]

$$U_{ij}^{\text{hs}} = \begin{cases} \frac{\gamma}{4\Delta t}(r-2a)^2 & \text{if } r < 2a \\ 0 & \text{if } r \geq 2a \end{cases}. \tag{2.20}$$

2.1.5 Implementation

All simulations are run in HOOMD-Blue, a software suite for particle simulations optimized on graphics processing units (GPUs).[139–141] The native HOOMD-Blue package can only integrate the equations of motion for the freely-draining model. For the hydrodynamic model, we utilize the positively-split Ewald method, implemented as a plugin to HOOMD-Blue.[128] To incorporate electro-/magnetostatic and electro-/magnetophoretic forces, we utilize mutual dipole and immersed boundary plugins to HOOMD-Blue discussed in the following sections.[142]

Calculations in simulations are performed on dimensionless quantities, so we must select a consistent set of units to nondimensionalize variables. All lengths are scaled by the particle radius a, all energies are scaled on the thermal energy k_BT, and all times are scaled by the bare diffusion time $\tau_D = \gamma a^2/k_BT$. A dimensionless version of a quantities is indicated with a tilde $\sim$. With this choice of dimensionless units, the Stokes drag is unity $\widetilde{\gamma} = 1$ and the solvent viscosity is $\widetilde{\eta} = 1/6\pi$.

2.2 Electric and Magnetic Forces for Spherical Particles

Dispersions of dielectric and paramagnetic particles that respond to electric and magnetic fields have additional interparticle and phoretic forces on top of the ones discussed in the previous section. These forces are long-ranged and many-bodied and are difficult to implement in simulations. In this section, we derive the forces induced among particles by external fields and discuss a rapid numerical implementation of the calculations.

2.2.1 Governing Equations

The electromagnetic interactions in colloidal dispersions are governed by Maxwell's equations. A useful form of Maxwell's equations is obtained by averaging them over volumes that are small compared to length scales of interest (like the particle size) but large compared to atomic length scales, which can be represented as[143,144]

$$\nabla \cdot \mathbf{F} = \rho, \quad \mathbf{F} = -\lambda\nabla\psi, \tag{2.21}$$

where $\psi(\mathbf{x})$ is the potential, $\mathbf{F}(\mathbf{x})$ is the flux, $\rho(\mathbf{x})$ is the free charge distribution, and $\lambda(\mathbf{x})$ is a conductivity. For the case of dielectric particles, $\mathbf{F}$ is the electric induction $\mathbf{D}$, $-\nabla\psi$ is the electric field $\mathbf{E}$, and λ is the electric permittivity ε. For the case of paramagnetic particles, $\mathbf{F}$ is the magnetic induction $\mathbf{B}$ (sometimes called the magnetic flux density), $-\nabla\psi$ is the magnetic field $\mathbf{H}$, and λ is the magnetic permeability μ. The mathematical analysis of both of these classes of materials is identical. For simplicity, we will cast our derivation in the context of dielectric particles in an electric field, with the understanding that all of the expressions also hold for paramagnetic particles in magnetic fields.

If we have colloids of permittivity λ_p in a solvent of permittivity λ_f and all the free charge is located on the particle surfaces, so that $\rho(\mathbf{x}) = 0$ everywhere in the fluid, (2.21) reduces to solving Laplace's equation

$$\nabla^2 \psi = 0 \tag{2.22}$$

for the potential inside ψ_p and outside ψ_f the particles subject to the boundary conditions on each of the particle surfaces S_i

$$\psi_p = \psi_f, \quad (\mathbf{F}_f - \mathbf{F}_p) \cdot \hat{\mathbf{n}} = q_0, \quad \text{for } \mathbf{x} \in S_i, \tag{2.23}$$

where q_0 is the free surface charge density and F_p and F_f are the fluxes inside and outside of the particles, respectively.[143–146] We also enforce periodic boundary conditions commensurate with the dimensions of the periodic simulation box L_x, L_y, and L_z.

These equations hold well when the time scales for electric and magnetic relaxation inside the particle and fluid are much smaller than time scales of interest. These intrinsic electric and magnetic relaxation times,[‡] $O(1\,\text{ns})$, are nearly always negligible compared to time scales for particle motion, $O(1\,\text{s})$, but can become important if rapidly varying external fields are present, like high-frequency AC electric fields.[125,144,147] Like the fluid velocity in the Stokes equations (2.4), the potential in (2.22) is pseudosteady, and time-dependence emerges only from the time-dependent boundary conditions (2.23) as particles move around or the external field varies. The linear relation between $\mathbf{F}$ and $\mathbf{E}$ holds well for small $\mathbf{E}$. As $\mathbf{E}$ increases, $\mathbf{F}$ "saturates" and nonlinear polarization models are needed.[144,148–150] These models preclude analytic progress, so we assume the linear limit is applicable in this thesis.

2.2.2 The Periodic Green's Function for Laplace's Equation

The Green's function solution $G(\mathbf{x})$ to Laplace's equation is the potential at a position $\mathbf{x}$ due to a point charge of unit magnitude at the origin within a fluid of unit permittivity.

$$-\nabla^2 G = \delta(\mathbf{x}). \tag{2.24}$$

G can be determined by taking the Fourier transform of this equation, solving for the transformed Green's function $\widetilde{G} = 1/k^2$, and inverting,

$$G(\mathbf{x}) = \frac{1}{(2\pi)^3} \int d\mathbf{k} \frac{1}{k^2} e^{i\mathbf{k}\cdot\mathbf{x}} = \frac{1}{4\pi x}, \tag{2.25}$$

where $x = |\mathbf{x}|$. Suppose now that the charge density is a periodic array of point charges,

$$-\nabla^2 G = \sum_{\mathbf{n}} \delta(\mathbf{x} - \mathbf{n}), \tag{2.26}$$

where $\mathbf{n} \in \{(n_x L_x, n_y L_y, n_z L_z) : (n_x, n_y, n_z) \in \mathbb{Z}\}$ and L_x, L_y, and L_z are the periodicities in each dimension. Because Laplace's equation is linear, we can immediately write the solution as a superposition of single point force solutions,

$$G(\mathbf{x}) = \sum_{\mathbf{n}} \frac{1}{4\pi\,|\mathbf{x} - \mathbf{n}|} \tag{2.27}$$

This sum, representing the potential from an infinite array of positive point charges, does not converge. To evaluate G, we assume there is an additional, uniform negative charge distribution throughout the medium that balances the positive charges and ensures the overall system is charge-neutral.[145] This renders the sum convergent, and we can use the Poisson summation formula to sum over the reciprocal lattice instead of the real lattice,

$$G(\mathbf{x}) = \frac{1}{V} \sum_{\mathbf{k} \neq 0} \frac{e^{i\mathbf{k}\cdot\mathbf{x}}}{k^2}, \tag{2.28}$$

where $\mathbf{k} \in \{(2\pi k_1/L, 2\pi k_2/L, 2\pi k_3/L) : (k_1, k_2, k_3) \in \mathbb{Z}\}$. Removing the $\mathbf{k} = 0$ term from the wave space sum enforces electroneutrality. This periodic solution will be convenient for the periodic boundary conditions of a simulation box with dimensions L_1, L_2, and L_3.

[‡]Here, we are referring to relaxation of atomic or magnetic domains (on length scales much smaller than those of interest) that contribute to λ and not relaxation of mobile ion species, which can have significantly longer relaxation times.

2.2.3 Spherical Harmonic Expansion of the Periodic Green's Function

Because the periodic Green's function satisfies Laplace's equation, it is possible to expand it in terms of spherical harmonics $Y_{\ell m}$ as,

$$G(\mathbf{x}-\mathbf{y}) = \frac{1}{V}\sum_{\mathbf{k}\neq 0}\frac{e^{i\mathbf{k}\cdot(\mathbf{x}-\mathbf{y})}}{k^2} = \sum_{\ell m}\left(A_{\ell m}r^{\ell} + B_{\ell m}r^{-\ell-1}\right)Y_{\ell m}(\theta,\phi), \tag{2.29}$$

where the spherical coordinates (r,θ,ϕ) of $\mathbf{y}$ are relative to some arbitrary point $\mathbf{x}_j$ and $\mathbf{x}$ is treated as a fixed parameter here. The geometry of this setup is illustrated in Figure 2.1. $\mathbf{x}$ and $\mathbf{y}$ are restricted to the primary box $\mathbb{L} \equiv [-L_1/2, L_1/2) \times [-L_2/2, L_2/2) \times [-L_3/2, L_3/2)$. $G(\mathbf{x})$ is finite everywhere in $\mathbb{L}$ except $\mathbf{x} = 0$, so $G(\mathbf{x}-\mathbf{y})$ is finite everywhere except $\mathbf{y} = \mathbf{x}$. Because the point $\mathbf{x}_j$ is not necessarily $\mathbf{x}$, $G(\mathbf{x}-\mathbf{y})$ is, in general, finite at $r = 0$. Therefore, all of the $B_{\ell m}$ coefficients are zero, and the expansion is

$$G(\mathbf{x}-\mathbf{y}) = \sum_{\ell m} A_{\ell m}r^{\ell}Y_{\ell m}(\theta,\phi). \tag{2.30}$$

This represents G as a local expansion about $\mathbf{x}_j$ that can be truncated for small r. If $\mathbf{x}$ is outside of the sphere of radius a centered at $\mathbf{x}_j$, we can determine the coefficients $A_{\ell m}$ by multiplying both sides of (2.30) by $Y_{\ell m}$, integrating $\mathbf{y}$ over the surface of this sphere, and using the orthonormality of spherical harmonics,

$$A_{\ell m} = \frac{a^{-\ell-2}}{V}\sum_{\mathbf{k}\neq 0}\frac{e^{i\mathbf{k}\cdot(\mathbf{x}-\mathbf{x}_j)}}{k^2}\int_S d\mathbf{r}\, e^{-i\mathbf{k}\cdot\mathbf{r}}Y_{\ell m}(\theta,\phi). \tag{2.31}$$

By orienting the coordinate system so that the z direction points along $\mathbf{k}$ for each $\mathbf{k}$ in the sum, the coefficients can be evaluated analytically,

$$A_{\ell m} = \begin{cases} \dfrac{a^{-\ell}}{V}\displaystyle\sum_{\mathbf{k}\neq 0}\frac{e^{i\mathbf{k}\cdot(\mathbf{x}-\mathbf{x}_j)}}{k^2}\sqrt{4\pi(2\ell+1)}i^{-\ell}j_{\ell}(ka), & \text{for } m = 0, \\ 0, & \text{for } m \neq 0, \end{cases} \tag{2.32}$$

where $j_{\ell}(ka)$ are the spherical Bessel functions of degree ℓ. The complete expansion of the periodic Green's function about $\mathbf{x}_j$ is,

$$G(\mathbf{x}-\mathbf{y}) = \frac{1}{V}\sum_{\mathbf{k}\neq 0}\frac{e^{i\mathbf{k}\cdot(\mathbf{x}-\mathbf{x}_j)}}{k^2}\sum_{\ell}\sqrt{4\pi(2\ell+1)}i^{-\ell}j_{\ell}(ka)\left(\frac{r}{a}\right)^{\ell}Y_{\ell}(\theta,\phi), \tag{2.33}$$

with $Y_{\ell} \equiv Y_{\ell 0}$. We will also need the normal derivative[§] of the Green's function,

$$\hat{\mathbf{n}}_{\mathbf{y}}\cdot\nabla_{\mathbf{y}}G(\mathbf{x}-\mathbf{y}) = \frac{1}{aV}\sum_{\mathbf{k}\neq 0}\frac{e^{i\mathbf{k}\cdot(\mathbf{x}-\mathbf{x}_0)}}{k^2}\sum_{\ell}\sqrt{4\pi(2\ell+1)}i^{-\ell}j_{\ell}(ka)\ell\left(\frac{r}{a}\right)^{\ell-1}Y_{\ell}(\theta,\phi). \tag{2.34}$$

2.2.4 Multipole Expansion of the Fluid Potential

For a point $\mathbf{x}$ in the fluid, the potential is given by the integral form of Laplace's equation,

$$\psi_f(\mathbf{x}) - \psi_0(\mathbf{x}) = \frac{1}{\lambda_f}\sum_j\int_{S_j} d\mathbf{y}\Big(G(\mathbf{x}-\mathbf{y})\mathbf{F}_f(\mathbf{y})\cdot\hat{\mathbf{n}}_{\mathbf{y}} + \lambda_f\psi_f(\mathbf{y})\hat{\mathbf{n}}_{\mathbf{y}}\cdot\nabla_{\mathbf{y}}G(\mathbf{x}-\mathbf{y})\Big) \tag{2.35}$$

where $\psi_0(\mathbf{x})$ is the externally imposed potential, and the sum goes over all N particles in $\mathbb{L}$. Because of the periodic boundary conditions, the potential $\psi_f(\mathbf{x}) - \psi_0(\mathbf{x})$ does not decay as $\mathbf{x} \to \infty$, so there is an additional integral in (2.35) over a surface at infinity to ensure the well-posedness of the problem. Bonnecaze and Brady

[§]This normal derivative requires us to use the specific expansion in equation (2.29) with a particular r dependence rather than an arbitrary spherical harmonic expansion with unspecified r dependence.

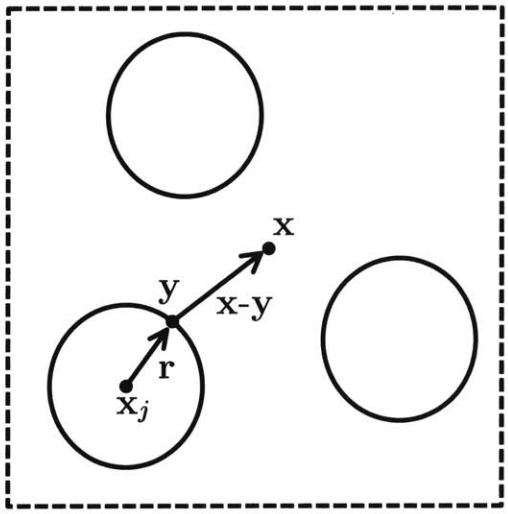

Figure 2.1: Schematic of the geometry of the multipole expansion.

showed that this term ends up canceling out,[145] so we neglect it from the beginning in our derivation here. For each of the terms in the j sum, we substitute the spherical harmonic expansion for the periodic Green's function about $\mathbf{x}_j$ and write the integral in terms of $\mathbf{r} \equiv \mathbf{y} - \mathbf{x}_j$, whose spherical coordinates are the same as that in the expansion,

$$\psi_f(\mathbf{x}) - \psi_0(\mathbf{x}) = \frac{1}{\lambda_f V} \sum_j \sum_{\mathbf{k}\neq 0} \frac{e^{i\mathbf{k}\cdot(\mathbf{x}-\mathbf{x}_j)}}{k^2} \sum_\ell \sqrt{4\pi(2\ell+1)} i^{-\ell} j_\ell(ka) \int_{S_j} d\mathbf{r} \left(Y_\ell \mathbf{F}_f \cdot \hat{\mathbf{n}} + \frac{\ell \lambda_f}{a} Y_\ell \psi_f \right). \quad (2.36)$$

Writing out the spherical harmonics for each ℓ, $Y_0 = 1/\sqrt{4\pi}$, $Y_1 = \sqrt{3/4\pi}\, z/a$, $Y_2 = \sqrt{5/16\pi}(3z^2/a^2 - 1)$, *etc.* and using the definitions of the particle charge, dipole, quadrupole, *etc.* moments

$$q_j \equiv \int_{S_j} d\mathbf{r}\, \mathbf{F}_f \cdot \hat{\mathbf{n}}, \quad (2.37)$$

$$\mathbf{S}_j \equiv \int_{S_j} d\mathbf{r}\, \left(\mathbf{r}\mathbf{F}_f \cdot \hat{\mathbf{n}} + \lambda_f \psi_f \hat{\mathbf{n}} \right), \quad (2.38)$$

$$\mathbf{Q}_j \equiv \int_{S_j} d\mathbf{r} \left(\left(\mathbf{r}\mathbf{r} - \frac{1}{3}(\mathbf{r}\cdot\mathbf{r})\mathbf{I} \right) \mathbf{F}_f \cdot \hat{\mathbf{n}} + \left(\mathbf{r}\hat{\mathbf{n}} + \hat{\mathbf{n}}\mathbf{r} - \frac{2}{3}(\mathbf{r}\cdot\hat{\mathbf{n}})\mathbf{I} \right) \psi_f \right), \quad (2.39)$$

the potential becomes

$$\psi_f(\mathbf{x}) - \psi_0(\mathbf{x}) = \frac{1}{\lambda_f V} \sum_j \sum_{\mathbf{k}\neq 0} \frac{e^{i\mathbf{k}\cdot(\mathbf{x}-\mathbf{x}_j)}}{k^2} \left(q_j f_q(\mathbf{k}) + \mathbf{S}_j \cdot \mathbf{f}_S(\mathbf{k}) + \frac{1}{2} \mathbf{Q}_j : \mathbf{f}_Q(\mathbf{k}) + \cdots \right), \quad (2.40)$$

where the "shape factors" associated with the particle moments are

$$f_q(\mathbf{k}) \equiv j_0(ka), \quad (2.41)$$

$$\mathbf{f}_S(\mathbf{k}) \equiv -\frac{3i}{a} j_1(ka) \hat{\mathbf{k}}, \quad (2.42)$$

$$\mathbf{f}_Q(\mathbf{k}) \equiv -\frac{15}{a^2} j_2(ka) \left(\hat{\mathbf{k}}\hat{\mathbf{k}} - \frac{1}{3}\mathbf{I} \right). \quad (2.43)$$

and serve to propagate the particle moments through wave space.[¶]

[¶]The quadrupole shape factor $\mathbf{f}_Q$ that comes from the integral of Y_2 actually only has a $\hat{\mathbf{k}}\hat{\mathbf{k}}$ component. However, because $\mathbf{Q}_j$ is traceless, we can include an isotropic tensor in the shape factor without modifying the result. We choose this particular isotropic tensor so that both $\mathbf{Q}_j$ and its propagator share the same traceless property.

2.2.5 Multipole Expansion of the Particle Potential

Now that we have an expression for $\psi_f(\mathbf{x})$ in the fluid outside of a particle, we need to derive an expression for $\psi_p(\mathbf{x})$ inside a particle. Because there is no charge distribution inside the particle, the potential satisfies Laplace's equation and must be of the form,

$$\psi_p(\mathbf{r}) = \sum_{\ell=0}^{\infty} \sum_{m=-\ell}^{\ell} A_{\ell m} r^{\ell} Y_{\ell m}(\theta, \phi). \tag{2.44}$$

where the spherical coordinates (r, θ, ϕ) are relative to the particle center $\mathbf{x}_i$ and the coefficients of the $r^{-\ell-1}$ terms must all be zero so that ψ is finite everywhere. Like (2.30), this represents ψ_p as a local expansion about $\mathbf{x}_j$. The normal component of the flux inside the particle is then,

$$\mathbf{F}_p \cdot \hat{\mathbf{n}} = -\lambda_p \sum_{\ell m} A_{\ell m} \ell r^{\ell-1} Y_{\ell m}(\theta, \phi). \tag{2.45}$$

The coefficients are determined in terms of the particle moments. The definitions of the moments (2.37)–(2.39) are in terms of the potential and flux in the *fluid*. With the boundary conditions (2.23), $\psi_f = \psi_p$ and $\mathbf{F}_f \cdot \hat{\mathbf{n}} = \mathbf{F}_p \cdot \hat{\mathbf{n}} + q_0$, we can substitute the *particle* potential and flux from (2.45) into the definitions of the charge, dipole, quadrupole, *etc*,

$$q_j = \int_{S_j} d\mathbf{r}\ (\mathbf{F}_p \cdot \hat{\mathbf{n}} + q_0) = -\lambda_p \sum_{\ell m} A_{\ell m} \ell a^{\ell-1} \int_S d\mathbf{r}\, Y_{\ell m} + q_{f,j} = q_{f,j}, \tag{2.46}$$

$$\mathbf{S}_j = \int_{S_j} d\mathbf{r} \left(\mathbf{r} \left(\mathbf{F}_p \cdot \hat{\mathbf{n}} + q_0 \right) + \lambda_f \psi_p \hat{\mathbf{n}} \right) = \sum_{\ell m} A_{\ell m} a^{\ell-1} \int_{S_j} d\mathbf{r}\ (-\lambda_p \ell \mathbf{r} Y_{\ell m} + \lambda_f a Y_{\ell m} \hat{\mathbf{n}}) + \mathbf{S}_{f,j} \tag{2.47}$$

$$= \sum_m A_{1m} a\,(\lambda_f - \lambda_p) \int_{S_j} d\mathbf{r}\, Y_{1m} \hat{\mathbf{n}} + \mathbf{S}_{f,j} \tag{2.48}$$

$$\mathbf{Q}_j = \int_{S_j} d\mathbf{r} \left(\left(\mathbf{rr} - \frac{1}{3}(\mathbf{r}\cdot\mathbf{r})\mathbf{I} \right) (\mathbf{F}_p \cdot \hat{\mathbf{n}} + q_0) + \left(\mathbf{r}\hat{\mathbf{n}} + \hat{\mathbf{n}}\mathbf{r} - \frac{2}{3}(\hat{\mathbf{n}}\cdot\mathbf{r})\mathbf{I} \right) \lambda_f \psi_p \right), \tag{2.49}$$

$$= \sum_{\ell m} A_{\ell m} a^{\ell-1} \int_{S_j} d\mathbf{r} \left(-\ell \lambda_p a^2 \left(\hat{\mathbf{n}}\hat{\mathbf{n}} - \frac{1}{3}\mathbf{I} \right) Y_{\ell m} + 2\lambda_f a^2 \left(\hat{\mathbf{n}}\hat{\mathbf{n}} - \frac{1}{3}\mathbf{I} \right) Y_{\ell m} \right) + \mathbf{Q}_{f,j} \tag{2.50}$$

$$= \sum_m 2A_{2m} a^3 (\lambda_f - \lambda_p) \int_{S_j} d\mathbf{r} \left(\hat{\mathbf{n}}\hat{\mathbf{n}} - \frac{1}{3}\mathbf{I} \right) Y_{\ell m} + \mathbf{Q}_{f,j}, \tag{2.51}$$

where $q_{f,j}$, $\mathbf{S}_{f,j}$, and $\mathbf{Q}_{f,j}$ are the *permanent* charge, dipole, and quadrupole from the fixed charge distribution q_0. For simplicity, we allow a fixed net charge on the particles, but assume that they have no permanent dipole, quadrupole, and higher order moments, $\mathbf{S}_{f,j} = \mathbf{Q}_{f,j} = \cdots = 0$.

2.2.6 Constructing the Potential Matrix

With an expression for the potential in the fluid (2.40) and an expression for the potential in each particle (2.44), we can systematically construct a linear system of equations by equating these two expressions at the surface of a particle using the boundary conditions (2.23) and integrating over the particle surface,

$$\frac{1}{4\pi a^2} \int_{S_i} d\mathbf{x} \Big(\psi_p(\mathbf{x}) - \psi_0(\mathbf{x}) \Big) = \frac{1}{\lambda_f} \sum_j \sum_{\mathbf{k}\neq 0} \frac{1}{4\pi a^2} \int_{S_i} d\mathbf{x}\, \frac{e^{i\mathbf{k}\cdot(\mathbf{x}-\mathbf{x}_j)}}{k^2} \left(q_j f_q + \mathbf{S}_j \cdot \mathbf{f}_S + \frac{1}{2}\mathbf{Q}_j : \mathbf{f}_Q + \cdots \right). \tag{2.52}$$

We denote the surface average of the potential of particle i as,

$$\langle \psi \rangle_i \equiv \frac{1}{4\pi a^2} \int_{S_i} d\mathbf{x}\, \psi_p(\mathbf{x}). \tag{2.53}$$

We perform the integration of the external potential by first Taylor expanding about the center of particle i,

$$\frac{1}{4\pi a^2}\int_{S_i} d\mathbf{x}\,\psi_0(\mathbf{x}) = \frac{1}{4\pi a^2}\int_{S_i} d\mathbf{r}\,\left(\psi_0(\mathbf{x}_i) + \mathbf{r}\cdot\nabla\psi_0(\mathbf{x}_i) + \frac{1}{2}\mathbf{rr}:\nabla\nabla\psi_0(\mathbf{x}_i) + \cdots\right) \tag{2.54}$$

$$= \left(1 + \frac{a^2}{6}\nabla^2 + \frac{a^4}{120}\nabla^4 + \cdots\right)\psi_0(\mathbf{x}_i) = \psi_0(\mathbf{x}_i), \tag{2.55}$$

where we have used the fact that $\nabla^2\psi_0(\mathbf{x}_i) = \nabla^4\psi_0(\mathbf{x}_i) = \cdots = 0$. The result of the integration of the right side of (2.52) comes immediately from the spherical harmonic expansion of the periodic Green's function,

$$\frac{1}{4\pi a^2}\int_{S_i} d\mathbf{x}\,e^{i\mathbf{k}\cdot\mathbf{x}} = e^{i\mathbf{k}\cdot\mathbf{x}_i} j_0(ka). \tag{2.56}$$

Therefore, the result of the integration of the total expression (2.52) is

$$\langle\psi\rangle_i - \psi_0(\mathbf{x}_i) = \frac{1}{\lambda_f V}\sum_j\sum_{\mathbf{k}\neq 0}\frac{e^{i\mathbf{k}\cdot(\mathbf{x}_i-\mathbf{x}_j)}}{k^2} f_q\left(q_j f_q + \mathbf{S}_j\cdot\mathbf{f}_S + \frac{1}{2}\mathbf{Q}_j:\mathbf{f}_Q + \cdots\right). \tag{2.57}$$

We have isolated the lowest order harmonic of the potential of particle i. Now we isolate higher order moments. Multiplying (2.40) by $\mathbf{x}/4\pi a^4$ and integrating over the surface of particle i,

$$\frac{1}{4\pi a^4}\int_{S_i} d\mathbf{x}\Big(\mathbf{x}\psi_p(\mathbf{x}) - \mathbf{x}\psi_0(\mathbf{x})\Big) = \frac{1}{\lambda_f V}\sum_j\sum_{\mathbf{k}\neq 0}\frac{1}{4\pi a^4}\int_{S_i} d\mathbf{x}\,\mathbf{x}\frac{e^{i\mathbf{k}\cdot(\mathbf{x}-\mathbf{x}_j)}}{k^2}\left(q_j f_q + \mathbf{S}_j\cdot\mathbf{f}_S + \frac{1}{2}\mathbf{Q}_j:\mathbf{f}_Q + \cdots\right). \tag{2.58}$$

We use the spherical harmonic expansion for the particle interior to evaluate the left side,

$$\frac{1}{4\pi a^4}\int_{S_i} d\mathbf{x}\,\mathbf{x}\psi_p(\mathbf{x}) = \frac{1}{4\pi a^4}\sum_{\ell m} A_{\ell m} a^\ell \int_{S_i} d\mathbf{r}\,\mathbf{r}Y_{\ell m} = \frac{1}{4\pi a^2}\sum_m A_{1m}\int_{S_i} d\mathbf{r}\,\hat{\mathbf{n}}Y_{1m}. \tag{2.59}$$

We already showed in (2.48) that this can be written in terms of the particle dipole,

$$\frac{1}{4\pi a^4}\int_{S_i} d\mathbf{x}\,\mathbf{x}\psi_p(\mathbf{x}) = \frac{\mathbf{S}_i}{4\pi a^3(\lambda_f - \lambda_p)}. \tag{2.60}$$

The integral of the external potential again proceeds by Taylor expansion about $\mathbf{x}_i$

$$\frac{1}{4\pi a^4}\int_{S_i} d\mathbf{x}\,\mathbf{x}\psi_0(\mathbf{x}) = \frac{1}{4\pi a^4}\int_{S_i} d\mathbf{r}\,\left(\mathbf{r}\psi_0(\mathbf{x}_i) + \mathbf{rr}\cdot\nabla\psi_0(\mathbf{x}_i) + \frac{1}{2}\mathbf{rrr}:\nabla\nabla\psi_0(\mathbf{x}_i) + \cdots\right) = \frac{1}{3}\nabla\psi_0(\mathbf{x}_i). \tag{2.61}$$

The integral on the right side of equation (2.58) is,

$$\frac{1}{4\pi a^4}\int_{S_i} d\mathbf{x}\,\mathbf{x}e^{i\mathbf{k}\cdot\mathbf{x}} = e^{i\mathbf{k}\cdot\mathbf{x}_i}\frac{ij_1(ka)}{a}\hat{\mathbf{k}} \tag{2.62}$$

Combining equations (2.60) – (2.62) for the integral of the total expression (2.58),

$$-\nabla\psi_0(\mathbf{x}_i) = \frac{3\mathbf{S}_i}{4\pi a^3(\lambda_p - \lambda_f)} + \frac{1}{\lambda_f V}\sum_j\sum_{\mathbf{k}\neq 0}\frac{e^{i\mathbf{k}\cdot(\mathbf{x}_i-\mathbf{x}_j)}}{k^2}\mathbf{f}_S^*\left(q_j f_q + \mathbf{S}_j\cdot\mathbf{f}_S + \frac{1}{2}\mathbf{Q}_j:\mathbf{f}_Q + \cdots\right). \tag{2.63}$$

To isolate the second order harmonic, we multiply (2.40) by $(\mathbf{xx} - a^2\mathbf{I}/3)/4\pi a^6$ and integrate over the surface of i,

$$\frac{1}{4\pi a^6}\int_{S_i} d\mathbf{x}\left(\mathbf{xx} - \frac{1}{3}(\mathbf{x}\cdot\mathbf{x})\mathbf{I}\right)\Big(\psi_p(\mathbf{x}) - \psi_0(\mathbf{x})\Big)$$

$$= \frac{1}{\lambda_f}\sum_j\sum_{\mathbf{k}\neq 0}\frac{1}{4\pi a^6}\int_{S_i} d\mathbf{x}\,\left(\mathbf{xx} - \frac{1}{3}(\mathbf{x}\cdot\mathbf{x})\mathbf{I}\right)\frac{e^{i\mathbf{k}\cdot(\mathbf{x}-\mathbf{x}_j)}}{k^2}\left(q_j f_q + \mathbf{S}_j\cdot\mathbf{f}_S + \frac{1}{2}\mathbf{Q}_j:\mathbf{f}_Q + \cdots\right). \tag{2.64}$$

Using the spherical harmonic expansion of the potential to evaluate the first term in the integral on the left side,

$$\frac{1}{4\pi a^6}\int_{S_i} d\mathbf{x}\left(\mathbf{xx}-\frac{1}{3}(\mathbf{x}\cdot\mathbf{x})\mathbf{I}\right)\psi_p(\mathbf{x}) = \frac{1}{4\pi a^2}\sum_m A_{2m}\int_{S_i} d\mathbf{r}\left(\hat{\mathbf{n}}\hat{\mathbf{n}}-\frac{1}{3}\mathbf{I}\right)Y_{2m} = \frac{\mathbf{Q}_i}{8\pi a^5(\lambda_f-\lambda_p)}. \tag{2.65}$$

Using a Taylor expansion of the external potential to evaluate the second term in the integral on the left side of (2.64),

$$\begin{aligned}
&\frac{1}{4\pi a^6}\int_{S_i} d\mathbf{x}\left(\mathbf{xx}-\frac{1}{3}(\mathbf{x}\cdot\mathbf{x})\mathbf{I}\right)\psi_0(\mathbf{x}) \\
&\quad= \frac{1}{4\pi a^6}\int_{S_i} d\mathbf{r}\left(\mathbf{rr}-\frac{r^2}{3}\mathbf{I}\right)\left(\psi_0(\mathbf{x}_i)+\mathbf{r}\cdot\nabla\psi_0(\mathbf{x}_i)+\frac{1}{2}\mathbf{rr}:\nabla\nabla\psi_0(\mathbf{x}_i)+\cdots\right) &(2.66)\\
&\quad= \frac{1}{15}\nabla\nabla\psi_0(\mathbf{x}_i). &(2.67)
\end{aligned}$$

Evaluating the right side of (2.64) directly,

$$\frac{1}{4\pi a^6}\int_{S_i} d\mathbf{x}\left(\mathbf{xx}-\frac{1}{3}(\mathbf{x}\cdot\mathbf{x})\mathbf{I}\right)\frac{e^{i\mathbf{k}\cdot(\mathbf{x}-\mathbf{x}_j)}}{k^2} = -e^{i\mathbf{k}\cdot\mathbf{x}_i}\frac{j_2(ka)}{a^2}\left(\hat{\mathbf{k}}\hat{\mathbf{k}}-\frac{1}{3}\mathbf{I}\right). \tag{2.68}$$

Combining equations (2.65) – (2.68) for the integral of the total expression (2.64),

$$-\nabla\nabla\psi_0(\mathbf{x}_i) = \frac{15\mathbf{Q}_i}{8\pi a^5(\lambda_p-\lambda_f)} + \frac{1}{\lambda_f V}\sum_j\sum_{\mathbf{k}\neq 0}\frac{e^{i\mathbf{k}\cdot(\mathbf{x}_i-\mathbf{x}_j)}}{k^2}\mathbf{f}_Q\left(q_jf_q+\mathbf{S}_j\cdot\mathbf{f}_S+\frac{1}{2}\mathbf{Q}_j:\mathbf{f}_Q+\cdots\right). \tag{2.69}$$

In summary,

$$\langle\psi\rangle_i-\psi_0(\mathbf{x}_i) = \frac{1}{\lambda_f V}\sum_j\sum_{\mathbf{k}\neq 0}\frac{e^{i\mathbf{k}\cdot(\mathbf{x}_i-\mathbf{x}_j)}}{k^2}f_q\left(q_jf_q+\mathbf{S}_j\cdot\mathbf{f}_S+\frac{1}{2}\mathbf{Q}_j:\mathbf{f}_Q+\cdots\right) \tag{2.70}$$

$$-\nabla\psi_0(\mathbf{x}_i) = \frac{3\mathbf{S}_i}{4\pi a^3(\lambda_p-\lambda_f)} + \frac{1}{\lambda_f V}\sum_j\sum_{\mathbf{k}\neq 0}\frac{e^{i\mathbf{k}\cdot(\mathbf{x}_i-\mathbf{x}_j)}}{k^2}\mathbf{f}_S^*\left(q_jf_q+\mathbf{S}_j\cdot\mathbf{f}_S+\frac{1}{2}\mathbf{Q}_j:\mathbf{f}_Q+\cdots\right) \tag{2.71}$$

$$-\nabla\nabla\psi_0(\mathbf{x}_i) = \frac{15\mathbf{Q}_i}{8\pi a^5(\lambda_p-\lambda_f)} + \frac{1}{\lambda_f V}\sum_j\sum_{\mathbf{k}\neq 0}\frac{e^{i\mathbf{k}\cdot(\mathbf{x}_i-\mathbf{x}_j)}}{k^2}\mathbf{f}_Q\left(q_jf_q+\mathbf{S}_j\cdot\mathbf{f}_S+\frac{1}{2}\mathbf{Q}_j:\mathbf{f}_Q+\cdots\right) \tag{2.72}$$

with

$$f_q(\mathbf{k})\equiv j_0(ka),\quad \mathbf{f}_S(\mathbf{k})\equiv -\frac{3i}{a}j_1(ka)\hat{\mathbf{k}},\quad \mathbf{f}_Q(\mathbf{k})\equiv -\frac{15}{a^2}j_2(ka)\left(\hat{\mathbf{k}}\hat{\mathbf{k}}-\frac{1}{3}\mathbf{I}\right). \tag{2.73}$$

We can write this in the condensed form,

$$\begin{bmatrix}\langle\Psi\rangle-\Psi_0\\ \mathscr{E}_0\\ \nabla\mathscr{E}_0\\ \vdots\end{bmatrix} = \begin{bmatrix}\mathscr{M}^E_{\psi q} & \mathscr{M}^E_{\psi S} & \mathscr{M}^E_{\psi Q} & \cdots\\ \mathscr{M}^E_{Eq} & \mathscr{M}^E_{ES} & \mathscr{M}^E_{EQ} & \cdots\\ \mathscr{M}^E_{\nabla q} & \mathscr{M}^E_{\nabla S} & \mathscr{M}^E_{\nabla Q} & \cdots\\ \vdots & \vdots & \vdots & \ddots\end{bmatrix}\cdot\begin{bmatrix}\mathscr{q}\\ \mathscr{S}\\ \mathscr{Q}\\ \vdots\end{bmatrix} \tag{2.74}$$

where now $\langle\Psi\rangle-\Psi_0\equiv[\langle\psi\rangle_1-\psi_0(\mathbf{x}_1),\ldots,\langle\psi\rangle_N-\psi_0(\mathbf{x}_N)]^T$, $\mathscr{E}_0\equiv[-\nabla\psi_0(\mathbf{x}_1),\ldots,-\nabla\psi_0(\mathbf{x}_N)]^T$, $\nabla\mathscr{E}_0\equiv[-\nabla\nabla\psi_0(\mathbf{x}_1),\ldots,-\nabla\nabla\psi_0(\mathbf{x}_N)]^T$, ... are lists of all particle potentials, external fields, and other gradients, $\mathscr{q}\equiv[q_1,\ldots q_N]^T$, $\mathscr{S}\equiv[\mathbf{S}_1,\ldots,\mathbf{S}_N]^T$, $\mathscr{Q}\equiv[\mathbf{Q}_1,\ldots,\mathbf{Q}_N]^T$, ... are lists of all particle charges, dipoles, and other moments, and the $\mathscr{M}^E_{pm}$ blocks are tensors that couple the p^{th} potential gradient to the m^{th} moment. The matrix $\mathscr{M}^E$ is called the potential matrix, as it converts moments to potentials and potential gradients, and is Hermitian and positive definite.[128,151,152] Each block is of the form of a wave space sum of the Green's function propagated by a product of two shape factors. The only difference between the blocks is which shape factors are present in the product. Moving rightward between blocks increases the second shape

factor by one degree (*i.e.* $f_q \to \mathbf{f}_S \to \mathbf{f}_Q \to \cdots$). Moving downward between the blocks increases the first shape factor by one degree, with every other shape factor complex conjugated (*i.e* $f_q \to \mathbf{f}_S^* \to \mathbf{f}_Q \to \cdots$). The diagonal blocks also contain an additional self term.

Typically, the particle charges $\mathscr{q}$, external field $\mathscr{E}_0$, and all higher external field gradients are known while the particle potentials $\langle\Psi\rangle - \Psi_0$, dipoles $\mathscr{S}$, and all higher order moments are unknown. If the expansion is truncated at the p^{th} moment, we have a linear system of p^2N equations and p^2N unknowns. The potential matrix $\mathscr{M}^E$ is dense and therefore takes $O(p^4N^2)$ operations to construct and $O(p^6N^3)$ operations to invert, both of which are infeasible when N is large. However, $\mathscr{M}^E$ is Hermitian positive definite, and (2.74) can be solved efficiently using a Krylov subspace method, of which we choose to use the general minimized residual (GMRES) method.[153] Rather than construct $\mathscr{M}^E$ explicitly, we compute its action on a vector $\mathscr{M}^E \cdot \mathbf{v}$ in $O(p^2N(\log N)^{d/(d+3)})$ calculations, where d is the fractal dimension of the particle configuration, as discussed in section 2.3.

2.2.7 Computing Forces

Once the unknown particle moments are found, we can compute forces. Let's consider the case of charge-free particles, in a constant external field. The total electric potential energy of the suspension is,[144,154]

$$U = -\frac{1}{2}\mathscr{S} \cdot \mathscr{E}_0. \tag{2.75}$$

The dipoles are computed from the external field as

$$U = -\frac{1}{2}\mathscr{M}_{ES}^{E\,-1} : \mathscr{E}_0\mathscr{E}_0. \tag{2.76}$$

The electric force on a particle i is calculated as the gradient of the electric potential energy,

$$\mathbf{F}_i^E = -\nabla_{\mathbf{x}_i} U = -\frac{1}{2}\nabla_{\mathbf{x}_i}\mathscr{M}_{ES}^E : \left(\mathscr{M}_{ES}^{E\,-1} \cdot \mathscr{E}_0\right)\left(\mathscr{M}_{ES}^{E\,-1} \cdot \mathscr{E}_0\right) = -\frac{1}{2}\nabla_{\mathbf{x}_i}\mathscr{M}_{ES}^E : \mathscr{S}\mathscr{S}, \tag{2.77}$$

or

$$\mathbf{F}_i^E = -\sum_j \nabla_{\mathbf{x}_i}\mathbf{M}_{ES}^E : \mathbf{S}_i\mathbf{S}_j. \tag{2.78}$$

If particles have a net charge, similar manipulations yield

$$\mathbf{F}_i^E = -\frac{1}{2}\begin{bmatrix}\mathscr{q} & \mathscr{S}\end{bmatrix} \cdot \begin{bmatrix}\nabla_{\mathbf{x}_i}\mathscr{M}_{\psi q}^E & \nabla_{\mathbf{x}_i}\mathscr{M}_{\psi S}^E \\ \nabla_{\mathbf{x}_i}\mathscr{M}_{Eq}^E & \nabla_{\mathbf{x}_i}\mathscr{M}_{ES}^E\end{bmatrix} \cdot \begin{bmatrix}\mathscr{q} \\ \mathscr{S}\end{bmatrix} \tag{2.79}$$

$$= -\sum_j \left(\nabla_{\mathbf{x}_i}\mathbf{M}_{\psi q}^E q_i q_j + \nabla_{\mathbf{x}_i}\mathbf{M}_{\psi S}^E \cdot q_i\mathbf{S}_j + \nabla_{\mathbf{x}_i}\mathbf{M}_{Eq}^E \cdot \mathbf{S}_i q_j + \nabla_{\mathbf{x}_i}\mathbf{M}_{ES}^E : \mathbf{S}_i\mathbf{S}_j\right) \tag{2.80}$$

2.3 Spectrally-Accurate Ewald Summation

To multiply one of the blocks of $\mathscr{M}^E$ with one of the particle moment vectors, *e.g.* $\mathscr{M}_{\psi q}^E \cdot \mathscr{q}$ or $\mathscr{M}_{ES}^E \cdot \mathscr{S}$, we must evaluate sums of the form,

$$\mathbf{p}_i^m(\mathbf{x}_i) = \frac{1}{\lambda_f V}\sum_{\mathbf{k}\neq 0}\mathbf{f}_p(\mathbf{k})\sum_j \frac{e^{i\mathbf{k}\cdot(\mathbf{x}_i-\mathbf{x}_j)}}{k^2}\mathbf{f}_m(\mathbf{k}) \cdot \mathbf{m}_j, \tag{2.81}$$

where $\mathbf{m}_j$ is any of the particle moments, $\mathbf{p}_i^m$ is the contribution to the potential or one of its gradients from the $\mathbf{m}$ moments, and $\mathbf{f}_p(\mathbf{k})$ and $\mathbf{f}_m(\mathbf{k})$ are their corresponding shape factors. For example, $\mathscr{M}_{\psi S}^E \cdot \mathscr{S}$ gives the dipole contribution to the potential, so $\mathbf{p} = \langle\psi\rangle - \psi_0$, $\mathbf{m} = \mathbf{S}$, $\mathbf{f}_p = f_q$, and $\mathbf{f}_m = \mathbf{f}_S$. It is not numerically efficient to evaluate (2.81) directly. Not only does this require $O(N^2)$ operations, the wave space sum only decays algebraically as $1/k^4$ (each shape factor decays as $1/k$), requiring a large number of terms to attain a

desired error tolerance.[‖] We can improve the rate of convergence by introducing an Ewald splitting kernel, $h(k) \equiv e^{-k^2/4\xi^2}$, to split the sum into two terms, one that converges quickly in real space and the other that converges quickly in wave space. Using the Poisson summation formula to evaluate one portion in real space,

$$\mathbf{p}_i^m(\mathbf{x}_i) = \frac{1}{\lambda_f}\sum_{\mathbf{n}}\sum_j \mathcal{F}^{-1}\left\{\frac{e^{i\mathbf{k}\cdot(\mathbf{x}_i-\mathbf{x}_j)}}{k^2}\left(1-h(k)\right)\mathbf{f}_p(\mathbf{k})\mathbf{f}_m(\mathbf{k})\right\}\cdot\mathbf{m}_j + \frac{1}{\lambda_f V}\sum_{\mathbf{k}\neq 0}\mathbf{f}_p(\mathbf{k})\sum_j \frac{e^{i\mathbf{k}\cdot(\mathbf{x}_i-\mathbf{x}_j)}}{k^2}h(k)\mathbf{f}_m(\mathbf{k})\cdot\mathbf{m}_j, \tag{2.82}$$

where $\mathcal{F}^{-1}$ indicates the inverse Fourier transform. The Ewald splitting parameter ξ controls the rate of convergence of the real space and wave space sums. The real space sum is computed pairwise by evaluating the inverse transform analytically, listed in Appendix A. The wave space sum $\mathbf{p}^k$ can be further split by introducing a spectral parameter η into $h(k)$,[155**]

$$\mathbf{p}_i^k(\mathbf{x}_i) = \frac{1}{\lambda_f V}\sum_{\mathbf{k}\neq 0}\mathbf{f}_p e^{i\mathbf{k}\cdot\mathbf{x}_i}\frac{e^{-(1-\eta)k^2/4\xi^2}}{k^2}\sum_j \mathbf{f}_m\cdot\mathbf{m}_j e^{-\eta k^2/4\xi^2}e^{-i\mathbf{k}\cdot\mathbf{x}_j}. \tag{2.83}$$

We treat a portion of this sum

$$\widehat{\mathbf{H}}(\mathbf{k}) \equiv \sum_j \mathbf{m}_j e^{-\eta k^2/8\xi^2}e^{-i\mathbf{k}\cdot\mathbf{x}_j}, \tag{2.84}$$

as the Fourier transform, indicated with a hat "$\widehat{\ }$", of a real space quantity

$$\mathbf{H}(\mathbf{x}) = \left(\frac{2\xi^2}{\pi\eta}\right)^{3/2}\sum_j \mathbf{m}_j e^{-2\xi^2(\mathbf{x}-\mathbf{x}_j)^2/\eta}. \tag{2.85}$$

Computing $\mathbf{H}(\mathbf{x})$ can be thought as spreading (or projecting) the particle moments in real space to $\mathbf{x}$.[††] We multiply $\widehat{\mathbf{H}}(\mathbf{k})$ by a scaling factor to define a new quantity,

$$\widehat{\widetilde{\mathbf{H}}}(\mathbf{k}) \equiv \frac{e^{-(1-\eta)k^2/4\xi^2}}{k^2}\mathbf{f}_p\mathbf{f}_m\cdot\widehat{\mathbf{H}}(\mathbf{k}). \tag{2.86}$$

The potential can then be computed in real space using Parseval's formula,

$$\mathbf{p}_i^k(\mathbf{x}_i) = \frac{1}{\lambda_f V}\sum_{\mathbf{k}\neq 0}e^{i\mathbf{k}\cdot\mathbf{x}_i}e^{-\eta k^2/8\xi^2}\widehat{\widetilde{\mathbf{H}}}(\mathbf{k}) = \frac{1}{\lambda_f}\left(\frac{2\xi^2}{\pi\eta}\right)^{3/2}\int_V d\mathbf{x}\,\widetilde{\mathbf{H}}(\mathbf{x})e^{-2\xi^2(\mathbf{x}-\mathbf{x}_i)^2/\eta}, \tag{2.87}$$

which can be thought of contracting (or interpolating) $\widetilde{\mathbf{H}}(\mathbf{x})$ to $\mathbf{x}_i$. To compute forces, we need to evaluate the gradient of (2.81). This is handled with the same Ewald implementation as above, with the gradient of the real space sum evaluated directly after Fourier inversion (Appendix A) and the gradient of the wave space sum handled during contraction,

$$\nabla_{\mathbf{x}_i}\mathbf{p}_i^k(\mathbf{x}_i) = \frac{2}{\pi^{3/2}\lambda_f}\left(\frac{2\xi^2}{\eta}\right)^{5/2}\int_V d\mathbf{x}\,(\mathbf{x}-\mathbf{x}_i)\,\widetilde{\mathbf{H}}(\mathbf{x})e^{-2\xi^2(\mathbf{x}-\mathbf{x}_i)^2/\eta} \tag{2.88}$$

[‖] The two "extra" factors of $1/k$ from the shape factors are a bonus of the specific way we derived the potential tensor in Section 2.2. Typical Ewald formulations[145,155] use the $a \to 0$ point-particle limit (Appendix A.9) where the wave space sums decay only as $1/k^2$.

[**] η can be different in different dimensions, in which case the exponentials take the form $e^{-\eta_x k_x^2/4\xi^2}e^{-\eta_y k_y^2/4\xi^2}e^{-\eta_z k_z^2/4\xi^2}$.

[††] The shape factor $\mathbf{f}_m$ can be excluded (as in (2.83)) or included in the spreading kernel. If the shape factor is excluded, we spread vectors and tensors (*i.e.* spread dipoles and quadrupoles) to a grid. This requires more FFTs, one for each component of the moment, but a smaller support on the grid.[156] If the shape factor is included, we spread scalars (*i.e.* charges), which requires only a single FFT, but a larger support.[156] We can also mix these two extremes and spread only a portion of the shape factor. For example, we can spread quadrupoles to the grid as dipoles by spreading $\mathbf{Q}\cdot\hat{\mathbf{k}}$ rather than using both $\hat{\mathbf{k}}$ in the shape factor. In practice, the FFTs are fast compared to spreading, so it is better to exclude the shape factors in the spreading kernel.

The following algorithm details an efficient scheme for implementing the Ewald summation on GPUs. This calculation is performed for every component of each block in (2.74) on each iteration.

1. Real Space Sum. The first sum in (2.82) can be rapidly computed in real space because its terms decay exponentially. We define a cutoff radius r_c and compute the sum between all pairs of particles that are separated by a distance less than r_c. Using a neighbor list constructed in $O(N)$ time to find particle pairs separated by less than r_c, the real space sum can be computed in $O(NN_{\text{nb}})$, where the average number of neighbors is $N_{\text{nb}} \sim r_c^d \phi$, ϕ is the particle volume fraction, and d is the fractal dimension of the particle configuration. By truncating the real space sum at r_c, we commit a truncation error ε_r. While it is possible to get rigorous bounds on the error,[128,129,155,156] it is convenient to use error *estimates*. Because the terms in the real space sum decay as $e^{-r^2\xi^2}$, the simplest estimate is

$$\varepsilon_r \leq Ce^{-r_c^2\xi^2}, \tag{2.89}$$

where C is some constant. On the GPU, the real space sum is performed using one thread per particle that loops through a particle's neighbors.

2. Spreading. The second sum in (2.82) can be rapidly computed in wave space because its terms decay exponentially as $e^{-k^2/4\xi^2}$. We define a cutoff wave vector k_c, and neglect terms with $|\mathbf{k}| > k_c$. Similarly to the real space sum, we suffer a truncation error estimated as,

$$\varepsilon_k \leq Ce^{-k_c^2/4\xi^2}. \tag{2.90}$$

k_c corresponds to a real/wave space cubic[‡‡] grid of $N_g = 1 + Lk_c/\pi$ nodes in each dimension with spacing $h \equiv L/N_g$ used to evaluate fast Fourier transforms (FFTs) and inverse fast Fourier transforms (IFFTs). Evaluating $\mathbf{H}(\mathbf{x}) = (2\xi^2/\pi\eta)^{3/2} \sum_j \mathbf{m}_j e^{-2\xi^2(\mathbf{x}-\mathbf{x}_j)^2/\eta}$ on these grid points corresponds to spreading (or projecting) the particle moments to a grid using Gaussians. Because the Gaussian decays rapidly, we can truncate the spread to a cubic array of the closest P grid points in each dimension in $O(NP^3)$ calculations, suffering a truncation error,

$$\varepsilon_t \leq Ce^{-h^2P^2\xi^2/2\eta} \tag{2.91}$$

On the GPU, spreading is performed using one block of P^3 threads per particle, with each thread corresponding to one of the P^3 supporting grid points.

3. Fast Fourier Transform. With $\mathbf{H}(\mathbf{x})$ evaluated on a regular grid, we can compute its Fourier transform $\widehat{\mathbf{H}}(\mathbf{k})$ using efficient $O(N_g^3 \log N_g^3)$ FFT algorithms, like those in the NVIDIA cuFFT library.[157]

4. Scaling. We compute $\widehat{\widetilde{\mathbf{H}}}(\mathbf{k})$ by scaling the $\widehat{\mathbf{H}}(\mathbf{k})$ values at each of the grid points in $O(N_g^3)$ calculations. The scaling operation converts the particle moments into potentials in wave space. On the GPU, scaling is performed using one thread per grid point.

5. Inverse Fast Fourier Transform. As with the FFT step, IFFTs yield $\widetilde{\mathbf{H}}(\mathbf{x})$ on the grid in $O(N_g^3 \log N_g^3)$ calculations.

6. Contraction. We contract (or interpolate) $\widetilde{\mathbf{H}}(\mathbf{x})$ from the grid to the particle positions $\mathbf{x}_i$ using Gaussians from the integration in (2.87), evaluated numerically using quadrature *via* the trapezoidal rule. Because the Gaussians decay rapidly, we can truncate the contraction to a cubic array of the closest P grid points in each dimension in $O(NP^3)$ calculations, suffering a truncation error (2.91) identical to the spreading step. Because our domain and integrand in (2.87) is periodic, the trapezoidal rule quadrature is spectrally accurate, with a quadrature error[128,129,155,156]

$$\varepsilon_q \leq Ce^{-\pi^2\eta/2\xi^2h^2}. \tag{2.92}$$

[‡‡]We assume a cubic domain here for simplicity, but this method works in general for orthorhombic geometries with unequal dimensions L_x, L_y, and L_z, which leads to different numbers of grid nodes in each direction, $N_{g,x}$, $N_{g,y}$, and $N_{g,z}$, for the same k_c.

We can relate η and P by requiring the quadrature and truncation errors to contribute equally to the total error in the contraction step, $\varepsilon_q \approx \varepsilon_t$,

$$\eta = \frac{h^2 \xi^2 P}{\pi}. \tag{2.93}$$

This establishes an optimum relationship between the decay of the Gaussian (controlled by η) and the support of the Gaussian (controlled by P) to ensure that the Gaussian is not so narrow that quadrature errors dominate nor so wide that truncation errors dominate. With this relationship, we can express the error for the entire contraction step as

$$\varepsilon_c \leq C e^{-\pi P/2}. \tag{2.94}$$

To summarize,

step	complexity	error estimate
real space sum	$O(N r_c^d)$	$\varepsilon_r \leq e^{-r_c^2 \xi^2}$
wave space sum	—	$\varepsilon_k \leq e^{-k_c^2/4\xi^2}$
FFT and IFFT	$O(N_g^3 \log N_g^3)$	—
spreading and contracting	$O(NP^3)$	$\varepsilon_c \leq e^{-\pi P/2}$

The total computation time is therefore,

$$t = C_1 N r_c^d + C_2 N_g^3 \log N_g^3 + C_3 N P^3. \tag{2.95}$$

We can use the error estimates to choose parameters based on our desired error tolerance ε,

$$r_c = \frac{\sqrt{-\ln \varepsilon}}{\xi}, \quad N_g = \frac{2L\xi\sqrt{-\ln \varepsilon}}{\pi}, \quad P = \frac{-2 \ln \varepsilon}{\pi} \tag{2.96}$$

Substituting into the total computation time, assuming all of the constants are $O(1)$, and keeping only the highest order terms in N,

$$t = N\xi^{-d} + N\xi^3 \log N + N \ln \varepsilon. \tag{2.97}$$

We choose the Ewald splitting parameter to be the value $\xi = \xi^*$ that minimizes the computation time,

$$\left.\frac{\partial t}{\partial \xi}\right|_{\xi=\xi^*} = 0 \Rightarrow \xi^* \sim \frac{1}{(\log N)^{1/(d+3)}}. \tag{2.98}$$

Substituting ξ^* back into the total computation time and keeping only the highest order in N,

$$t \sim N(\log N)^{d/(d+3)}. \tag{2.99}$$

In the worst case scenario of a fractal dimension of $d = 3$, t is $O(N\sqrt{\log N})$, which is still an enhancement over traditional $N \log N$ methods. Because solving (2.74) iteratively is limited by how quickly we can evaluate the Ewald sums in the matrix/vector dot product, this spectral Ewald method allows for rapid calculation of the many-bodied electric forces in dispersions.

Figure 2.2 shows the absolute error, *e.g.* $|\mathbf{S}_{\text{approx}} - \mathbf{S}_{\text{exact}}|$, in computing the dipoles and forces on a pair of uncharged particles in an electric field $\widetilde{E}_0 = 1/4\pi$, where $\widetilde{E}_0 \equiv E_0\sqrt{a^3\lambda_f/k_BT}$, compared to the specified error tolerance ε. The error agrees well with ε, so our error estimates prove reliable. Figure 2.2 also shows the computation time as a function of the error tolerance, which increases linearly as the error tolerance decreases exponentially, *i.e.* $t \sim -\log \varepsilon$, confirming that the method is spectrally accurate. Figure 2.2D shows that the computation time scales nearly linearly with the number of particles. Though we predicted the computation time should scale as $t \sim N(\log N)^{d/(d+3)}$, in practice, the $\sqrt{\log N}$ portion is not observed, and the Ewald sums are evaluated in nearly $O(N)$ time for up to at least 10^6 particles. Thus, our method allows us to accurately simulate very large systems.

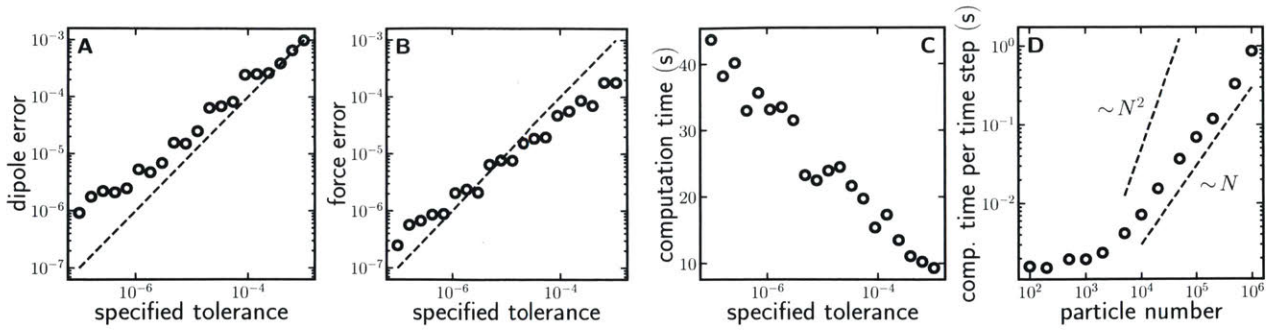

Figure 2.2: The absolute error in computing the dipoles (**A**) and forces (**B**) and the computation time (**C**) as a function of specified error tolerance for two particles separated a distance $\widetilde{r} = 3$ oriented parallel to an applied field $\widetilde{E}_0 = 1/4\pi$. The dashed black lines of unity slope indicate errors equal to the specified tolerance. These calculations were performed on an Intel(R) Xeon(R) E5-2620 CPU processor. Panel **D** is the computation time per time step as a function of the number of particles N for an initially random configuration of particles averages over 1000 time steps of a simulation. These calculations were performed on a GeForce GTX 980 Ti GPU.

2.4 An Immersed Boundary Method for Electric and Magnetic Forces of Arbitrarily-Shaped Conductors

The previous method works well for monodisperse dispersions of spherical particles of any permittivity. In principle, the method could be extended to spheres of different radii a_j, and the final expressions would simply substitute a_j for a for each term in the j sums. For particles that are not too different in size, this method can be numerically implemented efficiently. However, when the particle sizes become disparate, the method becomes computationally expensive to evaluate. Consider the interaction between a very large uncharged sphere and a very small charged sphere. The small sphere induces a surface charge on the large sphere that is concentrated in the region of the surface closest to the small sphere.[158] The charge distribution on the rest of the large sphere is only weakly perturbed to maintain a net zero charge. This highly asymmetric, localized charge distribution is not well represented by the first few charge moments (dipole, quadrupole), so a large number of moments must be maintained for accuracy. Additionally, the Ewald sum implementation requires apportioning the interaction into real and wave space contributions truncated according to a single error tolerance. However, what looks "far away" for the small particle appears to be very close to the large particle, so it is not obvious how to efficiently separate the two sums. For nonspherical particles, the method could, in principle, be applied, but the surface integrals in Section 2.2 are difficult to evaluate for complicated shapes.

These limitations are problematic because there are many systems where electrically andmagnetically responsive objects are not all equal-sized spheres, including proteins,[42,159–161] electrolytes,[162] rods,[163–166] and polyhedra.[167,168] To model the electro- and magnetokinetics of these systems, we must generalize our method to arbitrarily-shaped particles.

2.4.1 The Composite Bead Model

We can construct a particle of arbitrary shape (which we will refer to as a "body") by tessellating its surface with spheres (which we will refer to as "beads") whose centers lay on the body surface. The beads are constrained to move together rigidly, and the composite body serves as an approximation for the true body. Because we already derived a method for the electrostatic interactions among beads, we can leverage it to compute the net interactions of the composite body. There are many ways to construct this surface tessellation. Surface meshing algorithms can be used to construct a mesh, and then beads can be placed at the mesh points. For spherical bodies, a convenient tessellation can be constructed by placing beads at the vertices of an iscohedron and iteratively bisecting edges with more beads.[169] To use our previously developed method, the tessellating beads must all be the same size, but we are free to choose the bead

radius. We have found that setting the beads to be as large as possible without overlapping yields a good approximation of the true surface. This approach is called an "immersed boundary method" because we use different, incommensurate discretizations of the body surfaces and the fluid. The surfaces are discretized with the bead tesselation and are "immersed" in the Fourier grid that discretizes the fluid.

2.4.2 Induced Surface Charge Distribution

In equation (2.74), we typically know the net charges on all the particles. Here, we know the net charge of a body, but because the body can polarize, we generally do not know the induced surface charge distribution (*i.e.* the charge on each bead). We must construct a system of equations for the charge distribution on the surface of each body in the dispersion. We will consider this simplest case where each body is a perfect conductor, though the following method can be generalized to dielectric bodies.

Consider N_b rigid body conductors each with center of mass position $\mathbf{X}_i$ made up of N_i beads of radius a_b tesselated over the body surfaces at positions $\mathbf{x}_{ij}$. We will use lowercase variables to indicate individual bead quantities and uppercase variables to indicate rigid body quantities. Lowercase bead quantities with two indices (ij) indicate the j^{th} bead on the i^{th} rigid body while a single greek index (α) implies a global bead ID (*e.g* the j^{th} bead on the i^{th} rigid body has a global index of $\alpha = (i-1)N_i + j$). The total charge on a rigid body Q_i is known and equal to the sum of the unknown bead charges q_{ij} on that body

$$Q_i = \sum_j q_{ij}. \tag{2.100}$$

The system is immersed in a constant electric field $\mathbf{E}_0$ that establishes the external potential $\psi_0(\mathbf{x}) = -\mathbf{x}\cdot\mathbf{E}_0$. Because the rigid body is a conductor, the potential everywhere in the body is constant, and each bead's potential $\psi_{ij}(\mathbf{x}_{ij})$ is equal to the potential $\Psi_i(\mathbf{X}_i)$ of the rigid body to which it belongs. The difference between the bead potential and the external potential is therefore

$$\psi_{ij} - \psi_{0,ij} = \Psi_i + \mathbf{x}_{ij}\cdot\mathbf{E}_0 = \Psi_i - \Psi_{0,i} + \mathbf{r}_{ij}\cdot\mathbf{E}_0, \tag{2.101}$$

where $\mathbf{r}_{ij} \equiv \mathbf{x}_{ij} - \mathbf{X}_i$ is the position of the bead relative to the center of mass of the rigid body. The bead potentials are also related to the bead charges by the potential tensor block $\mathscr{M}^E_{\psi q}$, which we will simply denote as $\mathbf{M}$ as the other blocks will not be used,

$$\psi_\alpha - \psi_{0,\alpha} = \sum_\beta M_{\alpha\beta} q_\beta, \tag{2.102}$$

where the sum goes over all $N = \sum_i N_i$ beads. We can combine these three equations with the help of a summation tensor,

$$\mathbf{\Sigma} \equiv \begin{bmatrix} 1 & 1 & \cdots & 0 & 0 & \cdots & 0 & 0 & \cdots \\ 0 & 0 & \cdots & 1 & 1 & \cdots & 0 & 0 & \cdots \\ 0 & 0 & \cdots & 0 & 0 & \cdots & 1 & 1 & \cdots \\ \vdots & \vdots & & \vdots & \vdots & & \vdots & \vdots & \end{bmatrix}. \tag{2.103}$$

$\mathbf{\Sigma}$ is an $N_b \times N$ matrix whose rows correspond to rigid bodies and columns correspond to beads. Each row is entirely 0s, except for N_i consecutive 1s corresponding to the N_i beads in rigid body i. Letting $\mathbf{q} \equiv [q_{11}, q_{12}, \cdots, q_{21}, q_{22}, \cdots]^T$ be a list of all bead charges and $\mathbf{Q} \equiv [Q_1, Q_2, \cdots]^T$ be a list of all rigid body charges,

$$\mathbf{Q} = \mathbf{\Sigma}\cdot\mathbf{q}. \tag{2.104}$$

Equations (2.101) and (2.102) can be combined to

$$\mathbf{M}\cdot\mathbf{q} = \mathbf{\Sigma}^T\cdot(\mathbf{\Psi} - \mathbf{\Psi}_0) + \mathbf{r}\cdot\mathbf{E}_0, \tag{2.105}$$

where $\mathbf{\Psi} - \mathbf{\Psi}_0 \equiv [\Psi_1 - \Psi_{0,1}, \Psi_2 - \Psi_{0,2}, \cdots]^T$ is a list of rigid body potentials less the external potential and $\mathbf{r}\cdot\mathbf{E}_0 \equiv [\mathbf{r}_{11}\cdot\mathbf{E}_0, \mathbf{r}_{12}\cdot\mathbf{E}_0, \cdots, \mathbf{r}_{21}\cdot\mathbf{E}_0, \mathbf{r}_{22}\cdot\mathbf{E}_0, \cdots]^T$ is a list of relative bead positions dotted with the external field. Equations (2.104) and (2.105) can be written in saddle point form,

$$\begin{bmatrix} -\mathbf{M} & \mathbf{\Sigma}^T \\ \mathbf{\Sigma} & 0 \end{bmatrix} \cdot \begin{bmatrix} \mathbf{q} \\ \mathbf{\Psi} - \mathbf{\Psi}^0 \end{bmatrix} = \begin{bmatrix} -\mathbf{r}\cdot\mathbf{E}^0 \\ \mathbf{Q} \end{bmatrix}. \tag{2.106}$$

This equation can be solved iteratively for the bead charges and the rigid body potentials.

2.4.3 Preconditioner

Taking advantage of the the saddle point form, we can apply the "constraint" preconditioner[170]

$$\mathbf{P} \equiv \begin{bmatrix} -\widetilde{\mathbf{M}} & \mathbf{\Sigma}^T \\ \mathbf{\Sigma} & 0 \end{bmatrix} = \begin{bmatrix} -\mathbf{I}_N/4\pi a_b \lambda_f & \mathbf{\Sigma}^T \\ \mathbf{\Sigma} & 0 \end{bmatrix} \tag{2.107}$$

where $\widetilde{\mathbf{M}}$ is an easily invertible approximation of $\mathbf{M}$ chosen to be its diagonal elements $\widetilde{\mathbf{M}} = \mathbf{I}_N/4\pi a_b \lambda_f$, where $\mathbf{I}_N$ is the $N \times N$ identity tensor. $\mathbf{P}$ can be inverted analytically,

$$\mathbf{P}^{-1} = \begin{bmatrix} -\widetilde{\mathbf{M}}^{-1} + \widetilde{\mathbf{M}}^{-1} \cdot \mathbf{\Sigma}^T \cdot \widetilde{\mathbf{A}}^{-1} \cdot \mathbf{\Sigma} \cdot \widetilde{\mathbf{M}}^{-1} & \widetilde{\mathbf{M}}^{-1} \cdot \mathbf{\Sigma}^T \cdot \widetilde{\mathbf{A}}^{-1} \\ \widetilde{\mathbf{A}}^{-1} \cdot \mathbf{\Sigma} \cdot \widetilde{\mathbf{M}}^{-1} & \widetilde{\mathbf{A}}^{-1} \end{bmatrix}, \tag{2.108}$$

where $\widetilde{\mathbf{A}} \equiv \mathbf{\Sigma} \cdot \widetilde{\mathbf{M}}^{-1} \cdot \mathbf{\Sigma}^T$ is the Schur complement of $-\widetilde{\mathbf{M}}$,

$$\widetilde{\mathbf{A}} = 4\pi a_b \lambda_f \begin{bmatrix} N_1 & & & \\ & N_2 & & \\ & & \ddots & \\ & & & N_M \end{bmatrix}, \quad \widetilde{\mathbf{A}}^{-1} = \frac{1}{4\pi a_b \lambda_f} \begin{bmatrix} 1/N_1 & & & \\ & 1/N_2 & & \\ & & \ddots & \\ & & & 1/N_M \end{bmatrix} \equiv \frac{\mathbf{B}_M}{4\pi a_b \lambda_f}. \tag{2.109}$$

Other terms in $\mathbf{P}^{-1}$ include,

$$\widetilde{\mathbf{A}}^{-1} \cdot \mathbf{\Sigma} \cdot \widetilde{\mathbf{M}}^{-1} = \begin{bmatrix} 1/N_1 & 1/N_1 & \cdots & 0 & 0 & \cdots \\ 0 & 0 & \cdots & 1/N_2 & 1/N_2 & \cdots \\ \vdots & \vdots & & \vdots & \vdots & \ddots \end{bmatrix} \equiv \mathbf{\Sigma}', \tag{2.110}$$

where $\mathbf{\Sigma}'$ is a tensor that averages bead quantities within each body, and

$$\widetilde{\mathbf{M}}^{-1} \cdot \mathbf{\Sigma}^T \cdot \widetilde{\mathbf{A}}^{-1} \cdot \mathbf{\Sigma} \cdot \widetilde{\mathbf{M}}^{-1} = 4\pi a_b \lambda_f \begin{bmatrix} \mathbf{1}_{N_1}/N_1 & & & \\ & \mathbf{1}_{N_2}/N_2 & & \\ & & \ddots & \\ & & & \mathbf{1}_{N_M}/N_M \end{bmatrix} \equiv 4\pi a_b \lambda_f \mathbf{B}_N, \tag{2.111}$$

where $\mathbf{1}_{N_i}$ is an $N_i \times N_i$ matrix of ones. Thus, the preconditioner inverse is

$$\mathbf{P}^{-1} = \begin{bmatrix} 4\pi a_b \lambda_f (\mathbf{B}_N - \mathbf{I}_N) & \mathbf{\Sigma}'^T \\ \mathbf{\Sigma}' & \mathbf{B}_M/4\pi a_b \lambda_f \end{bmatrix}. \tag{2.112}$$

2.4.4 Rigid Body Dipole Moments

The rigid body dipole moments can be computed from the bead charges by

$$\mathbf{S}_i = \sum_j \mathbf{r}_{ij} q_{ij}. \tag{2.113}$$

If we define a new summation tensor,

$$\mathbf{\Sigma}'' \equiv \begin{bmatrix} 1 & 1 & \cdots & 0 & 0 & \cdots & 0 & 0 & \cdots \\ 0 & 0 & \cdots & 1 & 1 & \cdots & 0 & 0 & \cdots \\ 0 & 0 & \cdots & 0 & 0 & \cdots & 1 & 1 & \cdots \\ \vdots & \vdots & & \vdots & \vdots & & \vdots & \vdots & \\ \mathbf{r}_{11} & \mathbf{r}_{12} & \cdots & 0 & 0 & \cdots & 0 & 0 & \cdots \\ 0 & 0 & \cdots & \mathbf{r}_{21} & \mathbf{r}_{22} & \cdots & 0 & 0 & \cdots \\ 0 & 0 & \cdots & 0 & 0 & \cdots & \mathbf{r}_{31} & \mathbf{r}_{32} & \cdots \\ \vdots & \vdots & & \vdots & \vdots & & \vdots & \vdots & \end{bmatrix}, \tag{2.114}$$

we can compute the rigid body charges and dipoles in a single matrix/vector multiply,

$$\begin{bmatrix}\mathbf{Q}\\ \mathbf{S}\end{bmatrix} = \boldsymbol{\Sigma}'' \cdot \mathbf{q}, \tag{2.115}$$

where $\mathbf{S} = [\mathbf{S}_1, \mathbf{S}_2, \cdots]^T$ is a list of rigid body dipoles. The bead charges are given from the matrix inversion,

$$\mathbf{q} = \mathbf{M}^{-1}\left(\boldsymbol{\Sigma}^T \cdot (\boldsymbol{\Psi} - \boldsymbol{\Psi}_0) + \mathbf{r} \cdot \mathbf{E}_0\right) = \mathbf{M}^{-1} \cdot \boldsymbol{\Sigma}''^T \cdot \begin{bmatrix}\boldsymbol{\Psi} - \boldsymbol{\Psi}_0\\ \mathbf{E}_0\end{bmatrix}. \tag{2.116}$$

Therefore, the moments are related to the potential gradients as

$$\begin{bmatrix}\mathbf{Q}\\ \mathbf{S}\end{bmatrix} = \boldsymbol{\Sigma}'' \cdot \mathbf{M}^{-1} \cdot \boldsymbol{\Sigma}''^T \cdot \begin{bmatrix}\boldsymbol{\Psi} - \boldsymbol{\Psi}_0\\ \mathbf{E}_0\end{bmatrix}. \tag{2.117}$$

The quantity $\boldsymbol{\Sigma}'' \cdot \mathbf{M}^{-1}\boldsymbol{\Sigma}''^T$ is called the "grand capacitance tensor" of the dispersion.

2.4.5 Rigid Body Forces and Torques

The potential energy of the system is expressed as a sum of products of rigid body moments and potential derivatives

$$U = \frac{1}{2}\sum_i \left(Q_i \Psi_i - \mathbf{S}_i \cdot \mathbf{E}_0\right) = \frac{1}{2}\mathbf{Q} \cdot \boldsymbol{\Psi}_0 + \frac{1}{2}\begin{bmatrix}\mathbf{q} & \boldsymbol{\Psi} - \boldsymbol{\Psi}_0\end{bmatrix} \cdot \begin{bmatrix}-\mathbf{r} \cdot \mathbf{E}_0\\ \mathbf{Q}\end{bmatrix}. \tag{2.118}$$

The induced charge distribution and rigid body potentials are computed from the inversion of equation (2.106),

$$U = \frac{1}{2}\mathbf{Q} \cdot \boldsymbol{\Psi}_0 + \frac{1}{2}\begin{bmatrix}-\mathbf{r} \cdot \mathbf{E}_0 & \mathbf{Q}\end{bmatrix} \cdot \begin{bmatrix}-\mathbf{M} & \boldsymbol{\Sigma}^T\\ \boldsymbol{\Sigma} & 0\end{bmatrix}^{-1} \cdot \begin{bmatrix}-\mathbf{r} \cdot \mathbf{E}_0\\ \mathbf{Q}\end{bmatrix}. \tag{2.119}$$

The force on an individual bead α is the negative derivative of the potential energy with respect to the bead position $\mathbf{x}_\alpha$, given all other beads remain fixed. Because the rigid body charges and external potentials do not depend on the bead positions, the negative derivative of the first term in (2.119), $-\nabla_{\mathbf{x}_\alpha}\mathbf{Q} \cdot \boldsymbol{\Psi}_0/2$, vanishes. The product rule splits the negative derivative of the second term in (2.119) into three terms with the gradient acting only on one of the three matrices. The first of these terms is,

$$-\left(\nabla_{\mathbf{x}_\alpha}\begin{bmatrix}-\mathbf{r} \cdot \mathbf{E}_0 & \mathbf{Q}\end{bmatrix}\right) \cdot \begin{bmatrix}-\mathbf{M} & \boldsymbol{\Sigma}^T\\ \boldsymbol{\Sigma} & 0\end{bmatrix}^{-1} \cdot \begin{bmatrix}-\mathbf{r} \cdot \mathbf{E}_0\\ \mathbf{Q}\end{bmatrix} = \begin{bmatrix}\nabla_{\mathbf{x}_\alpha}\mathbf{r} \cdot \mathbf{E}_0 & 0\end{bmatrix} \cdot \begin{bmatrix}\mathbf{q}\\ \boldsymbol{\Psi} - \boldsymbol{\Psi}_0\end{bmatrix} = q_\alpha \mathbf{E}_0 \tag{2.120}$$

and similarly for the term with the gradient applied to the third matrix. Notice that only the α^{th} component of $\nabla_{\mathbf{x}_\alpha}\mathbf{r} \equiv [\nabla_{\mathbf{x}_\alpha}\mathbf{r}_1, \nabla_{\mathbf{x}_\alpha}\mathbf{r}_2, \ldots, \nabla_{\mathbf{x}_\alpha}\mathbf{r}_\alpha, \ldots] = [0, 0, \ldots, \mathbf{I}, \ldots]$ is nonzero, so only the q_α term survives the dot product. The second term is,

$$\begin{aligned}
&-\begin{bmatrix}-\mathbf{r} \cdot \mathbf{E}_0 & \mathbf{Q}\end{bmatrix} \cdot \left(\nabla_{\mathbf{x}_\alpha}\begin{bmatrix}-\mathbf{M} & \boldsymbol{\Sigma}^T\\ \boldsymbol{\Sigma} & 0\end{bmatrix}^{-1}\right) \cdot \begin{bmatrix}-\mathbf{r} \cdot \mathbf{E}_0\\ \mathbf{Q}\end{bmatrix}\\
&\quad = \begin{bmatrix}-\mathbf{r} \cdot \mathbf{E}_0 & \mathbf{Q}\end{bmatrix} \cdot \begin{bmatrix}-\mathbf{M} & \boldsymbol{\Sigma}^T\\ \boldsymbol{\Sigma} & 0\end{bmatrix}^{-1} \cdot \begin{bmatrix}-\nabla_{\mathbf{x}_\alpha}\mathbf{M} & \nabla_{\mathbf{x}_\alpha}\boldsymbol{\Sigma}^T\\ \nabla_{\mathbf{x}_\alpha}\boldsymbol{\Sigma} & 0\end{bmatrix} \cdot \begin{bmatrix}-\mathbf{M} & \boldsymbol{\Sigma}^T\\ \boldsymbol{\Sigma} & 0\end{bmatrix}^{-1} \cdot \begin{bmatrix}-\mathbf{r} \cdot \mathbf{E}_0\\ \mathbf{Q}\end{bmatrix} && (2.121)\\
&\quad = \begin{bmatrix}\mathbf{q} & \boldsymbol{\Psi} - \boldsymbol{\Psi}_0\end{bmatrix} \cdot \begin{bmatrix}-\nabla_{\mathbf{x}_\alpha}\mathbf{M} & 0\\ 0 & 0\end{bmatrix} \cdot \begin{bmatrix}\mathbf{q}\\ \boldsymbol{\Psi} - \boldsymbol{\Psi}_0\end{bmatrix} && (2.122)\\
&\quad = -\mathbf{q} \cdot \nabla_{\mathbf{x}_\alpha}\mathbf{M} \cdot \mathbf{q} && (2.123)
\end{aligned}$$

Notice that because the summation tensor is constant, its gradient is zero, $\nabla_{\mathbf{x}_\alpha}\boldsymbol{\Sigma} = 0$, and only the upper left block of the matrix survives. Thus, the force on bead α is

$$\mathbf{f}_\alpha = q_\alpha \mathbf{E}_0 - \frac{1}{2}\left(\nabla_{\mathbf{x}_\alpha}\mathbf{M}\right) : \mathbf{q}\mathbf{q} \tag{2.124}$$

Although the second term was written as $\mathbf{q} \cdot \nabla_{\mathbf{x}_\alpha} \mathbf{M} \cdot \mathbf{q}$ in (2.123), rewriting the equations in index notation shows that both dot products should contract the vector indices of the charges with the indices of the potential tensor, leaving the force with the same indices as the gradient. Therefore the proper vector notation is the double dot product in (2.124). The force and torque on a rigid body can then be computed from the distribution of bead forces,

$$\mathbf{F}_i = \sum_j \mathbf{f}_{ij}, \tag{2.125}$$

$$\mathbf{L}_i = \sum_j \mathbf{r}_{ij} \times \mathbf{f}_{ij}. \tag{2.126}$$

These forces and torques serve as the input to a rigid body hydrodynamic integrator that computes the rigid body velocities and angular velocities of the composites by solving[169,171]

$$\begin{bmatrix} \mathscr{M}^H & \Sigma'''^T \\ \Sigma''' & 0 \end{bmatrix} \cdot \begin{bmatrix} \mathbf{f}_c \\ \begin{pmatrix} \mathscr{U} \\ \mathbf{\Omega} \end{pmatrix} \end{bmatrix} = \begin{bmatrix} 0 \\ \begin{pmatrix} \mathscr{F} \\ \mathscr{L} \end{pmatrix} \end{bmatrix} \tag{2.127}$$

where $\mathbf{f}_c$ is a list of N constraint forces on each bead that hold the rigid composite together and Σ''' is a summation tensor defined in reference 169. $\mathscr{U} = [\mathbf{U}_1, \mathbf{U}_2, ...\mathbf{U}]^T$ is a list of rigid body velocities and similarly for the rigid body angular velocities $\mathbf{\Omega}$, rigid body forces $\mathscr{F}$, and rigid body torques $\mathscr{L}$. Each bead ij then moves with a velocity specified by the translational $\mathbf{U}_i$ and rotational $\mathbf{\Omega}_i$ velocities of the rigid body i to which it belongs

$$\mathbf{u}_{ij} = \mathbf{U}_i + \mathbf{\Omega}_i \times \mathbf{r}_{ij}. \tag{2.128}$$

2.4.6 Validating the Immersed Boundary Method

We validate our immersed boundary method for conductors by comparing our results with exact solutions for simple scenarios.

Single Sphere in an External Field

The dipole moment of a single conducting sphere in a constant external field $\mathbf{E}_0$ is

$$\mathbf{S} = 4\pi a^3 \lambda_f \mathbf{E}_0, \tag{2.129}$$

where a is the radius of the sphere. We construct spherical composite bodies out of a varying number of N beads and compute the dipole moment $\widehat{\mathbf{S}}$. The relative error $\varepsilon \equiv |\widehat{\mathbf{S}} - \mathbf{S}| / |\mathbf{S}|$ is shown as a function of number of beads in Figure 2.3. The error converges fairly slowly with bead number, $\varepsilon \sim N^{-1/2}$, but we are able to achieve reasonable accuracy (within $\approx 5\%$ for $O(1000)$ beads). This slow convergence is actually to be expected based on the differences in size between the bead composite and the body it is trying to approximate. The beads are constrained to sit on the surface of the body of radius a and then assigned a bead radius a_b so that the beads are in contact with neighboring beads. For small numbers of beads, the composite bead body is quite a bit larger than the real body it is trying to approximate. The dipole is proportional to the volume of the body, so the composite has a larger dipole strength than the real body. The error in dipole is dominated by this volume difference, and not on the finite discretization of the body surface. We can assign an effective radius a_{eff} to the bead composite so that $\widehat{\mathbf{S}} = 4\pi a_{\text{eff}} \lambda_f \mathbf{E}_0$, shown in Figure 2.3.

Two Spheres in an External Field

The dipole moment of two conducting spheres with center-to-center separation vector $\mathbf{r}$ in a constant external field is given as the power series

$$\mathbf{S} = 4\pi a^3 \lambda_f \sum_{p=0}^{\infty} \left(\frac{a}{r}\right)^p (A_p \mathbf{I} + B_p \hat{\mathbf{r}}\hat{\mathbf{r}}) \cdot \mathbf{E}_0. \tag{2.130}$$

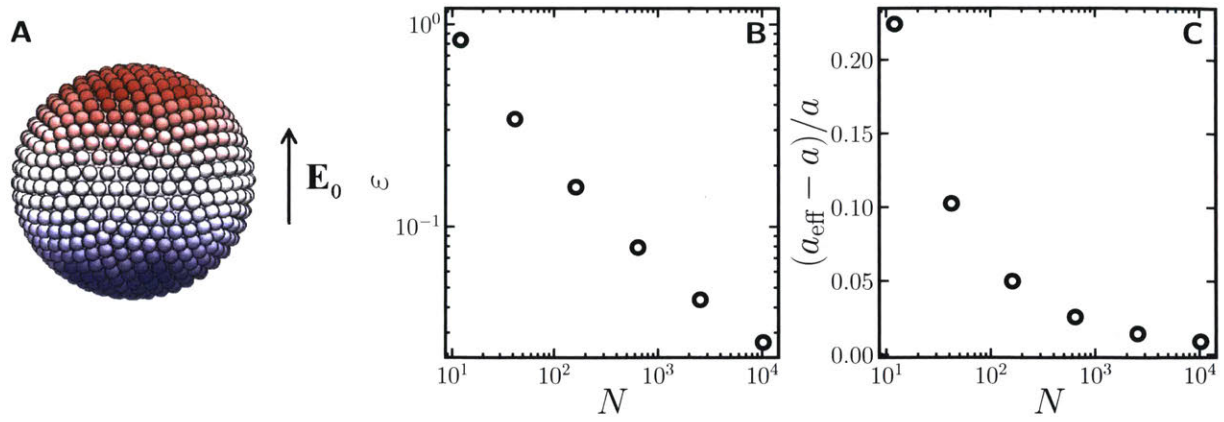

Figure 2.3: **A:** A spherical conductor constructed from N beads polarizes in an external field $\mathbf{E}_0$, acquiring the surface charge distribution indicated by bead color. Red indicates positive charge, white indicates zero charge, and blue indicates negative charge. **B:** The relative error in the dipole as a function of number of beads. **C:** The fractional increase in the effective radius a_{eff} of the composite sphere required so that (2.129) agrees with the computed dipole.

Jeffrey determined the coefficients A_p and B_p, which are given by recursion relations in Ref 172. The force on the spheres is related to the gradient of the dipole moments and can be evaluated directly from the gradient of (2.130) using the same coefficients

$$\mathbf{F} = -\nabla \mathbf{S} \cdot \mathbf{E}_0. \tag{2.131}$$

In Figure 2.4, we compute the dipole strength and the attractive force on a pair of particles oriented parallel to the external field using our method for various numbers of beads and compare the results to the analytic solution. Unlike the single sphere, where the induced charge distribution is symmetric about the sphere's equator, the induced charge distribution in one sphere is mostly localized to the region close to the other sphere. In this calculation, we assume a is fixed, so the bead radius a_b decreases as N increases. The field strength is $\widetilde{E}_0 = 1$, normalized by the fixed composite sphere radius as $\widetilde{E}_0 \equiv E_0\sqrt{a^3\lambda_f/k_BT}$, and similarly $\widetilde{S} \equiv S/\sqrt{a^3\lambda_f k_BT}$ and $\widetilde{F} = Fa/k_BT$. Both the dipole strength and the force increase as the particles move closer together. The numerical results converge to the exact result as the number of beads increase. From the single sphere calculation, we can use the effective radius a_{eff} rather than a to interpret the dipole calculation, improving the agreement with the exact solution. Each sphere's dipole is too large by a factor of $(a_{\text{eff}}/a)^3$, so the force is too large by a factor of $(a_{\text{eff}}/a)^6$. Correcting for a_{eff} improves the agreement with the exact force.

Face-Centered-Cubic Lattice of Conducting Spheres in an External Field

The exact dipole strength for cubic lattices of conducting spheres in an external field was calculated by Sangani and Acrivos.[173] In Figure 2.5, we compute the dipole strength of a face-centered-cubic (FCC) lattice of particles as a function of volume fraction ϕ. Like the two particle calculation, we hold a is fixed while a_b decreases as N increases. The field strength is $\widetilde{E}_0 = 1$, normalized as $\widetilde{E}_0 \equiv E_0\sqrt{a^3\lambda_f/k_BT}$, and $\widetilde{S} \equiv S/\sqrt{a^3\lambda_f k_BT}$. The dipole strength increases as the lattice becomes denser due to enhanced mutual polarization among the conducting spheres. At small volume fractions (2.5A), the dipole moment is the dominant contribution to the surface charge distribution which resembles that of an isolated sphere. At large volume fractions (2.5B), higher order moments contribute significantly and the charge distribution becomes concentrated to the spots near the bodies' neighbors, like the two-particle case. The numerical results converge to the exact solution as the number of beads increases, and the agreement is even better if we use the effective radius a_{eff} from the single sphere results to correct the dipoles as $\widetilde{S}(a/a_{\text{eff}})^3$.

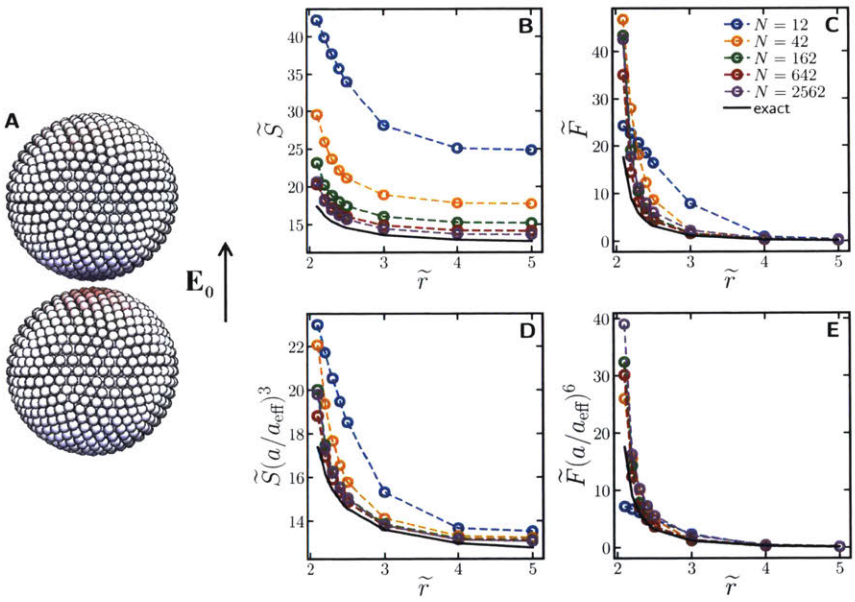

Figure 2.4: **A:** A pair of spherical conductors constructed from N beads each polarizes in the presence of an external field $\mathbf{E}_0$. **B** and **C:** The dipole strength $\widetilde{S}$ and force $\widetilde{F}$ (**C**) as a function of separation $\widetilde{r}$. **D** and **E:** The dipole and force corrected by factors of the effective radius a_{eff} determined from the single sphere calculation.

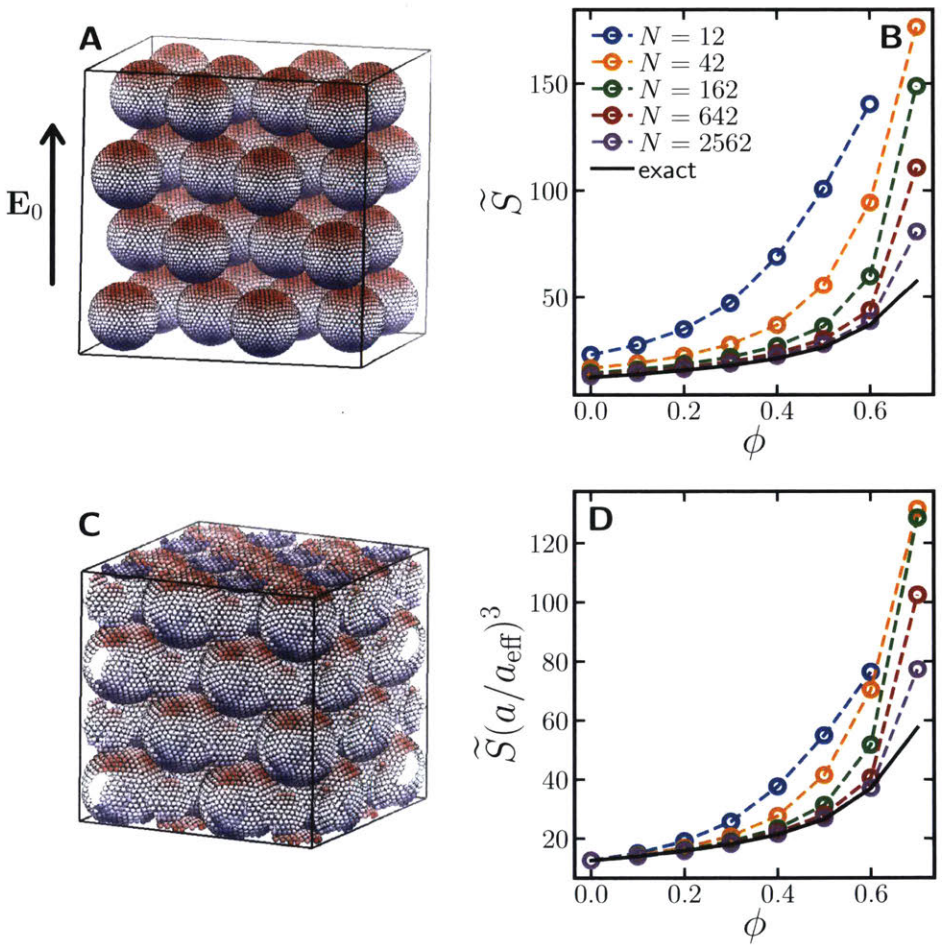

Figure 2.5: Conducting spheres oriented in a face-centered-cubic lattice at volume fractions of $\phi = 0.20$ (**A**) and $\phi = 0.60$ (**C**) polarized in an external field $\mathbf{E}_0$ oriented along one of the lattice directions. The dipole strength $\widetilde{S}$ (**B**) and corrected dipole $\widetilde{S}(a/a_{\text{eff}})^3$ (**D**) as a function of volume fraction ϕ.

Chapter 3

Dynamic, Directed Self-Assembly of Nanoparticles *via* Toggled Interactions: A Model System with Isotropic, Short-Ranged Attractions

In Chapter 1, we discussed numerous advantages of dynamic self-assembly of nanomaterials *via* toggled interactions over static self-assembly with steady interactions. The toggle protocol can avoid the propensity for particles to arrest in defective, disordered metastable states, as well as form new structures not observed with steady interactions. However, a major drawback of toggled self-assembly, along with other time-varying protocols, is the difficulty in predicting the assembled structures and their rates of formation. For steady interactions, the tools of statistical mechanics and equilibrium thermodynamics provide a straightforward and generic (albeit intractable in many cases) algorithm to compute equilibrium states. Several kinetic theories have been developed that rely on equilibrium thermodynamic principles to describe the dynamics of phase separation, such as classical nucleation theory,[119,120] Cahn-Hilliard kinetics,[121,122] and thermal barrier hopping.[174,175] Because of the cyclic driving force, structures formed by toggled self-assembly are not true, time-independent equilibrium states, but rather periodic-steady-states that are unchanged from cycle to cycle but vary within a toggle period. There is no generic theory to predict and describe such dissipative, out-of-equilibrium states or their rates of formation. This lack of understanding is the main obstacle to implementing toggled self-assembly for efficient, reliable nanomaterials fabrication.

To gain insight into toggled self-assembly, we investigate one of the simplest possible systems: a monodisperse suspension of spherical nanoparticles that interact with isotropic, short-ranged attractions that are toggled on for a time t_{on} and off for a time t_{off} periodically in time. Such systems have already been realized experimentally by decorating nanoparticles with photoswitchable ligands to induce short-ranged attractions that can be reversibly actuated by exposure to UV irradiation.[47,113] Short-ranged interactions are straightforward to incorporate into simulations, and the equilibrium phase behavior is well understood,[176–178] so toggled short-ranged attractions provide a useful prototype for dynamic toggled self-assembly that can be investigated experimentally, computationally, and *via* first principles theory. A fundamental understanding of this simple model will lead to methods for describing more complex processes. The more complicated cases of steady and toggled electric and magnetic field directed assembly is discussed in Chapters 3 and 4. As we will show, the assembly process modeled by toggled short-ranged attractions shares many features in common with experiments having more complicated interparticle interactions.

"Toggling" implies instantaneous switching between an "on" state in which particles are mutually attractive and an "off" state in which particles behave as hard spheres (*i.e.* a square wave time signal). The off switching state does not have to be one in which particles are non-interacting (for example, the particles could have attractions in the on state and repulsions in the off state, or particles could switch between two different types of attractive interactions), but we use the on/off notation for convenience. There are innumerable

other forms of time-varying control that could be used to switch between the on and off states. However, toggling is simple to implement in experiments and simulations and straightforward to analyze in theory. The signal is characterized by only two parameters, t_{on} and t_{off}. Equivalently, the signal can be described by its period $\mathscr{T} \equiv t_{on} + t_{off}$, duty cycle (which we will also refer to as the duty) $\xi \equiv t_{on}/(t_{on} + t_{off})$, duty ratio $\eta \equiv t_{on}/t_{off}$, or frequency $\omega \equiv 1/\mathscr{T}$. Some dynamic self-assembly simulations have shown that other periodic time signals lead to essentially the same phase behavior as the square wave toggle signal.[81]

For the functional form of the interparticle attraction, we choose to use the Asakura-Oosawa equation, which represents the effective pairwise attraction of colloidal spheres in the presence of a non-adsorbing depletant,[178,179]

$$U(r) = -\frac{\varepsilon(a+\delta)^3}{\delta^2(3a/2+\delta)}\left(1 - \frac{3}{4}\frac{r}{a+\delta} + \frac{1}{16}\left(\frac{r}{a+\delta}\right)^3\right), \quad \text{for } 2a \leq r \leq 2(a+\delta). \tag{3.1}$$

The particles also interact *via* the hard sphere repulsion in equation (2.20). Here, r is the center-to-center distance between two particles, a is their radius, ε is the interaction strength at contact, and δ is the interaction range. We make the particular choice of the depletion potential as a model for short-ranged attractions in general because it is an important and well-studied interaction in experiments, the functional form is continuous and differentiable beyond contact (compared to, say, a square well potential), and there are analytic expressions for the phase behavior of particles interacting *via* this potential.[178] The specific shape of the short-ranged attraction is irrelevant for the equilibrium phase behavior, as the Noro-Frenkel principle of corresponding states demonstrates that the equilibrium phase diagram of *any* dispersion with an arbitrary short-ranged attraction is generic.[177] For this work, we focus on cases where the attraction is strong compared to the thermal energy, $\varepsilon \sim 5 - 10k_BT$, and short in range compared to the particle size, $\delta = 0.1a$. Throughout this chapter we use the freely-draining simulation model and neglect interparticle hydrodynamic interactions for reasons of computational efficiency. The implications of ignoring HI are discussed later in the text.

In this chapter we develop a formal description of the phase behavior of dispersions self-assembled *via* periodically toggled attractions. First, we compare suspensions self-assembling with steady attractions versus those with toggled attractions, showing that toggling enhances the crystallization rate and crystal quality. Next, we measure the volume fractions of coexisting phases with a fixed $t_{off} = \delta^2/D$ while varying t_{on} and the volume fraction ϕ. Three different simulation techniques are used to make this measurement: crystal nucleation from a homogeneous fluid, fluid nucleation from a homogeneous crystal, and sedimentation equilibrium. We also measure the coexisting phases while fixing the volume fraction ϕ and varying t_{on} and t_{off} independently. We develop a first principles theory to predict the concentrations of the coexisting phases, which shows that the phase behavior is accurately predicted by appropriate time-averages of analytic equations of states for the dispersion in the attractive mode and the purely repulsive mode. Finally, we develop phenomenological models to explain two different kinetic mechanisms we observe in the self-assembling dispersions. The first model describes the coarsening of crystalline strands in percolated, gel-like networks. The second model describes nucleation and growth of large crystals via one-step or two-step mechanisms. These models are an important step to understanding the complicated kinetics involved in dynamically self-assembling systems. We conclude with a discussion of the results and their implication for dynamic nanoparticle self-assembly.

3.1 Steady versus Toggled Interactions

Figures 3.7 and 3.8 shows the equilibrium phase diagram for a dispersion with steady, short-ranged attractions. To navigate the equilibrium phase diagram, we can tune two parameters: the particle volume fraction ϕ and the attraction strength ε relative to the thermal energy k_BT. The range of the attraction δ also affects the phase behavior, but is kept fixed at $\delta = 0.1a$ in this work. We consider the case of an initially homogeneous, disordered suspension at constant volume fraction, say $\phi = 0.20$, and ε below the phase boundary. As ε increases across the phase boundary, the suspension will phase separate into dense crystal and dilute fluid. If ε is close to the fluid phase boundary, phase separation occurs via nucleation and growth. Because the thermodynamic driving force is small near phase boundaries, the dynamics are necessarily slow and tend

to create compact, low-defect crystals. The extent of crystallization is quantified with the crystal fraction $X_c \equiv N_c/N$, defined as the ratio of the number of particles incorporated into the crystal, N_c, to the number of total particles, N (see Methods for how we determine N_c). Figure 3.1 shows the crystallization kinetics in simulations of steady attractive suspensions with different attraction strengths. Near the phase boundary, a large fraction of the suspension crystallizes, but only after a significant induction period followed by slow growth.

If ε increases quickly and quenches the suspension deep into the coexistence region, the thermodynamic driving force for self-assembly is significantly enhanced. Initially, the aggregation speed is high, but the suspension quickly forms a disordered, percolated phase. Conversion from this metastable gel to the thermodynamic equilibrium crystalline state is incredibly slow, and the terminal state is treated as arrested over the time scales of interest. These kinetics are quantified in our simulations in Figure 3.1, where only a small fraction of the suspension crystallizes at large ε. Therefore, for static self-assembly, the kinetics and terminal structures are coupled; we can either form ordered crystals slowly or disordered states quickly.

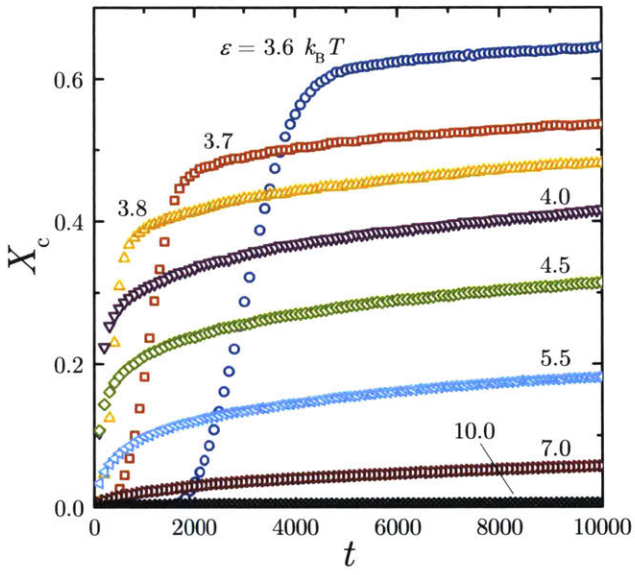

Figure 3.1: The crystal fraction X_c as a function of time t, made dimensionless by the diffusion time τ_D, for various steady attraction strengths ε.

In the case of toggled particle interactions, two extra parameters, t_{on} and t_{off}, in addition to ϕ and ε influence the suspension self-assembly. It is convenient to normalize t_{on} by the toggle period $\mathscr{T} \equiv t_{on} + t_{off}$ and treat the duty $\xi \equiv t_{on}/(t_{on} + t_{off})$ as an independent variable rather than t_{on}. Though we gain additional control over the self-assembly, we lose the predictive power of equilibrium thermodynamics, which is no longer valid with a time-dependent interaction potential. Note that in the toggled suspensions we refer to ε as the absolute attraction strength and $\varepsilon\xi$ as the time-averaged attraction strength. Unlike in the steady attractive suspension, the self-assembly kinetics in the toggled attractive suspension are not constrained by the location in the phase diagram, and (ξ, t_{off}) can be optimized to yield desired self-assembly kinetics, even at fixed (ϕ, ε). Thermal motion while the attractions are off helps to anneal defective, arrested configurations, opening out-of-equilibrium pathways towards the equilibrium crystalline state. Swan and coworkers argued that an optimal choice for t_{off} exists and is comparable to the time it takes for a particle to diffuse the range of the interaction, $t_{off} = \delta^2/D$, where D is the particle diffusivity.[67,68,82] This choice for t_{off} allows for the largest amount of structural rearrangement without dissolving aggregated structures, as explained in detail in Figure 3.2. With $\delta = 0.1a$, $t_{off} = \delta/D = 0.01\tau_D$.

Figure 3.3 shows that for any particular value of $\varepsilon\xi$, the toggled attractions produce more crystal after

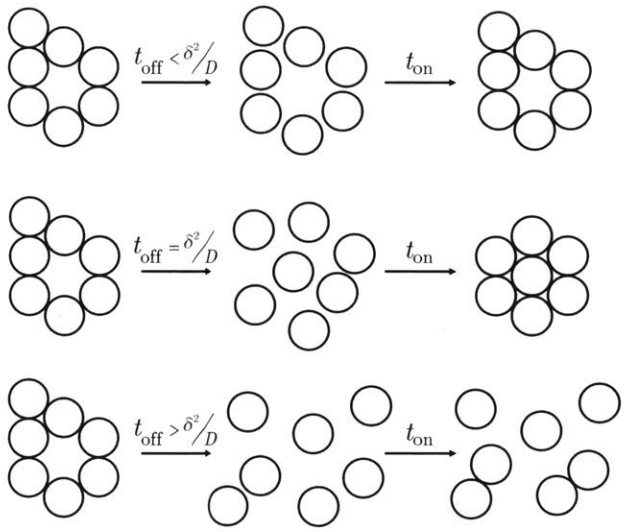

Figure 3.2: Schematic showing how toggled interactions can anneal defects and avoid kinetic arrest in a nanoparticle suspension. The particles diffuse as hard spheres for a time t_{off} in the "off" half-cycle and experience strong, short-ranged attractions for a time t_{on} in the "on" half-cycle. The left column shows a kinetically arrested configuration with a vacancy defect. If t_{off} is too short (top row), the particles cannot diffuse sufficiently far from their original positions in the off half-cycle, and the defect persists when the attractions are turned on. If t_{off} is too long (bottom row), the particles diffuse away farther than the range of the interaction in the off half-cycle and do not reaggregate when the attractions are turned on. If $t_{off} = \delta^2/D$ (middle row), the particles diffuse far enough to relax the defected structure but still reaggregate when the attractions are turned on and find their thermodynamically favorable crystalline configuration.

$10000\tau_D$ than steady attractions of equivalent absolute or time-averaged strength. Equivalently, the rate of crystallization is always faster with toggled attractions than with steady attractions of equivalent absolute or time-averaged strength. Though the proposed "optimum" $t_{off} = \delta^2/D = 0.01\tau_D$ does enhance the crystallization rate appreciably relative to steady attractions, a wide range of other t_{off} values work as well. In fact, the crystallization rate generally increases as the toggle frequency decreases beyond $t_{off} = \delta^2/D = 0.01\tau_D$.

Toggled attractions also produce, larger and higher quality crystals than steady attractions. The quality of crystal is quantified by $L_c \equiv N_c/N_i$, the ratio of the number of particles in the crystal interior to the number of particles at the crystal interface N_i (see Methods for how we determine N_i). N_c scales with the crystal volume, while N_i scales with the crystal surface area, so L_c estimates a quantity proportional to the length scale of bulk crystal. L_c tends to increase with crystal size, but fluid/crystal interface, grain boundaries, and defects all contribute to N_i and penalize L_c. At a given X_c, dispersions with a few large, high quality crystalline domains have a larger L_c than those with many small, defective or polycrystalline domains. Thus, L_c serves as one measure for overall crystal quality. Figure 3.3 shows that for any crystal fraction, L_c is always larger for toggled attractions than steady attractions. The crystal quality generally increases as the toggle frequency decreases.

A broad range of ξ and t_{off} at constant ε for toggled attractions lead to fast kinetics and high quality structures whereas only a narrow range of ε for steady attractions produces acceptable crystallization rates and qualities. Finding this narrow crystallization slot for steady attractions and then designing a control scheme to ensure the dispersion stays within it can be challenging. With toggled attractions, control over ε is not important, and only the toggle parameters, which are easily controlled, need to be adjusted.

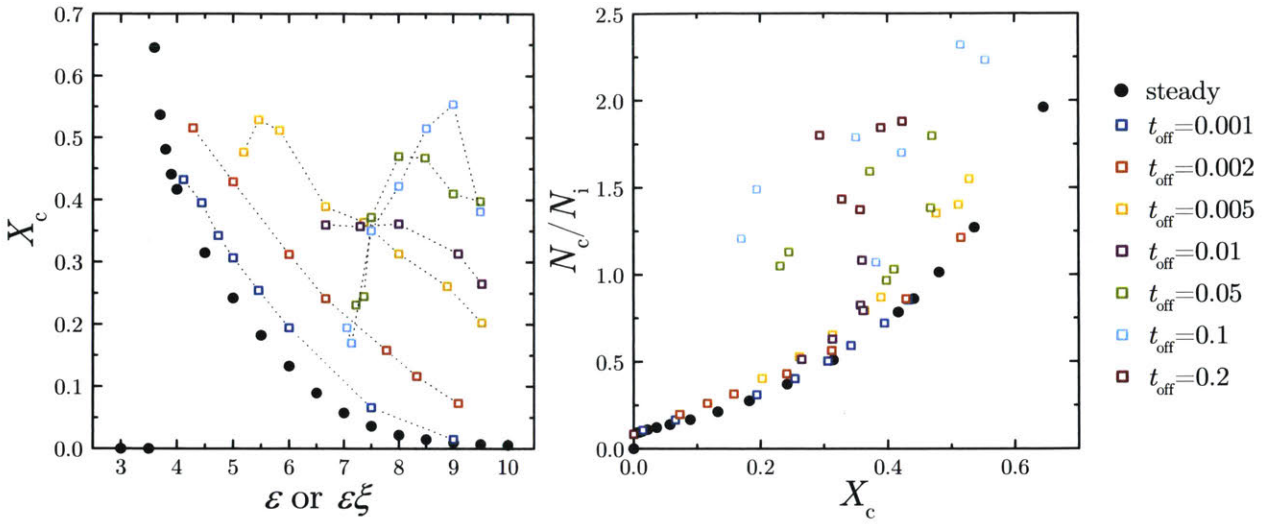

Figure 3.3: Left: The crystal fraction X_c as a function of steady attraction strength ε or toggled time-averaged attraction strength $\varepsilon\xi$, made dimensionless by the thermal energy k_BT, for various values of t_{off}. Right: The ratio of number of crystalline particles N_c to number of interfacial particles N_i as a function of crystal fraction. For the steady attractions, ε varies, but for the toggled attractions, $\varepsilon = 10k_BT$ is fixed and ξ varies. At any particular steady ε, the crystallinity is higher in toggled suspensions of equivalent $\varepsilon\xi$. At any particular crystallinity, N_c/N_i is larger in toggled suspensions. For clarity, not all of the data collected in Figure 3.5 is shown here.

3.2 Using the Toggle Parameters to Control the Terminal Structure and Kinetic Mechanism

3.2.1 Nucleation Line

Though toggling improves the crystallization rate and quality, not all choices of toggle parameters result in self-assembled states. If the duty ξ is too small, particles do not have enough time to sufficiently aggregate in the on half-cycle. Any small clusters dissolve in the off half-cycle, and the suspension will remain as a homogeneous fluid. As ξ grows, particles aggregate appreciably in the on half-cycle without completely dissolving in the off half-cycle, and large crystalline domains emerge after many toggle cycles. At fixed ε and t_{off}, the crystal nucleation line $\xi_f^*(\phi)$ separates these two regions. Below $\xi_f^*(\phi)$, crystal nucleation from the homogeneous fluid is not observed. Figure 3.4 shows the crystal nucleation line in terms of the duty ratio $\eta_f^* = \xi_f^*/(1-\xi_f^*)$ from Brownian dynamics simulations of 64000 particles at fixed $\varepsilon = 10k_BT$ and $t_{\text{off}} = 0.01\tau_D$. The lowest duty ratio at which crystal nucleation was observed within 10^5 toggle cycles in the initially homogeneous fluid for different volume fractions was designated as $\eta_f^*(\phi)$. η_f^* decreases quickly with increasing ϕ, as aggregation in the on half-cycle becomes easier with decreasing interparticle spacing.

Similarly, we can determine the fluid nucleation line $\xi_c^*(\phi)$ below which fluid nucleation within an initially homogeneous crystal is suppressed. In the on half-cycle, particles try to move away from their lattice positions and collapse into closest packings. However, because the hard sphere crystal is stable at large densities, the particles tend to move back to their lattice positions in the off half-cycle. If ξ is small, the particles do not deviate sufficiently far in the on half-cycle and always return back to their lattice positions in the off half-cycle. If ξ is large enough, there is enough time for density fluctuations to drive portions of the crystal to collapse into closest packings and open up a fluid pocket in which the crystal melts. Figure 3.4 shows the fluid nucleation line in terms of the duty ratio $\eta_c^* = \xi_c^*/(1-\xi_c^*)$ from Brownian dynamics simulations of 62500 particles following the same method as that to determine η_c^*. η_f^* generally increases slightly with increasing ϕ as it becomes more difficult for particles to move off-lattice with decreasing lattice spacing.

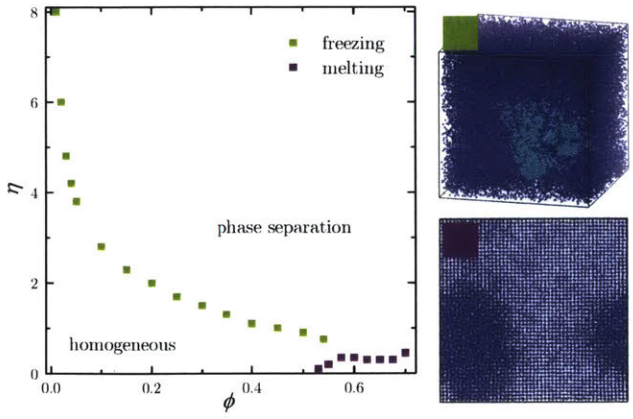

Figure 3.4: Nucleation lines determined from homogeneous nucleation simulations at fixed $\varepsilon = 10k_BT$ and $t_{\text{off}} = \delta^2/D = 0.01\tau_D$. The points correspond to the lowest duty ratio at which crystal nucleation in a homogeneous fluid (green) and fluid nucleation in a homogeneous FCC crystal (purple) was observed after 10^5 toggle cycles. Below these curves, the suspensions remains homogeneous while above them phase separation occurs.

3.2.2 Varying the Toggle Parameters

The volume fraction ϕ and attraction strength ε are set by the specific formulation of the dispersion. Typically, these are fixed once the dispersion is prepared and cannot easily be changed. The toggle parameters t_{off} and ξ, are controlled externally and are simple to modulate. Figure 3.5 summarizes the results of Brownian dynamics simulations of 64000 particles at fixed $\phi = 0.20$ and $\varepsilon = 10k_BT$ assembling from an initially homogeneous fluid for around $10000\tau_D$ for various t_{off} and ξ. The space is divided into five regions where different terminal structures formed through various kinetic mechanisms, shown in Figure 3.6. The final crystal fraction (like in Figure 3.3) after $10000\tau_D$ is also shown as a color density plot. For small duty fractions (region 5), there is insufficient driving force for self-assembly, and the suspension remains a homogeneous fluid. While some aggregation occurs in the on half-cycle, t_{off} is too long and the aggregated structures all dissolve in the off half-cycle. The nucleation line $\xi^*(t_{\text{off}})$, below which no phase separation is observed, is nonmonotonic with respect to t_{off}. Initially, ξ^* increases with with increasing t_{off} but eventually peaks and decreases with increasing t_{off}.

Above ξ^* are regions of fluid/crystal and fluid/fluid coexistence. Because of the annealing capabilities of the toggling protocal, the assembled domains are large and (for crystalline phases) highly-ordered, with very few defects. At low $t_{\text{off}} \leq 0.02\tau_D$ (region 4), the suspension phase separates into fluid and crystal phases by one-step nucleation, where crystal nucleates directly in the initial fluid (second and third rows of Figure 3.6). At moderate $t_{\text{off}} \geq 0.05\tau_D$ and $\xi \geq \xi_{c2}(t_{\text{off}})$ (region 2), the suspension reaches fluid/crystal coexistence by two-step nucleation, where droplets of dense fluid nucleate first and grow before crystal preferentially nucleates and grows within the dense fluid (fourth row of Figure 3.6). Two-step nucleation has been reported for short-ranged attractive colloid and protein dispersions with steady interactions.[180–182] $\xi_{c2}(t_{\text{off}})$ is the boundary above which the second crystal nucleation occurs. The transition between crystal nucleation and fluid nucleation occurs between $0.02\tau_D \leq t_{\text{off}} \leq 0.05\tau_D$ for all ξ. The maximum in the phase boundary $\xi^*(t_{\text{off}})$ occurs precisely at this transition between crystal and fluid nucleation. For sufficiently large t_{off} and $\xi < \xi_{c2}$ (region 3), the second crystal nucleation is suppressed entirely and only fluid/fluid phase separation occurs (fifth row of Figure 3.6). The boundary ξ_{c2} sharply increases with t_{off}. In fact, at $t_{\text{off}} \geq \tau_D$, crystal nucleation is suppressed entirely for all ξ we simulated. Fluid/fluid coexistence was also observed in experiments of paramagnetic colloids assembling in toggled magnetic fields at low frequencies.[67,68]

At small t_{off} and large ξ (region 1), the suspension undergoes a spinodal-like decomposition and initially forms a disordered, percolated gel. The toggling protocol allows the structure to relax defects, and the gel slowly coarsens and becomes more crystalline (first row of Figure 3.6). The coarsening is sufficiently slow that the structure remains percolated at the end of $10000\tau_D$. The gel line $\xi_{\text{gel}}(t_{\text{off}})$, above which the global

structure is percolated, is a monotonically increasing function of t_{off}. Below ξ_{gel}, phase separation may still proceed by gel coarsening, but the rate of coarsening is sufficiently high that the structure depercolates and condenses into more compact domains within the duration of observation. Thus, ξ_{gel} depends on the finite observation time. The space around ξ^* was sampled with high resolution, but ξ_{gel} was not, so the shape of ξ_{gel} is less certain than the shape of ξ^*.

In the one-step fluid/crystal, two-step fluid/crystal, and fluid/fluid coexistence regions, points on or very close to the boundary ξ^* exhibit nucleation and growth of a few, noninteracting nuclei, shown in the bottom three rows of Figure 3.6. Farther from the phase boundary, many nuclei form and significant coalescence and Ostwald ripening occur, as in the second row of Figure 3.6. As we approach the gel line ξ_{gel} from below, spinodal-like decomposition starts to occur along with nucleation and growth, coalescence, and ripening, and there is a complicated combination of many different kinetic mechanisms.

3.2.3 Self-Assembling the Largest, Highest Quality Crystals

In Figure 3.5, there are two regions of high crystallinity. The first is at small t_{off} and very close to the lower self-assembly boundary ξ^* in the one-step fluid/crystal region (region 4). Here, the crystal fraction is generally a monotonically decreasing function of ξ moving away from the ξ^* boundary at constant t_{off}. The second is in the middle of the two-step nucleation region (region 2). Here, the maximum in X_c at constant t_{off} shifts away from the phase boundary. Necessarily, the crystal fraction is zero in the fluid/fluid (region 3) and homogeneous fluid (region 5) regions. Both the one-step and two-step fluid/crystal regions achieve similar crystallinities, but for any particular X_c, the crystal size and quality as measured by $L_c = N_c/N_i$ in Figure 3.3, is much higher for the latter.

Because fluid particles are more mobile than crystalline particles, the initial fluid/fluid phase separation in the two-step region is very fast. Even if many dense fluid droplets nucleate, they rapidly coalesce and ripen to form a single bulk dense fluid domain. Crystal nucleates preferentially in the dense fluid, so all crystal domains are localized rather than dispersed throughout the suspension volume. It is easy for the crystals to coalesce and ripen into a single crystalline domain with very little interface and high quality. In contrast, crystals nucleate throughout the entire suspension volume in the one-step region. Coalescence is limited by the time it takes for the large crystal clusters to diffuse toward one another, which is long because of the reduced diffusivity of the cluster compared to individual particles. Ripening is limited by the number of particles in the crystalline domains that can diffuse sufficiently far in the off-cycle to escape the crystal and enter the bulk fluid. Because t_{off} is short in the one-step region, very few particles detach from the crystals and ripening is also slow. Reducing interface is therefore a very slow process in the one-step fluid/crystal region and so L_c is smaller here. Thus, adjusting t_{off} and ξ to drive two-step nucleation is a strategy for optimizing the quality of the assembled crystals.

3.3 Determining the Out-of-Equilibrium Phase Diagram

3.3.1 Sedimentation Equilibrium

Under a weak, constant gravitational force $\mathbf{F}_g = -F_g\hat{\mathbf{e}}_z$ the competing processes of sedimentation and diffusion in a suspension result in a nonhomogeneous equilibrium number density profile $n(z)$ as a function of height z that satisfies,

$$\frac{\partial P(z)}{\partial z} = -n(z)F_g, \tag{3.2}$$

where P is the (osmotic) pressure of the colloid particles. Note that the number density and volume fraction are related by $v_0 n = \phi$, where $v_0 = 4\pi a^3/3$ is the volume of a single particle. If the vessel containing the suspension is sufficiently tall, *i.e.* a tower, the suspension is so dilute at large z that the pressure at the top vanishes. Integrating from the top of the tower $z = L$ to any height z,

$$P(z) = -F_g \int_L^z dz'\, n(z). \tag{3.3}$$

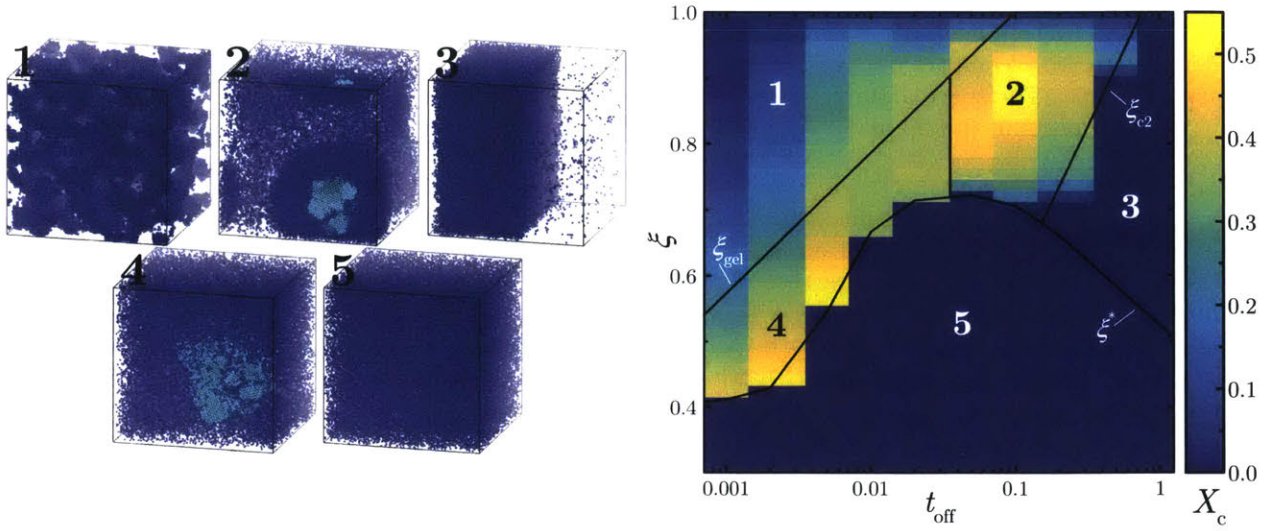

Figure 3.5: Color density plot showing the fraction of particles X_c that are crystalline after $10000\tau_D$ as a function of off duration t_{off}, made dimensionless by the diffusion time τ_D, and duty fraction ξ. The solid lines divide the space into five domains of different terminal structures and phase separation mechanisms, a representative image of which is shown in the legend. 1: gel coarsening, 2: fluid/crystal coexistence *via* two-step nucleation, 3: fluid/fluid coexistencce, 4: fluid/crystal coexistence *via* one-step nucleation, 5: homogeneous fluid (no self-assembly).

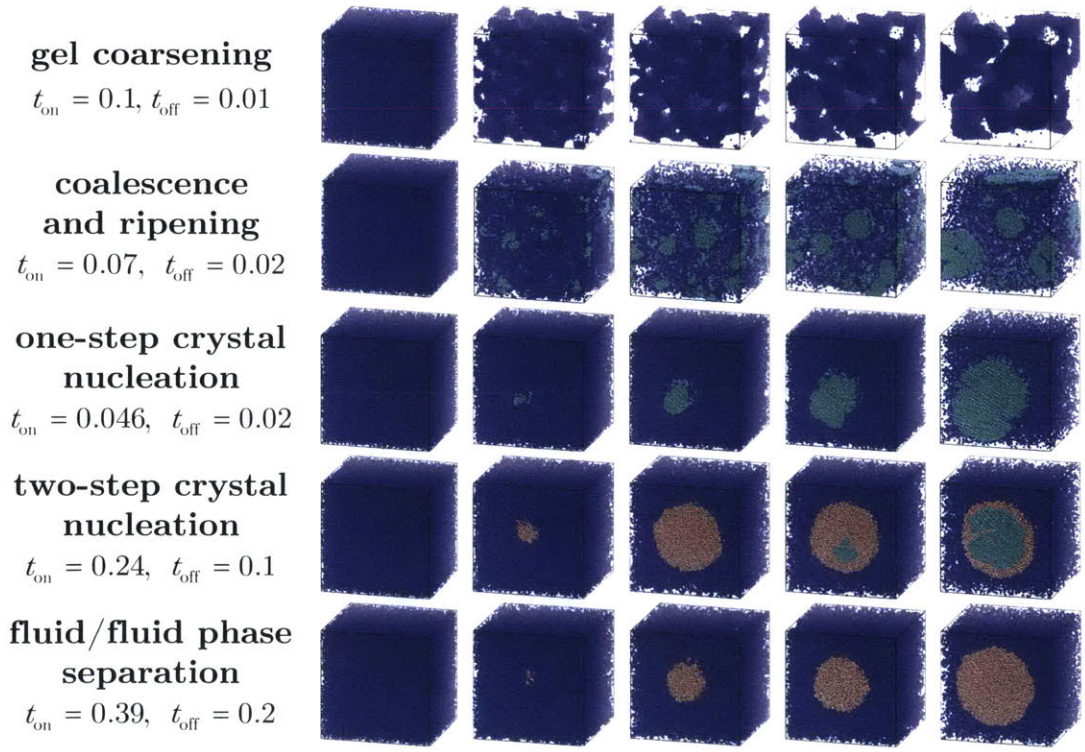

Figure 3.6: Kinetic mechanisms observed in simulations of toggled attractive suspensions. Each row shows snapshots of the self-assembling suspension over time, with the snapshots in the first column taken at time $t = 0$ and in the last column at around $t = 10000\tau_D$. Snapshots in the other columns do not correspond to the same time points. Crystalline particles are colored light blue in rows two through five and dense fluid is colored pink in rows four and five.

Therefore, if we measure the number density profile $n(z)$ we can obtain the pressure profile $P(z)$ using (3.3), from which we can infer the equation of state $P(n)$. If there is sufficient pressure, the bottom of the sample will crystallize under the weight of the particles above. At the height of the fluid/crystal interface, there is a single value of pressure but two values of density on either side of the interface. Thus, the equation of state will reflect phase coexistence, and the densities on either side of the interface are the coexisting densities of the two phases. This is a common technique used to obtain equations of state and phase diagrams of nanoparticle suspensions.[183–185]

Equations (3.2) and (3.3) only hold for equilibrium, time-independent systems. With time-periodic interparticle interactions, these equations will never hold, and the system is always instantaneously out of equilibrium. Instead, with a periodic driving force, the suspension evolves until it reaches a periodic-steady-state (PSS) where it does not change from cycle to cycle, $n(\mathbf{x}, t) = n(\mathbf{x}, t+\mathscr{T})$ for all future t. The number density evolves according to the conservation of mass law,

$$\frac{\partial n}{\partial t} = -\nabla \cdot \mathbf{J}, \tag{3.4}$$

where $\mathbf{J}$ is the particle flux. Integrating (3.4) over a pulse cycle and dividing by the pulse period $\mathscr{T}$,

$$\frac{1}{\mathscr{T}}\left(n(\mathbf{x}, t+\mathscr{T}) - n(\mathbf{x}, t)\right) = -\nabla \cdot \frac{1}{\mathscr{T}} \int_t^{t+\mathscr{T}} dt\, \mathbf{J}. \tag{3.5}$$

At periodic-steady-state, the left side vanishes. The system only varies in the z direction so, (3.5) simplifies to

$$\frac{\partial \bar{J}_z}{\partial z} = 0, \tag{3.6}$$

where the overbar indicates a quantity time-averaged over a pulse cycle,

$$\bar{X}(t) \equiv \frac{1}{\mathscr{T}} \int_t^{t+\mathscr{T}} dt\, X. \tag{3.7}$$

Therefore, the time-averaged flux is constant. Because particles cannot escape, there is a no-flux boundary condition at the bottom of the tower. Thus, the time-averaged flux must vanish everywhere at periodic-steady-state, $\bar{\mathbf{J}} = 0$. To make further progress, a constitutive relation is needed for the time-averaged particle flux. In the linear regime of nonequilibrium thermodynamics, the particle flux is, at constant T, proportional to the gradient in chemical potential,

$$\mathbf{J} = -Mn\nabla\mu', \tag{3.8}$$

where M is the mobility.[19,36] The chemical potential is,

$$\mu' = \frac{\partial f'}{\partial n}, \tag{3.9}$$

where f' is the free energy density, which can be written as

$$f'(n, z) = f(n) + nzF_g, \tag{3.10}$$

with $f(n)$ as the free energy density of a homogeneous system at density n in the absence of the gravitational field. Therefore,

$$\mu'(n, z) = \mu(n) + zF_g \tag{3.11}$$

where μ is the chemical potential of a homogeneous system at density n in the absence of the gravitational field. Substituting (3.11) into the flux expression (3.8),

$$J_z = Mn\left(\frac{\partial \mu}{\partial z} + F_g\right). \tag{3.12}$$

Using the Gibbs-Duhem relation, $n\, d\mu = dP$,

$$J_z = M\left(\frac{\partial P}{\partial z} + nF_g\right). \tag{3.13}$$

Taking the time-average of this equation,

$$\bar{J}_z = M\left(\frac{\partial \bar{P}}{\partial z} + \bar{n}F_g\right), \tag{3.14}$$

In this step, we have assumed that M is constant within a toggle cycle. The mobility is a function of only the particle configuration. The only effect the interparticle potential has on the mobility is through its effect on the particle configuration. For short toggle periods, the configuration of the particles cannot change appreciably, and so the mobility is nearly constant within a cycle. Note that this is not true for the pressure, which is highly sensitive to the interparticle potential. Examples where M varies appreciably within a toggle cycle are discussed in Chapter 5. Because the time-averaged particle flux vanishes at periodic-steady-state,

$$\frac{\partial \bar{P}}{\partial z} = -\bar{n}F_g \tag{3.15}$$

and

$$\bar{P}(z) = -F_g \int_L^z dz' \, \bar{n}(z), \tag{3.16}$$

and equations (3.2) and (3.3) hold for time-averaged quantities in the toggled suspension. In particular, the validity of (3.16) implies that there exists an equation of state $\bar{P} = \bar{P}(\bar{n})$ that relates the time averaged pressure and density. It is not immediately obvious that such an equation should be valid. Additionally, if phase separation occurs in the suspension, we can use (3.16) to extract coexistence points and determine the phase diagram of the toggled suspension. Because the average in (3.16) is over a single toggle cycle, the equation of state is independent of frequency, and only depends on the duty cycle.

We performed Brownian dynamics simulations of 32076 particles at an overall volume fraction of $\phi = 0.50$ sedimenting under a weak, constant gravitational force $F_g = 0.1k_BT/a$ (Figure 3.7). The attaction strength and off duration were fixed at $\varepsilon = 10k_BT$ and $t_{\text{off}} = \delta^2/D = 0.01\tau_D$, and the duty was varied. To test the result that the phase behavior is independent of frequency, we performed simulations at two other off durations $t_{\text{off}} = 0.005\tau_D$ and $t_{\text{off}} = 0.02\tau_D$. We also performed simulations with $t_{\text{off}} = 0.01\tau_D$ but different attraction strengths $\varepsilon = 5k_BT$ and $\varepsilon = 15k_BT$. The suspension was supported below by a wall that repelled particles with a strong, short-ranged Lennard-Jones potential truncated at its minimum for purely repulsive interactions. The aspect ratio of the simulation cell was 16, oriented in the direction of F_g, to ensure that the pressure near the bottom of the suspension was large enough to sustain a crystal. While traditional sedimentation experiments start with a homogeneous fluid and then allow the particles to sediment downward, this setup is quite slow in simulation. We choose to implement the reverse scheme where all particles are initially in a closest packed FCC crystal at the base of the tower and allowed to melt from the interface until periodic-steady-state is achieved. While the terminal density profile is identical in either the downward or upward sedimentation schemes, the equilibration time in the upward setup is much shorter. Once periodic-steady-state was achieved, the volume fraction profile $\phi(z)$ was determined by dividing the tower into thin, rectangular volume slices and measuring the fraction of slice volume occupied by particles. This profile was then time-averaged over many pulse cycles and smoothed over space using Gaussian convolution. The equation of state $\bar{P}(\bar{\phi})$ was then obtained from (3.16). The coexistence points are the volume fractions on either side of the crystal/fluid interface. These points appear as cusps in the equation of state and can be extracted from a plot of $\bar{P}$ versus $\bar{\phi}$. Because the cusp was not always sharp, error bars were also computed as a reasonable range of volume fractions around the cusp. The results are plotted in Figure 3.7.

3.3.2 Coexistence Criteria/Theoretical Phase Diagram

The appearance of the time-averaged equation of state $\bar{P}(\bar{\phi})$ in the periodic-steady-state condition for sedimentation equilibrium suggests that the toggled suspension may be described by equilibrium thermodynamics if instantaneous quantities are replaced by their time averages. Suppose a toggled suspension phase separates into bulk dense and dilute phases such that the interface between them is flat and reaches periodic-steady-state, which is observed in the present simulations as well as elsewhere.[82] This requirement of macroscopic

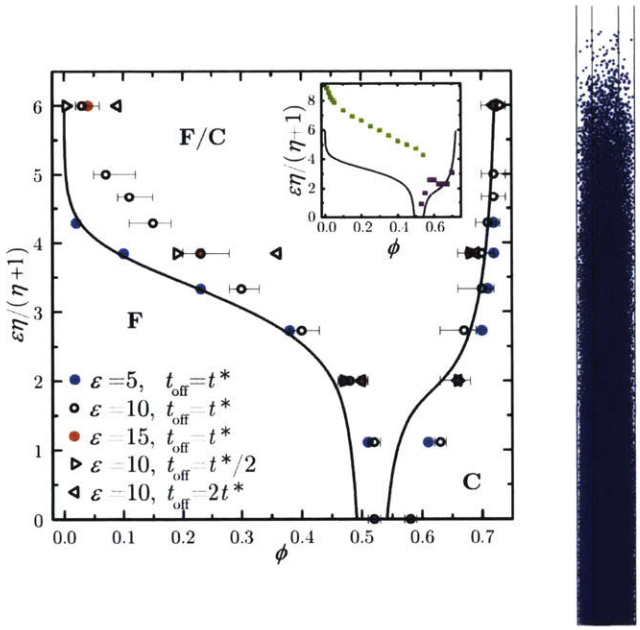

Figure 3.7: Fluid/crystal (F/C) phase diagram for the toggled depletion suspension. The phase behavior is completely determined by the volume fraction ϕ and time-averaged strength $\varepsilon\eta/(1+\eta)$, made dimensionless by the thermal energy k_BT. The solid lines are the coexisting volume fractions predicted by the time-average of the equilibrium equations of state, and the points are those extracted from Brownian dynamics sedimentation equilibrium simulations with a variety of strengths ε, duty ratios η, and off durations t_{off}, where $t^* = \delta^2/D$. For clarity, error bars are rendered only for a single set of data. Also shown in the inset are the data from Figure 3.4, the phase boundaries determined from homogeneous nucleation in a metastable fluid (green squares) and in a metastable crystal (purple squares).

phase separation restricts the following derivation to t_{on} and t_{off} short compared to the time to homogeneously nucleate one phase within the bulk of the other. Else, if nucleation occurs, the dispersion is not well described by two homogeneous bulk phases. If we designate z as the direction normal to the interface, the analysis of the time evolution of the volume fraction profile is similar to the sedimentation analysis without the gravitational field. In particular, equations (3.12) and (3.13) imply

$$\overline{\phi \frac{\partial \mu}{\partial z}} = v_0 \frac{\partial \bar{P}}{\partial z} = 0, \tag{3.17}$$

where we have used the result that the time-averaged particle flux vanishes everywhere at periodic-steady-state. The pressure and chemical potential are very sensitive to the interparticle potential. Because we are modulating the potential over time, the pressure and chemical potential vary greatly within a single pulse cycle. However, the volume fraction profile does not. At periodic-steady-state, the volume fraction satisfies $\phi(\mathbf{x}, t) = \phi(\mathbf{x}, t + \mathscr{T})$. If ϕ is to return to its profile at the start of a cycle, it cannot deviate too far within the cycle. Thus, ϕ is relatively time-independent at periodic-steady-state,

$$\phi(\mathbf{x}, t) = \phi(\mathbf{x}, t + \mathscr{T}) \approx \phi_{\text{PSS}}(\mathbf{x}) \tag{3.18}$$

This approximation is good when the toggle period is small compared to the time scale on which the particles move. At larger time scales, this approximation may break down. With ϕ constant within a toggle cycle the left side of (3.17) becomes,

$$\frac{1}{\mathscr{T}} \int_{\mathscr{T}} dt\, \phi \frac{\partial \mu}{\partial z} = \phi \frac{\partial}{\partial z} \frac{1}{\mathscr{T}} \int_{\mathscr{T}} dt\, \mu = \phi \frac{\partial \bar{\mu}}{\partial z} \tag{3.19}$$

Therefore, for coexistence in a periodic-steady-state,

$$\bar{\mu} = \text{constant} \quad \bar{P} = \text{constant}. \tag{3.20}$$

In particular, far away from the interface, the time-averaged quantities are given by their bulk values so the time-averaged chemical potential and the time-averaged pressure must be equal in the two bulk phases at periodic-steady-state,

$$\bar{\mu}_1(\phi_1) = \bar{\mu}_2(\phi_2) \quad \bar{P}_1(\phi_1) = \bar{P}_2(\phi_2). \tag{3.21}$$

This is analogous to the coexistence criteria of equal pressure and chemical potential for equilibrium with steady interactions. Of course, the equilibrium coexistence conditions will never hold in the toggled suspension, so the suspension is always instantaneously out of equilibrium. However, the nonequilibrium periodic-steady-state phase diagram can be determined solely from the equilibrium equations of state using equations (3.21).

For the time averages, we split the integral over a toggle period $\mathscr{T}$ into two integrals over the half-cycles,

$$\bar{P} = \frac{1}{\mathscr{T}} \left(\int_{t_{\text{on}}} dt\, P_{\text{on}} + \int_{t_{\text{off}}} dt\, P_{\text{off}} \right), \tag{3.22}$$

where the subscripts of P indicate which half-cycle the quantity is evaluated in. In general P_{on} and P_{off} may change slowly over many cycles, but because the volume fraction profile is essentially constant within a cycle, the pressure does not change significantly within a half-cycle. Thus, we may approximate the time-average as,

$$\bar{P} = \frac{t_{\text{on}} P_{\text{on}} + t_{\text{off}} P_{\text{off}}}{t_{\text{on}} + t_{\text{off}}} = \xi P_{\text{on}} + (1 - \xi) P_{\text{off}}, \tag{3.23}$$

and similarly for the time-averaged chemical potential $\bar{\mu}$. Within a half-cycle, the suspension behaves as either an equilibrium hard sphere system or an equilibrium depletion system, albeit in a state far from equilibrium. Thus, the pressure and chemical potential of each phase in the off and on half-cycles are given by the equilibrium equations of state (EoS) for hard spheres (HS) and depletion (dep), respectively: $P_{\text{off}} = P_{\text{HS}}$, $\mu_{\text{off}} = \mu_{\text{HS}}$, $P_{\text{on}} = P_{\text{dep}}$, and $\mu_{\text{on}} = \mu_{\text{dep}}$. The depletion equations of state are computed using free volume and scaled particle theories and are of the form,

$$P_{\text{dep}} = P_{\text{HS}} + \varepsilon f(\phi), \tag{3.24}$$

$$\mu_{\text{dep}} = \mu_{\text{HS}} + \varepsilon g(\phi), \tag{3.25}$$

where $f(\phi)$ and $g(\phi)$ are functions of only volume fraction.[178] The time-averaged equations of state are then

$$\bar{P} = P_{\mathrm{HS}} + \xi\varepsilon f(\phi), \quad \bar{\mu} = \mu_{\mathrm{HS}} + \xi\varepsilon g(\phi). \tag{3.26}$$

Comparing to (3.24), the time-averaged EoS are equal to the equilibrium depletion EoS with the interaction strength scaled by the duty cycle ξ. The phase diagram for the toggled system, Figure 3.8, obtained by solving (3.21) is therefore a scaled version of the equilibrium depletion phase diagram, which has already been calculated.[178] Thus, the nonequilibrium states of the toggled assembly can be calculated solely from equilibrium equations of state. Additionally, the out-of-equilibrium phase behavior depends only on the time-averaged interaction strength $\xi\varepsilon$ and is independent of the toggle frequency.

The functional forms of the equations of state used to generate the phase diagram are explained in detail in Appendix B. For the hard sphere fluid equation of state, we use an extension of an equation of state derived by Torquato that diverges at random close packing.[186,187] For the hard sphere crystal EoS, the Lennard-Jones-Devonshire lattice model is used.[188] The depletion equations of state are derived from these hard sphere EoS using free volume and scaled particle theories.[178] The phase behavior predicted by the time average of these equations of state is in good agreement with the fluid/crystal coexistence points extracted from our sedimentation equilibrium simulations, Figure 3.7, and the fluid/fluid coexistence points extracted from our homogeneous nucleation simulations Figures 3.5 and 3.8.

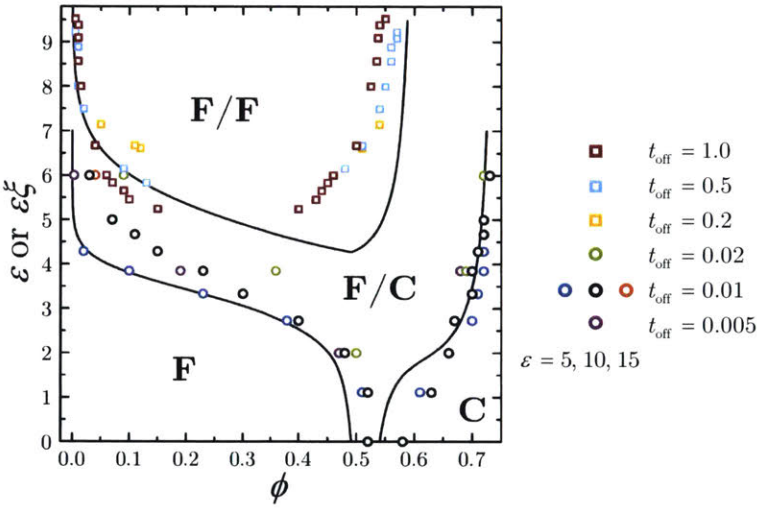

Figure 3.8: Phase diagram for suspensions of particles interacting with steady or toggled depletion attractions of fixed range $\delta = 0.1a$, where a is the particle radius. The points are the volume fractions ϕ at periodic-steady-state of coexisting fluid (F) and crystal (C) phases (circles) or coexisting dilute and dense fluid phases (squares) in simulations of toggled suspensions for various time-averaged strengths $\varepsilon\xi$, made dimensionless by the thermal energy k_BT. Each color represents a data set of varying t_{on} at a particular ε and t_{off}, all of which collapse together when plotted in terms of $\varepsilon\xi$. The solid lines are the coexisting volume fractions predicted by the time-average of equilibrium equations of state, which corresponds exactly with the phase diagram for steady depletion attractions with $\varepsilon\xi$ substituted for ε.

3.3.3 Discussion

In the limit of very large toggle frequencies, particles experience an effectively steady, time-averaged interparticle potential.[82,83,85] The dynamics are identical to that of steady interactions, and the suspensions eventually relaxes to the same thermodynamic equilibrium state. We have shown that, even outside the large frequency limit, where the dynamics of toggled dispersions is very different that the dynamics of dispersions with steady interactions, the out-of-equilibrium periodic-steady-states can be predicted with only knowledge of equilibrium equations of state using the criteria of equal time-averaged pressure and time-averaged chemical potential in equation (3.21). This is a general result that holds for toggling between any two arbitrary interparticle potentials. For the specific case of toggling between short-ranged attractions and hard sphere

repulsions, the densities of coexisting phases at periodic-steady-state is controlled entirely by the parameters $\xi\varepsilon$ and ϕ, so the dimensionality of the parameter space describing phase behavior reduces from four (t_{on}, t_{off}, ε, and ϕ) to two ($\xi\varepsilon$ and ϕ). Notably, this implies that the limiting phase behavior is independent of the pulse frequency ω. Figures 3.7 and 3.8 show fluid/fluid and fluid/crystal coexistence points extracted from simulations. While these points correspond to a variety of different interaction strengths, duties, and frequencies, the data collapse together when plotted in terms of $\xi\varepsilon$ and ϕ and agree well with the phase behavior predicted by the time-averaged equations of state.

These conclusions hold when t_{on} and t_{off} are short compared to the time scale for homogeneous nucleation of one phase within the bulk of the other. If this is true, all the particle flux occurs at the interface between the two phases in periodic-steady-state, and the bulk phases are homogeneous. We find that t_{on} and t_{off} up to order τ_D are short enough to suppress homogeneous nucleation and lead to structures that are well described by our theory. For t_{on} and t_{off} between $2\tau_D$ and $10\tau_D$, significant nucleation occurs within the bulk phases in coexistence. The two phases are quite heterogeneous and it is difficult to assign a single value of ϕ to them. For t_{on} and t_{off} above $20\tau_D$, the on and off half-cycles are so long that the suspension forms a percolated, disordered gel in every on half-cycle which completely dissolves in the subsequent off half-cycle. Thus, no sustained, macroscopic phase separation was observed.

Although we did not account for hydrodynamic interactions between particles in our simulations, the way we have formulated our analysis, hydrodynamic interactions do not affect the criteria of equal time-averaged pressure and time-averaged chemical potential in two coexisting phases at periodic-steady-state. Hydrodynamic interactions will only affect the value of the particle mobility M in equation (3.4), but they will not change the fact that M does not vary much over a toggle cycle, and so we will arrive at the same periodic-steady-state criteria whether or not hydrodynamics are accounted for. The effect of hydrodynamics on the self-assembly kinetics is discussed in the following section.

The limiting phase behavior of the toggled suspension is only a function of $\xi\varepsilon$ and ϕ and is not dependent on both t_{on} and t_{off}. However, the *kinetics* of phase separation are sensitive to both of the toggling parameters. The inset of Figure 3.7 shows the phase boundary extracted from homogeneous nucleation simulations overlayed with the predicted phase boundary (*i.e.* the periodic-steady-state analogue to the binodal). Although free energy barriers delay the onset of homogeneous nucleation, in the thermodynamic infinite time limit, these boundaries should agree. However, because all simulations have finite duration, it may be exceedingly improbable to observe nucleation as the phase boundary is approached from above. In this case, the suspension will remain in its metastable homogeneous state, and coexistence is inaccessible. The inset of Figure 3.7 shows that the fluid nucleation line ξ_f^* predicted from homogeneous nucleation lies above the predicted PSS "binodal". In fact, from Figure 3.5, ξ_f^* shifts as t_{off} varies, unlike the PSS binodal, which is independent of t_{off} (at constant $\xi\varepsilon$). The crystal nucleation line ξ_c^* coincides well with the predicted phase boundary. This suggests that fluid nucleation in the crystal has a relatively small nucleation barrier while crystal nucleation in the fluid has a larger nucleation barrier that limits the envelope of self-assembly. Note that this is purely a kinetic effect, and the homogeneous crystal nucleation results are still consistent with the phase behavior predicted by (3.21), as they lie within the coexistence region.

The sedimentation results lie much closer to the phase boundary than the homogeneous nucleation results. In the classical downward sedimentation setup, the supporting wall at the bottom of suspension offers a surface for heterogeneous crystal nucleation. In the reverse scheme that we implemented, the interface at the top of the initial crystal block allows for heterogeneous fluid nucleation, *i.e.* interfacial melting. In either case, the nucleation barrier for heterogeneous nucleation is lower than that for homogeneous nucleation. Because the nucleation induction time decreases with decreased barrier height, it is much easier to observe phase separation with finite duration simulations *via* sedimentation rather than homogeneous nucleation, and so the results are in better agreement with the theory.

The effects of toggle parameters on the phase separation kinetics are even more striking in Figure 3.5. Our theory predicts a single value for the fluid phase boundary ξ^* at fixed ϕ and ε for any t_{off}. However, ξ^* is not constant and is a nonmonotonic function of t_{off}. At small t_{off}, the duty ξ_f^* required for self assembly increases with increasing t_{off}. Here, one-step nucleation is observed and crystal nucleates directly in the

homogeneous fluid phase. ξ_f^* peaks at the first appearance of dense fluid nucleation. Beyond this point, dense fluid nucleation occurs in the homogeneous fluid rather than crystal nucleation. While ξ_f^* increased with increasing t_{off} for crystal nucleation, ξ_f^* now decreases with increasing t_{off} for fluid nucleation. Because of this, it is possible to observe four different terminal structures (from left to right: percolated, fluid/crystal coexistence, homogeneous fluid, fluid/fluid coexistence) assembled *via* a variety of kinetic mechanisms for a single value of $\xi\varepsilon$. Clearly both t_{on} and t_{off} are important for controlling the dynamics of the toggled assemblies.

Several researchers have reported fluid/fluid phase separation in short-range attractive colloidal suspensions in the context of two-step nucleation before.[180–182] The two-step nucleation mechanism, where a dense fluid drop nucleates and grows before crystal nucleates within the dense fluid, is an alternative to the classical one-step nucleation mechanism, where crystal nucleates directly in a dilute homogeneous fluid. Because the dense fluid is closer in density and structure to the initial dilute homogeneous fluid than the crystal phase is, the fluid/fluid interfacial tension is lower than the fluid/crystal interfacial tension. Thus, the barrier to nucleation is smaller for the dense fluid than the crystal, and the fluid nucleates first. Similarly, the interfacial tension between the dense fluid and crystal is less than that for the dilute fluid and crystal, so crystal nucleation preferentially occurs within the dense fluid. The increased density of the fluid layer around the growing crystal provides particles to the crystal and enhances the rate of crystal growth. Two-step nucleation is only possible within a metastable fluid/fluid coexistence region. Outside of a fluid/fluid coexistence region there is no thermodynamic driving force for the first dense fluid nucleation. If fluid/fluid coexistence was thermodynamically *stable* relative to fluid/crystal coexistence rather than metastable, there would be no thermodynamic driving force for the second crystal nucleation.

Two-step nucleation is also observed in the toggled suspensions, and the time-averaged equations of state do predict fluid/fluid coexistence, Figure 3.8, suggesting that the observed two-step nucleation likely is rooted in the periodic-steady-state coexistence diagram. But from Figure 3.5, one-step crystal nucleation, two-step nucleation, and simple fluid/fluid phase separation are all observed within the fluid/fluid PSS binodal envelope depending on the value of t_{off}. While $\xi\varepsilon$ and ϕ are still descriptive of the terminal structure, the frequency too is important for the growth mechanism and to select whether the terminal coexistence is fluid/fluid or fluid/crystal.

In an equilibrium short-ranged attractive suspension, fluid/fluid coexistence is metastable to fluid/crystal coexistence for sufficiently short attractions (the $\delta = 0.1a$ used in this work satisfies this condition). Even if fluid/fluid phase separation occurs first, the suspension must eventually crystallize. In the out-of-equilibrium toggled suspension, there is nothing to preclude fluid/fluid coexistence from an acceptable periodic-steady-state. Energy is constantly added to and removed from the system, so the same thermodynamic variational principles that favor fluid/crystal over fluid/fluid coexistence in the equilibrium suspension are not valid in the toggled suspension. This is not to say that the periodic-steady-state criteria, $\bar{P}_1 = \bar{P}_2$ and $\bar{\mu}_1 = \bar{\mu}_2$, are invalid. Only that we cannot make any assertions on the relative stabilities of two different phase coexistences that both satisfy the periodic-steady-state conditions. We cannot predict whether or not phase separation will occur or which coexistence is favored, only that *if* it does, the phases must satisfy (3.21). The fact that we observe fluid/crystal and fluid/fluid coexistence at different frequencies but the same $\xi\varepsilon$ is therefore not an inconsistency within our analysis, but rather a fascinating result that the out-of-equilibrium self-assembly process can stabilize structures that are only metastable in static self-assembly.

Why low pulse frequencies should favor fluid/fluid phase separation rather than fluid/crystal phase separation is presently unclear. One may hypothesize that at low pulse frequencies, the particles are more mobile in the off half-cycle and thus the crystal phase may be kinetically unstable, like the Lindemann melting criterion.[189,190] However, we do not observe instabilities in the crystal at large frequencies. Figure 3.9 shows that if we increase the pulse frequency in a fluid/fluid coexisting suspension, crystal nucleation and growth occurs within the dense fluid. However, if we then decrease the frequency to its original value, the suspension remains in fluid/crystal coexistence rather than return to its fluid/fluid state. This hysteresis implies that the terminal state is path dependent, since both fluid/fluid and fluid/crystal coexistence are observed at the same point in parameter space.

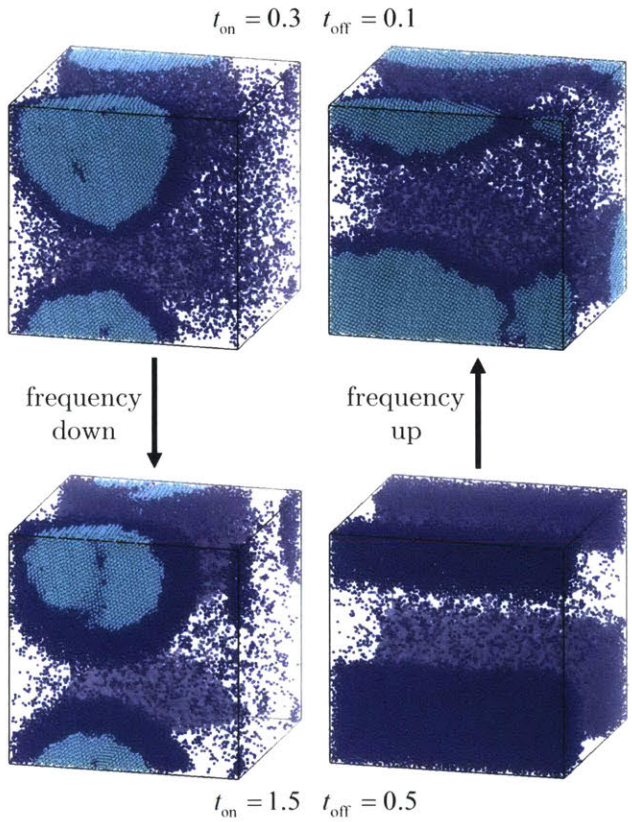

Figure 3.9: Path dependence of the periodic-steady-state of the toggled suspension. A suspension toggled at $t_{on} = 1.5\tau_D$, $t_{off} = 0.5\tau_D$ reaches fluid/fluid coexistence (right bottom). If the toggle frequency is raised, crystallization occurs in the dense fluid and the suspension reaches fluid/crystal coexistence (right top). A suspension toggled at $t_{on} = 0.3\tau_D$, $t_{off} = 0.1\tau_D$ reaches fluid/crystal coexistence (left top). If the toggle frequency is lowered, the suspension remains in fluid/crystal coexistence (left bottom). Crystalline (light blue) and liquid-like (dark-blue) particles are distinguished.

3.4 Kinetic Models

Because only two parameters $(\phi, \varepsilon\xi)$ are needed to specify a location in the periodic-steady-state coexistence diagram, the other two (ξ, t_{off}) can be optimized to yield desired self-assembly kinetics. However, without estimates for the rates of assembly, it is difficult to perform this optimization *a priori*. Instead, the kinetics must be investigated explicitly in simulations and experiments to find the optimal choices of toggle parameters, a time-consuming endeavor. Here, we develop phenomenological models to describe the self-assembly rates for two observed kinetic mechanisms: coarsening of percolated, gel-like networks and nucleation and growth of dense phases. These models can be leveraged to design efficient fabrication processes using toggled assembly.

3.4.1 Gel Coarsening

Colloidal gels formed by steady, strong, and short-ranged attractions coarsen slowly over time according to a power law,

$$L = L_0 + kt^n, \tag{3.27}$$

where L is the characteristic length scale of the gel strands, L_0 is the length scale of the initial network formed, k is a rate constant dependent on the attraction strength ε and particle volume fraction ϕ, and n is the power law exponent. The power law exponent is set by the kinetic mechanism that dominates coarsening. $n = 1/3$ when the kinetics are limited by bulk diffusion, $n = 1/4$ when the kinetics are limited by surface diffusion,[191] and $n = 1/6$ is observed at early times in spinodal decomposition.[192] Although the strong attractions favor a compact, crystalline conformation in thermodynamic equilibrium, the local microstructure is arrested in a disordered configuration, with an average contact number around $N_{\text{nb}} = 6$ – 7[137] rather than a fully occupied nearest neighbor shell of $N_{\text{nb}} = 12$.

To coarsen, thermal fluctuations must break the interparticle "bonds" in the gel to allow the particles to rearrange. Because the bond strength is $O(\varepsilon)$ and many times larger than the thermal energy in the gel-forming regime, bond-breaking is incredibly slow and the coarsening process takes on the order of days or weeks.[192] In our simulations at $\varepsilon = 10k_BT$, steady attractions form an arrested gel that only reaches a crystal fraction of $X_c = 0.005$ in $10000\tau_D$ (see Figure 3.1). If this average crystallization rate held constant, it would take around $10^6\tau_D$ (or around 10 days for a typical $\tau_D = 1\,\text{s}$) to crystallize half of the particles, consistent with experimental time scales.

Toggling the particle attractions greatly enhances the rate of coarsening by accelerating the rate of bond-breaking. In the off half-cycle, all particle bonds are immediately broken, so there is no kinetic barrier preventing microstructural rearrangement. Figure 3.10 shows that the coarsening rate of the toggled attractive gel is orders of magnitude faster than the coarsening rate of the steady attractive gel at $\varepsilon = 10k_BT$. Unlike the steady attractive gel, the local microstructure of the toggled attractive gel is highly crystalline with $N_{\text{nb}} = 12$. Although the global structure is disordered and percolated, the toggling protocol anneals local defects and allows the particles to find low energy, closest-packed crystalline configurations. If the time scale for local crystallization is short compared to the time scale for global coarsening, the gel strands are nearly entirely crystalline and slowly grow larger over time, as in the top row of Figure 3.6. We observe this to hold in nearly the entire range of the gel coarsening regime, with the local crystallization and coarsening rates becoming comparable only at the large $t_{\text{off}} \geq 0.05\tau_D$ edge of the region. In this case, $L_c = N_c/N_i$ serves as a good estimate for a quantity proportional to the characteristic length scale L of the gel strands.

We performed Brownian dynamics simulations of toggled attractive gels at $\phi = 0.20$, $\varepsilon = 10k_BT$, and a variety of points (t_{off}, ξ) in the gel coarsening region of Figure 3.5. Figure 3.10 shows the evolution of the gel length scale L_c over time. We observe that coarsening of toggled attractive gels is also described by the power law in equation (3.27). (3.27) is relevant on time scales long compared to the toggle period, and is not intended to describe the fast dynamics within a single toggle period, which are of little interest compared to the slow dynamics of phase separation.

The rate constant k for the steady attractive gel is a function of ε and ϕ. For the toggled attractive gel, k is also a function of t_{on} and t_{off}, even with ε and ϕ fixed. The dependence of k on the toggle parameters

reflects the competing processes of aggregation in the on half-cycles and structural rearrangement in the off half-cycles. Because the attraction is strong compared to the thermal noise, the suspension microstructure quickly freezes in place at the start of each new on half-cycle. For the remaining duration of the on half-cycle, essentially no more structural changes occur because the strong bonds are difficult to break. Time is "wasted" sitting in the frozen configuration until the bonds are broken at the end of the on half-cycle. The value of t_{on} has no effect on the rate of coarsening other than delaying the next off half-cycle. The larger t_{on}, the longer it takes between structural rearrangements in the off half-cycles, and the slower the coarsening rate. We can remove the effect of t_{on} by tracking the coarsening kinetics in terms of the number of toggle cycles that have occurred, $N_{\text{cycle}} \equiv t/\mathscr{T}$, rather than the absolute time t. Recasting (3.27) in terms of N_{cycle},

$$L = L_0 + k' \left(\frac{t}{\mathscr{T}} \right)^n, \tag{3.28}$$

where the new rate constant $k'(t_{\text{off}}) \equiv k\mathscr{T}^n$ is a function of t_{off} only. t_{on} only affects the rate constant k through its effect on the period $\mathscr{T}$. Figure 3.10 shows that when L_c is plotted versus N_{cycle}, all kinetic curves with the same t_{off}, but different t_{on}, collapse together. Equation (3.28) holds when $t_{\text{on}} \gg t_{\text{off}}$, but may break down for $t_{\text{on}} \approx t_{\text{off}}$, where the amount of rearrangement in the on and off half-cycles become comparable.

The extent of structural rearrangement in the off half-cycle depends on the amount of time the particles diffuse. $k'(t_{\text{off}})$ increases with increasing t_{off}, indicating that particles with more time to rearrange tend to promote enhanced coarsening. If t_{off} is short, particles will not diffuse very far from their initial positions in the off half-cycle, and the amount of structural rearrangement will be small. It is difficult for the suspension to sample new configurations, and coarsening proceeds slowly. Presumably then, it is easier to sample new configurations the longer the particles diffuse, and coarsening occurs faster at longer t_{off}. One way to quantify the extent of structural "arrangement" is to track the fraction of particles f that diffuse a sufficient distance ℓ in the off half-cycle. We assume that the $1 - f$ fraction of particles that failed to diffuse sufficiently far in the off half-cycle return to their same configuration when the attractions are turned back on and cannot contribute to coarsening. The f fraction of particles that succeeded in diffusing a distance ℓ find a new configuration and can contribute to coarsening. At every cycle then, the coarsening rate dL/dN_{cycle} is a factor of f smaller than we might expect if all particles could contribute to coarsening. Thus, we can recast (3.28) again as

$$L = L_0 + k'' f \left(\frac{t}{\mathscr{T}} \right)^n, \tag{3.29}$$

where now the rate constant $k'' \equiv k\mathscr{T}^n/f$ is independent of both t_{on} and t_{off} and is constant for all simulations. A good choice for ℓ is the capture radius r_c, the separation distance at which the strength of the interparticle attraction $|U(r)|$ is equal to the thermal energy k_BT. With this choice, particles that diffuse $r < r_c$ in the off half-cycle have $|U| > k_BT$ and are recaptured when the attractions are turned on while particles that diffuse $r > r_c$ have $|U| < k_BT$, with enough thermal energy to avoid capture. For the particular choice of the depletion attraction (3.1), $r_c = 0.14a$. We estimate f by integrating the probability distribution $P(\mathbf{x}, t = t_{\text{off}})$ for ideal Gaussian diffusion,

$$f = \int_{r_c}^{\infty} d\mathbf{x} \frac{1}{\sqrt{4\pi D t_{\text{off}}}} e^{-|\mathbf{x}|^2/4Dt_{\text{off}}} = \frac{r_c}{\sqrt{\pi D t_{\text{off}}}} e^{-r_c^2/4Dt_{\text{off}}} + \operatorname{erfc} \frac{r_c}{\sqrt{4Dt_{\text{off}}}}. \tag{3.30}$$

In reality, the particles have hard repulsions that modify their diffusion. Some particles will diffuse more slowly than ideal diffusion because they are caged while others will diffuse more quickly due to stronger osmotic pressure gradients, so the true f is different than the one here. Figure 3.10 shows that when L_c/f is plotted versus $t/\mathscr{T}$, all the kinetic data collapse to a single master curve. The best fit values of the power law exponent and the rate constant in (3.29) are $n = 0.24 \pm 0.05$ and $k'' = 0.057 \pm 0.021$ (see Methods for details on the fit). We ignore the effect of L_0, which only affects the short time kinetics, by assuming $L_0 = 0$ for the fits. The average value of $n = 0.24$ supports that surface diffusion ($n = 1/4$) likely plays the dominant role in setting the coarsening rate, though it is difficult to distinguish between the other possible power laws (*e.g.* $n = 1/3$ or $n = 1/6$).

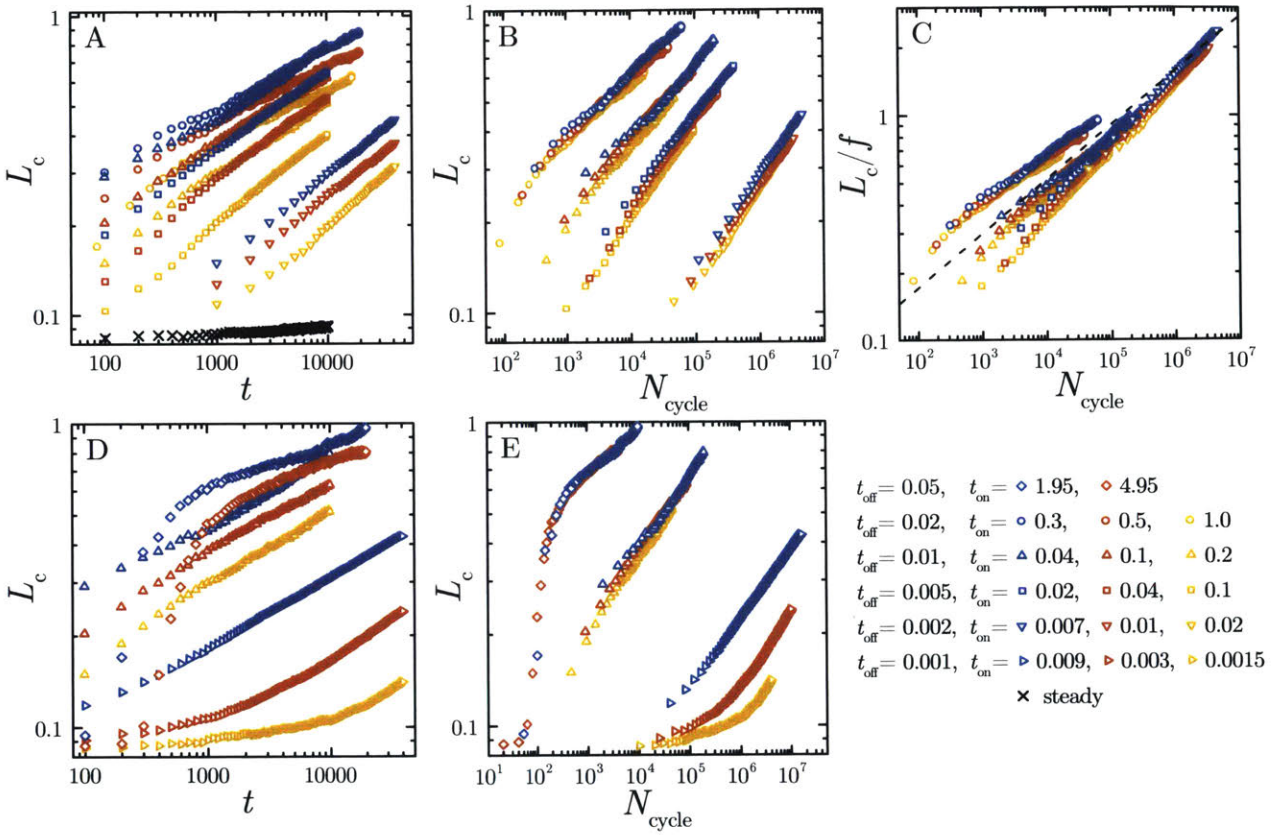

Figure 3.10: Evolution of the characteristic length scale $L_c = N_c/N_i$ of toggled dispersions in the gel coarsening region of Figure 3.5 for fixed $\varepsilon = 10k_BT$ and varying t_{on} and t_{off}, made dimensionless by the diffusion time τ_D. The top row shows data in the regime where our model applies. A: The length scale increases as a power law in time t, dimensionless on τ_D. B: In terms of number of cycles, $N_{\text{cycle}} \equiv t/(t_{\text{on}} + t_{\text{off}})$, curves with the same t_{off} collapse together. C: Dividing L_c by the fraction of particles f diffusing the capture radius r_c from equation (3.30), the curves all collapse to a single universal curve (dashed line). The bottom row shows data outside of where our model applies. In moving from panel D to panel E, the curves at $t_{\text{off}} = 0.001$ do not collapse, while the curves at $t_{\text{off}} = 0.05$ show a different kinetic mechanism, indicating that our model does not describe these regimes. Only the $t_{\text{off}} = 0.01$ curves behave like the model predicts.

Maximizing the Coarsening Rate

As t_{off} increases, the fraction of particles f able to diffuse r_c in t_{off} increases, enhancing coarsening. However, increasing t_{off} also increases the toggle period $\mathscr{T} = t_{\text{on}} + t_{\text{off}}$, which reduces the number of toggle cycles and hinders coarsening. There is an optimal $t_{\text{off}} = t^*_{\text{off}}$ given by $\partial k/\partial t_{\text{off}} = 0$, where $k \equiv k'' f/\mathscr{T}^n$, at which the rate constant k (and therefore the coarsening rate dL/dt) is maximized. At constant t_{on}, the value of t^*_{off} depends on t_{on}. At constant ξ, t^*_{off} is independent of ξ because $\mathscr{T} = t_{\text{off}}/(1-\xi)$ and so ξ contributes only to the coefficient in $k = k''(1-\xi)^n f/t^n_{\text{off}}$. Maximizing k with respect to t_{off} at constant ξ yields

$$\left.\frac{\partial k}{\partial t_{\text{off}}}\right|_{\xi} = 0, \quad \Rightarrow \quad t^*_{\text{off}} = 0.011\tau_D. \tag{3.31}$$

This is very close to the time it takes for a particle to diffuse the range of the interaction, $\delta^2/D = 0.01\tau_D$, allowing for the most structural rearrangement in the off half-cycle while still reaggregating in the on half-cycle, which Swan and coworkers argued was the optimal choice for t_{off}.[36,67,68,82] The local maximum $t_{\text{off}} \approx 0.01\tau_D$ at constant ξ can be seen in the crystal fraction X_c in Figure 3.5 at large $\xi > 0.9$ in the gel region, where our kinetic model works best. For any particular t_{off}, k also increases with decreasing ξ. This agrees with the monotonic trend of the crystal fraction at constant t_{off} in the left half of Figure 3.5 with $t_{\text{off}} \leq 0.02\tau_D$.

Relevant Domain of the Model

Equation (3.29) describes the coarsening data well in the decade $0.002\tau_D \leq t_{\text{off}} \leq 0.02\tau_D$ when $t_{\text{on}} \gg t_{\text{off}}$, but breaks down elsewhere in the gel coarsening regime. For $t_{\text{off}} \leq 0.001\tau_D$ (with $\xi \geq \xi_{\text{gel}}$), the coarsening data does not collapse together when plotted in terms of N_{cycle}, shown in the bottom row of Figure 3.10. Although the coarsening rate at constant t_{off} increases with decreasing t_{on} (as in (3.29)), evidently the value of t_{on} influences k more than just its effect on the toggle period. One possibility is that the time scale for toggling ($\mathscr{T}$) is so fast relative to time scale for particle diffusive motion (τ_D) that the particles see a steady attraction of time-averaged strength $\varepsilon\xi$. Figure 3.3 shows the crystallinity of the toggled attractive gel approaching that of the steady attractive gel of equivalent time-averaged strength as t_{off} decreases, although even at the shortest times investigated here, $t_{\text{off}} = 0.001\tau_D$, there is still decent enhancement (a factor of ≈ 2) in the crystallization rate for the toggled gel. The approach to an effectively steady attraction may prevent collapsing the coarsening data in terms of N_{cycle}.

At larger $t_{\text{off}} \geq 0.05\tau_D$ (with $\xi \geq \xi_{\text{gel}}$), the time scale for local crystallization is slow compared to the time scale for global coarsening. As a consequence, fluid/fluid phase separation occurs rather than fluid/crystal phase separation and the local microstructure of the percolated network is fluid-like initially. After some time, crystal nucleates within the dense fluid network and rapidly grows to crystallize the entire network, at which point the structure slowly coarsens like usual in the gel coarsening regime. From the way we estimate $L_c = N_c/N_i$, the gel length scale rapidly increases after crystal nucleation, even though the true length scale set by the dense fluid network is already large here. Interestingly, the data still collapse when plotted in terms of N_{cycle}, but equation (3.29) does not account for two-step nucleation and cannot describe the full suite of coarsening kinetics.

3.4.2 Nucleation and Growth

In the fluid/crystal and fluid/fluid coexistence regions of Figure 3.5, distinct clusters nucleate in the toggled suspensions rather than many nuclei forming a network as in the gel region. The clusters grow, coalesce, and Ostwald ripen as the suspension heads toward a periodic-steady-state of two-phase coexistence. As the self-assembly boundary ξ^* is approached from above by lowering the duty cycle, the driving force for self-assembly decreases and few nuclei form. Very close to the phase boundary, only a single nucleation event occurs. Here, coalescence and Ostwald ripening are entirely suppressed, and phase separation occurs purely by nucleation and growth. This is the simplest place to understand the self-assembly kinetics in the coexistence regions, so we focus on a kinetic model for the nucleation and growth of a single, spherical nuclei close to the phase boundary, as in the bottom three rows of Figure 3.6.

Suppose a dense spherical nucleus of radius R and volume fraction ϕ_n has already formed in the surrounding dilute fluid at volume fraction ϕ_f. The nucleus can be composed of crystal, dense fluid, or both. When the attractions are on, particles prefer the dense phase and the nucleus grows. Particles within δ of the nucleus are quickly driven towards the nucleus at the beginning of the on half-cycle by the strong interparticle attractions. The number of particles in this δ layer is

$$N_{\text{layer}} = \frac{\delta \phi_{\text{layer}} A}{v_0}, \tag{3.32}$$

where $A = 4\pi R^2$ is the surface area of the nucleus, $v_0 = 4\pi a^3/3$ is the volume of a single particle, and ϕ_{layer} is the volume fraction of the layer, which is unknown but between the densities of the nucleus and the surrounding fluid, $\phi_f \leq \phi_{\text{layer}} \leq \phi_n$. The time it takes for a particle δ away from the nucleus to reach the nucleus directed by the interparticle force of ε/δ is $t_{\text{layer}} \approx \delta^2 k_B T \tau_D / a^2 \varepsilon$. For $\varepsilon = 10 k_B T$ and $\delta = 0.1a$, as in the all the simulations presented, $t_{\text{layer}} = 10^{-3}\tau_D$. If $t_{\text{on}} \geq t_{\text{layer}}$, all of the particles in the thin δ layer will be incorporated into the nucleus in the on half-cycle, independent of t_{on}.

Because the attractions are strong and short-ranged, the remaining particle flux into the nucleus in the on half-cycle is diffusion-limited,

$$J_{\text{on}} = -\frac{D_f^s \phi_f}{a v_0}, \tag{3.33}$$

where the self diffusivity in the fluid D_f^s is used to estimate a characteristic diffusive speed D_f^s/a of the fluid particles. Notice that the flux is negative, indicating that particles are moving into the nucleus.

When the attractions are off, particles are pushed out of the dense phase and the nucleus shrinks. The particles interact only through hard repulsions, so the particle flux out of the nucleus is also diffusive,

$$J_{\text{off}} = \frac{D_n^c \phi_n}{a v_0}, \tag{3.34}$$

but the appropriate diffusivity is the collective diffusivity D_n^c of the particles in the nucleus. While the self-diffusivity describes the motion of a single particle in a homogeneous phase, the collective diffusivity describes motion of a collection of particles moving along concentration gradients. The two diffusivities are related as $D^c = D^s \phi (\partial(\mu/k_B T)/\partial\phi)$, so D^c contains additional thermodynamic information capturing interactions between particles. Here, D_n^c/a estimates the enhanced speed (over D_n^s/a) of particles out of the nucleus when the attractions are off due to the high osmotic pressure of the dense nucleus.

At constant volume and number of particles, the background fluid becomes depleted in particles as the nucleus grows because $\phi_n > \phi_f$,

$$\phi_f = \frac{\phi_0 - \phi_n 4\pi R^3 n_{\text{nuc}}/3}{1 - 4\pi R^3 n_{\text{nuc}}/3} = \phi_0 + (\phi_0 - \phi_n)\frac{4\pi n_{\text{nuc}}}{3} R^3 + O(\phi_{\text{nuc}}^2), \tag{3.35}$$

where ϕ_0 is the overall particle volume fraction, n_{nuc} is the number density of nuclei, and $\phi_{\text{nuc}} \equiv 4\pi R^3 n_{\text{nuc}}/3$ is the overall volume of the growing nuclei relative to the system volume (and not the volume fraction within the nuclei itself, ϕ_n). The largest ϕ_{nuc} can become is ϕ_0, when all particles are incorporated into the nucleus, so we can drop the $O(\phi_{\text{nuc}}^2)$ terms and higher. Here, $\phi_0 = 0.20$, so neglecting higher order terms suffers only a 4% error in the worst-case scenario and only near the end of the phase separation. While ϕ_f decreases as the nucleus grows, we assume ϕ_n is constant and given as the known coexisting volume fraction at periodic-steady-state from Figure 3.8.[36]

If t_{on} and t_{off} are not too long compared to a^2/D_f^s and a^2/D_n^c, the nucleus cannot change size appreciably within a single half-cycle, and the change in the number of particles in the nucleus, ΔN_n, over one toggle cycle may be approximated as,

$$\frac{\Delta N_n}{\mathscr{T}} = \frac{1}{\mathscr{T}}\left(N_{\text{layer}} - J_{\text{on}} A t_{\text{on}} - J_{\text{off}} A t_{\text{off}}\right), \tag{3.36}$$

On time scales long compared to the toggle period $\mathscr{T}$, $\Delta N_n/\mathscr{T} \approx dN_n/dt$, and we have a first-order ordinary differential equation for the nucleus radius,

$$\frac{dR}{dt} = \frac{1}{\mathscr{T}\phi_n}\left(\delta\phi_{\text{layer}} + \frac{D_f^s\phi_0}{a}t_{\text{on}} - \frac{D_n^c\phi_n}{a}t_{\text{off}} - \frac{D_f^s}{a}t_{\text{on}}\left(\phi_n - \phi_0\right)\frac{4\pi n_{\text{nuc}}}{3}R^3\right) \tag{3.37}$$

$$\equiv k_1 - k_2 R^3, \tag{3.38}$$

where

$$k_1 = \frac{\delta\phi_{\text{layer}}}{\mathscr{T}\phi_n} + \frac{D_f^s\phi_0}{a\phi_n}\xi - \frac{D_n^c}{a}(1-\xi), \tag{3.39}$$

$$k_2 = \frac{D_f^s}{a\phi_n}\xi\left(\phi_n - \phi_0\right)\frac{4\pi n_{\text{nuc}}}{3}, \tag{3.40}$$

and we have used $N_n = \phi_n(R/a)^3$ to write $dN_n/dt = (3\phi_n R^2/a^3)\,dR/dt$. $k_2 > 0$, so the second term, arising from the depletion of the background particle concentration, acts to shrink the nucleus. k_1 must be positive for any growth to occur, so the condition $k_1 > 0$ sets a critical duty necessary for growth. However, this does not take into account nucleation barriers, so the true ξ^* from Figure 3.5 may be different. Whether this critical duty from the $k_1 > 0$ conditions coincides with the predicted phase boundary in Figure 3.8 from is unclear.

From (3.38), we immediately extract the limiting behavior. Initially, the growing nucleus is small, and so the second term in (3.38) is negligible. The nucleus grows linearly in time at a constant rate k_1. As the nucleus grows, so does the magnitude of the $O(R^3)$ term. Eventually, growth ceases when the two terms in equation (3.38) exactly cancel and the nucleus reaches a terminal size,

$$R_f \equiv \left(\frac{k_1}{k_2}\right)^3, \tag{3.41}$$

where the suspension is at periodic-steady-state. Recasting (3.38) in terms of $\widetilde{R} \equiv R/R_f$ and $\widetilde{t} = k_1 t$,

$$\frac{d\widetilde{R}}{d\widetilde{t}} = 1 - \widetilde{R}^3. \tag{3.42}$$

While $R(t)$ in (3.38) depends on the values of t_{on} and t_{off}, $\widetilde{R}(\widetilde{t})$ in (3.42) does not, and the kinetics have universal behavior. Separating variables in (3.42) and integrating from $\widetilde{R} = 0$ at $\widetilde{t} = 0$ to $\widetilde{R}$ at $\widetilde{t}$, we obtain an expression implicit in $\widetilde{R}$

$$\widetilde{t} = \frac{1}{6}\ln\frac{1+\widetilde{R}+\widetilde{R}^2}{(1-\widetilde{R})^2} + \frac{\sqrt{3}}{3}\tan^{-1}\frac{\sqrt{3}\widetilde{R}}{2+\widetilde{R}}. \tag{3.43}$$

We could have begun the integration from $\widetilde{R} = \widetilde{R}^*$ at $\widetilde{t} = \widetilde{t}_i$, where $\widetilde{R}^*$ is the initial size of the nucleus at the nucleation event occurring after an induction time t_i, which adds a constant factor to the right side of (3.43). We observe that $\widetilde{R}^* \lesssim 0.1$ for nucleation events that occur in the simulations, so we ignore this term, with the understanding that $\widetilde{t}$ refers to time after nucleation. As $\widetilde{t} \to \infty$, $\widetilde{R} \to 1$ with the asymptotic form

$$\widetilde{R} \approx 1 - Ce^{-3\widetilde{t}}, \quad C \equiv \sqrt{3}e^{\sqrt{3}\pi/6}. \tag{3.44}$$

Figure 3.11 shows the growth of nuclei in Brownian dynamics simulations of toggled attractive dispersions at different points close to the phase boundary ξ^* in Figure 3.5. Each curve corresponds to a different point along ξ^* and a single curve represents the average growth for 5-10 replicates of the same point. The terminal radius R_f of each curve was easily extracted from the late time data, and the rate constant k_1 was determined from a least squares linear fit of (3.43) to the data. The values of k_1 and R_f along the phase boundary ξ^* are shown in Figure 3.12. All of the data collapses to a single curve when plotted as $\widetilde{R} = R/R_f$ versus $\widetilde{t} = k_1 t$ and agrees well with (3.43) and (3.44).

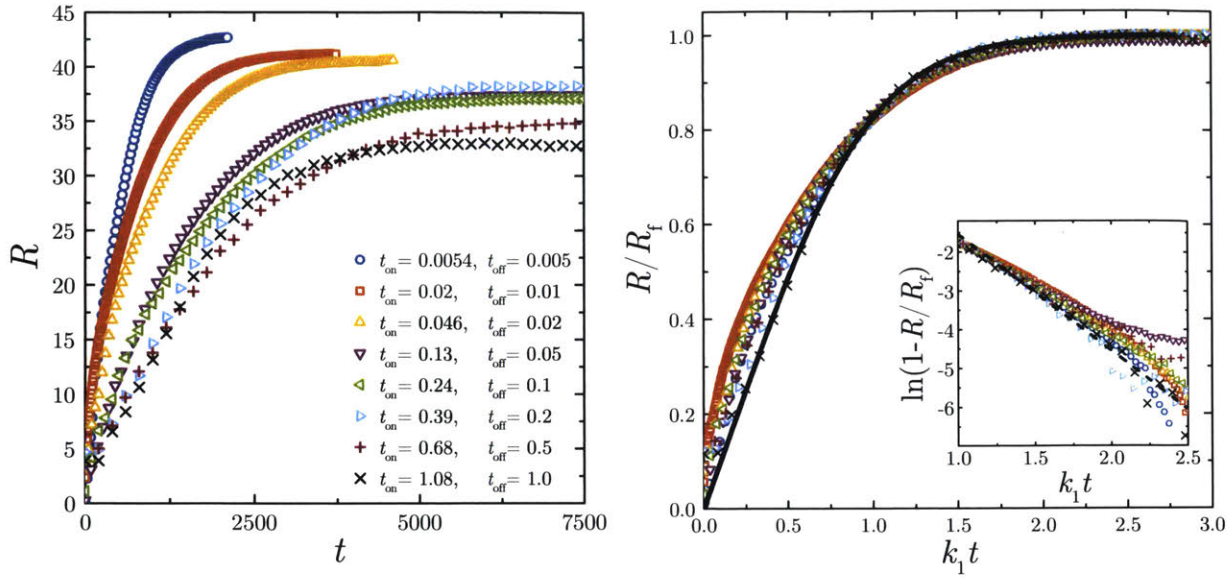

Figure 3.11: Left: Growing radius R, made dimensionless by the particle radius a, of a single, spherical nucleus in the toggled suspensions as a function of time t after nucleation, made dimensionless by the diffusion time τ_D, for different points along the nucleation boundary ξ^* in Figure 3.5. Right: The data collapse to a single master curve when the radius is scaled by the terminal radius R_f and time multiplied by the fit rate constant k_1. The curve agrees well with the solid line from equation (3.43). The inset shows that the asymptotic behavior of the data as $R/R_f \to 1$ also agrees with the dashed line from equation (3.44).

Estimating k_1 and R_f Parameters

The terminal nucleus size R_f is set by the number of particles leaving the nucleus in the off half-cycle balancing the number of particle condensing to the nucleus in the on half-cycle. One way to estimate R_f is to estimate the kinetic parameters k_1 and k_2 and then use equation (3.41), which reflects the balance between particle fluxes in the on and off half-cycles. At periodic-steady-state, the dense phase in the nucleus is in coexistence with the surrounding dilute fluid phase. Therefore, another way to estimate R_f is to use the phase diagram in Figure 3.8 to compute the nucleus size that yields nucleus and background fluid volume fractions equal to their coexisting volume fractions. For each duty fraction ξ, we extract the coexisting volume fractions ϕ_n and ϕ_f. With a known overall volume fraction ϕ_0, the lever rule sets the total fraction (by volume) of the dense phase to be $(\phi_0 - \phi_f)/(\phi_n - \phi_f)$. From the known nucleation density $n_{\text{nuc}} = 1/V$, where V is the total dispersion volume in our simulations, we can then compute the terminal volume and radius of the dense phase. The predicted R_f is shown in Figure 3.12 along with the R_f from the simulations.

Generally, R_f decreases in the simulations as t_{off} increases. The predicted R_f overestimates the true R_f and remains fairly constant with t_{off} until it sharply decreases at large t_{off}, where the coexisting volume fractions of the dense and dilute phases approach each other. The predictions assume a sharp interface between the nucleus at ϕ_n and the surrounding fluid at ϕ_f to compute a precise nucleus radius. However, the real interface is diffuse, with the volume fraction decaying continuously from ϕ_n to ϕ_f moving away from the nucleus. The discrepancy between the simulation data and the prediction could be due to the diffuse interface region growing larger as t_{off} increases. In the worse case scenario, the theory only overpredicts the true R_f by $\approx 20\%$ and can still provide a fair estimate of its magnitude over a wide parameter range.

The initial growth rate k_1 is more difficult to estimate. From equation (3.39), k_1 is a sum of three terms. The first term represents the particles in the thin δ layer that rapidly condense to the nucleus at the beginning of each on half-cycle. This happens once per cycle, so the contribution to k_1 decreases as $1/\mathscr{T}$ as the cycles become longer. The second and third terms in equation (3.39) are from the diffusive contributions in the on and off half-cycles. Assuming that all the parameters in (3.39) do not change significantly compared to t_{off}

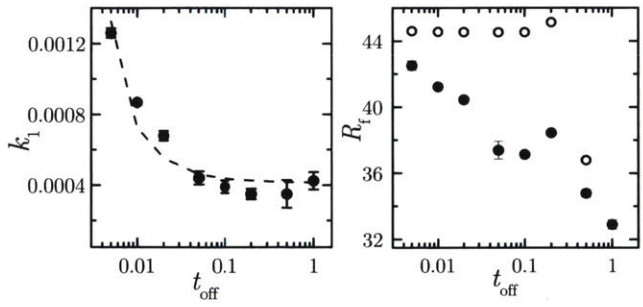

Figure 3.12: Left: Growth rate constant k_1 in equation (3.38), made dimensionless by a/τ_D, as a function of t_{off}, made dimensionless by τ_D, along the nucleation bounday ξ^* from Figure 3.5. The points are data extracted from simulations while the dashed line is a fit of (3.45). Right: The terminal nucleus radius R_f, made dimensionless by the particle radius a, extracted from simulations (filled points) and predicted (open points) from the phase diagram in Figure 3.8.

as we move along the nucleation boundary $\xi^*(t_{\text{off}})$, k_1 follows the form

$$k_1 \approx \frac{C_1}{\mathscr{T}} + C_2, \tag{3.45}$$

where C_1 and C_2 are constant. Figure 3.12 shows that the k_1 observed in the simulations agrees with (3.45) with the linear least squares fit values of $C_1 = 10^{-5}a$ and $C_2 = 4 \times 10^{-4}a/\tau_D$.

We can estimate C_1 and C_2 by estimating the terms in (3.39). ϕ_0, ϕ_{layer}, ϕ_n, and ξ are all $O(0.1-1)$. If we assume that the diffusivities D_f^s and D_n^c are on the same order of magnitude as the diffusivity of an isolated particle, $O(a^2/\tau_D)$, equation (3.39) predicts that $C_1 \approx O(0.01a)$ and $C_2 \approx O(0.1a/\tau_D)$ about 10^3 times larger than observed in the simulations. There is likely a multiplicative prefactor missing in (3.39) that slows the growth time scales by several orders of magnitude. Though we cannot quantitatively predict the C_1 and C_2 parameters, the variation of k_1 with t_{off} agrees with our model.

Critical Radius

In classical nucleation theory, the change in Gibbs free energy ΔG of forming a spherical nucleus of radius R at volume fraction ϕ_n in a homogeneous phase at volume fraction ϕ_f is given as,[119]

$$\Delta G = 4\pi R^2\gamma + \Delta\mu\phi_n\left(\frac{R}{a}\right)^3. \tag{3.46}$$

The first term is the surface energy of the nucleus and contains the interfacial tension γ between the two phases. This term is positive and always contributes an energy penalty to phase separation. The second term is the bulk Gibbs energy difference between the nucleus and the equivalent number of particles in the surrounding phase and contains the difference in chemical potential $\Delta\mu \equiv \mu_n(\phi_n) - \mu_f(\phi_f)$ between the two phases. This term is negative in the phase coexistence regime. Whether the nucleus grows or shrinks is dictated by the sign of $d\Delta G/dN_n$. Because the surface and bulk terms in (3.46) scale differently with R, there is a critical nucleus size

$$R^* = \frac{2\gamma v_0}{\phi_n(\mu_f - \mu_n)}, \tag{3.47}$$

at which $\partial\Delta G/\partial N_n = 0$ and ΔG has a maximum. Clusters smaller than R^* reduce ΔG by shrinking, while clusters larger than R^* reduce ΔG by growing. Because only clusters with $R > R^*$ can grow, there is a finite induction time t_i for fluctuations in the dispersion to produce a critical cluster before growth can occur. The induction time grows exponentially with the nucleation barrier height, $\Delta G(R^*)$,[119]

$$t_i \sim e^{\Delta G(R^*)/k_BT} = e^{4\pi\gamma R^{*2}/3k_BT}. \tag{3.48}$$

Equation (3.47) gives the critical size R^*_{stdy} a nucleus must reach to grow for *steady* attractions. For toggled attractions, all nuclei will shrink in the off half-cycle and only those larger than R^*_{stdy} will grow in the on half-cycle. The critical radius R^* for toggled attractions must be at least as large as R^*_{stdy}. We can estimate R^*_{stdy} using the equations of state for short-ranged attractions,[178] which gives $\Delta\mu = -22k_BT$ between the equilibrium crystal phase $\phi_c = 0.730$ and metastable fluid phase $\phi_f = 0.20$ at $\varepsilon = 10k_BT$. The interfacial tension of colloidal dispersions with short-ranged attractions is small and on the order $\gamma = O(0.1 - 1k_BT/a^2)$.[193–195] Thus, $R^*_{\text{stdy}} \approx a$ and individual particles are already the size of the critical nucleus. Because the induction time goes as $t_i \sim e^{(R^*/a)^2}$, there is essentially no barrier to nucleation and nucleation should occur immediately. However, we do observe a finite induction time in our simulations. This implies that there must be another mechanism that is setting a second critical radius $R^* > R^*_{\text{stdy}}$.

One possibility is that R^* must be the size of the smallest cluster that survives a single off half-cycle. If $R < R^*$, the cluster will completely dissolve in the off half-cycle and cannot grow in the subsequent on half-cycle. If $R > R^*$, the cluster does not dissolve completely in the off half-cycle and continues to grow in the on half-cycle. This seems plausible for longer toggle periods, where t_{off} is long enough for significant dissolution, but does not necessarily explain the finite induction time for short toggle periods. For example, a cluster of any size is unlikely to dissolve completely in $t_{\text{off}} = 0.001\tau_D$, yet we still observe a significant induction time in this case.

Whatever the mechanism is to set R^*, it is certain that this critical cluster must form in the on half-cycle (or over several consecutive on half-cycles), as all clusters shrink in the off half-cycle. The longer t_{on}, or equivalently the larger ξ, the more likely it is to form a cluster of the critical size. When ξ becomes large enough that nucleation of a critical cluster becomes likely in the simulation time, a nucleation event will occur. This sets the boundary ξ^* for a given finite observation time. This ξ^* must be at least the ξ that guarantees $k_1 > 0$ in equation (3.39), because $k_1 > 0$ is required for *any* cluster to grow (according to our model).

3.4.3 Effect of Excluding Hydrodynamics

Our Brownian dynamics simulations neglect interparticle hydrodynamic interactions and instead use the freely draining model, where each particle experiences the hydrodynamic resistance of an isolated particle in a solvent. This neglects both long-ranged, many-bodied hydrodynamic couplings as well as pairwise near-field lubrication interactions.[130] Without capturing the correct fluid mechanics of the solvent in which the particles are immersed, our simulation model is not a completely accurate picture of real suspensions. We should be careful to consider how choosing not to incorporate these physics impacts our results. As discussed earlier, hydrodynamic interactions do not affect the coexistence criteria at periodic-steady-state (3.21), but they do influence the phase separation kinetics.

The lubrication interactions are only important for particles that are very close together. As two particles approach each other, an increasingly large force is needed to squeeze out the thin fluid layer in the gap between them, with the force increasing as the reciprocal of gap width. This tends to slow down the dynamics of nearly touching particles and prevents them from coming into contact. This is likely not important for condensation in our suspension with strong attractions, because the attractions allow the particles to get "close enough" to condense before lubrication plays a significant role. It is possible that lubrication makes it more difficult for a particle to diffuse away from dense clusters in the off half-cycle, but is likely a small effect because of the strong osmotic driving force for dissolution of the dense phases with hard repulsions. Simulations of colloidal gelation have found that including lubrication does not modify the general self-assembly behavior of suspensions.[137,196]

The long-ranged hydrodynamic couplings on the other hand are crucial for capturing the correct kinetic behavior of suspensions. Without far-field hydrodynamic couplings, each particle in a cluster contributes to the diffusivity of the entire cluster, and so the cluster diffusivity decreases as R^{-3}, where R is the cluster radius. With far-field hydrodynamics, only the overall cluster size affects the diffusivity, so the cluster diffusivity scales as R^{-1}.[137] Within dense phases, hydrodynamic interactions are screened and do not contribute to local rearrangements of individual particles. The enhanced cluster aggregation relative to local

crystallization tends to promote gelation when far-field hydrodynamics are included[137] and may shift some of the boundaries in Figure 3.5.

Within the gel coarsening region, the microstructure evolves from surface diffusion of individual particles. While the diffusivity of these particles is modified by HI, the mechanism is not. The progression of equation (3.27) (L vs. t) to equation (3.28) (L vs. N_{cycle}) to equation (3.29) (L/f vs. N_{cycle}) is still valid with inclusion of HI, though the value of k'' in (3.29) may change quantitatively. Similarly, our model of nucleation and growth only accounts for a single growing nucleus, whose cluster diffusivity is not relevant. HI will change the diffusivities D_f^s and D_n^c in (3.37), but not the growth mechanism.

Conclusion

Fabricating nanoscale materials on a commercial scale requires well-characterized, efficient processing techniques. Dynamic self-assembly methods hold much promise in this area over their equilibrium counterparts in three critical areas: speed of assembly, quality of product, and ease of control. In fact, nearly all materials in nature are self-assembled using such out-of-equilibrium pathways. Out-of-equilibrium methods are also capable of forming novel structures that equilibrium methods cannot. As the nature of materials becomes more complex, dynamic self-assembly will play a bigger role in nanomaterial fabrication. The main obstacle to implementing dynamic self-assembly processing techniques in practice so far has been a lack of understanding of their governing principles and little exploration into the large parameter spaces involved.

In this chapter, we have answered some key questions about dynamic self-assembly by examining the phase behavior and phase separation kinetics of a dispersion of nanoparticles with isotropic, short-ranged attractions that are toggled on and off cyclically in time. Because this simple toggling model is only a "first-order" perturbation away from static self-assembly with steady interactions, we were able to derive analytic expressions governing the assembly. The limiting out-of-equilibrium phase behavior was described with only two parameters, the time-averaged strength of interaction $\xi\varepsilon$ and the volume fraction ϕ, and could be predicted in terms of equilibrium equations of state. The dynamics are easily controlled with the external toggle parameters, so t_{on} and t_{off} can be optimized to enhance the self-assembly rate and quality of the assembled structure as well as be tuned to stabilize structures that are only metastable in static-self assembly. We developed simple models to describe the toggled assembly kinetics for several different mechanisms. This predictive framework will aid in the design of scalable dynamic self-assembly processes to synthesize useful nanomaterials.

We believe that the results in this chapter represent the first detailed view of a model dynamically self-assembled material, and thus may be applied quite generally to a broad range of materials driven to assemble by toggling protocols. Our analysis can be extended to more complicated particle interactions or different forms of time-variation, as we will show in Chapter 5 with toggled electric/magnetic field assembly.

Methods

The Brownian dynamics simulations were performed using the freely-draining model discussed in Chapter 2, which neglects hydrodynamic interactions among particles. In the simulations, lengths are made dimensionless by the particle radius a, energies are made dimensionless by the thermal energy k_BT, and times are made dimensionless on the bare particle diffusion time $\tau_D \equiv 6\pi\eta a^3/k_BT$. All simulations are performed with around 64000 identical particles for around $10000\tau_D$. The integration time step was chosen sufficiently small to resolve the fastest time scale in the suspension. For long t_{on} and t_{off}, the diffusive motion of a single particle is the fastest time scale, and we use a time step of $\Delta t = 10^{-4}\tau_D$ when *both* t_{on} and t_{off} are longer than or equal to $0.01\tau_D$. This time step is sufficiently short to accurately capture the dynamics of colloidal particles with our simulation method. Where *either* t_{on} or t_{off} fall below $0.01\tau_D$, we use a smaller time step $\Delta t = 10^{-5}\tau_D$ to resolve the dynamics within each individual half-cycle.

Because we consider only strong, short-ranged attractions, any crystal phase that forms is nearly closest packed $\phi \approx 0.74$ for almost any ε/k_BT, with each particle contacting $N_{\text{nb}} = 12$ neighboring particles. The

densest disordered packing is much lower, $\phi \approx 0.64$, so disordered particles contact fewer than $N_{\rm nb} < 12$ particles. We can distinguish between crystalline and fluid-like particles using the contact number. We consider particles separated by a distance less than $r \leq 2.1a$ as "contacting". A particle is designated as "crystalline" if it has a contact number of $N_{\rm nb} = 12$. We denote the number of crystalline particles as N_c and the crystal fraction as $X_c \equiv N_c/N$. A particle is designated as "interfacial" if it is contacting a crystalline particle, but doesn't have 12 contacts itself. These particles are not necessarily disordered, because they sit on a crystal lattice site, but do not have the same local structure as the bulk crystal particles due the fluid phase on one side. We denote the number of interfacial particles as N_i. A particle that is neither crystalline nor interfacial (*i.e.* has a contact number less than 12 and is not contacting a crystalline particle) is designated "fluid-like".

In the case of fluid/fluid phase separation, we can distinguish between particles belonging to the dense and dilute fluid phases using the particles' local volume fraction ϕ_ℓ. The local volume fraction was determined by looking at a sphere of radius $6a$ centered around a particle and calculating the fraction of this search sphere's volume that was occupied by particles. The central particle's volume was included as well as partial intersections of particle volume with the search sphere surface. Strictly, this represents density only conditionally around a central particle and so overestimates the true local density. However, this allows us to assign a local density unambiguously to a particle rather than to a position in space, and so is more useful as a particle-based order parameter. The error in using our approach is small for all but the most dilute regions. The distribution of ϕ_ℓ has two peaks associated with the coexisting volume fractions of the two phases. These are the fluid/fluid coexistence points shown in Figure 3.8.

The power law fit for the gel coarsening data in Figure 3.10 was computed by first performing a two parameter linear least squares fit of $\log(L_c/f)$ versus $\log N_{\rm cycle}$ data to find n and k'' in equation (3.29) for each data set in Figure 3.10. The values of n for each data set were averaged together to give the average n, with an uncertainty given by the standard deviation. Then, an additional one parameter linear least squares fit was performed to find k'' again for each data set, assuming the average value of $n = 0.24$. The values of k'' for each data set were averaged together, and the uncertainty is given by the standard deviation. This procedure ensures that each data set contributes equally to the fit parameters rather than biasing the fit toward the data sets containing more data points.

To determine the size of the nucleus in Figures 3.11 and 3.12, we used $R = a((N_c+N_i+N_d)/\phi_n)^{1/3}$, where N_d is the the number of dense fluid particles and ϕ_n is the average volume fraction of the nucleus. This allows us to track one-step crystal growth, two-step crystal growth, and dense fluid growth. Particles were designated as dense fluid if they were neither crystalline nor interfacial and have a local volume fraction larger than some threshold volume fraction. We select $\phi = 0.35$ as the threshold for one-step crystal nucleation and fluid nucleation, and $\phi = 0.40$ for two-step nucleation. ϕ_n was measured when the nucleus reached its terminal size and assumed constant throughout the growth process. In the case where two-step nucleation occurs, both crystal and dense fluid are present in the nucleus, so we average the densities of both phases (ϕ_c and ϕ_d), weighted by the fraction of particles in each phase, $\phi_n = (N_c+N_i)\phi_c/(N_c+N_i+N_d)+N_d\phi_d/(N_c+N_i+N_d)$.

Chapter 4

Field-Directed Self-Assembly of Mutually Polarizable Nanoparticles in Steady External Fields

With an understanding of dynamic self-assembly in the simple toggled depletion model of Chapter 3, we would like to extend our results and analysis to toggled electric and magnetic fields, which have already been investigated experimentally.[64,65,67,68,73–77,197] In toggled fields, the coexistence criteria at periodic steady state in equation (3.21) involve time averages of chemical potential and pressure. These are constructed in (3.23) using equilibrium equations of state in steady fields. This was well-understood for the depletion system, but the complete phase diagram and equilibrium equations of state for field-directed assembly of dielectric and paramagnetic colloids has not been computed, even for steady electric and magnetic fields.

In this chapter, we develop a complete thermodynamic description of these polarizable dispersions in steady fields. We show how an important physical feature of these types of particles, mutual polarization, sculpts the free energy landscape and has a remarkably strong influence on the nature of the self assembled states. Our theoretical predictions agree with the phase behavior we observe in dynamic simulations of these dispersions as well as that in experiments of field-directed structural transitions. This new model also predicts the existence of a eutectic point at which two crystalline phases and a disordered phase of nanoparticles all simultaneously coexist. Understanding the thermodynamics of these dispersions in steady fields will allow us to compute the periodic-steady-states in toggled fields, which is the focus of Chapter 5.

Introduction

Dielectric and paramagnetic nanoparticles in suspension polarize and interact in the presence of an externally applied electric or magnetic field. Because of this simple scheme for controlling particle interactions on the nano- and colloidal scale, these materials have found many applications in technologies important for society. The external field may be used to control the viscosity of electrorheological[7,8] and magnetorheological[9,10] fluids used in automobile break lines, artificial joints, and vibrational dampers in earthquake resistant buildings. The optical response of crystals composed of dielectric/paramagnetic particles can be controlled by using the external field to modulate the crystal lattice spacing.[198] Electric and magnetic fields are also used to facilitate self-assembly of permanent structures with useful photonic and transport properties, such as nanowires,[199] two-dimensional[62,200,201] and three-dimensional[61,202,203] crystals of spherical colloidal particles, and aligned phases of anisotropic particles.[163,204] These fields are especially convenient for self-assembly because they are two of the few means of imparting long-ranged interactions to building blocks at the colloidal scale.[18,46] Magnetically actuated microswimmers have been synthesized that mimic the dynamics of motile bacteria.[98] Novel out-of-equilibrium materials have been fabricated from dielectric/paramagnetic suspensions in toggled[67,68] and rotating magnetic fields.[89,205]

These applications take advantage of the ability of dielectric/paramagnetic dispersions to form structures in

an external field. For fields held steady in time, these structures evolve towards a thermodynamic equilibrium state, so the underlying equilibrium phase behavior governs many of the useful properties of these materials. Accurate predictions for the equilibrium phase diagram are vital to facilitate rational design and use of dielectric and paramagnetic nanomaterials. However, the simplest models of this assembly process fail to describe the self-assembled states in terms of experimentally controllable variables. The best predictions to date[206,207] require that particles within coexisting phases possess the same dipole moment regardless of the local organization of that phase or the bulk density. This is problematic because the dipole moments that determine what phases self assemble are *induced* by both the externally applied field as well as a local field arising from the dipole induced in all the surrounding particles through a process of mutual polarization. For conducting particles, the induced dipole is enhanced in a concentrated phase relative to a dilute one, while for insulating particles the converse is true. Thus coexistence and stability of any self-assembled states should depend intimately on the nature of these induced dipoles and through them the polarizability of the particles within a particular solvent. In this article, we develop a first-principles framework understanding these effects on assembly of polarizable nanoparticles and predicting the assembled phases.

It is important to note a contrast between polarizable particles with *induced* dipoles and particles with *permanent* dipole moments which assemble even in the absence of an external field. While rotational diffusion is important for particles with permanent dipoles, which reorient thermally, it is largely irrelevant for isotropic particles with induced dipoles as the timescale for relaxation of the induced dipoles is typically orders of magnitude shorter than that for rotational diffusion. Additionally, permanent dipoles interact differently with an applied field than do induced dipoles as the permanent dipoles are driven to align with the field. The phase behavior of dispersions of particles with permanent dipoles has been studied elsewhere[208] and is not the focus of this work.

We begin by introducing two models of dielectric and paramagnetic dispersions, the commonly used constant dipole model and the more accurate mutual dipole model. We show that the constant dipole model does not account for key qualitative features of real dielectric/paramagnetic dispersions, and its predictions for bulk phase behavior fail to satisfy thermodynamic criteria for coexisting phases at equilibrium. Next, we develop a thermodynamic theory for dispersions of dielectric/paramagnetic nanoparticles using the mutual dipole model and calculate the complete equilibrium phase diagram. The theory satisfies all thermodynamic coexistence criteria and contains solid/solid coexistence and eutectic points, which are lacking from the constant dipole predictions.[206,207] We then perform Brownian dynamics simulations of self-assembling dielectric/paramagnetic suspensions using the mutual dipole model and compute equilibrium phase diagrams *in silico*. Finally, we summarize our results that show quantitative agreement between our theory, simulations, and experiments and discuss key features of equilibrium self-assembly of dielectric/paramagnetic nanoparticles.

4.1 Constant Dipole Model versus Mutual Dipole Model

4.1.1 Constant Dipole Model

A single, spherical dielectric/paramagnetic particle of radius a and conductivity λ_p placed in a solvent of conductivity λ_f polarizes in a constant external field $\mathbf{E}_0$ and acquires a dipole moment[144]

$$\mathbf{S} = 4\pi a^3 \lambda_f \beta \mathbf{E}_0, \tag{4.1}$$

where

$$\beta = \frac{\lambda_p/\lambda_f - 1}{\lambda_p/\lambda_f + 2}. \tag{4.2}$$

Here, "conductivity" quantifies the degree of polarizability of the media and is used generically to refer to the electric permittivity in the case of dielectric particles in an elcctric field or the magnetic permeability in the case of paramagnetic particles in a magnetic field. The mathematical analysis of both classes of materials is identical, so we refer to a generic conductivity and field in this work. If the particle is more polarizable than the solvent ($\lambda_p > \lambda_f$), $\beta > 0$ and the particle polarizes parallel to the external field. If the particle is less polarizable than the solvent ($\lambda_p < \lambda_f$), $\beta < 0$ and the particle polarizes in the opposite direction of the

applied field. If the particle and the solvent have equal conductivities ($\lambda_p = \lambda_f$), $\beta = 0$ and the particle does not polarize. A perfectly conducting particle ($\lambda_p \to \infty$) has $\beta = 1$ and acquires the largest dipole strength for a given field while a perfectly insulating particle ($\lambda_p = 0$) has $\beta = -1/2$ and acquires the most negative dipole.

For dispersions of many particles in an external field, the simplest model used for numerical and theoretical calculations assumes that each particle acquires the same dipole moment as a single, isolated particle, as in equation (4.1).[146] This is correct in the limit of infinitely dilute suspensions, but is only an approximation at finite concentrations. The particles interact with the pairwise dipole-dipole interaction potential

$$u_{ij}(\mathbf{r}_{ij}) = 4\varepsilon \left(\frac{a}{r_{ij}}\right)^3 \left(1 - 3\cos^2\theta_{ij}\right), \tag{4.3}$$

where $\mathbf{r}_{ij} \equiv \mathbf{x}_i - \mathbf{x}_j$ is the distance vector from the center of particle j at position $\mathbf{x}_j$ to the center of particle i at position $\mathbf{x}_i$, $r_{ij} \equiv |\mathbf{r}_{ij}|$, and θ_{ij} is the angle between $\mathbf{r}_{ij}$ and the applied field $\mathbf{E}_0$. The parameter $\varepsilon \equiv S^2/16\pi a^3 \lambda_f = \pi a^3 \lambda_f \beta^2 E_0^2$, where the dipole strength is $S \equiv |\mathbf{S}|$ and the field strength is $E_0 \equiv |\mathbf{E}_0|$, characterizes the strength of the dipole-dipole interactions. $u_{ij} = -\varepsilon$ when the pair of particles are in contact, $r_{ij} = 2a$, and oriented parallel to the applied field, $\theta_{ij} = 0$. ε depends only on the product βE_0 and not on β or E_0 independently, implying that dispersions of different β behave identically at the same ε. Because the particle dipoles are all identical and constant over time, this model is called a "constant dipole" or "fixed dipole" model.[146,209]

4.1.2 Mutual Dipole Model

For an isolated particle i at position $\mathbf{x}_i$, the presence of the particle modifies the field $\mathbf{E}(\mathbf{x})$, generating the disturbance field[144]

$$\mathbf{E}_i(\mathbf{x}) \equiv \mathbf{E}(\mathbf{x}) - \mathbf{E}_0 = \frac{1}{4\pi r^3}\left(3\hat{\mathbf{r}}\hat{\mathbf{r}} - \mathbf{I}\right) \cdot \mathbf{S}_i, \tag{4.4}$$

where $\mathbf{r} \equiv \mathbf{x} - \mathbf{x}_i$, $r \equiv |\mathbf{r}|$, and $\hat{\mathbf{r}} \equiv \mathbf{r}/|\mathbf{r}|$. In real suspensions, particles are polarized not only by the external field, but also by the disturbance fields produced by the dipoles in other particles. If the disturbance field of each particle is approximated with the disturbance field (4.4) of an isolated particle, we can construct the linear system of equations for the N particle dipoles

$$\begin{bmatrix} \mathbf{E}_0 \\ \mathbf{E}_0 \\ \vdots \end{bmatrix} = \begin{bmatrix} \mathbf{M}_{11} & \mathbf{M}_{12} & \cdots \\ \mathbf{M}_{21} & \mathbf{M}_{22} & \cdots \\ \vdots & \vdots & \ddots \end{bmatrix} \cdot \begin{bmatrix} \mathbf{S}_1 \\ \mathbf{S}_2 \\ \vdots \end{bmatrix}, \tag{4.5}$$

where

$$\mathbf{M}_{ij} = \begin{cases} \dfrac{1}{4\pi\lambda_f r_{ij}^3}\left(\mathbf{I} - 3\hat{\mathbf{r}}_{ij}\hat{\mathbf{r}}_{ij}\right) & i \neq j \\ \dfrac{1}{4\pi a^3 \lambda_f \beta}\mathbf{I} & i = j \end{cases} \tag{4.6}$$

and $\hat{\mathbf{r}}_{ij} \equiv \mathbf{r}_{ij}/|\mathbf{r}_{ij}|$. All the dipoles are coupled and must be solved for simultaneously. We derived this system of equations formally in Chapter 2, equation (2.74), from a multipole expansion of the integral representation of Laplace's equation truncated at the dipole level, neglecting quadrupole and higher order moments. For the charge-free particles we consider here, we only need the $\mathscr{M}^E_{ES}$ block of the grand potential tensor $\mathscr{M}^E$, coupling the particle dipoles to the external field. For clarity in this chapter, we denote this $\mathscr{M}^E_{ES}$ block as $\mathscr{M}$ and refer to it as the grand potential tensor, with the understanding that we do not need the other blocks (*e.g.* $\mathscr{M}^E_{Eq}$, $\mathscr{M}^E_{\psi S}$) particles with only dipole moments. $\mathscr{M}$ has diagonal block entries $\mathbf{M}_{ii}$ that represent polarization of particle i due to the external field and off-diagonal block entries $\mathbf{M}_{ij}$ that represent polarization of particle i due to the disturbance field from particle j. The inverse $\mathscr{C} \equiv \mathscr{M}^{-1}$ is called the grand capacitance tensor. Regardless of the number of moments included in the multipole expansion, the equations governing the dispersion can always be cast in the form of (4.5), with the accuracy of $\mathscr{M}$ and $\mathscr{C}$

improving as the number of included moments increases.[145] As described in section 2.2.7, the force on a particle i is determined by first computing the total potential energy of the dispersion,[144,145]

$$U = -\frac{1}{2}\sum_i \mathbf{S}_i \cdot \mathbf{E}_0, \tag{4.7}$$

and then taking the negative gradient with respect to the coordinates of that particle,

$$\mathbf{F}_i = -\nabla_{\mathbf{x}_i} U = -\frac{1}{2}\sum_{jk} (\nabla_{\mathbf{x}_i} \mathbf{M}_{jk}) : \mathbf{S}_j \mathbf{S}_k. \tag{4.8}$$

The unknown dipoles in (4.7) and (4.8) require solving the many-body system of equations (4.5), so U and $\mathbf{F}_i$ are many-body quantities that cannot be decomposed into the sum of pairwise potentials u_{ij} and forces $\mathbf{f}_{ij}$ that only depend on the separations of pairs of particles, $U \neq \sum_{ij} u_{ij}(\mathbf{r}_{ij})$, $\mathbf{F}_i \neq \sum_j \mathbf{f}_{ij}(\mathbf{r}_{ij})$.

Because particles mutually polarize/depolarize each other, models of the form of equation (4.5) are called "mutual dipole" models.[146,209] In mutual dipole models, the particle dipoles are a function of the suspension configuration and, in general, not all equal. In dynamic simulations, the potential tensor $\mathscr{M}$ must be inverted at every time step to solve the system of linear equations (4.5) for the unknown particle dipoles. Because the entries of $\mathscr{M}$ decay slowly as $1/r^3$, it is not possible to define a local truncation radius and ignore couplings between particles separated beyond that radius.[145] $\mathscr{M}$ is dense, and inverting it to solve (4.5) is computationally expensive. If the polarization due to the disturbance fields of other particles (the off-diagonal blocks of $\mathscr{M}$) is neglected and only the polarization due to the external field (the diagonal blocks of $\mathscr{M}$) is included, $\mathscr{M}$ becomes block diagonal and can be inverted analytically, reducing to the constant dipole result (4.1) with pairwise potential (4.3). As $|\beta|$ becomes small, the diagonal elements of $\mathscr{M}$ that go as $1/\beta$ become large compared to the off-diagonal elements that are independent of β, and the constant dipole model approaches the mutual dipole model asymptotically. We may formally consider the constant dipole model as equivalent to the mutual dipole model in the limit of $\beta = 0$. For any finite field strength, $\beta = 0$ implies that $S = 0$ and $\varepsilon = 0$, so there are no dipolar interactions. However, if we keep βE_0 finite as $\beta \to 0$, both S and ε remain finite as well. While this requires infinitely large fields $E_0 \to \infty$, it poses no difficulty mathematically.

4.1.3 Comparing the Two Models

Because of the computational cost of solving the system of equations (4.5) for the mutual dipole model, computational and theoretical studies overwhelmingly use constant dipole models.[90,206,207,210–218] The complete phase behavior for dielectric/paramagnetic particles interacting with the pairwise dipole-dipole potential (4.3) was computed by Hynninen and Dijkstra using Monte Carlo simulations.[206,207] Because the interaction potential is characterized by a single parameter ε, the phase behavior from the constant dipole model is controlled solely by ε and the particle volume fraction ϕ. Suspensions of particles with different conductivities (*i.e* different β) have identical phase behavior in terms of ε.

Results involving mutual dipole, or more exact, models are limited. Most computational and theoretical work incorporating these higher fidelity models is limited to configurations involving only a few particles,[146,172,219–221] one or two interacting chains,[8,222–225] the $E_0 \to \infty$ ground state,[226] static calculations of a few particular lattice configurations,[145,227,228] and dynamic simulations of small systems in two-dimensions[154,229] and three-dimensions[209] that captured chaining but were too short to observe further structural evolution. Large, concentrated suspensions, where the effects of mutual polarization are most important, have not been studied with the mutual dipole model, and the phase behavior predicted by the mutual dipole model is unknown.

Figures 4.1A and 4.1B show the strengths of the dipoles and forces on a pair of perfect conductors ($\beta = 1$) oriented parallel and orthogonal to an applied field calculated with the constant dipole and mutual dipole models. For the mutual dipole model, the dipole strength increases as the pair moves toward one another in the parallel orientation and decreases in the orthogonal orientation leading to stronger attractive forces in the parallel orientation and weaker repulsive forces in the orthogonal orientation compared to the constant

dipole model calculations. These trends hold for all $\beta > 0$ while particles with $\beta < 0$ have the opposite trends. For $\beta < 0$, particles depolarize one another as they approach in the parallel configuration and polarize in the orthogonal configuration.

For most pair separations, the constant dipole model is a reasonable approximation to the mutual dipole model. The two models only differ near contact, but the error is not too significant compared to the thermal noise in the dispersion. The computational cost of implementing the mutual dipole model is large for only a marginal increase in the accuracy of forces on a particle pair. This reasoning is common to justify using the constant dipole model over the mutual dipole model for concentrated suspensions with many particles. However, because the constant dipole model fails to capture important many-body effects, the errors in dipoles and forces are many times larger in concentrated suspensions than for a particle pair. Figure 4.1C shows the particle dipole strength for a body-centered-tetragonal (BCT) lattice of different β at fixed aspect ratio $A \equiv L_z/L_x = \sqrt{2/3}$ as a function of lattice volume fraction ϕ, where L_z is the unit cell dimension parallel to the external field and L_x is the dimension orthogonal to the field (depicted in Figure 4.3). The constant dipole result is the same for all ϕ and coincides with the $\phi \to 0$ limit for each β value. For the mutual dipole model, as ϕ increases to closest packing ($\phi = 2\pi/9 \approx 0.698$), the particles polarize more strongly for $\beta > 0$ and depolarize for $\beta < 0$. Compared to Figure 4.1A, the polarization of the lattice is much larger than for a pair of particles. As $|\beta| \to 0$, the dipole strength becomes less sensitive to volume fraction, and the constant dipole model improves in accuracy (which we asserted earlier by examining the elements of $\mathscr{M}$). The equilibrium phase behavior of dielectric/paramagnetic dispersions necessarily involves bulk concentrated phases for which the constant dipole model is inaccurate, so the constant dipole model is generally not appropriate for simulations of self-assembly and calculations of the equilibrium phase diagram, unless $|\beta|$ is small.

Figure 4.1D shows the particle dipole strength of a BCT lattice at fixed unit cell dimension $L_z = 2a$ rather than fixed aspect ratio. This corresponds to contacting particles in field-aligned chains with an interchain spacing set by the volume fraction. The $\phi \to 0$ limit corresponds to a single chain. Compared to the $\phi \to 0$ limit for a well-dispersed suspension, particles enhance their polarization ($\beta > 0$) or enhance their depolarization ($\beta < 0$) by chaining. By increasing ϕ and bringing the chains closer together, additional polarization/depolarization occurs. For the limiting values of $|\beta|$, the increase in polarization/depolarization from bringing chains together is comparable to the increase in polarization/depolarization from chaining in the first place. For small values of $|\beta|$ however, essentially no additional polarization/depolarization occurs after chaining. Suspensions with different β have qualitatively different behavior, which the constant dipole model, with only the single parameter ε, cannot capture.

4.1.4 Implications for Self-Assembly

For insight into how the phase behavior differs between the two models, we appeal to equilibrium thermodynamics. The reversible electric/magnetic work[143,144] associated with polarizing a dielectric/paramagnetic dispersion is $dW = \mathbf{E}_0 d\mathbf{S}_{\text{tot}}$, where the total dipole moment $\mathbf{S}_{\text{tot}} = \sum_i^N \mathbf{S}_i$ is the sum of the individual particle dipoles $\mathbf{S}_i$. This work contributes an additional term to the typical fundamental relation for simple thermodynamic systems,[19]

$$dU = Td\mathcal{S} - PdV + \mu dN + \mathbf{E}_0 \cdot d\mathbf{S}_{\text{tot}}, \tag{4.9}$$

where U is the internal energy, T is the temperature, $\mathcal{S}$ is the entropy, P is the pressure, V is the volume, μ is the chemical potential, and N is the number of particles. At equilibrium, coexisting phases (1 and 2) in the dispersion must satisfy equality of all intensive parameters, $T_1 = T_2$, $P_1 = P_2$, $\mu_1 = \mu_2$, and $\mathbf{E}_{0,1} = \mathbf{E}_{0,2}$. Because of the linearity of the governing electrostatic/magnetostatic equations, there is a linear relation between the applied field and the average particle dipole $\mathbf{S} \equiv \mathbf{S}_{\text{tot}}/N = \mathbf{C} \cdot \mathbf{E}_0$.[145] $\mathbf{C}$ is called the capacitance tensor and is related to the ensemble average $\langle \cdot \rangle$ of the grand capacitance tensor $\mathbf{C} = \boldsymbol{\Sigma} \cdot \langle \mathscr{C} \rangle / N$, where $\boldsymbol{\Sigma}$ is a tensor that sums the particle dipoles $\mathbf{S}_{\text{tot}} = \boldsymbol{\Sigma} \cdot [\mathbf{S}_1, \ldots, \mathbf{S}_N]^T$ and the T superscript indicates transposition. As $\mathscr{C}$ depends explicitly on the particle configuration, so must $\mathbf{C}$. Because coexisting phases are different in structure and density, their capacitance tensors are in general not equal, $\mathbf{C}_1 \neq \mathbf{C}_2$. As a result, the coexisting average particle dipoles in the two phases are also not generally equal, $\mathbf{S}_1 \neq \mathbf{S}_2$. The constant dipole model, however, requires the particle dipole strengths in the two phases to be equal, $\mathbf{S}_1 = \mathbf{S}_2$. This

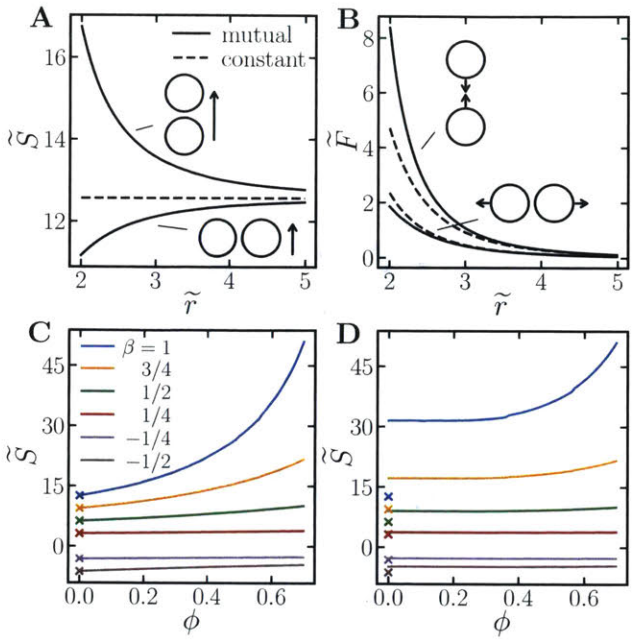

Figure 4.1: Top row: Dimensionless dipole strength $\widetilde{S} = S/\sqrt{a^3\lambda_f k_B T}$ (**A**) and force $\widetilde{F} = Fa/k_B T$ (**B**) induced in a pair of perfectly conducting particles $\beta = 1$ oriented parallel and perpendicular to an applied field $E_0 = 1\sqrt{k_B T/a^3\lambda_f}$ as a function of dimensionless separation $\widetilde{r} = r/a$ using the mutual dipole and constant dipole models. **Bottom row:** Dipole strength of a BCT lattice of particles of various conductivities with $E_0 = 1\sqrt{k_B T/a^3\lambda_f}$ as a function of volume fraction ϕ at fixed aspect ratio $A = \sqrt{2/3}$ (**C**) and fixed unit cell dimension in the field direction $L_z = 2a$ (**D**). The well-dispersed dilute limit is shown with crosses. $\widetilde{S} < 0$ implies that the dipoles are in the direction opposite the field.

approximation is good for small $|\beta|$, where nearly all polarization is due to the external field, and becomes exact in the limit $\beta \to 0$. For larger $|\beta|$, the capacitance is different in the two phases, and the external field must be different in the two phases $\mathbf{E}_{0,1} \neq \mathbf{E}_{0,2}$ to ensure the dipole strengths are equal. Thus, the constant dipole model predicts phase coexistence that fails to satisfy the thermodynamic criteria of equality of intensive parameters in coexisting phases for $\beta \neq 0$. This is analogous to forcing the molar volume, V/N, of two coexisting phases to be equal while allowing their pressures to be different, a case that also violates the coexistence criteria. Additionally, the constant dipole model only offers phase behavior predictions in terms of ε, or equivalently in terms of dipole strength $S = 4\sqrt{\pi a^3\lambda_f \varepsilon}$. However, there is no direct way to set and control the dipole strength of a dielectric/paramagnetic dispersion experimentally. Rather, predictions in terms of the external field are more useful because $\mathbf{E}_0$ can be controlled in experiments. This is analogous to the case where thermodynamic expressions in terms of temperature are significantly more useful than those in terms of the conjugate variable entropy, as temperature is a variable directly controlled in experiments. Note that it is tempting to say that the constant dipole model *does* predict behavior in terms of E_0 because S and ε can be written in terms of the product βE_0. However, we showed earlier that this model only applies in the limit of $\beta \to 0$ and $\mathbf{E}_0 \to \infty$ with βE_0 finite. But this finite βE_0 value is essentially the S and ε over which it is difficult to exert experimental control.

Figure 4.2 shows dramatic differences in phase behavior between the two models for perfectly conducting particles $\beta = 1$ at fixed $\phi = 0.50$. At large field/dipole strengths, dynamic simulations of both models yield coexistence between a very dilute fluid and a dense BCT crystal. As the dipole strength is lowered at constant volume fraction, the constant dipole dispersion freezes entirely into a homogeneous BCT crystal. For the mutual dipole model, the crystal melts as the field is lowered to reach coexistence with a dense fluid. The phase predictions from the constant dipole model deviate qualitatively from the more exact model, suggesting that the constant dipole model is a poor choice for use in the design of dielectric/paramagnetic materials, where accurate predictions of the structure are necessary for their function. Despite the shortcomings of the

constant dipole model, the equilibrium phase diagram of the mutual dipole model has not been computed. In the next few sections, we report the complete phase diagram of dielectric/paramagnetic colloidal suspensions using first-principles thermodynamic theory as well as Brownian dynamics simulations taking into account mutual polarization among particles.

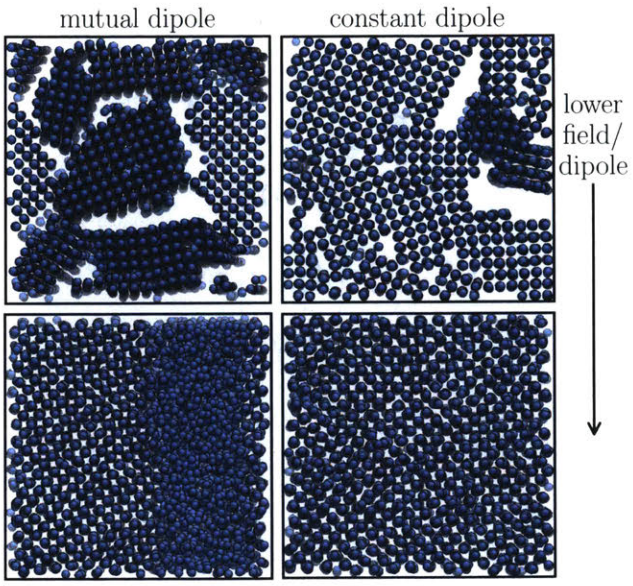

Figure 4.2: Snapshots of the phase behavior of dielectric/paramagnetic nanoparticles in an external field from Brownian dynamic simulations using the mutual dipole model (left column) and constant dipole model (right column). The field is oriented orthogonal to the plane of view, so the three-dimensional cubic dispersion extending into the page appears here as a two-dimensional projection. At high field/dipole strength (top row), both models predict coexistence between a dense BCT crystal phase and a very dilute fluid phase. Lowering the field/dipole strength (bottom row), the mutual dipole model predicts that the crystal melts to reach coexistence between a BCT crystal and dense fluid. The constant dipole model predicts that the crystal expands and the dispersion volume freezes to reach a homogeneous BCT crystal phase.

4.2 Thermodynamic Theory

Although the internal energy $U = U(\mathcal{S}, V, N, \mathbf{S}_{\text{tot}})$ in (4.9) is written as a function of entropy, volume, particle number, and total dipole moment, it is more convenient to work with a free energy $L = L(T, V, N, \mathbf{E}_0)$ that swaps entropy and total dipole for temperature and external field as independent variables,

$$L \equiv U - T\mathcal{S} - \mathbf{E}_0 \cdot \mathbf{S}_{\text{tot}}, \tag{4.10}$$

$$dL = -\mathcal{S}dT - PdV + \mu dN - \mathbf{S}_{\text{tot}} \cdot d\mathbf{E}_0. \tag{4.11}$$

This is convenient because T and $\mathbf{E}_0$ are typically the variables controlled in experiments rather than $\mathcal{S}$ and $\mathbf{S}_{\text{tot}}$. At constant T and $\mathbf{E}_0$, L is the quantity that is minimized at thermodynamic equilibrium.[19] Additionally, this choice of thermodynamic ensemble automatically guarantees that the $T_1 = T_2$ and $\mathbf{E}_{0,1} = \mathbf{E}_{0,2}$ coexistence criteria are satisfied in multiphase dispersions. Shown explicitly by the form of the total differential of the free energy dL in (4.11), we have the thermodynamic relation

$$\mathbf{S}_{\text{tot}} = -\left(\frac{\partial L}{\partial \mathbf{E}_0}\right)_{T,V,N}, \tag{4.12}$$

which we can integrate from $\mathbf{E}_0 = 0$ using the linear relation $\mathbf{S} = \mathbf{C} \cdot \mathbf{E}_0$,

$$L(T, V, N, \mathbf{E}_0) = F_{\text{hs}}(T, V, N) - N \int_0^{\mathbf{E}_0} d\mathbf{E}_0' \cdot \mathbf{C}(\mathbf{E}_0) \cdot \mathbf{E}_0, \tag{4.13}$$

where F_{hs} is the hard sphere Helmholtz energy at zero field. The capacitance tensor $\mathbf{C} = \boldsymbol{\Sigma} \cdot \langle \mathscr{C} \rangle / N$ contains the ensemble average of the grand capacitance tensor $\langle \mathscr{C} \rangle$ over all possible particle configurations. Because the field changes the equilibrium particle configuration as it increases, $\mathbf{C}$ is a function of $\mathbf{E}_0$ and the integration in (4.13) is difficult.

For crystalline phases, particles fluctuate about a lattice configuration $\mathbf{x} \equiv [\mathbf{x}_1, \mathbf{x}_2, \ldots, \mathbf{x}_N]$, where $\mathbf{x}_i$ is the lattice position of particle i. We modify the free energy for a crystalline phase, L_c, to

$$L_c(T, V, N, \mathbf{E}_0; \mathbf{x}) = F_{\text{hs},c}(T, V, N; \mathbf{x}) - N \int_0^{\mathbf{E}_0} d\mathbf{E}_0' \cdot \mathbf{C}(\mathbf{E}_0; \mathbf{x}) \cdot \mathbf{E}_0, \tag{4.14}$$

where $L_c(T, V, N, \mathbf{E}_0; \mathbf{x})$ and $F_{\text{hs},c}(T, V, N; \mathbf{x})$ are the free energy and hard sphere Helmholtz energy of a crystal constrained to have lattice configuration $\mathbf{x}$. $L_c(T, V, N, \mathbf{E}_0; \mathbf{x})$ is *not* the free energy at thermodynamic equilibrium $L_c(T, V, N, \mathbf{E}_0)$, rather it is the free energy associated with a particular lattice configuration. If we computed $L_c(T, V, N, \mathbf{E}_0; \mathbf{x})$ for all possible lattice configurations $\mathbf{x}$, the lattice configuration $\mathbf{x}_{eq}$ with the lowest free energy will be the equilibrium lattice configuration with free energy $L_c(T, V, N, \mathbf{E}_0; \mathbf{x}_{eq}) = L_c(T, V, N, \mathbf{E}_0)$. If the particles were confined only to their lattice positions, we would know the particle positions exactly and the integration in (4.14) could be evaluated. Because particles fluctuate about their lattice configurations, the ensemble average $\langle \mathscr{C} \rangle$ and $\mathbf{C}$ are affected by the fluctuations. As the field is increased, these fluctuations change and the integration is not straightforward. To make progress, we neglect these fluctuations so that the ensemble averaged capacitance tensor is modeled as the capacitance tensor for the lattice configuration, $\langle \mathscr{C} \rangle(\mathbf{E}_0, \mathbf{x}) \approx \mathscr{C}(\mathbf{x})$. In this case, $\mathbf{C}$ is completely independent of $\mathbf{E}_0$ and the integration is simple,

$$L_c(T, V, N, \mathbf{E}_0; \mathbf{x}) = F_{\text{hs},c}(T, V, N; \mathbf{x}) - \frac{N}{2} \mathbf{C}(\mathbf{x}) : \mathbf{E}_0 \mathbf{E}_0. \tag{4.15}$$

The probability of observing a particular particle configuration is proportional to $e^{\mathbf{E}_0 \cdot \mathbf{S}_{\text{tot}} / k_B T}$.[123] At high field strengths, this probability will be sharply peaked at the lattice positions, where the total polarization is largest, and neglecting fluctuations is reasonable. At low field strengths, this approximation may break down, but the integrand in (4.14) is small here anyway. Thus, we incur little error with the approximation $\langle \mathscr{C} \rangle(\mathbf{E}_0, \mathbf{x}) \approx \mathscr{C}(\mathbf{x})$ and (4.15) is likely to yield good predictions. By incorporating the lattice configuration $\mathbf{x}$ into the crystal free energy, we gain the ability to compute L_c accurately but now must minimize L_c over all possible lattice configurations $\mathbf{x}$ to find the equilibrium lattice configuration. Fortunately, we can narrow the possible lattice configurations to just a few candidate crystal structures. First, we assume that the equilibrium lattice only has anisotropy in the field direction, while there is no bias in the two directions orthogonal to the field. A single parameter, the aspect ratio A, is enough to quantify this anisotropy. This hypothesis is commensurate with the symmetry of the applied field, is consistent with the low density and high density ground states, and is observed in constant dipole simulations.[206,207] The $\mathbf{E}_0 \to \infty$ ground state crystal is known to be BCT, as this orients the particles in interdigitated chains aligned with the field, as in Figure 4.3.[230] The $\mathbf{E}_0 = 0$ hard sphere equilibrium crystal state is also known to be face-centered-cubic (FCC). The hexagonally-close-packed (HCP) hard sphere crystal has nearly the same free energy as the FCC hard sphere crystal[231] and is the high density $\mathbf{E}_0 \to \infty$ ground state for ϕ larger than BCT closest packing $\phi = 2\pi/9 \approx 0.698$.[206,207] Both HCP and FCC structures have been observed at equilibrium in dipolar systems.[206,207,232] The crystals orient so that their (111) hexagonal planes are orthogonal to the applied field, as in Figure 4.3. Because the HCP lattice puts particles aligned in the field direction closer together than the FCC lattice does, it is more stable than FCC for nearly all choices of $\mathbf{E}_0$ and ϕ.[206,207,232] Therefore, we consider only BCT and HCP as candidates for the equilibrium crystal phase. The orientation of the crystals are fixed relative to the applied field, and the free energy

$$L_c(T, V, N, \mathbf{E}_0; A) = F_{\text{hs},c}(T, V, N; A) - \frac{N}{2} \mathbf{C}(A) : \mathbf{E}_0 \mathbf{E}_0. \tag{4.16}$$

is minimized over all possible aspect ratios A to find the equilibrium aspect ratio and free energy. For the BCT crystal, A is defined as the ratio of the dimension of the unit cell in the field direction L_z to the dimension of the unit cell in either of the orthogonal directions L_x. When $A = 1$, the structure is body-centered-cubic (BCC). For the HCP crystal, A is defined as the ratio of the distance between (111) hexagonal planes (i.e. half the unit cell dimension in the field direction L_z) and the distance between particles within

the (111) planes L_x. $A = \sqrt{2/3}$ corresponds to an isotropic HCP lattice, where a particle is equidistant to its 12 nearest neighbors. These geometries are pictured in Figure 4.3. The minimizations are performed separately for BCT and HCP structures and the lower of the two free energies corresponds to the equilibrium crystal structure.

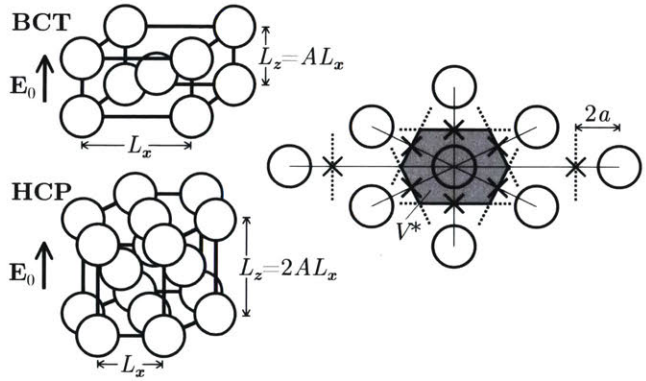

Figure 4.3: Left: BCT and HCP unit cells oriented relative to an applied field $\mathbf{E}_0$. The aspect ratio A is defined differently for the two structures. **Right:** Two-dimensional sketch of estimating the free volume V^*. Boundaries (dashed lines) are placed at the contact points (crosses) of the center particle with its neighbors along the line of centers (thin lines). The boundaries are extended orthogonally to the line of centers. Their intersections form a small, convex region (thick lines) estimating the free volume (shaded region) around the central particle.

During minimization of the free energy L, we must compute $F_{\text{hs},c}$ and $\mathbf{C}$. With our approximation $\langle \mathscr{C} \rangle \approx \mathscr{C}$, we can compute $\mathbf{C} = \boldsymbol{\Sigma} \cdot \mathscr{C}/N$ by inverting $\mathscr{M}$ to find $\mathscr{C}$ for a particular particle configuration. Direct inversion is costly, so instead we use the fast iterative approach based on Ewald summation discussed in section 2.3 for evaluating $\mathscr{M}$ and a Krylov subspace method for the inversion.[155] We compute $F_{\text{hs},c}$ using free volume theory,[178] where a single crystalline particle moves in the free volume V^* constrained by its neighboring particles fixed to their lattice positions,

$$F_{\text{hs},c}(T, V, N; A) = -k_B T N \ln V^*. \tag{4.17}$$

There is an additional contribution to the free energy $k_B T N \ln(\Lambda^3/v_0)$ containing the deBroglie wavelength Λ that is not necessary in the present calculations. For isotropic crystals, V^* can be approximated with simple, analytic expressions.[178] There are no simple analytic expressions for the size of the free volume in anisotropic crystals, so we approximate the complicated free volume[233] with a simple, convex region constructed from the following algorithm and sketched in Figure 4.3. If a particle moves from its lattice position towards a neighbor along the line of centers, the closest the center of the free particle can approach the center of its neighbor is $r = 2a$. We construct a plane at this contact point, orthogonal to the line of centers of the pair, to approximate the boundary of the free volume near this neighbor. Similar planes are placed at the contact point for each of the free particle's neighbors. If the planes are extended and allowed to intersect, they will form the boundary of a small convex polyhedron centered around the free particle's lattice position. The volume of this polyhedron is an approximation for the true free volume V^*. This approximation for V^* is good because it only neglects thin concave regions that contribute little to V^*.[233] It is able to capture the anisotropy in the crystal lattice, but agrees nearly perfectly with simple expressions[178] for isotropic crystals. Errors in computing $F_{\text{hs},c}$ are dominated by the assumptions of free volume theory and not in our ability to compute V^*.

Unlike crystalline phases, particles in a fluid phase are not confined to fluctuations about a known configuration. Instead, the mobile fluid particles sample many more configurations than in the crystal phase. Although the sampled equilibrium structures are disordered, they are not isotropic because of a bias for alignment in the field direction. If we defined an order parameter (or several order parameters) to reflect the anisotropy in the fluid structure and were able to compute $F_{\text{hs},f}$ and $\mathbf{C}$ as a function of this order parameter, we could take (4.13) and construct an expression like (4.16) for the fluid phase. Without these

structure-property relations, we can only make analytic progress by assuming that the fluid configuration is isotropic and independent of the field strength. In this case, the integration in (4.13) is simple,

$$L_f(T,V,N,\mathbf{E}_0) = F_{\mathrm{hs},f}(T,V,N) - \frac{N}{2}\mathbf{C}:\mathbf{E}_0\mathbf{E}_0. \tag{4.18}$$

This equation is asymptotically valid in the limit of low field strengths but is only an approximation at higher field strengths. Although our ability to compute L_f accurately is limited, (4.18) is an explicit expression with no structural parameters which need to be determined. This is in contrast to L_c, which we can compute accurately, but requires minimizing over aspect ratio A to find the equilibrium L_c.

For $F_{\mathrm{hs},f}$ in the fluid, we use an expression constructed from the the Carnahan-Starling equation,[178,234] which is very accurate for isotropic hard sphere configurations

$$F_{\mathrm{hs},f}(T,V,N) = k_BTN\left(\ln\phi - 1 + \frac{4\phi - 3\phi^2}{(1-\phi)^2}\right). \tag{4.19}$$

Again, there is an additional $k_BTN\ln(\Lambda^3/v_0)$ contribution to $F_{\mathrm{hs},f}$ that we neglect. The fluid capacitance tensor is approximated by assuming that each particle interacts with the mean disturbance field of the other particles which yields the self-consistent mean-field expression,[7,172]

$$\mathbf{C} = \frac{4\pi a^3\lambda_f\beta}{1-\beta\phi}\mathbf{I}. \tag{4.20}$$

This expression assumes a completely structureless dispersion and is one of the simplest equations for the fluid capacitance. Not surprisingly, this expression is only accurate to $O(1)$. A slightly more accurate expression to $O(\phi)$ for a structureless dispersion we could have chosen was given by Jeffrey by considering the exact solution to the two body problem.[172] Because we know that our assumptions prevent us from computing L_f accurately anyway, we choose to use the simpler mean field expression (4.20).

Both the crystal free energy (4.16) and the fluid free energy (4.18) can be written as $L = F_{\mathrm{hs}} - \mathbf{S}_{\mathrm{tot}}\cdot\mathbf{E}_0/2$, where we have used $\mathbf{S}_{\mathrm{tot}} = N\mathbf{C}\cdot\mathbf{E}_0$. L is the sum of an entropic hard sphere contribution, F_{hs}, and an energetic contribution from the total dipole moment in the field direction, $-\mathbf{S}_{\mathrm{tot}}\cdot\mathbf{E}_0/2$. At low field strengths, the entropic term will be the dominant contribution to L while at high field strengths the dipole term will dominate. Figure 4.4A shows the entropic and energetic contributions for the BCT crystal phase, with the HCP and fluid phases having similar trends.

The entropic contribution is always positive and contributes a free energy penalty. F_{hs} increases with volume fraction as the free volume available to the particles decreases. The entropic term diverges at closest packing, where the free volume goes to zero. For a fixed volume fraction, there is a minimum allowable aspect ratio where particles in the unit cell come into contact. Here, the free volume also goes to zero so F_{hs} diverges for small aspect ratios.

For $\beta > 0$ ($\lambda_p > \lambda_f$), the dispersion polarizes in the same direction as $\mathbf{E}_0$, so $\mathbf{S}_{\mathrm{tot}}\cdot\mathbf{E}_0 > 0$ and the energetic contribution to L is negative. The dispersion evolves to increase its total dipole strength, which decreases L. $\mathbf{S}_{\mathrm{tot}}$ increases as the volume fraction increases or as the crystal aspect ratio decreases. Increasing the volume fraction or decreasing the aspect ratio both move particles aligned in the field direction closer together, greatly enhancing the mutual polarization. For $\beta < 0$ ($\lambda_p < \lambda_f$), the dispersion polarizes in the opposite direction to $\mathbf{E}_0$, so $\mathbf{S}_{\mathrm{tot}}\cdot\mathbf{E}_0 < 0$ and the energetic contribution to L is positive. The dispersion evolves to reduce its total dipole strength, which decreases L. As the volume fraction increases or the aspect ratio decreases, mutual depolarization is enhanced and $\mathbf{S}_{\mathrm{tot}}$ decreases. Therefore, the trends of the energetic contribution to L with respect to ϕ and A for $\beta < 0$ are the same as the $\beta > 0$ case. For all β, the energetic contribution to L decreases with increasing ϕ or decreasing A, which corresponds to an increase in $\mathbf{S}_{\mathrm{tot}}$ for $\beta > 0$ and a decrease in $\mathbf{S}_{\mathrm{tot}}$ for $\beta < 0$.

At a fixed volume fraction, the competition between the entropic and energetic contributions leads to an equilibrium aspect ratio that minimizes L. Figure 4.4B shows the equilbrium aspect ratio for a homogeneous

BCT crystal with $\beta = 1$ at several different ϕ. As the field strength increases, the energetic contribution dominates the free energy and the particles in field-aligned chains move closer to one another to enhance mutual polarization. Because ϕ is fixed, the decrease in L_z is accompanied by an increase in L_x and the the aspect ratio decreases. For lower values of ϕ, the equilibrium aspect ratios tend to be lower. This implies that, at constant field, particles prefer to decrease their density by increasing the interchain spacing (or equivalently L_x) rather than their intrachain spacing (or equivalently L_z) to maximize $\mathbf{S}_{\text{tot}}$.

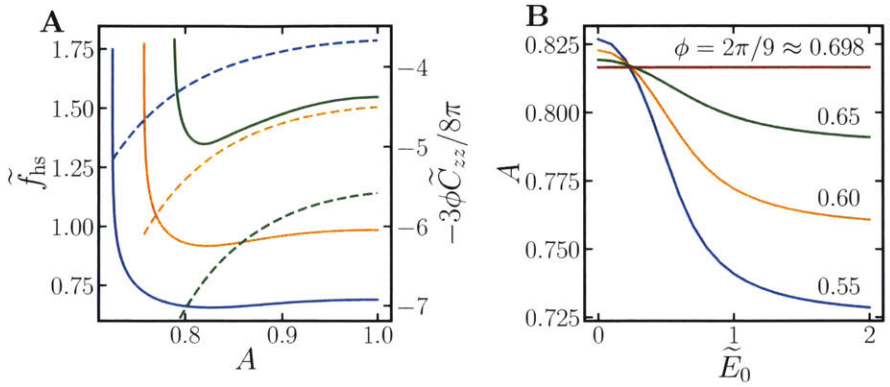

Figure 4.4: **A:** Entropic and energetic contributions to the BCT dimensionless free energy per volume $\widetilde{\ell} \equiv La^3/Vk_BT = \widetilde{f}_{\text{hs}} - 3\phi\widetilde{C}_{zz}E_0^2/8\pi$ for $\beta = 1$. Solid lines correspond to the left axis and are the hard sphere BCT dimensionless Helmholtz energy per volume $\widetilde{f}_{\text{hs}} \equiv F_{\text{hs}}a^3/Vk_BT$ as a function of aspect ratio A for various ϕ contours. Dashed lines correspond to the right axis and are the energetic contribution (divided by E_0^2) to $\widetilde{\ell}$, containing the zz component of the dimensionless capacitance tensor $\widetilde{C}_{zz} \equiv C_{zz}a^3\lambda_f$, the only component that contributes to $\widetilde{\ell}$ with $\mathbf{E}_0$ oriented along the z axis. **B:** Equilibrium $\beta = 1$ BCT aspect ratio minimizing the free energy at constant volume fraction as a function of dimensionless field strength $\widetilde{E}_0 \equiv E_0\sqrt{a^3\lambda_f/k_BT}$ for various ϕ contours. In both panels, blue, yellow, green, and red colors correspond to volume fractions $\phi = 0.55$, 0.60, 0.65, and $2\pi/9 \approx 0.698$, respectively, as indicated by the labels in the lower panel.

For a multiphase dispersion with two coexisting phases (1 and 2), the total free energy is a sum of the free energy of each phase $L(N, V, T, \mathbf{E}_0) = L_1(N_1, V_1, T, \mathbf{E}_0) + L_2(N_2, V_2, T, \mathbf{E}_0)$ where $N = N_1 + N_2$ and $V = V_1 + V_2$. It is convenient to work with a dimensionless free energy per volume,

$$\widetilde{\ell}\left(\phi, \widetilde{\mathbf{E}}_0\right) = \widetilde{\ell}_1\left(\phi_1, \widetilde{\mathbf{E}}_0\right)\frac{\phi_2 - \phi}{\phi_2 - \phi_1} + \widetilde{\ell}_2\left(\phi_2, \widetilde{\mathbf{E}}_0\right)\frac{\phi - \phi_1}{\phi_2 - \phi_1}, \tag{4.21}$$

where $\widetilde{\ell} \equiv La^3/Vk_BT$, $\widetilde{\ell}_1$ and $\widetilde{\ell}_2$ are the dimensionless free energies per volume of the pure phases, and $\widetilde{\mathbf{E}}_0 \equiv \mathbf{E}_0\sqrt{a^3\lambda_f/k_BT}$ is the dimensionless external field. This choice of dimensionless field strength defines a dimensionless dipole moment $\widetilde{\mathbf{S}} \equiv \mathbf{S}/\sqrt{a^3\lambda_f k_BT}$. Equation (4.21) expresses the overall free energy per volume as a linear interpolation between the free energies per volume of the pure phases, a scheme that is often called the lever rule.

$\widetilde{\ell}(\phi, \widetilde{\mathbf{E}}_0)$ is minimized over all possible ϕ_1 and ϕ_2 to find the coexisting volume fractions at a particular $\widetilde{\mathbf{E}}_0$. The coexisting volume fractions are independent of the overall ϕ provided it is intermediate the coexisting volume fractions, $\phi_1 < \phi < \phi_2$. If one or both of the phases is crystalline, we must also minimize over all possible aspect ratios of the crystal phase/s to find the equilibrium aspect ratio/s. This scheme satisfies the thermodynamic coexistence criteria, $T_1 = T_2$, $P_1 = P_2$, $\mu_1 = \mu_2$, and $\mathbf{E}_{0,1} = \mathbf{E}_{0,2}$. Equality of temperature and applied field is automatically satisfied by the choice of constant T and $\mathbf{E}_0$ ensemble, which corresponds with the independent variables of the free energy $L = L(T, V, N, \mathbf{E}_0)$. The lever rule constrains $\widetilde{\ell}(\phi, \widetilde{\mathbf{E}}_0)$ for the multiphase dispersion to lay on a line in $\widetilde{\ell}$ versus ϕ space connecting the $\widetilde{\ell}_1(\phi_1, \widetilde{\mathbf{E}}_0)$ and $\widetilde{\ell}_2(\phi_2, \widetilde{\mathbf{E}}_0)$ for the two coexisting phases. To minimize $\widetilde{\ell}$, this line must lay tangent to the free energy curves $\widetilde{\ell}_1(\phi, \widetilde{\mathbf{E}}_0)$ and $\widetilde{\ell}_2(\phi, \widetilde{\mathbf{E}}_0)$.[178] From the Euler relation,[19] $\widetilde{\ell} = -\widetilde{P} + \widetilde{\mu}\phi$, the tangent line has a slope equal to $\widetilde{\mu} \equiv \mu/k_BT$ and a y-intercept equal to $-\widetilde{P} \equiv -Pa^3/k_BT$. Because both phases are on this line, they have equal pressure

and chemical potential and all the coexistence criteria are satisfied. In contrast, the constant dipole model requires the particle dipoles in coexisting phases to be equal $\mathbf{S}_1 = \mathbf{S}_2$ at the expense of allowing the external field to be different $\mathbf{E}_{0,1} \neq \mathbf{E}_{0,2}$. The constant dipole approach is thermodynamically consistent in the $\beta \to 0$ limit, where both $\mathbf{S}_1 = \mathbf{S}_2$ and $\mathbf{E}_{0,1} = \mathbf{E}_{0,2}$ hold, but fails to satisfy all of the coexistence criteria for $\beta \neq 0$.

With three candidate phases, fluid, BCT, and HCP, there are 6 possible phase coexistences: fluid/fluid, fluid/BCT, fluid/HCP, BCT/BCT, BCT/HCP, HCP/HCP. If coexistence regions overlap, the one with the lowest free energy will be the coexistence observed at thermodynamic equilibrium. Coexistence between like phases, fluid/fluid, BCT/BCT, and HCP/HCP, has not been observed in suspensions of dipolar particles,[206,207] so it is likely that these are not good candidates for free energy minimizers. Instead, we consider only fluid/BCT, fluid/HCP, and BCT/HCP coexistences. Minimizing (4.21) for many different $\tilde{\mathbf{E}}_0$ generates the binodal curves for each of the three phase coexistences. Computing all binodals is equivalent to knowing the entire phase diagram, as areas outside coexistence regions are single phase regions. The results of the thermodynamic model are shown in Figures 4.5–4.8.

4.3 Brownian Dynamics Simulations

Phase behavior can be directly observed in dynamic simulations of self-assembling dielectric/paramagnetic nanoparticle suspensions. As described in detail in section 2.1, we performed Brownian dynamics simulations of $N = 8000$ mutually polarizable spherical particles in a three-dimensional cubic box with periodic boundary conditions using the freely-draining model. The simulation results can be used to validate the predictive capability of our previous thermodynamic theory as well as illustrate the usefulness of our simulations as a computational tool.

At high applied field strengths, BCT crystal nucleates in an initially homogeneous disordered fluid phase. The crystal grows until the crystal and fluid volume fractions reach their coexisting values. The aspect ratio of the crystal is the one that minimizes the crystal's free energy. If the dispersion has fully equilibrated, we can measure the coexisting volume fractions in the simulation at this field strength. We repeat these nucleation simulations for progressively lower field strengths, recording the coexisting volume fractions at each step to construct binodal curves. Each simulation is independent of the others, all beginning from a disordered fluid state. Eventually the field strength will become too small compared to thermal motion and the dispersion will remain a fluid rather than phase separate. The equilibrium state at this point may be two phases, but nucleation barriers prevent the dispersion from realizing its equilibrium state within the time and size constraints of the simulation. In this case, we begin with the fully equilibrated, phase separated dispersion at the lowest field strength that nucleated crystal and slowly lower the field. If the rate that the field is lowered is slow compared to the rate at which the dispersion equilibrates, the volume fraction and aspect ratio of the coexisting phases will respond to the changing field by tracing their equilibrium values on the binodal. Because the initial configuration is already phase separated, homogeneous nucleation barriers are avoided completely. In practice, we do not change the field continuously but rather make a small jump in the field, let the dispersion equilibrate, make another small jump, and so on. We could begin this protocol at any field strength that nucleated crystal, but we choose the lowest field strength because these configurations tend to have the smallest number of defects.

This protocol traces out the fluid/BCT binodal curves, beginning with a high field close to the ground state and lowering the field. We can also trace out the fluid/HCP binodal curves by beginning at the zero field, hard sphere limit and slowly raising the field. Because the driving force for crystallization is small at low field strengths, it is difficult to observe HCP crystal nucleation in a homogeneous fluid. Rather than begin the simulations from a fluid state, we begin with all particles incorporated into an HCP lattice at some volume fraction ϕ_c in a simulation volume with a lower overall volume fraction $\phi < \phi_c$. There is empty solvent around the crystal in which particles can melt off the crystal surface and reach fluid/HCP coexistence. After equilibrating at $\mathbf{E}_0 = 0$, the field was slowly raised to trace the fluid/HCP binodals. Again, this was not done continuously but rather in discrete jumps, where the equilibrated final configuration at a particular field strength was used as the initial configuration for the next field strength. It is possible for the fluid/BCT and fluid/HCP regions to overlap. In this case, only one of the phase coexistences is actually the thermodynamic equilibrium state while the other is metastable. Had we waited long enough and/or increased the system size, the metastable coexistence would convert to the stable equilibrium coexistence.

We did not simulate BCT/HCP coexistence. Because of the lattice mismatch, there is a large interfacial tension between the two crystal phases. The system volume must be large enough that the bulk free energy driving phase separation overcomes the large interfacial penalty. At the large densities where BCT/HCP coexistence is stable, the kinetics are incredibly slow and long simulations are needed to fully equilibrate the dispersion. Additionally, there is a not a simple, continuous deformation of lattice parameters to diffusionlessly transform between BCT and HCP structures. To convert between the two crystals, a portion of one crystal must melt and reform into the other crystal. This mechanism has many energetic barriers which further slows the kinetics. Because of the size and time constraints of our simulations, we did not perform dynamic simulations of BCT/HCP coexistence. Our theoretical thermodynamic calculations did trace out the BCT/HCP binodals, but we do not have dynamic simulation data with which to compare. Solid/solid coexistence may be better probed using specialized Monte Carlo simulations,[235,236] which is beyond the

current scope of the work here. To our knowledge, no such simulations have been performed for mutually polarizable dispersions.

For each field strength, we compute the dipole moment and local volume fraction of each particle in the dispersion's final configuration, as described in the Methods section. This forms a two-dimensional distribution of particle dipoles and particle local volume fractions. No such distribution exists for a constant dipole model, as all the particles have identical dipole strengths. The two-dimensional distribution has two peaks, one associated with the dipole strength and volume fraction of the bulk fluid phase and the other corresponding to the dipole strength and volume fraction of the coexisting crystal. We assume that the total distribution is the sum of two multivariate Gaussians, with one population corresponding to particles in the fluid and the other corresponding to particles in the crystal. We use a maximum likelihood analysis to fit the Gaussians to the measured distribution and extract means and standard deviations (see Methods for more details). The means give the coexisting dipole and volume fraction of the two phases. These simulation results are shown in Figures 4.5–4.7 along with the results from the theoretical thermodynamic calculations.

The standard deviations in the distribution correspond to equilibrium fluctuations in the dipole moment and volume fraction. The size of the fluctuations is related to the electric/magnetic susceptibility and the compressibility of the dispersion and is not a measure of the uncertainty in our calculations of the coexisting fluid and crystal phases.[123] To obtain a measure of the error in our methodology, we compute the parameter

$$\delta = \frac{1}{V}\left|\frac{N}{\phi} - \frac{N_f}{\phi_f} - \frac{N_c}{\phi_c}\right|, \tag{4.22}$$

where the total number of fluid particles N_f and crystal particles N_c is determined by designating each particle as either fluid or crystalline using the posterior probability that the particle belongs to one of the populations. If we had exact measurements, indicated by hats "$\wedge$", $N/\phi = \hat{N}_f/\hat{\phi}_f + \hat{N}_c/\hat{\phi}_c$, and $\delta = 0$. Thus, δ is one measure of the relative error in our ability to extract ϕ_f and ϕ_c. The largest errors ($\delta \approx 0.1$) occur where the binodal varies rapidly with field strength while the errors are smaller ($\delta \approx 0.01$) where the binodal varies slowly with field. If the system size is too small, the amount of interface, grain boundaries, and defects can become large compared to the amount of bulk fluid and crystal and obscure the calculation of the bulk coexisting quantities, leading to large δ. However, our system size ($N \approx 8000$) is large enough that the majority of particles belong to bulk phases and δ remains small.

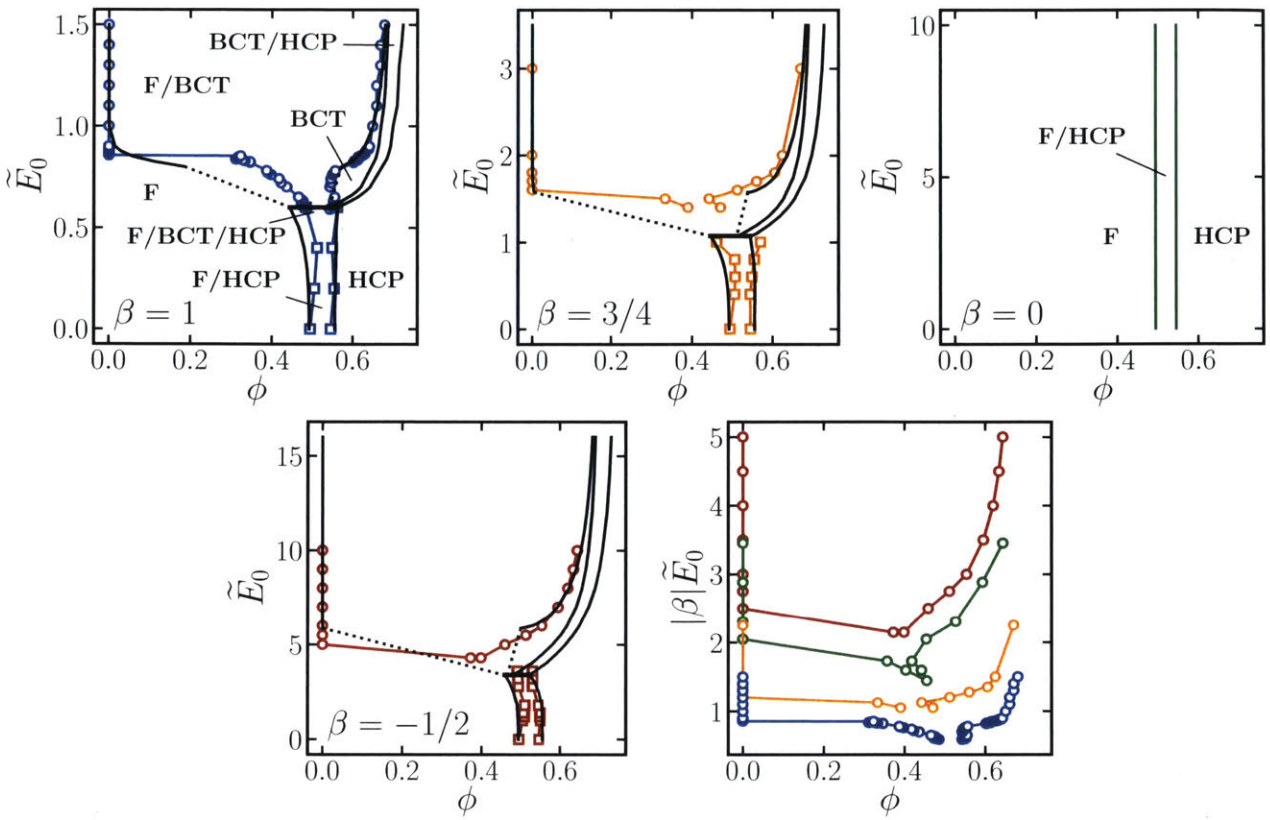

Figure 4.5: $\widetilde{E}_0 \equiv E_0\sqrt{a^3\lambda_f/k_BT}$ versus ϕ phase diagrams for different values of β in different colors. Circles correspond to fluid/BCT coexistence while squares correspond to fluid/HCP coexistence, both extracted from Brownian dynamics simulations. Colored lines simply connect the simulation data points. Solid black lines are the theoretical binodal predictions using our thermodynamic theory and include BCT/HCP coexistence, for which we do not have simulation data. Tie lines (not pictured) connecting coexisting phases are horizontal, and the fluid/BCT/HCP eutectic tie lines are highlighted with thick lines. Dotted lines span a portion of the F/BCT binodals where we were unable to obtain coexistence points using our thermodynamic model and connect points on either side of this region where we did obtain solutions. The fluid/BCT simulation data for each β are combined in the bottom right plot. The constant dipole ($\beta = 0$) results are from Monte Carlo simulations in references 206 and 207 and can only be meaningfully plotted in the bottom right plot.

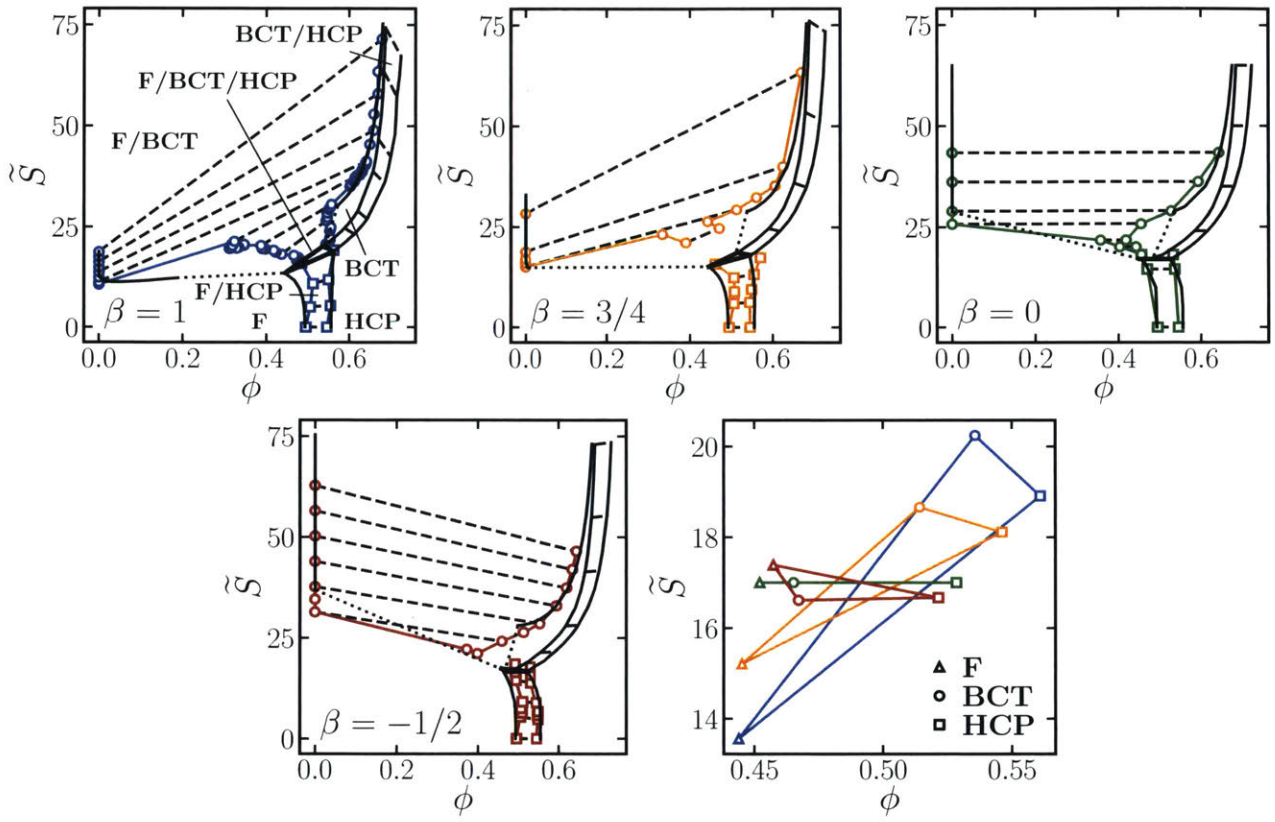

Figure 4.6: $\tilde{S} \equiv S/\sqrt{a^3 \lambda_f k_B T}$ versus ϕ phase diagrams for different values of β in different colors. Circles correspond to fluid/BCT coexistence while squares correspond to fluid/HCP coexistence, both extracted from Brownian dynamics simulations. The constant dipole ($\beta = 0$) simulation results are from Monte Carlo simulations in references 206 and 207. Colored lines simply connect the simulation data points. Solid black lines are the theoretical binodal predictions using our thermodynamic theory and include BCT/HCP coexistence, for which we do not have simulation data, as well as the constant dipole ($\beta = 0$) case. Tie lines (dashed lines) connecting coexisting phases are sloped, and the fluid/BCT/HCP eutectic tie line triangles are highlighted with thick lines. Dotted lines span a portion of the F/BCT binodals where we were unable to obtain coexistence points using our thermodynamic model and connect points on either side of this region where we did obtain solutions. The fluid/BCT/HCP eutectic triangles determined from the theoretical calculations for each β are combined in the bottom right plot.

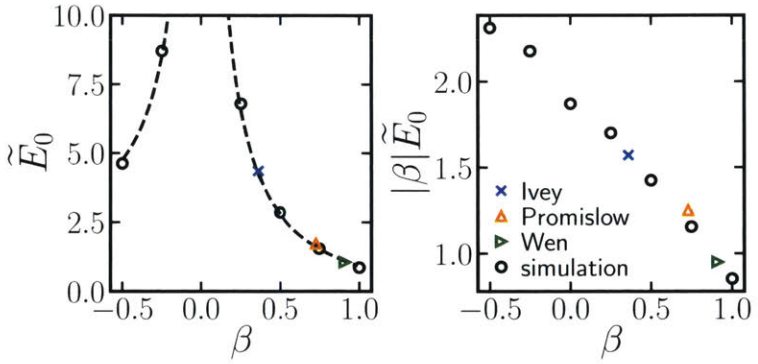

Figure 4.7: Dimensionless field strength $\widetilde{E}_0 \equiv E_0\sqrt{a^3\lambda_f/k_BT}$ corresponding to a coexisting fluid volume fraction $\phi_f = 0.20$ at fluid/BCT coexistence for different β. This is, absent kinetic barriers, the field necessary to induce phase separation in a homogeneous fluid at $\phi = 0.20$. These data are extracted from the equilibrium binodals determined by Brownian dynamics simulations. Also shown are values extracted from a variety of experiments in references 237 (Ivey), 64 (Promislow), and 238 (Wen). The dashed line in the left plot is equation (4.24) obtained from a linear fit to the simulation data in the right plot.

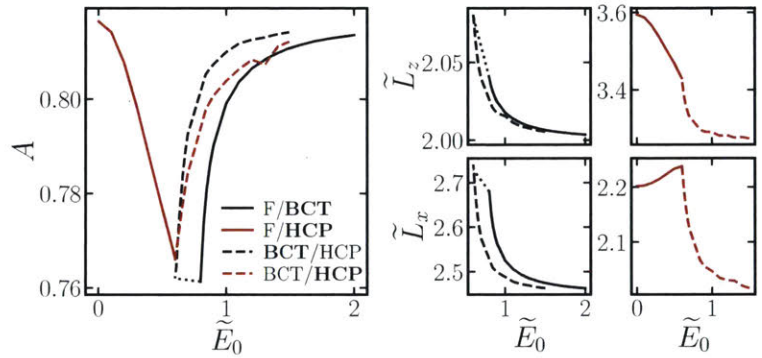

Figure 4.8: Equilibium crystal aspect ratio A and unit cell dimensions parallel $\widetilde{L}_z \equiv L_z/a$ and orthogonal $\widetilde{L}_x \equiv L_x/a$ to the applied field $\widetilde{E}_0 \equiv E_0\sqrt{a^3\lambda_f/k_BT}$ along the binodals of fluid/BCT, fluid/HCP, and BCT/HCP coexistence for $\beta = 1$. These data are from the theoretical thermodynamic calculations. Dotted lines span a portion of the F/BCT binodals where we were unable to obtain coexistence points using our thermodynamic model and connect points on either side of this region where we did obtain solutions.

4.4 Results and Discussion

Figures 4.5 and 4.6 show the equilibrium phase diagrams obtained from our thermodynamic theory and from our Brownian dynamics simulations for several different particle conductivities. The theoretical predictions agree very well with the simulation results. For the $\beta = 0$ simulation data, we use the results of Hynninen and Dijkstra from Monte Carlo simulations.[206,207] The $\beta = 0$ theoretical predictions are from our thermodynamic model and agree well with the Monte Carlo simulations. Figure 4.5 contains the phase diagrams in terms of applied field strength, showing the coexisting volume fractions for various $\widetilde{E}_0 \equiv E_0\sqrt{a^3\lambda_f/k_BT}$. Figure 4.6 casts the phase diagrams in terms of induced particle dipole strength, where the coexisting volume fractions and coexisting dimensionless dipole strengths $\widetilde{S} \equiv S/\sqrt{a^3\lambda_f k_BT}$ are shown together. Figure 4.7 is a different projection of the $\widetilde{E}_0$ versus ϕ phase diagrams of Figure 4.5, showing the $\widetilde{E}_0$ corresponding to a coexisting fluid volume fraction $\phi_f = 0.20$ at fluid/BCT coexistence for different β. This is, absent kinetic barriers, the minimum field strength necessary to induce phase separation in a homogeneous dispersion at $\phi = 0.20$. These data were extracted from the simulation binodal data. Also shown are the critical field

strengths extracted from several experiments of field-induced structural transitions, which agree well with our predictions. Finally, Figure 4.8 displays how the aspect ratios and unit cell dimensions of the crystal phases change along the binodal, from our theoretical thermodynamic calculations.

On the E_0 versus ϕ phase diagrams (Figure 4.5), the tie lines connecting coexisting phases are horizontal due to the constant applied field coexistence criteria, $\mathbf{E}_{0,1} = \mathbf{E}_{0,2}$. Fluid/BCT coexistence is observed at high field strengths and moderate volume fractions, BCT/HCP coexistence is observed at high field strengths and large volume fractions, and fluid/HCP coexistence is observed at low field strengths. The three coexistences meet at a field strength $\mathbf{E}_{0,\text{eut}}$. This type of phase behavior shares the same generic features of a eutectic, which is typically associated with phase separated binary mixtures.[19] The eutectic point, (ϕ_{eut}, $\mathbf{E}_{0,\text{eut}}$), is the point with coordinates at the eutectic field $\mathbf{E}_{0,\text{eut}}$ and the eutectic volume fraction ϕ_{eut}, which is the BCT volume fraction at the eutectic field $\phi_{\text{eut}} \equiv \phi_{\text{BCT}}(\mathbf{E}_{0,\text{eut}})$. Along the eutectic line, there is simultaneous fluid/BCT/HCP coexistence. This is consistent with the Gibbs phase rule,[19]

$$N_{\text{DOF}} = N_{\text{var}} - N_{\text{phase}}, \tag{4.23}$$

for the degrees of freedom (dimensionality) N_{DOF} of coexistence regions with N_{phase} phases and N_{var} total independent variables. Here, $N_{\text{var}} = 4$, corresponding to a choice of one of each of the following conjugate pairs as an independent variable: T or $\mathcal{S}$, P or V, μ or N, and $\mathbf{E}_0$ or $\mathbf{S}_{\text{tot}}$. Thus, the $N_{\text{phase}} = 3$ fluid/BCT/HCP coexistence region spans an $N_{\text{DOF}} = 1$ dimensional line, the eutectic line, in $\mathbf{E}_0$ versus ϕ space. Because the applied field is constant in all three phases, this line is horizontal at $\mathbf{E}_{0,\text{eut}}$.

On the S versus ϕ phase diagrams (Figure 4.6), the tie lines connecting coexisting phases are sloped because the two phases polarize differently and have different dipole strengths. For $\beta > 0$, the BCT and HCP crystals have larger dipole strengths than the coexisting fluids, so the fluid/BCT and fluid/HCP tie lines have a positive slope. Because the spacing of particles within a field-aligned chain is smaller in the BCT lattice than the HCP lattice, the BCT crystal has a larger dipole strength than the HCP crystal even though the BCT crystal is at lower ϕ and the tie lines have a negative slope. These trends are reversed for $\beta < 0$ where particle depolarize one another; the fluid/BCT and fluid/HCP tie lines have negative slope while the BCT/HCP tie lines have positive slope. As $|\beta|$ decreases, the mutual polarization/depolarization weakens and the dipole strengths of the coexisting phases approach each other. In the limit of $\beta = 0$, *i.e.* the constant dipole model, the tie lines are flat.

The fluid/BCT/HCP eutectic line on the E_0 versus ϕ plot appears as a eutectic triangle on the S versus ϕ plot (Figure 4.6) because the three phases all have different dipole strengths. For $\beta > 0$, as β decreases the eutectic triangle flattens and the dipole strengths of the coexisting phases approach one another. In the limit of $\beta = 0$, all particles have equal dipole strengths and the eutectic triangle becomes a eutectic line. As β continues to decrease to negative values, the triangle opens up again but is inverted compared to the positive β case. The range of volume fractions the eutectic triangles span also decreases as β decreases, with the trend continuing for $\beta < 0$. The coexisting fluid volume fraction at the eutectic increases with decreasing β while the coexisting BCT and HCP volume fractions generally decrease with decreasing β. From the Gibbs phase rule (4.23), there is only one degree of freedom available at the eutectic, which seems to forbid the three phase eutectic from spanning a two-dimensional triangular region. This apparent contradiction is resolved by noticing that no phase can reside arbitrarily inside the eutectic triangle on the S versus ϕ plot. The particle dipole strength is *not* a controllable variable and is calculated from the applied field and overall volume fraction from an equation of state, $S = S(E_0, \phi)$. Because there is a single eutectic field strength, the dipole strength at the eutectic is given by the one-dimensional curve $S(E_{0,\text{eut}}, \phi)$ inside the eutectic triangle, satisfying the Gibbs phase rule. No combination of E_0 and ϕ yields arbitrary points inside the eutectic triangle. An alternate explanation that the Gibbs phase rule holds is to notice that the two-phase coexistence tie lines do not pass through the inside of the eutectic triangle, but rather are constrained by its one-dimensional perimeter.

For certain β values, the fluid dipole strength at fluid/BCT coexistence is nonmonotonic with respect to volume fraction or field strength. As we travel along the fluid binodal from left to right, the applied field decreases while the coexisting fluid volume fraction increases. The fluid dipole strength decreases with decreasing field strength but increases with increasing volume fraction, equation (4.20), so these competing

effects produce a coexisting fluid dipole strength that is nonmonotonic along the binodal. This is attributed to the rapid increase in coexisting fluid volume fraction over a small decrease in field strength on the E_0 versus ϕ phase diagram, Figure 4.5. The increased polarization due to densifying outpaces the decrease in field creating an interval where the coexisting dipole strength increases along the binodal on the S versus ϕ plot. The nonmonotonicity becomes less dramatic as β decreases, as the mutual polarization from densifying weakens relative to polarization due to the applied field. For sufficiently low $\beta > 0$, densifying is never able to overpower the effect of decreasing the field, and the coexisting fluid dipole is a monotonically decreasing function of volume fraction. For $\beta < 0$ both densifying and decreasing the field act to depolarize the fluid, so there are no competing effects that could lead to nonmonotonicity. The constant dipole model fails to capture nonmonotonicity, instead predicting a monotonic fluid dipole strength along the binodal for any β.

As β decreases, the BCT binodals in fluid/BCT coexistence extend to lower volume fractions, with the trend continuing for $\beta < 0$. In fact, because the BCT binodal for F/BCT coexistence must meet the BCT binodal for BCT/HCP coexistence, the BCT binodals for F/BCT have a "nose" point where the coexisting volume fraction transitions from decreasing with decreasing field to increasing with decreasing field. The BCT volume fraction at the nose point is the most dilute possible BCT crystal for a given β. Figure 4.1D showed that there is enhanced polarization/depolarization from aligning particles in chains, but only large $|\beta|$ values have significant additional polarization/depolarization from bringing chains together. Because there is nearly zero energetic advantage to bringing chains together, small $|\beta|$ values have an entropic driving force to keep chains well separated and increase the free volume. For a homogeneous crystal phase at a constant volume fraction, an increase in chain separation (increase in L_x) must be accompanied with a decrease in the intrachain spacing (decrease in L_z). Chains can only separate a finite distance until a minimum aspect ratio is met where particles within a chain are at or near contact ($L_z = 2a$). In a coexistence region however, the overall volume fraction is fixed, but the crystal phase is free to take whatever density lowers the total free energy of the dispersion. For small $|\beta|$, the entropic driving force to separate chains pushes the coexisting crystal volume fractions to more dilute values as E_0 decreases. Thus, the BCT volume fraction at the nose point decreases with decreasing β. This trend continues to negative β, with perfectly insulating particles having the most dilute BCT crystal. Although $|\beta|$ increases as $\beta \to -1/2$ and would seem to favor bringing chains together, the increased depolarization from the large negative β value weakens the energetic contribution enough to outpace this effect and favor more dilute crystals. The trend in the BCT nose point mimics the trend of the BCT volume fraction at the eutectic, which generally decreases with decreasing β.

Figure 4.7 shows the field strength corresponding to a coexisting fluid volume fraction $\phi_f = 0.20$ at fluid/BCT coexistence for dispersions of different β. Absent kinetic barriers, this is the minimum field needed to induce phase separation in a homogeneous disordered dispersion at volume fraction $\phi = 0.20$. As $|\beta|$ decreases, a larger E_0 is needed to induce phase separation. The magnitude of the interaction potential and forces driving the phase transition is set by the magnitude of the particle dipole moments. Because the particles polarize less in the applied field as $|\beta|$ decreases, higher fields are needed to compensate for the reduced dipole strength. This trend is also seen in the E_0 versus ϕ phase diagrams, where the binodals shift upward in field as $|\beta|$ decreases. In the limit of $\beta = 0$, an infinite field is required to induce a finite dipole strength and the E_0 versus β curve diverges. In fact, the E_0 versus ϕ phase diagram for $\beta = 0$ in Figure 4.5 simply has the F/HCP hard sphere coexistence points for all finite fields. Recall that, although the true hard sphere equilibrium crystal is actually FCC, we excluded FCC from the phase diagrams here. In terms of free volume theory, FCC and HCP crystals have identical free energy[178] and we cannot distinguish them, so we indicate F/HCP in Figure 4.5 to be consistent with the other plots. If there were *only* polarization from the applied field, as in the constant dipole model, the product $|\beta|E_0$ necessary for phase separation at a given ϕ would be independent of the value of β itself. However, Figure 4.7 shows that the $|\beta|E_0$ necessary for phase separation at $\phi = 0.20$ increases with decreasing β. This is confirmed on the $|\beta|$ E_0 versus ϕ phase diagram in Figure 4.5, where the binodals of dispersions with different β do not collapse together, in contrast to what the constant dipole model predicts. As β decreases, not only does the polarization from the external field decrease but the mutual polarization from other particles decreases as well. Even if the polarization from the external field were the same, larger E_0 would be needed to compensate for the reduced mutual polarization. In other words, at constant $|\beta|E_0$, the dipole strength decreases with decreasing β, so a larger $|\beta|E_0$ is needed for phase separation. This trend continues for negative β. Because particles depolarize one another for $\beta < 0$,

even higher $|\beta|E_0$ is necessary for phase separation compared to the $\beta = 0$ case where there is no mutual depolarization. The critical $|\beta|E_0$ appears to be a linearly decreasing function of β over the entire range of β, though we do not have an explanation for why the dependence should be linear. Because the fluid volume fraction on the binodal changes rapidly with a small decrease in field strength, Figure 4.7 would look similar had we chosen any fluid volume fraction over an appropriate range, say $0.05 \lesssim \phi_f \lesssim 0.40$. This suggests that the critical field strength $\widetilde{E}_0^*$ necessary to induce large scale structure formation in dielectic/paramagnetic dispersions satisfies

$$\widetilde{E}_0^* = \frac{\alpha_1}{|\beta|} + \alpha_2 \operatorname{sgn}\beta \tag{4.24}$$

for a wide range of volume fractions, where α_1 and α_2 are constants and $\operatorname{sgn}\beta \equiv \beta/|\beta|$ is the sign of β and equal to 1 for $\beta > 0$, -1 for $\beta < 0$, and 0 for $\beta = 0$. $\widetilde{E}_0^*$ could be, for example, the operating field strength required to induce a significant rheological response in electrorheological/magnetorheological suspensions. From a linear least squares fit to the $|\beta|\widetilde{E}_0$ versus β data in Figure 4.7, we find $\alpha_1 \approx 1.9$ and $\alpha_2 \approx -1.0$.

In Figure 4.7, we also compare the critical field strength $\widetilde{E}_0^*$ observed in experiments of field-driven structural transitions with that in our simulations and theory. Although there are numerous experimental studies on dielectric and paramagnetic suspensions, few rigorously examine phase transitions and provide detailed materials characterization necessary for accurate comparison. Ivey *et. al.* used light transmission measurements to carefully infer structural transitions in an oil-in-water emulsion of $a = 150\,\text{nm}$ radius paramagnetic kerosene droplets containing Fe_3O_4 magnetite grains.[237] The oil droplets had a measured magnetic permeability of $\lambda_p = 2.7\mu_0$, where μ_0 is the vacuum permeability, while water is nonmagnetic ($\lambda_f = \mu_0$), so the dispersion corresponds to $\beta = 0.36$. As the external magnetic field slowly increased, the amount of light transmitted through the dispersion initially decreased as the oil droplets began to chain in the field direction and then dramatically increased as the dispersion phase separated. At $\phi = 0.10$, Ivey *et. al.* observe fluid/crystal phase separation at a field strength of $E_0^* = 4\,\text{kA/m}$, which corresponds to $\widetilde{E}_0^* = 4.4$ in our dimensionless units and matches our predictions in Figure 4.7. Promislow and Gast investigated phase separation in a similar paramagnetic oil-in-water emulsion of radius $a = 380\,\text{nm}$ and permeability $\lambda_p = 9.25\mu_0$ ($\beta = 0.73$) octane droplets containing iron oxide Fe_2O_3 grains in toggled magnetic fields.[64] Although coexisting phases with toggled interactions are not true thermodynamic equilibrium states, they can be mapped to the equilibrium phase diagram using appropriately time-averaged quantities, as discussed in section 3.3.2.[36] Following this analysis, the appropriate quantity in the experiments to compare with our simulations and theory is the time average of the squared field, or in other words the quantity $\overline{E}_0 \equiv E_0/\sqrt{2}$. Using video microscopy, Promislow and Gast observed rapid fluid/BCT phase separation at high toggled field strengths and melting as the toggled field strength was gradually lowered. With measurements of the volume of the condensed phase, the authors estimated the coexisting crystal volume fractions as a function of (time-averaged) field strength. The coexisting fluid volume fraction was not reported. Below a certain field strength, the coexisting crystal volume fraction drops dramatically with decreasing field, going from $\phi_c = 0.56$ at $\widetilde{\overline{E}}_0 = 1.99$ to $\phi_c = 0.44$ at $\widetilde{\overline{E}}_0 = 1.44$. We take the field intermediate these values, $\widetilde{\overline{E}}_0^* = 1.72$, as the melting transition at constant ϕ, which corresponds with the critical $\widetilde{E}_0^*$ in Figure 4.7. Wen and coworkers performed rheological measurements on dense $\phi = 0.15 - 0.50$ electrorheological fluids consisting of $a = 40\,\text{nm}$ barium titanyl oxalate $BiTiO(C_2O_4)_2$ nanoparticles with a highly polarizable urea coating ($\lambda_p = 60\varepsilon_0$) dispersed in silicone oil ($\lambda_p = 2\varepsilon_0$), where ε_0 is the vacuum permittivity.[238,239] Because of the large dielectric constant contrast, $\beta = 0.91$, the electrorheological fluid showed a dramatic increase in yield stress of hundreds of kPa above an AC field strength of about $E_0^* = 2\,\text{V/}\mu\text{m}$, or $\widetilde{E}_0^* = 1.05$, for the entire volume fraction range.[238] The appearance of a yield stress is attributed to the formation of solid-like structures within the fluid,[7–10] and likely indicates crossing the fluid/BCT binodal into the coexistence region. The E_0^* from the experiments matches well with our predicted E_0^* in Figure 4.7. Ramos and coworkers performed similar rheological measurements on magnetorheological fluids consisting of $a = 100, 200$, and $375\,\text{nm}$ nonmagnetic silica particles ($\lambda_p = \mu_0$) dispersed in a magnetite based non-aqueous ferrofluid.[149,150] The magnetic permeability of the ferrofluid decreases with increasing external magnetic field as the magnetization of the permanent dipoles in the ferrofluid saturates, yielding variable $\beta = -0.18$ to $\beta \approx 0$. The authors report an increase in the zero shear viscosity[150] and elastic modulus[149] over a range of $|\beta|\,\widetilde{E}_0^* = 2.5 - 5.0$. The data was quite noisy and ran against the noise limit of the rheometer, so we could not extract a single

representative value to put on Figure 4.7, but the observed phenomena are consistent with our predictions, laying not too far above the $|\beta| \widetilde{E}_0^*$ versus β curve necessary for significant structure formation. In particular, because $\widetilde{E}_0^*$ scales as $a^{3/2}$, the authors found that the smallest $a = 100\,\text{nm}$ particles could not cross the threshold $|\beta| \widetilde{E}_0^*$ for any E_0 studied, and therefore functioned as a very poor magnetorheological fluid with no viscosity increase upon applying an external field. This illustrates the importance of understanding the phase behavior of such dispersions for rational functional materials design. Yethiraj and van Blaaderen used confocal microscopy to directly observe fluid/BCT coexistence in $a = 1\,\mu\text{m}$ charged polymethyl methacrylate (PMMA) particles ($\lambda_p = 5.6\varepsilon_0$) in a mixture of cycloheptyl bromide and *cis*-declain ($\lambda_f = 4.0\varepsilon_0$) above an AC electric field strength of $E_0 = 0.5\,\text{V}/\mu\text{m}$, corresponding to $\beta = -0.11$ and $|\beta| \widetilde{E}_0^* = 5.8$. This value lays above our predictions in Figure 4.7, but the particles in the experiments also had a strong, soft, and unscreened electrostatic repulsion, rather than the hard sphere repulsions used in this work, which significantly increases the field strength necessary for phase separation.[206,207] The authors added salt to reduce the range of the electrostatic repulsions, but did not report the detailed phase behavior in this case. Hynninen and Dijkstra examined dipolar particles with soft repulsions in detail and found qualitatively different phase behavior than for dipolar particles with hard repulsions, so adding this experimental E_0^* to Figure 4.7 is not the correct comparison. However, the value is consistent with our predictions, which provide a lower bound for phase separation for any soft dipolar particles.

Figure 4.8 shows the aspect ratio and unit cell dimensions of the coexisting crystal phases in fluid/HCP, fluid/BCT, and BCT/HCP coexistence for $\beta = 1$, though other β values have similar trends. At large field strengths, the BCT crystal in both fluid/BCT and BCT/HCP coexistence approaches the ground state of a closest packed BCT crystal at $\phi = 2\pi/9 \approx 0.698$ and aspect ratio $A = \sqrt{2/3} \approx 0.817$. As the field strength decreases, the entropic contribution to the free energy favoring more open crystal structures becomes larger and the coexisting BCT volume fraction decreases. While both the unit cell dimensions parallel, L_z, and orthogonal, L_x, to the field direction increase with decreasing field, the increase in L_z is small compared to the increase in L_x and the coexisting aspect ratio decreases with decreasing field. Because mutual polarization is so strong between field-aligned particles, particles prefer to be near contact with neighboring particles in the same field-aligned chain ($L_z \approx 2a$) while lowering their density by moving chains apart rather than increasing the intrachain spacing. As E_0 approaches the eutectic, the aspect ratio flattens out and the A, L_z, and L_x for the BCT crystal in fluid/BCT coexistence approaches A, L_z, and L_x for the BCT crystal in BCT/HCP coexistence, as the Gibbs phase rule requires. Although it was difficult to obtain coexistence points from our thermodynamic model here, the simulations show that the BCT volume fraction is relatively constant for $\beta = 1$ as the F/BCT binodals approach the eutectic. Figure 4.4 shows that decreasing the field strength at constant volume fraction increases the crystal aspect ratio. Therefore, we expect the BCT aspect ratio in F/BCT coexistence to have a minimum close to the eutectic. This minimum is likely related to the BCT nose points on the E_0 versus ϕ and S versus ϕ phase diagrams, where the coexisting BCT crystal volume fraction obtains its minimum value. Although the BCT crystal volume fraction for $\beta = 1$ does not drop significantly below the eutectic BCT volume fraction, as β decreases, the minimum BCT volume fraction decreases far below the eutectic BCT volume fraction. We expect the minimum BCT aspect ratio to also decrease with decreasing β.

The coexisting aspect ratio of the HCP crystal in BCT/HCP coexistence has a similar trend with decreasing field strength as that of the BCT crystal. At large field strengths, the coexisting HCP crystal approaches closest packing $\phi = \pi/3\sqrt{2} \approx 0.740$ at isotropic aspect ratio $A = \sqrt{2/3} \approx 0.817$. As the field strength decreases, the coexisting volume fraction decreases. Both L_z and L_x increase, but the increase in L_z is small compared to the increase in L_x, so the HCP aspect ratio decreases with decreasing field. This keeps the (111) hexagonal planes close together, keeping the distance between field-aligned particles small, while increasing the spacing between particles in the same (111) plane. The coexisting HCP aspect ratio in fluid/HCP coexistence shows the opposite trend with field strength compared to that in BCT/HCP coexistences. For $E_0 = 0$, the coexisting hard sphere HCP crystal has $\phi = 0.545$ and isotropic aspect ratio $A = \sqrt{2/3}$. As the field increases, the coexisting density of the HCP crystal does not change much but the aspect ratio decreases. The distance between hexagonal (111) planes L_z decreases with increasing field strength while the spacing within hexagonal (111) planes increases with increasing field strength. A, L_z, and L_x for the HCP crystal in fluid/HCP coexistence approaches A, L_z, and L_x for the HCP crystal in BCT/HCP coexistence at the

eutectic point, as the Gibbs phase rule requires.

As the F/BCT binodals approach the eutectic from above we were unable to obtain coexistence points using our thermodynamic model. In this region, the fluid phase is dense and particles align with the field into disordered chains. However, our expressions for the fluid free energy, equations (4.18)-(4.20), assume isotropic, hard sphere configurations. We underestimate the fluid dipole strength (for $\beta > 0$ and overestimate for $\beta < 0$) because we do not take into account the anisotropic structure of the fluid. At large E_0, where bias for field alignment might be large, the coexisting fluid phase is very dilute while at small E_0, the particle configuration is nearly an isotropic, hard sphere configuration, so our expression for the fluid free energy is accurate. The coexisting BCT phase in the region slightly above the eutectic is dilute with a small aspect ratio. Free volume theory, which assumes that a particle diffuses ideally in the small free volume constrained by its stationary neighbors, is not a good description for the large, highly anisotropic free volumes so equation (4.17) is not accurate for the hard sphere BCT free energy. Additionally, there are large fluctuations in the lattice configuration so our assumption that the ensemble averaged capacitance tensor is equal to the capacitance tensor of the ideal lattice with no fluctuations, $\langle \mathscr{C} \rangle(\mathbf{E}_0, \mathbf{x}) \approx \mathscr{C}(\mathbf{x})$, is not valid and equation (4.15) is inaccurate. In this region, expressions which take into account interactions between fluctuating chains[222,240] may be useful, but were not incorporated here. At large E_0, the BCT crystal becomes denser and fluctuations decrease, so our expressions for the crystal free energy are accurate. At small E_0, fluctuations may be large but the dipolar contribution to the free energy is small. The BCT crystal becomes denser and more isotropic, so the hard sphere free volume theory is accurate. Only at moderate field strengths slightly above the eutectic does our model break down. At the eutectic point our thermodynamic model is valid, and we were able to obtain accurate coexistence points for the F/BCT binodals, which match the values at the F/HCP and BCT/HCP binodals. In Figures 4.5, 4.6, and 4.8, dotted lines span the small region of the F/BCT binodals where we were unable to obtain coexistence points. The dotted lines connect the F/BCT coexistence points at the eutectic, which we were able to obtain with our model, to the next highest field strength for which we could obtain coexistence points as a crude interpolation in this region. Nonetheless, our thermodynamic model works well for nearly all of phase space and its predictions agree very well with the simulation results.

Our model includes only dipolar interactions and neglects quadrupolar and higher order moments. Including higher order moments does not change the general form of equation (4.5), but does increase the accuracy of $\mathscr{M}$ and therefore $\mathscr{C}$.[145] Neglecting these moments, we underestimate the actual particle dipole strengths and therefore overestimate the field strengths necessary for phase separation. Because the mutual dipolar interactions capture many-body effects, which we believe are the most important governing phase behavior, our results are general and accurate even without including higher order moments. Including higher order moments does not qualitatively change the many-bodied nature of the particle interactions, only the accuracy of the induced dipole moments. This acts to shift the binodal curves down to lower fields, but we believe this will be a small quantitative correction without qualitative modifications. The same cannot be said for the constant dipole model, which neglects many-bodied interactions and is therefore a qualitatively different description of dielectric/paramagnetic dispersions. The higher order terms contribute more polarization/depolarization as the particle density increases and as $|\beta|$ increases. In fact, for perfectly conducting particles $\beta = 1$, the exact dipole strength diverges for a particle chain or crystal as the particles approach contact.[145,241] In this case though, the free volume vanishes and the entropic contribution to the free energy also diverges. A careful asymptotic analysis is needed to compare these two diverging interactions and yield finite dipole strengths and free volumes at thermodynamic equilibrium, which is beyond the scope of the work here. It is not straightforward to apply analyses of competing divergences to real suspensions, where particles can never truly come into contact and other effects like van der Waals interactions, particle sintering (for a nonstabilized suspension), and electrostatic repulsion (for a stabilized suspension) are significant for nearly touching particles. For all $\beta \neq 1$ there are no diverging contributions to the polarization and as β decreases from 1, higher order moments quickly become negligible compared to the dipolar contributions.[145,241]

Our model also does not account for any structural changes within the solvent phase. These effects are important in low-frequency dielectrophoretic assembly of particles in electrolytes, where the ionic double layers around particles interact and respond to changes in the applied AC electric field.[62,86,200] In this case, the ion cloud contributes additional polarization, and the β parameter is frequency dependent. The

structure of the double layers changes as the particles assemble and lead to additional electrostatic and osmotic pressure effects.[125] Polarizable colloids in electrolytes are investigated in Chapter 7.

Conclusion

Because of their simplicity and the availability of external control, dispersions of dielectric/paramagnetic particles responsive to electric/magnetic fields are widely used in industrial applications from shock absorbers[9] to tunable photonic crystals[198] and also provide a robust platform for controlling nanoparticle and colloidal self-assembly.[46] The equilibrium phase behavior of these materials, a crucial piece of information for their design and operation, has only been investigated using the constant dipole model,[206,207] which fails to capture qualitative features of real suspensions. To address this issue, we have developed a simple numerical and thermodynamic framework to describe the phase behavior of polarizable particles in an applied field. We have taken into account mutual polarization of particles, which makes our framework a better representation of real suspensions than constant dipole models. Our model leads to theoretical predictions that are simple to evaluate and in quantitative agreement with the phase behavior observed in dynamic simulations and experiments. In contrast to constant dipole model predictions, we find that coexisting phases have different polarization strengths and dispersions of particles with different dielectric constant or magnetic permeability have qualitatively different phase behavior. We have also fully characterized the eutectic behavior of these dispersions, a quality that is usually missed in other descriptions of dipolar phase behavior.[206,207] The existence of a eutectic is an exciting feature for a nanoparticle dispersion as it can be manipulated to achieve hierarchical assembly. In atomic alloys, for example, the eutectic can be used to form meso-phases of two different solid compositions organized into patterns on a macroscopic scale such as lamellae or rods. Control of hierarchical assembly is a grand challenge in the field of nanoscience, and polarizable particles near their eutectic offer a new pathway for achieving that control.

Our work will be useful in the design and operation of responsive materials containing dielectric/paramagnetic nanoparticles. In particular, we have provided detailed results about the relevant operating field strengths, concentrations, and conductivities as well as enumerated the equilibrium structures in suspensions of spheres. The thermodynamic framework can be extended to other systems whose interactions and assembly can be understood in terms of coupled multipole moments and hard repulsions. For example, spherical particles pinned to a fluid/fluid interface interact and assemble due to quadrupolar interactions.[242,243] The strengths of the quadrupole moments are coupled in a similar way to our mutually polarized dipoles. The developed dynamic simulations will also be useful to directly observe the assembly kinetics of dielectric/paramagnetic dispersions, and our thermodynamic theory can improve existing theoretical kinetic descriptions[217,218] that incorporate equilibrium thermodynamic calculations. Finally, our simulations can be extended to dynamic self-assembly processes of dielectric/paramagnetic dispersions, such as modulating the particle interactions cyclically in time by toggling or rotating the external field.[67,68,89] Our thermodynamic model will also be useful in analyzing these dynamic self-assembly processes, which in some cases can be understood in terms of equilibrium phase behavior.[36]

Methods

We perform dynamic simulations of a monodisperse suspension of $N \approx 8000$ spherical colloidal particles using the freely-draining model of section. 2.1.4 All lengths are made dimensionless by the particle radius a, all energies are made dimensionless by the thermal energy k_BT, and all times are made dimensionless on the characteristic particle diffusion time $\tau_D \equiv 6\pi\mu_s a^3/k_BT$. Additionally, conductivities are made dimensionless by the fluid conductivity λ_f which immediately sets the units of field $\sqrt{k_BT/a^3\lambda_f}$ and dipole $\sqrt{a^3\lambda_f k_BT}$.

For homogeneous nucleation simulations, we used $N = 8000$ particles beginning from a disordered initial configuration, generated by allowing the particles to equilibrate for $100\tau_D$ with no applied field. We then apply the field and allow the dispersion to evolve for around $1000\tau_D$. We observed that this time was long enough for the dispersion to nearly equilibrate, though some slowly resolving defects and kinetically arrested configurations were still present. We do not expect these to obscure our results, as the vast majority of

particles belonged to nearly perfect bulk phases. For simulations beginning with an HCP crystal, we initialize all particles on an isotropic HCP lattice oriented so that its closest packed (111) planes are orthogonal to the applied field. The volume fraction of the initial HCP crystal is lower than that of the overall system, so there is empty solvent around the crystal. We choose to allow the crystal to span the periodic simulation box in the two directions orthogonal to the field so that the empty space is located in the field direction relative to the crystal. This allows the closest packed planes to change their spacing in the field direction in response to the applied field, changing the equilibrium aspect ratio as a function of the applied field strength.

For cases where the field strength was modulated, a fully equilibrated configuration at one field strength is used as the initial configuration for a simulation with a different field strength. The field strength was changed by a small amount and allowed to equilibrate for around $250\tau_D$. Regions where the coexisting structures changed slowly with field strength had larger field jumps than regions where the coexisting structure changed rapidly. By adjusting our field step size, we always ensured that the structures equilibrated in around $250\tau_D$.

For $\varepsilon = \pi a^3 \lambda_f \beta^2 E_0^2 = 1$, a time step of $\Delta t = 10^{-3}$ is small enough to accurately resolve the dynamics of the dispersion. As the field increases, the forces and displacements in the dispersion grow. We reduce Δt by a factor of ε to ensure that our numerical integration is always accurate.

From equilibrated simulation configurations, we construct multivariate distributions of particle dipoles and local volume fractions. The particle dipoles are computed using (4.5), while the local volume fraction of each particle was determined using two methods. In the first method, the local volume fraction around a particle is equal to the ratio of the particle's volume to the volume of its Voronoi cell. In the second method, the local volume fraction was determined by looking at a sphere of radius $6a$ centered around a particle and calculating the fraction of this "search" sphere's volume that was occupied by particles. The central particle's volume was included as well as partial intersections of particle volume with the search sphere surface. Strictly, both methods represent density only conditionally around a central particle and so overestimate the true local density. However, this allows us to assign a local density unambiguously to a particle rather than to a position in space and is more useful as a particle-based order parameter. The error in using our approach is small for all but the most dilute regions. The Voronoi method gives more accurate results at high field strengths than the search sphere method for dense, highly anisotropic crystals in coexistence with a very dilute fluid because the shape of the Voronoi cell takes on the shape of the crystal unit cell. As the field strength decreases, the crystal becomes less dense, the fluid becomes more dense, fluctuations in both phases increase, and the search sphere method becomes more reliable than the Voronoi method to distinguish fluid-like and crystalline particles. We switch between the Voronoi and search sphere methods around the field strength where the coexisting fluid volume fraction transitions from nearly 0 to a finite, measurable value.

In the Gaussian fits of the multivariate distribution of particle dipoles and local volume fractions, the Gaussian peak heights are proportional to the number of particles in each phase. The dense crystal peak is much larger than the dilute fluid peak, so the fluid values may have larger error than the crystal values. Additionally, a third peak is sometimes observed corresponding to particles on the fluid/crystal interface, which have dipole strength and volume fraction intermediate the fluid and crystal values. As the system size L grows, the number of bulk fluid and crystal particles grows as L^3 while the number of interfacial particles grows as L^2. For large enough systems, the interfacial peak will be insignificant compared to the fluid and crystal peaks. Although we are not in this large system limit, we can remove the effect of interfacial particles by adding a third Gaussian to the total distribution. First, we use a maximum likelihood analysis to fit the distribution to three Gaussians and sort the particles into three populations (fluid, crystal, and interface) using the posterior probabilities. The interfacial particles are removed and another maximum likelihood analysis with two Gaussians is performed to extract the fluid and crystal dipole strengths and volume fractions. Note that while we remove interfacial particles to determine ϕ_f and ϕ_c, we include them in N_f and N_c to compute δ in (4.22) by sorting the interfacial particles into either the fluid or crystal phase using posterior probabilities, enforcing conservation of particles $N = N_f + N_c$. This allows for robust evaluation of the numerical error in the analysis method as well as the sampling.

Chapter 5

Transmutable Colloidal Crystals and Active Phase Separation *via* Dynamic, Directed Self-Assembly with Toggled External Fields

In Chapter 1, we discussed two main engineering challenged that have prevented robust, scalable fabrication of functional nanomaterials *via* static self-assembly. The first was designing and synthesizing building blocks whose interactions drive a dispersion toward a specific, often ordered, target structure. While simple structures have been synthesized with simple particle interactions, more complex structures require increasingly complicated interactions, which may be difficult to engineer. The second challenge involves the kinetics of assembling the target structure. The forces driving assembly tend to trap particles in kinetically-arrested defective or disordered metastable states. There is an intrinsic coupling between the thermodynamic driving force and the assembly kinetics that forces a tradeoff between quality of the self-assembled microstructure and its rate of formation.[36,37]

If particle interactions are varied in time, the dispersion is driven out of equilibrium and non-equilibrium kinetic pathways can be leveraged to speed the rate of assembly, to enhance the quality of the assembled structure, and to access states not available at thermodynamic equilibrium. Toggling the the interactions on for a time t_{on} and off for a time t_{off} cyclically in time is a particularly effective mode of time-variation and drives rapid crystallization, even when interparticle forces are orders of magnitude larger than thermal forces.[64,65,67,68,73–77,197] The toggle protocol can be used to assemble a variety of different structures, including those that are not observed with steady interactions.[36,37,78–84]

In Chapter 3, we used linear irreversible thermodynamics to show that coexisting phases at periodic-steady-state (PSS) in toggled dispersions satisfy[36]

$$\overline{P}_1 = \overline{P}_2, \quad \overline{\mu}_1 = \overline{\mu}_2, \tag{5.1}$$

where P_i and μ_i are the pressure and chemical potential in phase i, and the overbar indicates the time average, $\overline{X} = \mathscr{T}^{-1} \int_{\mathscr{T}} dt X(t)$, over one toggle period $\mathscr{T} \equiv t_{\text{on}} + t_{\text{off}}$. The time-averaged equations of state (EoS) depend only on the duty cycle, $\xi \equiv t_{\text{on}}/(t_{\text{on}} + t_{\text{off}})$, and not on the toggle frequency. The time-averaged EoS, and therefore the periodic-steady-states, can be constructed using analytic EoS for steady interactions. The phase behavior and equations of state for dispersions of polarizable particles in steady fields were computed in Chapter 4. In this chapter, we apply this theory to toggled field-directed assembly. Magnetic fields are particularly convenient for toggling because they are easy to control, and time scales for magnetic relaxation inside particles are small compared to time scales for particle motion, so dispersions respond essentially instantaneously to changes in the field. Toggled electric fields may also be used if conditions are controlled to prevent unwanted currents, electroosmotic flows, and electrochemical reactions. A complete theoretical

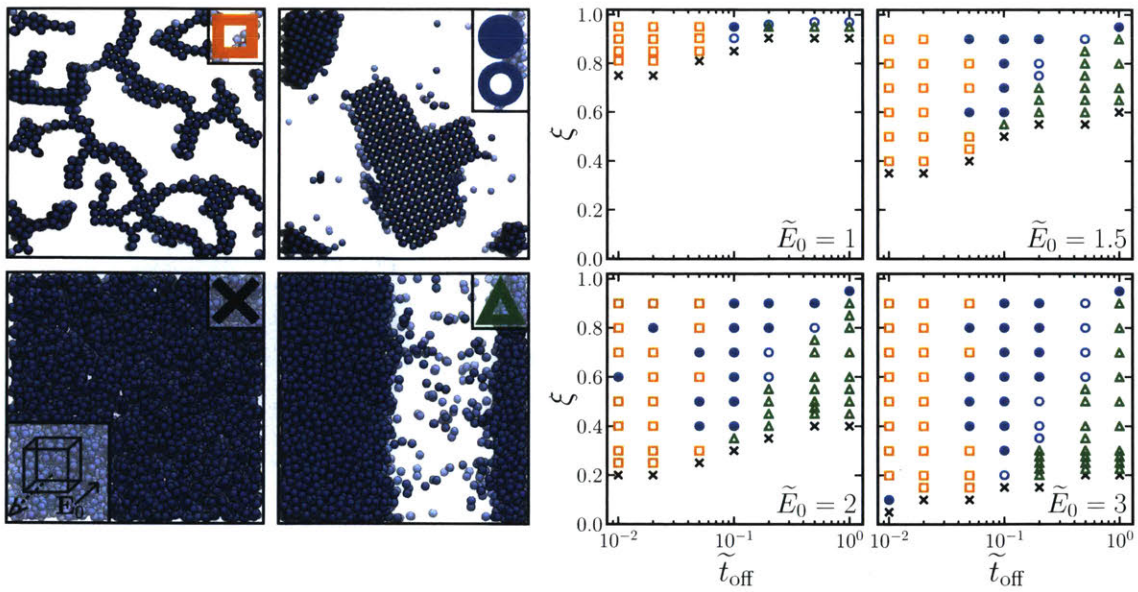

Figure 5.1: Structures observed in Brownian dynamics simulations of perfectly conducting ($\beta = 1$) particles at volume fraction $\phi = 0.20$ assembing in toggled fields of varying strength $\widetilde{E}_0$, duty cycle ξ, and off duration $\widetilde{t}_{\text{off}}$. Symbols indiate different structures: arrested (orange squares), fluid/BCT coexistence (blue circles) *via* a one-step (filled cirlces) or two-step (open circles) nucleation mechanism, homogeneous fluid (black crosses), and fluid/fluid coexistence (green triangles). The field points into the page, as indicated by the schematic in the lower left.

description of self-assembly in toggled magnetic and electric fields will facilitate experimental design for robust self-assembly.

In this chapter, we investigate dynamic, directed self-assembly in dispersions of polarizable, spherical nanoparticles driven by toggled electric/magnetic fields. First, we use freely-draining, dynamic simulations to elucidate the effect of the toggled field parameters on the terminal structures, their kinetic pathways, and the quality of self-assembled crystals. Then, we construct appropriate time-averaged equations of state for the dispersion and use these to predict the coexisting phases observed at periodic-steady-state. Finally, we investigate body-centered-orthorhombic (BCO) crystals, which spontaneously form as a single phase with toggled fields in the neighborhood of a eutectic line on the equilibrium phase diagram. These active crystals are only metastable at equilibrium and are never observed to nucleate in steady fields. The lattice parameters of these BCO crystals can be varied continuously by changing the strength and duty cycle of the toggled field.

5.1 Out-of-Equilibrium Phase Diagram

Figures 5.1 and 5.2 show the results of Brownian dynamics simulations of dispersions of $N = 8000$ polarizable nanoparticles assembling at constant volume fraction $\phi = 0.20$ in toggled fields of varying strength E_0, duty ξ, and off duration t_{off}. In these simulations, the many-bodied forces between polarizable particles are computed with the model from sections 2.2 and 4.1.2 in which the dipole moments induced within a given particle depend linearly on the dipoles induced in other particles.[142] For reasons of computational efficiency, many-bodied hydrodynamic interactions are neglected. These interactions are unimportant for durations t_{on} and t_{off} short relative to the bare particle diffusion time,[36] and limited testing with a far-field approximation of the hydrodynamic interactions[128] confirm there are no qualitative changes to the simulation results. The field is made dimensionless as $\widetilde{E}_0 \equiv E_0\sqrt{a^3\lambda_f/k_BT}$, and time is made dimensionless as $\widetilde{t}_{\text{off}} \equiv t_{\text{off}}/\tau_D$, where $\tau_D \equiv 6\pi\eta a^3/k_BT$ is the bare diffusion time, a is the particle radius, η is the solvent viscosity, λ_f is the solvent permittivity/permeability, and k_BT is the thermal energy. After $1000\tau_D$, the final state of the dispersion was classified according the legend in Figure 5.1, and the crystal fraction, $X_c \equiv N_c/N$, the fraction of total particles N that are locally crystalline N_c, was computed in Figure 5.2 for dispersions that crystallized by

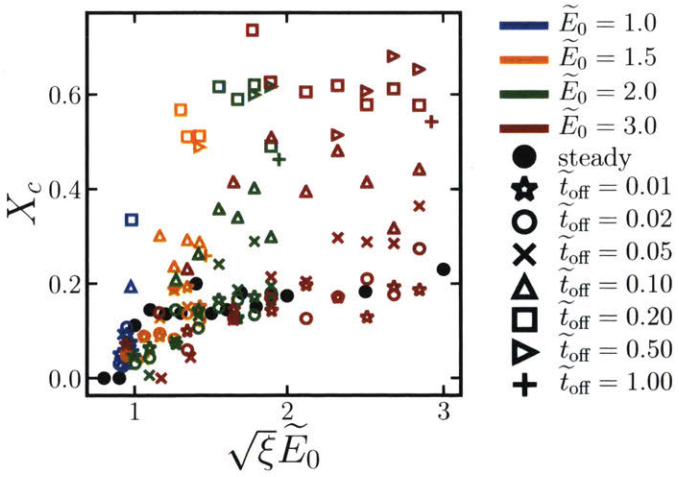

Figure 5.2: Crystal fraction X_c after $1000\tau_D$ for perfectly conducting ($\beta = 1$) dispersions assembling at volume fraction $\phi = 0.20$ in steady (black filled; $\xi = 1$) and toggled (colored open) fields at various strengths $\widetilde{E}_0$, duties ξ, and off durations $\widetilde{t}_{\text{off}}$.

designating particles as crystalline if their local density exceeds a threshold value of $\phi = 0.60$. Crystalline and disordered particles can be distinguished by density alone for sufficiently dense crystal, as disordered configurations are excluded above the random close-packing limit, $\phi \approx 0.64$, which is close to our threshold value. Higher threshold values yielded the same classification as did classification with local bond order parameters. Interface, grain boundaries, defects, or disorder tend to decrease the local packing density, so dispersions with few large, crystalline domains have a larger X_c than those with many small, defective ones. Thus, X_c is one representative measure of the quality of the assembled structure.

For small duty cycles, the field is not on long enough to drive assembly, and the suspension remains a homogeneous disordered fluid. The critical duty ξ^* necessary for assembly increases with increasing $\widetilde{t}_{\text{off}}$ and decreases with increasing $\widetilde{E}_0$. Above ξ^*, at small $\widetilde{t}_{\text{off}}$ the dispersion begins to assemble towards fluid/body-centered-tetragonal (BCT) coexistence, but arrests in a percolated structure with many defects. The corresponding crystal fractions in Figure 5.2 are small, and the toggled field does no better in assembling crystal than a steady field of strength $\sqrt{\xi}\widetilde{E}_0$. As with the first row of Figure 5.3, particles do not have enough time to diffuse away from their arrested configurations within the span $\widetilde{t}_{\text{off}}$, and defects persist from cycle to cycle. Experiments with paramagnetic spheres also observed arrest at large toggle frequencies.[67,68] As $\widetilde{t}_{\text{off}}$ increases, the dispersion assembles into large, high-quality crystals and reaches a periodic-steady-state with fluid/BCT coexistence. The crystal fraction with toggled fields is several times larger than that with steady fields. Two different kinetic mechanisms are observed in this region: one-step (second row of Figure 5.3) and two-step (third row of Figure 5.3) nucleation. In the one-step mechanism, crystal nucleates directly from a homogeneous fluid phase. Particles have enough time to diffuse while the field is off to anneal local defects from cycle to cycle. Diffusion while the field is off also resolves grain boundaries, and smaller crystalline domains coalesce to a few large, high-quality domains. In the two-step mechanism, fluid/fluid phase separation occurs before crystal nucleation. Because there are no grain boundaries, dense fluid drops quickly coalesce. Crystal nucleates preferentially in the dense fluid and, because all nuclei are localized to the dense fluid, the crystal quickly grows into a single, high-quality phase. The toggle parameters select which kinetic mechanism is observed. Smaller $\widetilde{t}_{\text{off}}$ and larger ξ increase the rate of crystal nucleation relative to fluid nucleation and favor the one-step mechanism while larger $\widetilde{t}_{\text{off}}$ and smaller ξ favor the two-step mechanism. In fact, if $\widetilde{t}_{\text{off}}$ is sufficiently large or ξ is sufficiently small, crystal nucleation within the dense fluid is suppressed for the simulation duration, and fluid-fluid coexistence persists as the PSS rather than fluid/BCT. Particles diffuse far enough while the field is off that they cannot maintain a stable crystalline lattice from cycle to cycle, consistent with the classical Lindemann criterion. While fluid/BCT coexistence is observed for steady fields, fluid/fluid coexistence is metastable and can only be observed in toggled fields. Experiments also

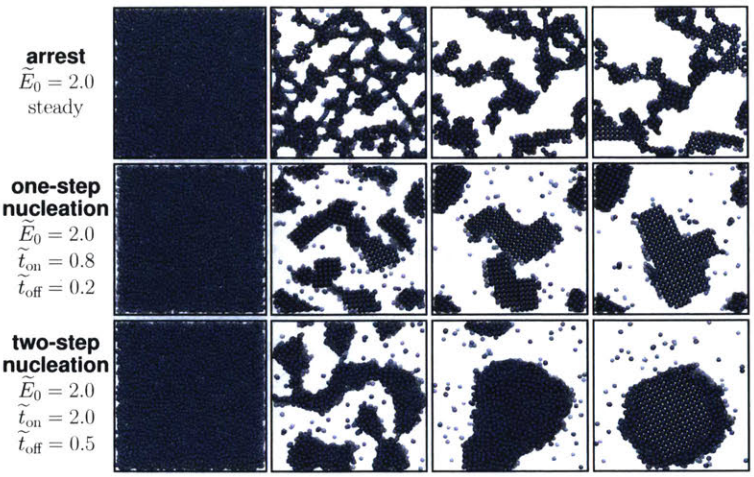

Figure 5.3: Snapshots over time of perfectly conducting ($\beta = 1$) dispersions at $\phi = 0.20$ evolving *via* different kinetic mechanisms. Suspensions begin as a homogeneous, disordered fluid (first column) and evlove for $1000\tau_D$ (last column). The middle columns at intermediate time points are different among rows.

observed crystallization only for a range of toggle frequencies while fluid/fluid phase separation occurred at smaller frequencies,[67,68] and both one-step and two-step nucleation mechanisms were observed in our previous simulations with toggled isotropic, short-ranged attractions from Chapter 3.[36,37]

For dispersions that phase separate, structures evolve until the two phases satisfy (5.1), $\overline{P}_1 = \overline{P}_2$ and $\overline{\mu}_1 = \overline{\mu}_2$.[36] If we had expressions for the time-averaged EoS, we could equate them in the two different phases and compute the PSS diagram for toggled fields. In Chapter 4, we showed that for steady fields, the EoS can be calculated by first computing the free energy at constant temperature T, volume V, particle number N, and external field $\mathbf{E}_0$,[142]

$$L(T, V, N, \mathbf{E}_0) = F_{\text{hs}} - N\mathbf{C} : \mathbf{E}_0\mathbf{E}_0/2, \tag{5.2}$$

where F_{hs} is the hard sphere free energy at zero field and $\mathbf{C}$ is the capacitance tensor relating the average particle dipole moment $\mathbf{S}$ to the field, $\mathbf{S} = \mathbf{C} \cdot \mathbf{E}_0$. $\mathbf{C}$ accounts for polarization due solely to the external field and many-bodied polarization from the fields generated by the dipoles of all other particles. $\mathbf{C}$ depends on particle configuration as well as the ratio of particle permittivity/permeability λ_p to solvent permittivity/permeability λ_f through the contrast parameter $\beta \equiv (\lambda_p/\lambda_f - 1)/(\lambda_p/\lambda_f + 2)$. The pressure and chemical potential are then computed from derivatives of the free energy,

$$P \equiv -\left(\frac{\partial L}{\partial V}\right)_{T,N,\mathbf{E}_0} = P_{\text{hs}} + \frac{N}{2}\frac{\partial \mathbf{C}}{\partial V} : \mathbf{E}_0\mathbf{E}_0, \tag{5.3}$$

and similarly for the chemical potential, where P_{hs} is the hard sphere pressure at zero field. For toggled fields, the time-averaged EoS take the form $\overline{P} = (1-\xi)P_{\text{off}} + \xi P_{\text{on}}$, where P_{on} and P_{off} are the pressures (or chemical potentials) while the field is on and off, respectively.[36] When the field is off, $P_{\text{off}} = P_{\text{hs}}$, and while the field is on, P_{on} is given by (5.3), so the time-average is

$$\overline{P} = P_{\text{hs}} + \frac{N}{2}\frac{\partial \mathbf{C}}{\partial V} : \xi\mathbf{E}_0\mathbf{E}_0, \tag{5.4}$$

and similarly for the chemical potential. The time-averaged EoS for toggled fields are equivalent to the EoS for steady fields if the steady field strength $E_0 \equiv |\mathbf{E}_0|$ is replaced with $\sqrt{\xi}E_0$. In other words, a dispersion in a toggled field with duty ξ and strength E_0 can assemble into the same phases as a dispersion in a steady field of strength $\sqrt{\xi}E_0$. In steady fields, there is a single, well-defined equilibrium state that minimizes the free energy in (5.2) for a given $\widetilde{E}_0$. In toggled fields however, no equivalent criterion exists, and there can be multiple periodic-steady-states for a given $\sqrt{\xi}\widetilde{E}_0$. *If* any of the PSSs have multiple phases, the phases must

satisfy (5.1). Therefore, the PSS phase diagram for toggled fields looks identical to the phase diagram for steady fields of strength $\sqrt{\xi}\widetilde{E}_0$, but phases that are only metastable with steady fields, such as fluid/fluid coexistence, can be stable and long-lived in toggled fields. However, whether or not phase separation occurs and which types of structures assemble depend on the specific choice of toggle parameters.

In Chapter 4, we computed the complete phase diagram for polarizable suspensions in steady fields.[142] A portion of this phase diagram, the fluid/BCT binodal, is shown in Figure 5.4 in terms of $\sqrt{\xi}\widetilde{E}_0$ for perfectly conducting ($\beta = 1$) and perfectly insulating ($\beta = -1/2$) particles. Using the same thermodynamic model, we also calculate here the metastable fluid/fluid binodal using explicit expressions for P and μ. Details of the simulation method are described in sections 2.1, 2.2, and 4.1.2 and details of the thermodynamic calculations are discussed in section 4.2 and Appendix B. Using the procedure from Chapter 4, we also extract coexistence points from our Brownian dynamics simulations by computing the distribution of local volume fractions around each particle, which has two peaks associated with the coexisting volume fractions of the two phases. The presented data come from simulations with $N = 8000$ at a bulk volume fraction of $\phi = 0.20$ and $N = 64000$ at $\phi = 0.35 - 0.52$. The coexisting volume fractions are independent of the number of particles and the bulk volume fraction, which only affects the relative volume of each phase *via* the typical lever rule.

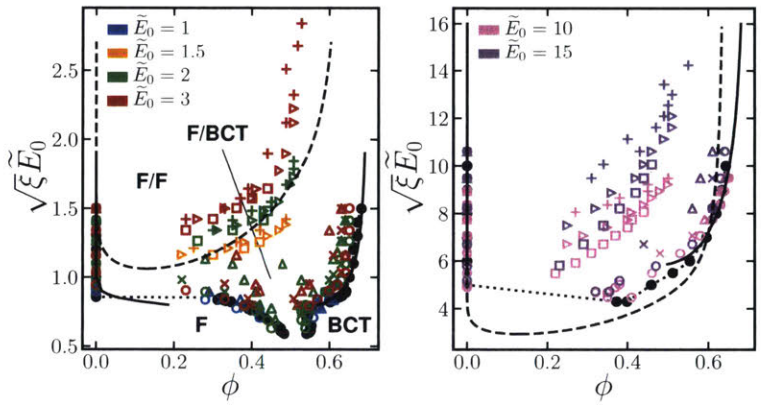

Figure 5.4: Periodic-steady-state phase diagram for perfect conductors with $\beta = 1$ (left) and perfect insulators with $\beta = -1/2$ (right). The colored points are the coexisting volume fractions of fluid/fluid (F/F) coexistence and fluid/BCT (F/BCT) coexistence from Brownian dynamics simulations in toggled fields at various strengths $\widetilde{E}_0$ (different colors), duty cycles ξ, and off durations $\widetilde{t}_{\text{off}}$ (different symbols; see legend of Figure 5.2 for values), the filled black circles (connected by dotted lines to guide the eye) are the coexisting volume fractions from simulations in steady fields of strength $\sqrt{\xi}\widetilde{E}_0$ from Ref. 142, and the lines are the predicted F/BCT (solid) and F/F (dashed) coexisting volume fractions from our theoretical thermodynamic model. The dilute fluid phase in fluid/fluid coexistence is not shown for the simulation data because the volume fractions were too small to accurately measure.

Because only the product $\sqrt{\xi}\widetilde{E}_0$ appears in the time-averaged EoS, $\widetilde{E}_0$ and $\widetilde{t}_{\text{off}}$ cannot independently affect the coexisting volume fractions, which are unchanged by $\widetilde{t}_{\text{off}}$. For both fliud/fluid and fluid/BCT coexistence, the data collected at different $\widetilde{E}_0$, ξ, and $\widetilde{t}_{\text{off}}$ collapse together in terms of $\sqrt{\xi}\widetilde{E}_0$. These collapsed curves agree with the theoretical predictions for the PSS phase diagram from our linear irreversible thermodynamic model. Just as $\widetilde{E}_0$ is the thermodynamic "control variable" for steady fields, one can use either the duty cycle ξ or the field strength $\widetilde{E}_0$ to navigate the toggled field PSS phase diagram. The toggle frequency, set by $\widetilde{t}_{\text{off}}$, appears to select which coexisting phases are observed, but does not affect the coexisting volume fractions.

Perfect conductors ($\beta = 1$) and perfect insulators ($\beta = -1/2$) are the limiting cases of particle permittivity/permeability, with real dispersions having intermediate values of β. Both conductors and insulators assemble into the same types of structures at PSS that can be understood in terms of the equilibrium phase diagram at their respective β values, so we expect dispersions of intermediate β to behave similarly. Dispersions of different β can be compared most easily in terms of the product $|\beta|\,\widetilde{E}_0$. Because of many-body,

mutual polarization/depolarization among the particles, the fluid/fluid and fluid/BCT binodals in steady fields shift to lower $|\beta|\,\widetilde{E}_0$ as β increases from $-1/2$ to 1. Thus, the fluid/fluid and fluid/BCT PSS curves in toggled fields shift to lower $\sqrt{\xi}\,|\beta|\,\widetilde{E}_0$ as β increases. The effect of β on the equilibrium phase diagram is discussed further in Ref. 142.

The simulation results have small but systematic deviations from our predictions. The PSS coexistence curves tend to shift slightly upward with increasing $\widetilde{E}_0$, and at constant ξ, the coexisting volume fraction of the dense phase (either fluid or BCT) decreases slightly as $\widetilde{t}_{\text{off}}$ increases. We attribute these deviations to large structural changes occurring within each toggle cycle. The PSS criteria in (5.1) are only valid if a particle's local environment does not change significantly within a toggle cycle. However, for strong fields and/or long toggle periods, the microstructure can switch from anisotropic chains while the field is on to a diffuse, isotropic state while the field is off. In fact, in experiments these intracycle transitions can lead to an elastohydrodynamic buckling instability in the self-assembled domains at every cycle.[73] Additionally, the predicted metastable fluid/fluid binodal for insulating particles underestimates the fluid/fluid PSS from simulations, likely due to the EoS failing to capture the anisotropy of the dense fluid. These deviations appear to be only second-order effects, and our theoretical predictions still provide a useful description of the periodic-steady-states for a wide range of parameters.

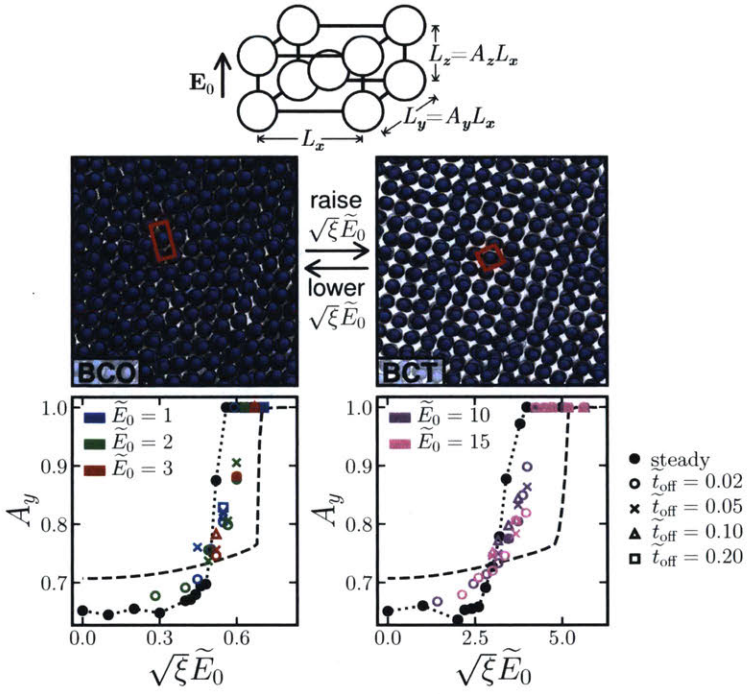

Figure 5.5: Lateral aspect ratio $A_y \equiv L_y/L_x$ of the homogeneous BCO crystal phase for perfect conductors $\beta = 1$ (bottom left) and perfect insulators $\beta = -1/2$ (bottom right) at volume fraction $\phi = 0.55$ assembled in steady ($\xi = 1$) and toggled fields of various strengths $\widetilde{E}_0$, duties ξ, and off durations $\widetilde{t}_{\text{off}}$. The open colored points are extracted from simulations of BCO nucleation in toggled fields, the filled black circles (connected by dotted lines to guide the eye) are from simulations of BCT to BCO lattice deformations upon lowering a steady field, and the black dashed line is the metastable BCO aspect ratio calculated by minimizing (5.2) using our thermodynamic model for steady fields.

5.2 Transmutable Body-Centered-Orthorhombic Crystals

At large volume fractions and low duty cycles, particles assemble into a homogeneous body-centered-orthorhombic (BCO) crystal, with the three unit cell dimensions, L_x, L_y, and L_z, all having different values as shown in Figure 5.5. For a BCT crystal, the typical crystal phase observed in steady fields, the

two dimensions orthogonal to the field, L_x and L_y, are equal but different from the dimension parallel to the field $L_z \neq L_x = L_y$. While BCT breaks symmetry in the field direction, the appearance of BCO crystal is surprising because it breaks symmetry in the plane orthogonal to the field, where there is no preferred direction. For $\phi > 0.50$ and steady, weak fields, HCP crystal (with its 111 face orthogonal to the field) is thermodynamically favored over BCT because the HCP lattice has a larger free volume.[142] However, converting between BCT and HCP requires melting one lattice and nucleating the other. BCO crystal also has a larger free volume than BCT, but is accessible from BCT through a diffusionless lattice distortion. When a steady field is applied to a BCT crystal and then the field strength is reduced, we observe this diffusionless BCO transition, which has lower kinetic barriers than those for HCP nucleation. A pure BCT crystal breaks symmetry and transitions to the metastable BCO phase as the steady field strength is lowered. The lateral aspect ratio $A_y \equiv L_y/L_x$ of the BCO crystal is that which balances entropic and energetic contributions to locally minimize the free energy in (5.2). However, defects and sufficient time will eventually drive a transition to the stable phase through melting and nucleation of HCP crystal.

In toggled fields, particles prefer a BCT structure when the field is on and an isotropic HCP or FCC structure when the field is off. The particles do not have enough time to switch between crystal structures within a cycle, so they choose to assemble into BCO as a compromise between their preferred structures in the field-on and field-off half-cycles. Unlike in steady fields, where BCO is only accessible by first nucleating a pure BCT phase at high fields and then lowering the field strength, BCO nucleates and grows directly in toggled fields. The lateral aspect ratio A_y of the BCO crystal can be tuned with the duty or the field strength. Figure 5.5 shows A_y for homogeneous BCO crystals assembled in Brownian dynamics simulations of $N = 100000$ conducting ($\beta = 1$) and insulating ($\beta = -1/2$) particles at volume fraction $\phi = 0.55$ and steady and toggled fields of various $\widetilde{E}_0$, ξ, and t_{off}. A_y was determined by identifying particles in the same plane orthogonal to the field and then computing the radial distribution function among particles in the same plane. The first two peaks correspond to the unit cell dimensions, L_x and L_y, orthogonal to the field. Also shown are theoretical predictions for A_y from locally minimizing (5.2) using our thermodynamic model.[142] At large $\sqrt{\xi}\widetilde{E}_0$, BCT crystal ($A_y = 1$) is always stable over BCO. The point where BCT transitions to BCO is close to the fluid/BCT/HCP eutectic line on the equilibrium phase diagram.[142] Below this BCO/BCT transition point, the aspect ratio of the BCO crystal decreases with decreasing $\sqrt{\xi}\widetilde{E}_0$, approaching $A_y = 1/\sqrt{3} \approx 0.58$ as $\sqrt{\xi}\widetilde{E}_0 \to 0$ which places field-aligned chains in a hexagonal arrangement, though this structure is metastable with respect to hard sphere FCC. While the BCO aspect ratio could be a function of $\widetilde{t}_{\text{off}}$, ξ, and $\widetilde{E}_0$ independently, we observe that only $\sqrt{\xi}\widetilde{E}_0$ controls A_y, and the data collapse to a single curve. In fact, the aspect ratio A_y from nucleation in a toggled field at ξ and $\widetilde{E}_0$ is identical to A_y from lattice deformations in a steady field of strength $\sqrt{\xi}\widetilde{E}_0$ and close to the theoretical predictions for metastable BCO. This is similar to fluid/fluid and fluid/BCT coexistences in Figure 5.4, where $\sqrt{\xi}\widetilde{E}_0$ dictated the PSSs assembled in toggled fields and corresponded to the steady field phase diagram. For a homogeneous phase however, there are not criteria like (5.1) that must be satisfied at PSS, yet the observed BCO structures at PSS are identical to the metastable BCO in steady fields of strength $\sqrt{\xi}\widetilde{E}_0$. We might hypothesize that *any* PSS assembled at a given $\widetilde{E}_0$, ξ, and t_{off} in toggled fields must be a metastable or stable state in steady fields of strength $\sqrt{\xi}\widetilde{E}_0$, even if the metastable state is not actually observed for steady fields. This would allow all PSSs to be described in terms of equilibrium thermodynamic expressions. This hypothesis requires further investigation but is supported by all data in this chapter.

To form a *thermodynamically stable* BCO phase with steady fields, additional interactions on top of dipolar interactions must be introduced. Polarizable particles that also have electrostatic repulsions due to a net charge can have a thermodynamically stable BCO phase.[61,206,207] However, two energy scales as well as an (screened) electrostatic length scale must be cooperatively engineered to favor BCO over other crystal phases. Toggled interactions offer a simpler route to a stable, transmutable BCO periodic-steady-state using a single energy scale $\sqrt{\xi}\widetilde{E}_0$ that can be robustly controlled.

The formation of BCO is one example where a complex crystal is assembled by toggling between two states that prefer simpler crystals, BCT and HCP/FCC. We believe this idea can be extended to form other exotic crystal structures by changing the two toggle states. That is, if a dispersion is engineered to switch between two states that prefer different, incommensurate crystal structures at equilibrium, the toggle parameters

can be optimized to assemble a third crystal by examining possible metastable structures predicted by appropriate time-averages of equilibrium equations of state. Because these switching states can, in principle, be any two states (*e.g.* two different types of interparticle attraction, two different orientations of the external field, *etc.*), we believe growth of many interesting structures may be possible *via* toggled assembly.

Conclusion

In this chapter, we investigated active self-assembly of polarizable colloidal particles in toggled electric/magnetic fields using Brownian dynamics simulations and thermodynamic theory. The toggling protocol offers a simple and easily controlled scheme for driving self-assembly of large, high-quality crystals at significantly faster rates and with many fewer defects than assembly in steady fields. The toggle parameters can be tuned to independently change the type of assembled structures and their growth mechanism. Phases that are only metastable in steady fields, including a dense fluid phase and body-centered-orthorhombic crystal, can be reliably assembled in toggled fields. In particular, the lattice parameters of the active BCO crystals can be continuously modulated with changes in the toggle duty cycle. Such transmutable crystals can be useful for sensing applications and as responsive materials capable of rapid changes in optical and mechanical properties. Though the dissipative nature of active assemblies preculdes a generic description in terms of statistical mechanics and equilibrium thermodynamics, we used linear irreversible thermodynamics to leverage thermodynamic calculations in steady fields to theoretically predict the periodic-steady-states in toggled fields. The data extracted from our simulations agree well with the theoretical predictions. We observe that the assembled periodic-steady-states in toggled fields are always selected from candidates that are at least metastable in steady fields. This suggests that all out-of-equilibrium assemblies in toggled fields can be described in terms of equilibrium thermodynamic expressions. These results will facilitate the design and operation of robust assembly processes for colloids and nanoparticles directed by toggled fields, offering a way to assemble complicated nanomaterials efficiently rather than relying on complex particle and/or process engineering.

Chapter 6

Enhanced Diffusion and Magnetophoresis of Paramagnetic Colloidal Particles in Rotating Magnetic Fields

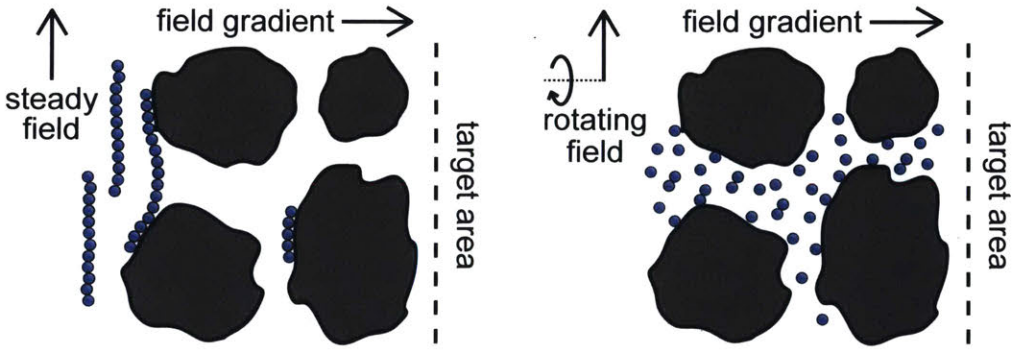

Figure 6.1: Schematic of magnetophoresis in steady (left) and rotating (right) fields through a porous material.

In the previous chapters we have discussed how electric and magnetic fields can faciliate self-assembly of structures of polarizable particles aligned with the field[61,202] as well as modulate their macroscopic material properties on-the-fly.[7,10,198] If the field is held steady in time, the dispersion can only respond by relaxing toward thermodynamic equilibrium, so its structure and dynamics are coupled. This coupling can be problematic when designing processes involving field-induced forces. For example, in Chapters 3 and 5, we saw that large interparticle dipolar forces that drive self-assembly of crystals also tend to cause kinetic arrest;[67,244] large field strengths that drive rapid magnetophoresis lead to particle aggregation that reduces mobility in porous media.[38] If energy is supplied to vary the field in time, the dispersion is driven out of equilibrium. Unlike its equilibrium counterpart, the dispersion structure and dynamics can be tuned independently and optimized for a target application.[37] Several types of field modulation have been investigated including toggling the field on and off,[64,65,67,68,73–75,244,245] which was the focus of Chapters 3 and 5, and switching the field's polarity,[62,86–88] but a particularly effective mode is rotating the field direction.[246] The dipolar interactions among particles drive them to align in the field direction, forming chains that rotate with the field. This has been used to enhance mixing at the micron scale,[93,94] amplify signals from biochemical sensors,[95–97] propel artificial microswimmers,[98–100] and assemble magnetic "conveyor-belts" to transport cargo.[101]

Many researchers have considered paramagnetic nanoparticles as a means to transport drugs and molecules for targeted therapeutic applications.[38,88,245,247] The nanoparticles can be localized to a specific site using magnetic field gradients to guide the particles magnetophoretically. In many cases, the target sites (*e.g.* tumor cells) are surrounded by dense, porous tissue through which the particles must navigate. It is advantageous to use large field strengths and large gradients to increase the flux of particles to the target site. If the field orientation is held steady during magnetophoresis, the dipole moments induced in the paramagnetic particles attract one another and the particles aggregate into long chains. The aggregate size can be much larger than the characteristic pore size, hindering the particles' mobility through the tissue or even preventing penetration into the tissue entirely. Soheilian, Erb, and coworkers proposed using rotating magnetic fields to suppress particle aggregation during magnetophoresis.[38] The dispersed nanoparticles fit within the pores and readily navigated the tortuous porous network in rotating fields, so the flux of particles was greatly enhanced over magnetophoresis with a steady field. Figure 6.1 illustrates these differences between magnetophoresis with steady and rotating fields. Understanding the transport of paramagnetic particles in rotating fields will facilitate their use for promising targeted therapeutic applications.

The case of individual chains at very dilute concentrations in a rotating field has been thoroughly investigated theoretically, computationally, and experimentally.[94,248–256] At low rotation frequencies, the chains rotate at the same frequency as the field, but lag behind it. The steady-state lag angle balances the magnetic torque driving rotation with the viscous torque opposing it.[248,252,253] The magnetic and viscous forces vary along the chain, causing the chain to adopt a slight "S" shape as it rotates.[253] As the rotation frequency increases, the viscous shear forces along the chain overpower the attractive intrachain dipolar forces holding the chain together. The chain can break up with increasing frequency to reduce its drag while still rotating synchronously at the field frequency,[249,250,257] or the chain can rotate asynchronously with the field and have complicated breakup and orbiting dynamics.[38,258–261]

Concentrated suspensions at very large rotation frequencies have also been investigated.[89–92,262–264] When the rotation frequency is much larger than the characteristic diffusion time of the particles, the particles experience an effectively steady interparticle potential. This interaction is isotropically attractive in the plain of rotation and repulsive out of the plane of rotation, and the functional form is identical to that of regular dipolar interactions of half-strength oriented out-of-plane, but with the sign of attractions and repulsions switched (*i.e* an "opposite" dipole interaction).[262] High-frequency rotating fields are especially effective at forming large, two-dimensional sheets of particles in experiments.[89,264] The complete phase diagram in high-frequency fields has been computed in simulations and reveals that the equilibrium phases are three-dimensional crystals.[90]

The dynamics and transport properties of concentrated dispersions of polarizable particles in rotating fields at intermediate frequencies have not been reported. Because many of the applications of such dispersions are governed by their out-of-equilibrium response to rotating fields, understanding the transport properties is crucial to effectively utilize rotating fields in practice. In this chapter, we use Brownian dynamics simulations with and without hydrodynamic interactions to investigate diffusion and magnetophoretic transport of a three-dimensional dispersion of spherical, polarizable particles driven by a two-dimensional rotating magnetic field. Though either magnetic or electric fields can be used for rotation, magnetic fields are more common in experiments because their effects on the dispersion are easier to control, as electric fields can generate unwanted currents, electroosmotic flows, and electrochemical reactions. In this simulation study, we interpret our results from the perspective of a magnetic field-driven experiment. However, the mathematical treatment of either class of experiments is identical, so our results can apply to both rotating magnetic and electric fields. First, we describe our simulation method which takes into account many-bodied, mutual polarization among the particles as well many-bodied, hydrodynamic interactions. Next, we describe the steady-state response of the dispersion as a function of various system parameters. We quantify the long-time self-diffusivity of the particles, which is enhanced in rotating fields over steady fields. Then, we compute the magnetophoretic mobility of the particles in the bulk and propose a simple model to calculate the mobility in porous media. Finally, we elucidate the effect of porous confinement on the diffusion and magnetophoretic transport in porous media.

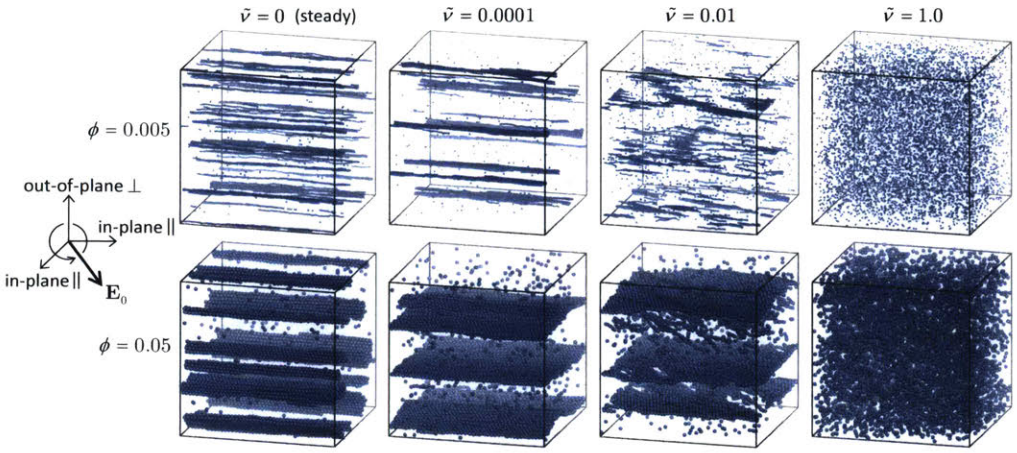

Figure 6.2: Snapshots from simulations of paramagnetic particles at two different volume fractions ϕ in steady and rotating fields of different frequencies $\tilde{\nu}$. For $\phi = 0.005$, the field strength pictured is $\tilde{E}_0 = 1.2$, and for $\phi = 0.05$, $\tilde{E}_0 = 1.0$.

6.1 Simulation Method

In this chapter, we use both the hydrodynamic (HI) model and the freely draining (FD) model detailed in Section 2.1 for the equations of motion and the mutual dipole model in Sections 2.2 and 4.1.2 for the magnetic forces. Unless the FD model is specifically referenced, assume the HI model is used for the simulations. We compute the set of particle velocities $\mathscr{U}$ from the set of particle forces $\mathscr{F}$ using the Rotne-Prager-Yamakawa grand mobility tensor $\mathscr{M}^H$ (2.8), *i.e.* $\mathscr{U} = \mathscr{M}^H \cdot \mathscr{F}$. The magnetic forces first require finding the set of unknown particle dipoles $\mathscr{S}$ by solving $\mathscr{E}_0 = \mathscr{M}^E \cdot \mathscr{S}$, where $\mathscr{E}_0$ is the set of external fields and $\mathscr{M}^E$ is the $\mathscr{M}^E_{ES}$ block of the grand potential tensor (2.74). Then, the set of magnetic forces is $\mathscr{F}^E = -\left(\nabla \mathscr{M}^E\right) : \mathscr{S}\mathscr{S}/2$.[142,154]

The external field rotates in the xy-plane with frequency ν

$$\mathbf{E}_0(t) = E_0 \left[\cos \omega t, \sin \omega t, 0\right], \tag{6.1}$$

where $E_0 \equiv |\mathbf{E}_0|$ is the field strength and $\omega \equiv 2\pi\nu$ is the angular frequency. We assume the rotation speed is small compared to time scales associated with magnetic relaxation within the particles so that the dispersion responds instantaneously to changes in the field. At each time step, the particle dipoles and forces are computed for the current orientation of the field.

This description for the magnetic interactions assumes the magnetization of a particle is linearly dependent on the local field. This is a good approximation for small field strengths, but the dipole moment eventually saturates to a finite value at large field strengths. Above the saturation field, the particles can no longer mutually polarize one another and a constant dipole model can be descriptive of the suspension. Such a model is not considered here, and we assume the field strength is small enough to be in the linear limit. The magnitude of the contrast parameter $|\beta|$, usually written as the susceptibility $\chi \equiv 3\beta$ for magnetic particles, controls how strong mutual polarization among particles is relative to the polarization due solely to the external field $\mathbf{H}_0$. This qualitatively changes the many-body description of the dispersion and has a substantial effect on the phase behavior.[142] Here, we focus on the limit of "perfectly susceptible" particles with $\chi = 3$ ($\beta = 1$) and $\lambda_p \to \infty$. This is the magnetic analogue to perfect electrical conductors. We could have picked an arbitrary χ value, but this limiting case at the maximum possible $|\chi|$ lets us easily probe the effects of mutual polarization. Real suspensions have $\chi < 3$, so mutual polarization is not as strong as those observed in our simulations. For perfectly susceptible particles, the force between a pair at contact and the dipole moments for a chain of particles in contact diverges if an infinite number of moments are accounted for.[145,265] It is possible to include this divergence with "lubrication-like" pairwise interactions.[145] However, this divergence is not realized in real systems because particles never come into true contact and

other surface forces dominate particle interactions on these short length scales. Because we only include dipole moments, all forces and dipoles are finite at contact. The interactions are regularized as the particles overlap, $r < 2a$, so that they remain solutions to the governing magnetostatic equations but stay finite as $r \to 0$.[142] From Chapter 4, the level of detail we have included in the simulations reproduces the phase behavior observed in experiments with steady fields.[142]

The natural nondimensionalization scheme scales lengths by the particle radius a, energies by the thermal energy k_BT, time by the bare diffusion time $\tau_D \equiv 6\pi\eta a^3/k_BT$, and external field by $\sqrt{k_BT/a^3\lambda_f}$. Other quantities are nondimensionalized by combinations of these four, such as dipoles scaled by $\sqrt{a^3\lambda_f k_BT}$ (*i.e.* $a^3\lambda_f$ times the field scale). A tilde is used to indicate the nondimensionalized version of a dimensional quantity, for example frequency $\widetilde{\nu} = \nu\tau_D$. We choose a time step of $\Delta\widetilde{t} = 10^{-3}$ for frequencies $\widetilde{\nu} \leq 10$, which is short enough to resolve dynamics within a single rotation. For higher frequencies $\widetilde{\nu} > 10$, we decrease the time step to $\Delta\widetilde{t} = 10^{-4}$. For all simulations, we use $N = 8000$ particles in a cubic, periodic simulation box. Limited testing with larger system sizes of $N = 64000$ did not change our results. We first thermalized the dispersion for $100\tau_D$ with no applied field to obtain a random configuration. The rotating field is then turned on, and the dispersion is allowed to equilibrate for $500 - 2500\tau_D$. Data is then collected and averaged over $100 - 2500\tau_D$. The wide range of simulation times was required for simulations at low frequencies, which needed long acquisition times to resolve full rotation cycles. Simulations at larger frequencies equilbrated quickly and only needed short data acquisition times. Snapshots depicting the simulation geometry and typical configurations are shown in Figure 6.2.

6.2 Steady-State

In a steady, nonrotating field, particles align and form chains in the direction of the applied field. At low field strengths $\widetilde{E}_0$ and volume fractions ϕ, there is an equilibrium distribution of chain lengths whose mean N_c increases as the field or volume fraction increases.[7] Because the particles mutually polarize each other as they chain, there is a distribution of dipole moments whose mean $\mathbf{S}$ also increases in magnitude $S \equiv |\mathbf{S}|$ with $\widetilde{E}_0$ and ϕ.[142] For sufficiently large field strengths and volume fractions, chain-chain interactions drive crystallization, and the dispersion reaches fluid/body-centered tetragonal (BCT) crystal coexistence.[142,222]

At sufficiently low densities and low field strengths, the chains are much shorter than the interchain distance, and the dispersion in rotating fields can be described by the well-studied single chain results.[94,248–256] For small rotation frequencies, the equilibrium distribution of chain lengths and dipole strengths in steady fields is not perturbed much, but the viscous drag on the chains causes them to lag behind the field by an angle θ. For a straight chain of length N_c and rotation frequency ν, the lag angle is that which balances the total magnetic torque driving the rotation, $\Gamma^E_{\text{tot}} = N_c\,|\mathbf{S} \times \mathbf{E}_0| \sim N_c \sin 2\theta$, with the hydrodynamic torque opposing it, $\Gamma^H_{\text{tot}} \sim \nu N_c^3$, and so the lag angle goes as $\sin 2\theta \sim \nu N_c^2$, increasing with rotation frequency.[253] Because the chain length and dipole strength are relatively constant, the magnetic torque increases with ν. As the frequency becomes too large, increasing the lag angle cannot provide enough magnetic torque to sustain the rotation. Instead, the chain breaks up to lower its hydrodynamic torque, so the magnetic torque attains a maximum value at intermediate frequencies around where chains begin to break up. This breakup hinders mutual polarization and the dipole strength S of each particle drops with rotation frequency.

At larger $\widetilde{E}_0$ and ϕ, several other factors complicate theoretical analysis. Chains of size N_c sweep out discs of radius aN_c, and interchain interactions become important when these discs overlap. Because N_c can become quite large as $\widetilde{E}_0$ and ϕ increase, especially for low frequencies, chain-chain interactions are important even at small volume fractions. Hydrodynamic flows generated within the dispersion as the chains rotate contribute additional shear forces that may affect chain break up. As chains bump into each other, they can break apart, reform, and assemble into different kinds of structures like platelets, sheets, and three-dimensional crystals (as seen in Figure 6.2), so even the concept of "rotating chains" may not be appropriate for many real dispersions in rotating fields.[89–91]

Figure 6.3 shows several steady-state quantities, the average cluster size N_c, the average dimensionless particle dipole strength $\widetilde{S} \equiv S/\sqrt{a^3\lambda_f k_BT}$, and the average dimensionless magnetic torque per particle

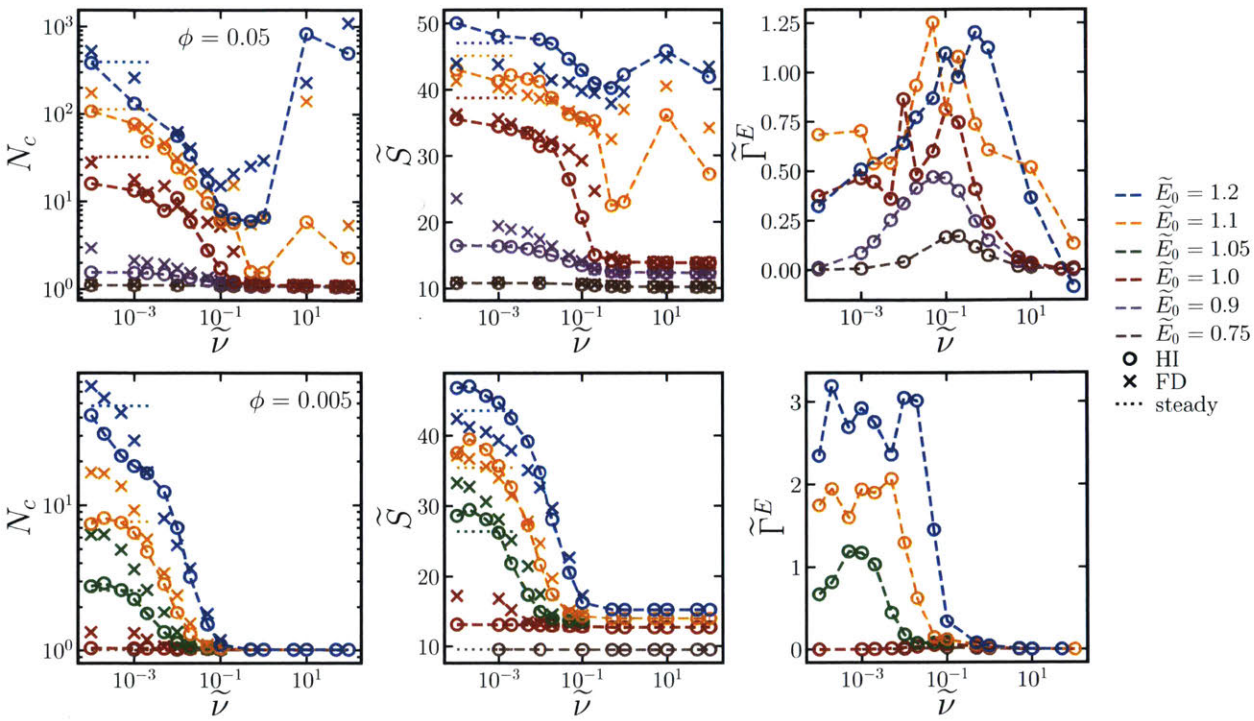

Figure 6.3: Average cluster size N_c (left column), average particle dipole $\widetilde{S}$ (middle column), and average magnetic torque per particle $\widetilde{\Gamma}^E$ (right column) as a function of rotation frequency $\widetilde{\nu}$ for two different volume fractions $\phi = 0.05$ (top row) and $\phi = 0.005$ (bottom row) and several different field strengths $\widetilde{E}_0$ (different colors). Circles correspond to simulations with long-ranged hydrodynamic interactions (HI) while crosses neglect these in the freely draining (FD) model. The values for steady fields (with HI) at $\widetilde{\nu} = 0$ are shown with dotted lines.

$\widetilde{\Gamma}^E \equiv \Gamma^E/k_BT \equiv \Gamma^E_{\text{tot}}/Nk_BT$ in dispersions with different volume fractions, field strengths, and rotation frequency. Particles were considered part of the same cluster if they were within a threshold distance of $2.1a$ of any other particle in the cluster, and then the cluster sizes were averaged over the set of observed clusters to obtain N_c. Γ^E was computed from the mean dipole $\mathbf{S}$ as $\Gamma^E = |\mathbf{S} \times \mathbf{E}_0|$. Note that this is the total magnetic torque on the entire dispersion normalized by the number of particles. An individual paramagnetic particle does not rotate due to this magnetic torque alone because the particle's induced magnetic moment rotates freely. At low field strengths ($\widetilde{E}_0 \leq 1.05$ for the dispersion at $\phi = 0.005$ and $\widetilde{E}_0 \leq 0.9$ for the dispersion at $\phi = 0.05$), the trends of the steady-state quantities are similar to the dilute, single chain trends discussed above. At higher field strengths, the complicated interchain interactions become important and the steady-state quantities are not described by the single-chain model. At very low frequencies, the rotation does not generate enough shear force to break chains apart, but rather helps chains "find" one another and facilitates the formation of platelets and crystalline sheets. In some cases, the mean cluster size is larger for the rotating fields than steady fields, where chains can only coalesce due to fluctuation- or defect-driven interactions, which aren't particularly long-ranged.[222,240] Thermodynamically, there is no preference for chains to coalesce in-plane or out-of-plane, but rotation enhances the rate of in-plane aggregation so the formation of platelets and sheets in the low frequency regime is a *kinetic* effect. These kinetic signatures were also observed in experiments of paramagnetic particles,[249] where the steady-state chain length was larger in low-frequency rotating fields than steady fields, as well as simulations of particles with *permanent* dipoles,[266] that formed large sheets similar to Figure 6.2 at low rotation frequencies. The dipole strength of crystalline configurations is significantly larger than that of chains for highly susceptible particles, so there are also cases where the dipole in rotating fields of low frequency is larger than that in steady fields.[142] These crystal platelets and sheets rotate with the field, which requires large magnetic torques, even at low frequencies. This can be avoided in experiments by using slightly incommensurate frequencies in a biaxial field setup[91] or a randomly fluctuating field orientation.[89] As the frequency increases, chains break up

before they coalesce in the plane of rotation, and the mean cluster size drops, accompanied by drops in the dipole strength and magnetic torque, suppressing aggregation altogether as $\widetilde{\nu}$ gets large. Because the high-frequency limit results in an effectively steady, "opposite dipole" interaction, aggregation can only be suppressed for field strengths below the crystal phase boundary, where there is a *thermodynamic* driving force for sheet formation.[90] The strength of the dipolar attractions decreases as the interactions become time-averaged. For a constant dipole model (no mutual polarization), the strength of the high-frequency attraction is exactly one-half of the strength of attractions in a steady field.[262] For mutual dipole models, the strength of the high-frequency attraction is even lower than one-half of the steady case, since anisotropy of the structures with the field in the steady case give a huge mutual polarization boost compared to the more isotropic configuration in the rotating case.[91,142] If the field is sufficiently large, particles form sheets and crystallize at any rotation frequency, owing to thermodynamic phase boundaries in the low-frequency (dipole) and high-frequency ("opposite dipole") limits, and particle aggregation cannot be prevented with rotation.

Figure 6.3 also compares the average cluster sizes in dispersions with long-ranged hydrodynamic interactions (HI) and those without (FD), where the drag on each particle is simply the Stokes drag. We find that the mean cluster size, average particle dipole, and magnetic torque are similar for both models, with the mean cluster size being a bit larger for the FD model at low frequencies. In the FD model, each particle in an aggregate feels Stokes drag, and the total drag of the aggregate goes as N_c, the number of particles in the aggregate, regardless of aggregate shape. With long-ranged III, the drag on an aggregate goes as $N_c^{1/d}$, where d is the aggregate's fractal dimension.[126,137,267] Solvent flows around the object, so particles on the interior of the aggregate feel little drag compared to those on the exterior. Because the particles align with the rotating field, the fractal dimension is close to $d \approx 1$, especially at early times, and the aggregates feel similar drag whether HI are included or not. Additionally, the solvent can reach each particle and the distribution of drag force along the aggregates is similar in both HI and FD models, so break up occurs at similar frequencies. Therefore, we expect the steady-state quantities to be similar whether or not HI are included, as observed in our simulations.

6.3 Diffusivity

On sufficiently long time scales, the motion of particles is diffusive and the mean squared displacement of a particle grows linearly in time,

$$\lim_{\tau\to\infty} \langle \mathbf{r}(\tau)\mathbf{r}(\tau)\rangle = 2\mathbf{D}_s^{\infty}\tau \tag{6.2}$$

where $\mathbf{r}(\tau) \equiv \mathbf{x}(t+\tau) - \mathbf{x}(t)$, τ is the lag time, $\langle\cdot\rangle$ indicates an ensemble average over particles and time, and $\mathbf{D}_s^{\infty}$ is the long time self-diffusivity tensor.[125] For lag times much larger than the period of rotation, $\tau \gg \nu^{-1}$, the two directions in the plane of rotation are equivalent as the field sweeps many revolutions within τ. Therefore, the self-diffusivity tensor is characterized with three quantities, the in-plane $D_{\parallel}$, out-of-plane $D_{\perp}$, and cross $D_{\parallel,\perp}$ long-time self-diffusivities

$$\left\langle r_{\parallel}^2(\tau)\right\rangle = 4D_{\parallel}\tau, \quad \langle r_{\perp}^2(\tau)\rangle = 2D_{\perp}\tau, \quad \langle (r_x(\tau)+r_y(\tau))r_z(\tau)\rangle = 4D_{\parallel,\perp}\tau, \tag{6.3}$$

where $r_{\parallel} \equiv \sqrt{r_x^2 + r_y^2}$ is the in-plane displacement and $r_{\perp} \equiv |r_z|$ is the out-of-plane displacement. It is convenient to consider these diffusivities relative to the Stokes-Einstein diffusivity $D_0 \equiv k_B T/6\pi\eta a$ of an isolated particle, $\widetilde{D}_{\parallel} \equiv D_{\parallel}/D_0$, $\widetilde{D}_{\perp} \equiv D_{\perp}/D_0$, $\widetilde{D}_{\parallel,\perp} \equiv D_{\parallel,\perp}/D_0$. We observe that the cross diffusivity $\widetilde{D}_{\parallel,\perp}$ is always very small, so diffusive motion in the plane of rotation is decoupled from diffusive motion out of plane, and only the diagonal elements of $\mathbf{D}_s^{\infty}$ are nonzero. Figure 6.4 shows $\widetilde{D}_{\parallel}$ and $\widetilde{D}_{\perp}$ for different volume fractions, field strengths, and rotation frequencies.

A particle's self-diffusivity is related to its drag γ^H (which is generally different than the Stokes drag γ) *via* the Einstein relation $D = k_B T/\gamma^H$. When particles are aggregated, their self-diffusivity is constrained by the self-diffusivity of the aggregate, which moves as a single unit. Because the fractal dimension is $d \approx 1$, the drag on aggregates increase linearly with their lengths, and the self-diffusivity of the particles is small.

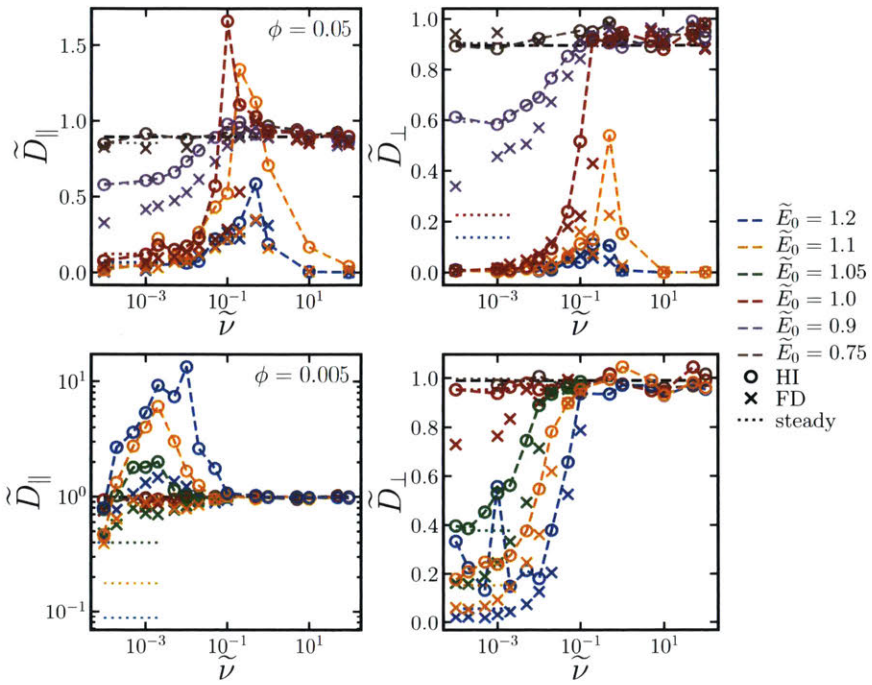

Figure 6.4: Long-time self-diffusivity in the plane of rotation $\widetilde{D}_{\parallel}$ (left column) and out of the plane of rotation $\widetilde{D}_{\perp}$ (right column) as a function of rotation frequency $\widetilde{\nu}$ for two different volume fractions $\phi = 0.05$ (top row) and $\phi = 0.005$ (bottom row) and several different field strengths $\widetilde{E}_0$ (different colors). Circles correspond to simulations with long-ranged hydrodynamic interactions (HI) while crosses neglect these in the freely draining (FD) model. The values for steady fields (with HI) at $\widetilde{\nu} = 0$ are shown with dotted lines. The theoretical prediction for hard spheres $D_0(1 - 2.1\phi)$ is shown with a black dashed line.

Figure 6.4 shows that, at low frequencies, both $\widetilde{D}_{\parallel}$ and $\widetilde{D}_{\perp}$ decrease as the field increases since the aggregate size increases with field. As chains break up in the rotating field, the aggregates become smaller and the self-diffusivity of the particles increases. Both $\widetilde{D}_{\parallel}$ and $\widetilde{D}_{\perp}$ increase as the rotation frequency increases. At large frequencies, both self-diffusivities approach the self-diffusivity of a hard sphere suspension, $D_0(1 - 2.1\phi)$ at small ϕ, which is a bit less than D_0 of an isolated particle due to hydrodynamic and steric interactions.[268,269] If the field strength is too large, significant crystallization occurs for all rotation frequencies, and the self-diffusivities are small and relatively independent of $\widetilde{\nu}$.

For intermediate field strengths, there is a maximum in $\widetilde{D}_{\parallel}$ at intermediate frequencies. Not only is the maximum $\widetilde{D}_{\parallel}$ larger than the hard sphere self-diffusivity at high rotation frequencies, it is also larger than $\widetilde{D}_0$. Thus, the rotating field facilitates faster diffusion for a range of frequencies. This diffusivity peak is observed for all volume fractions between $\phi = 0.005$ and $\phi = 0.05$. The frequency $\widetilde{\nu}^*$ at the peak $\widetilde{D}_{\parallel}^*$ is fairly independent of field strength for the field strengths investigated. Figure 6.5 shows that $\widetilde{\nu}^*$ increases as a power law with increasing ϕ, while $\widetilde{D}_{\parallel}^*$ decreases with ϕ. A power law fit yields $\widetilde{\nu}^* \sim \phi^{2.0}$, and the peak frequency is quadratic in volume fraction in at least the range $\phi = 0.005 - 0.05$. As the volume fraction increases, aggregation competes against diffusion, and the peak self-diffusivity $\widetilde{D}_{\parallel}^*$ drops as does the window where $\widetilde{D}_{\parallel} > D_0$. In fact, if ϕ or $\widetilde{E}_0$ become too large, bulk crystallization occurs and the diffusivity remains small for all rotation frequencies. The out-of-plane diffusivity does not have a maximum and increases monotonically to the hard-sphere result as frequency increases.

The scaling of $\nu^* \sim \phi^2$ can be explained by considering chains of N_c particles that sweep out disks of volume $V_d = 2a^3\pi N_c^2$ as they rotate. If there are $N_d = N/N_c$ of these disks, the disk volume fraction is $\phi_d = N_d V_d/V \sim N N_c/V \sim N_c\phi$, where $\phi = 4\pi a^3 N/3V$ is the particle volume fraction. From the balance of

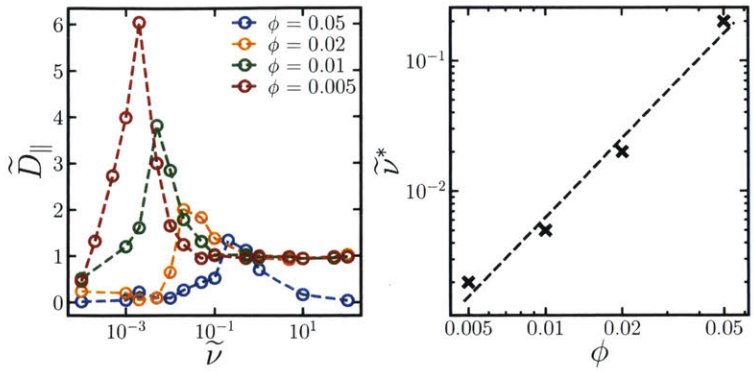

Figure 6.5: Long-time self-diffusivity in the plane of rotation $\widetilde{D}_{\parallel}$ (left) as a function of rotation frequency $\widetilde{\nu}$ for different volume fractions ϕ (different colors) at fixed $\widetilde{E}_0 = 1.1$, and the frequency $\widetilde{\nu}^*$ at the peak diffusivity (right) with a fit of $\widetilde{\nu}^* \sim \phi^{2.0}$.

magnetic and shear forces, the chain length decreases with frequency as $N_c \sim \nu^{-1/2}$,[249,253] so $\phi_d \sim \nu^{-1/2}\phi$. We hypothesize that the peak frequency occurs when $\phi_d \sim 1$, where the disks begin to overlap. Thus, the critical frequency goes as $\nu^* \sim \phi^2$, consistent with the scaling we observe in the simulations.

Enhanced diffusion above D_0 can have contributions from two sources, illustrated in Figure 6.6. First, the "interchain mechanism", aggregates can exchange particles as they break up and reform in the rotating field. Particles can "hop" from chain to chain and be shuttled along due to interparticle forces alone. Second, the "hydrodynamic mechanism", as the chains rotate they generate flow fields that entrain and move other particles around. Each chain functions as a magnetic "stir bar" that produces mixing flows in the dispersion. Figure 6.4 compares the diffusivities in dispersions with (HI) and without (FD) long-ranged hydrodynamic interactions. When hydrodynamic interactions are turned off, the diffusivity peak disappears and $\widetilde{D}_{\parallel}$ increases monotonically with $\widetilde{\nu}$ to the hard-sphere value at high frequencies. From the steady-state quantities in Figure 6.3, the structures in the two models are fairly similar, so the qualitative differences in diffusivities is not solely a result of differences in structure. Without HI, enhanced diffusion can only be due to the interchain mechanism, since the solvent flows in the hydrodynamic mechanism are absent. Even though particles in the FD model assemble into large rotating chains and platelets that strongly interact, this does not lead to fast diffusive transport. Because we do not observe enhanced diffusion when HI are turned off, we conclude that the enhanced diffusion above D_0 is due mainly to hydrodynamic mixing flows. As $\widetilde{\nu}$ increases, the aggregates rotate faster, increasing mixing, but they also break up and become smaller, decreasing mixing. Therefore, there is an optimal frequency range that balances these competing effects and yields the maximum in $\widetilde{D}_{\parallel}$ we observe in Figures 6.4 and 6.5. This mixing mechanism is consistent with experimental observations of enhanced *tracer* diffusion of noninteracting tracer particles in a dispersion with rotating paramagnetic chains.[93,94] Because the tracer particles are not magnetically responsive, enhanced diffusion above the tracer's Stokes-Einstein diffusivity is due solely to the hydrodynamic flow mechanism. Our results show that this is true even for *self*-diffusion of paramagnetic particles, whose motion due to solvent flows overpowers motion due to interparticle forces.

We observe that $\widetilde{D}_{\perp} \leq \widetilde{D}_{\parallel}$ for the entire field and frequency range. Particles have attractive interactions in the plane of rotation but purely repulsive interactions out of plane. Thus, particles tend to move more within the same plane parallel to the rotation than they do orthogonally to it. Additionally, hydrodynamic mixing flows mostly have the same orientation as the rotating field driving it, so these flows push particles around within the plane of rotation. Finally, the bare diffusivity of an isolated chain is larger in the direction of its long axis than in the orthogonal direction.[126] Because the long axis is always oriented in the plane of rotation, the bare chain diffusivity contributes more to in-plane motion than to out-of-plane motion.

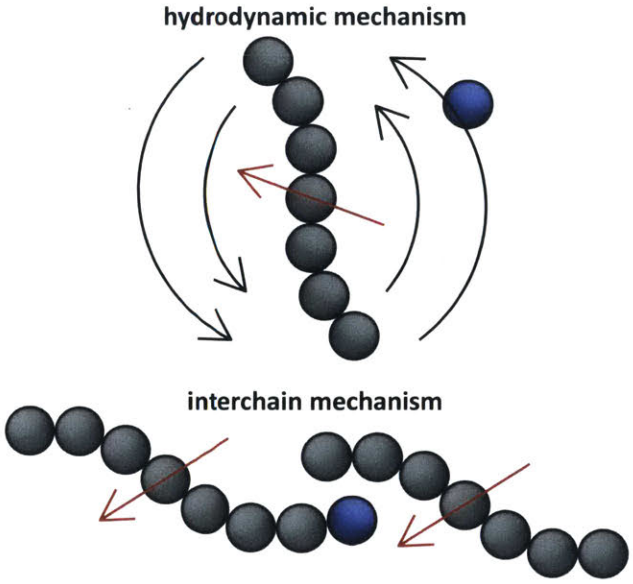

Figure 6.6: Two possible mechanisms for self-diffusion in rotating fields (red arrows). A tagged particle (blue) can move by the hydrodynamic flows (black arrows) generated by other particles (gray) or by interchain interactions.

6.4 Magnetophoretic Mobility

Polarizable particles will move in a nonuniform field *via* magnetophoresis. Here, we consider a rotating field with a small spatial gradient oriented arbitrarily. If the components of the applied field gradient $\nabla\mathbf{E}_0$ are small compared to E_0/a, the steady-state structure of the dispersion is only weakly perturbed by the magnetophoretic forces. In this case, the average phoretic velocity can be computed from the steady-state structure with no field gradient. The magnetophoretic force on a particle i, $\mathbf{F}_i^P$, is equal to the dot product of its dipole $\mathbf{S}_i$ with the field gradient, $\mathbf{F}_i^P = (\nabla\mathbf{E}_0)\cdot\mathbf{S}_i \equiv \mathbf{G}\left(\hat{\mathbf{E}}_0\cdot\mathbf{S}_i\right)$, where $\mathbf{G} = \nabla E_0$ and $\hat{\mathbf{E}}_0 \equiv \mathbf{E}_0/E_0$. Because the dispersion's structure and dipole moment are *induced* by the field and align with it, the absolute field direction is not important and only its magnitude matters. We do not need to consider the field gradient tensor $\nabla\mathbf{E}_0$, which has both the field and gradient directions, but rather the field gradient vector $\mathbf{G} = \nabla E_0$, which has only the gradient direction and the field magnitude. Note that this would not be true for an arbitrary, *permanent* structure or dipole in a field gradient, for which both the field direction and the gradient direction matter.

The dipoles are determined from the steady-state configuration at zero field gradient by computing $\mathscr{S} = \mathscr{C}\cdot\mathscr{E}_0$, and the set of phoretic forces $\mathscr{F}^P \equiv [\mathbf{F}_1^P, \mathbf{F}_2^P, \ldots, \mathbf{F}_N^P]^T = \mathbf{G}(\mathscr{S}\cdot\hat{\mathbf{E}}_0)$ produce velocities $\mathscr{U} = \mathscr{M}^H\cdot\mathscr{F}^P$. The average phoretic velocity $\mathbf{u} \equiv \boldsymbol{\Sigma}\cdot\mathscr{U} \equiv \sum_i \mathbf{u}_i/N$, where $\boldsymbol{\Sigma}$ is a summation tensor, can then be written as

$$\mathbf{u} = \mathbf{M}^P\cdot\mathbf{G}, \quad \mathbf{M}^P \equiv \boldsymbol{\Sigma}\cdot\mathscr{M}^H\cdot\mathscr{S}\cdot\hat{\mathbf{E}}_0 \tag{6.4}$$

where the magnetophoretic mobility $\mathbf{M}^P$ is a 2-tensor whose elements M_{ij}^P couple the gradient in direction j to the velocity in direction i. For an isolated particle, the dipole is $\mathbf{m} = 4\pi a^3\lambda_f\beta\mathbf{E}_0$ and the hydrodynamic mobility tensor is $\mathbf{M}^H = \mathbf{I}/6\pi a\eta$, so the magnetophoretic mobility is $\mathbf{M}_0^P = 2a^2\mu_f\beta E_0\mathbf{I}/3\eta \equiv M_0\mathbf{I}$, or in dimensionless terms $\widetilde{\mathbf{M}}_0^P = 4\pi\beta\widetilde{E}_0\mathbf{I} \equiv \widetilde{M}_0\mathbf{I}$. M_0 increases with both β and E_0, and, unlike $\widetilde{D}_0$, $\widetilde{M}_0$ is not normalized to 1 in our choice of dimensionless units.

In the rotating field, the field gradient $\mathbf{G}$ can point either in the plane of rotation or out of plane. We observe that the gradient in-plane does not produce an appreciable velocity out of plane and vice-versa, so $\mathbf{M}^P$ only has two non-zero, diagonal elements, $M_\parallel^P$ and $M_\perp^P$, like the self-diffusivity

$$u_\parallel = M_\parallel^P G_\parallel, \quad u_\perp = M_\perp^P G_\perp \tag{6.5}$$

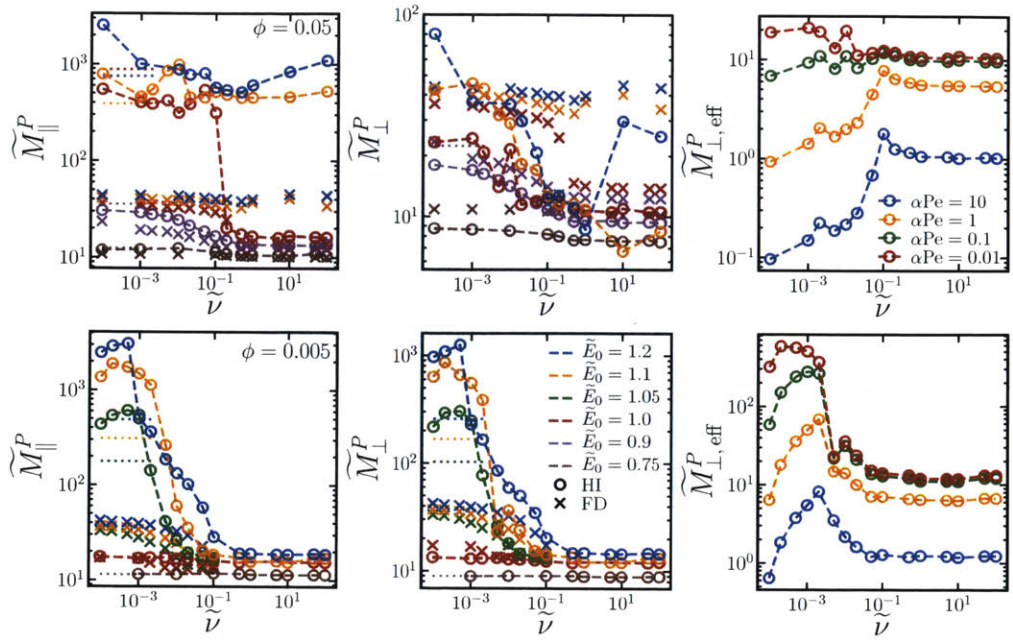

Figure 6.7: Small-gradient magnetophoretic mobility in the plane of rotation $\widetilde{M}_{\parallel}^{P}$ (left column) and out of the plane of rotation $\widetilde{M}_{\perp}^{P}$ (middle column) as a function of rotation frequency $\widetilde{\nu}$ for two different volume fractions $\phi = 0.05$ (top row) and $\phi = 0.005$ (bottom row) and several different field strengths $\widetilde{E}_0$ (different colors). Circles correspond to simulations with long-ranged hydrodynamic interactions (HI) while crosses neglect these in the freely draining (FD) model. The values for steady fields (with HI) at $\widetilde{\nu} = 0$ are shown with dotted lines. The effective out-of-plane magnetophoretic mobility in porous media $\widetilde{M}_{\perp,\mathrm{eff}}^{P}$ (right column) at $\widetilde{E}_0 = 1.0$ (top) and $\widetilde{E}_0 = 1.1$ (bottom) for different values of $\alpha\mathrm{Pe}$ (different colors) from equation (6.6).

Figure 6.7 shows the magnetophoretic mobility as a function of field strength and rotation frequency for both the HI and FD models. Both the in-plane and out-of-plane mobilities decrease as rotation frequency increases, approaching a value slightly larger than $\widetilde{M}_0$ at large $\widetilde{\nu}$ due to mutual polarization. Because the hydrodynamic mobility tensor is isotropic for the FD model, both $\widetilde{M}_{\perp}^{P} = \widetilde{M}_{\parallel}^{P}$. For the HI model however, like the self-diffusivities, $\widetilde{M}_{\perp}^{P} \leq \widetilde{M}_{\parallel}^{P}$ for the entire field and frequency range due to increased drag in the direction orthogonal to the field. When particles are aggregated, the magnetophoretic force on each particle contributes to the total magnetophoretic force on the aggregate, $F^P \sim N_c$. The drag on the aggregate only scales with the aggregate's characteristic length $F^P \sim N^{1/d}$.[126,137,267] In the limiting case where the particles aggregate into chains with fractal dimension $d = 1$, it would seem like these effects should cancel out as the chains break up with increasing rotation frequency, and the magnetophoretic mobility should remain constant. However, the dipole strength, which contributes to the magnetophoretic force, decreases as the aggregates break up. Additionally, because the magnetophoretic forces on each particle are oriented in the same direction, the hydrodynamic flows from each particle in an aggregate entrain the others and decrease the drag on the aggregate. This particular drag-reduction mode is very strong for our hydrodynamic model, which treats each particle as an isolated point force and point quadrupole. If an aggregate is treated as a rigid collection of particles constrained to move together, which may be appropriate given the strong interparticle forces, the rigidity constraints significantly increase the drag, so the drag reduction may not be quite so dramatic.[42,171] Such a refined hydrodynamic model was not implemented here. If the particles form platelets and sheets ($d \approx 2$) or crystals ($d \approx 3$), the mobility decreases even faster as the aggregates break up, with the rate increasing the larger the fractal dimension. Compared to the FD model, where the drag on each particle is constant, the in-plane mobilities are significantly larger in the HI model. At low volume fractions, the out-of-plane mobility is also larger for the HI model, but fall below the values for the FD model at larger volume fractions. These effects cause the magnetophoretic mobility to decrease with increasing frequency and decreasing field. Therefore, in the bulk, particles can generally be magnetophoretically transported more

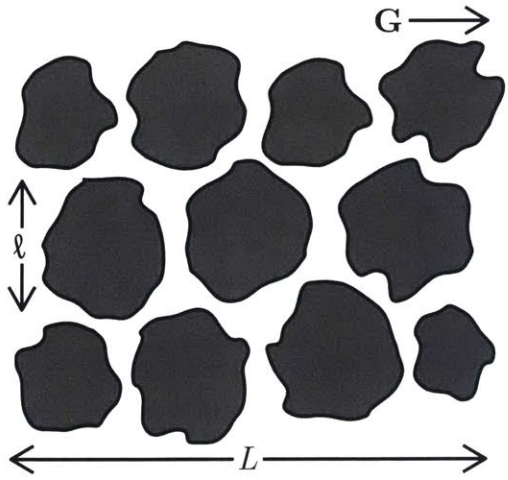

Figure 6.8: Schematic of magnetophoresis in a field gradient **G** through a model porous material of length L composed of obstacles of size ℓ.

quickly in steady fields than in rotating fields.

This is not necessarily the case in porous media, as illustrated in Figure 6.1. Soheilian, Erb, and coworkers showed that the magnetophoretic flux of paramagnetic colloids through synthetic porous tissue in steady fields was smaller than that in rotating fields.[38] The large aggregates formed in steady fields had difficultly navigating the small tortuous pores, while aggregation was suppressed in rotating fields allowing individual particles to more easily pass through the porous network. We can derive a simple phenomenological model to explain this observation. Consider a porous material of length L illustrated in Figure 6.8. In a gradient of strength $G_\perp$ oriented out of the plane of rotation, the particles can travel that distance magnetophoretically in a minimum time $t = L/u_\perp$, where $u_\perp = M_\perp^P G_\perp$ is the magnetophoretic velocity in the bulk. However, because the porous material is tortuous, particles cannot move straight through the material. We imagine that, as particles travel phoretically in the gradient direction, they run into obstacles of characteristic length ℓ. Because the phoretic force is directed toward an obstacle, the only way the particle can get around it is diffusively, which takes a time $t = \ell^2/D_\parallel$. The relevant diffusivity is $D_\parallel$, as diffusion is taking place orthogonally to the out-of-plane gradient. Diffusion in the gradient direction $D_\perp$ does not help traverse the obstacle because it is directed towards and away from the obstacle and is usually negligible compared to the phoretic forces. If there are N such obstacles across the length L, the total time to traverse the porous material is $t = L/u_\perp + N\ell^2/D_\parallel$. Thus, the effective phoretic velocity through the porous material is $u_{\perp,\text{eff}} = u_\perp/(1 + N\ell^2 u_\perp/LD_\parallel)$. If the gradient is directed in the plane of rotation instead, the relevant phoretic velocity is $u_\parallel$ while the relevant diffusivity is $D_\perp$, and the effective phoretic velocity is $u_{\parallel,\text{eff}} = u_\parallel/(1 + N\ell^2 u_\parallel/LD_\perp)$. Therefore, the effective magnetophoretic mobility in the porous material is

$$M_{\perp,\text{eff}}^P = \frac{M_\perp^P}{1 + \alpha\,\text{Pe}\,(M_\perp^P/M_0)(D_0/D_\parallel)}, \quad M_{\parallel,\text{eff}}^P = \frac{M_\parallel^P}{1 + \alpha\,\text{Pe}\,(M_\parallel^P/M_0)(D_0/D_\perp)}, \tag{6.6}$$

where $\alpha \equiv N\ell/L$ is a dimensionless function of the tortuosity and porosity of the porous network (through N/L and ℓ) and the Péclet number $\text{Pe} \equiv \ell M_0 G/D_0$ depends on the field strength (through M_0) and the field gradient. Figure 6.7 shows the effective mobility in porous materials of different αPe as a function of $\tilde{\nu}$. If the porous material has high porosity and low tortuousity, there are very few, small obstacles and α is small. Particles do not need to diffuse much in the direction orthogonal to the field and can pass nearly straight through the porous network phoretically, so (6.6) simplifies to $M_{i,\text{eff}}^P \approx M_i^P$. The Péclet number is small if the gradient or field is weak. In this case, for any pore geometry, diffusion around obstacles is fast compared to magnetophoresis in the gradient direction, so transport is limited by magnetophoresis and again (6.6) simplifies to $M_{i,\text{eff}}^P \approx M_i^P$. In this latter case, diffusion in the gradient direction may become important, and a more complicated model might be needed. Because both $M_\parallel^P$ and $M_\perp^P$ decrease with increasing ν, the effective porous mobility in steady fields is larger than that in rotating fields and decreases with ν. For

porous networks with low porosity and high tortuousity in strong fields and field gradients, $\alpha\mathrm{Pe}$ is large and diffusion orthogonal to the gradient dominates the transport, so (6.6) reduces to $M^P_{i,\mathrm{eff}} \approx D_i M_0/\alpha\mathrm{Pe}\, D_0$. Both $D_\parallel$ and $D_\perp$ increase with ν, and the phoretic velocity through porous material in rotating fields is larger than in steady fields. In fact, because $\widetilde{D}_\parallel$ has a maximum at intermediate rotation frequency, so does $M^P_{\perp,\mathrm{eff}}$ at small $\alpha\mathrm{Pe}$, and the fastest transport through porous media occurs at intermediate frequencies. These trends are consistent with the experimental results of Soheilian *et. al.* of magnetophoresis through porous media in rotating fields, so it is possible their experiments live in the large $\alpha\mathrm{Pe}$ regime.[38] This kind of model was also used to explain enhanced diffusion of charged species through porous media in rotating electric fields compared to steady fields.[102] In that case, the electrophoretic driving force changed direction over time allowing the charged species to navigate around obstacles phoretically. This is similar, but of a different nature, than our setup here, where the magnetophoretic driving force (*i.e* the field gradient) is constant in time, and particles navigate around obstacles diffusively with a diffusivity enhanced by the rotating field.

This simple model does not consider the effects of the pore walls on the magnetophoretic mobility. Steric interactions, for example, can prevent aggregates from entering the pores at all if the pore size is smaller than the aggregate size, and the flux through the material will be smaller than expected,[38] as in Figure 6.1. Hydrodynamic interactions with the wall tend to slow both diffusive and phoretic motion of particles as the confining walls get closer together.[270,271] Thermodynamic interactions with the wall (*e.g.* van der Waals, electrostatic, hydrophobic/philic) modify particle motion, with attractions tending to hinder particle travel through pores. Amin *et. al.* showed *in vivo* that paramagnetic particles aggregated and stuck to vessel walls in mice during magnetophoresis in steady fields leading to poor transport.[88] This could be suppressed by flipping the direction of the applied field gradient in time to detach particles from walls and increase the transport rate, a different but analogous strategy to the setup discussed here. Finally, modes of transport through walls, like endocytosis which is particularly important for transport in biological systems, are not considered here but can be enhanced using time-dependent fields to suppress particle aggregation during magnetophoresis.[245]

As a first attempt to understand these wall effects, we simulated dispersions in a rigid cage scaffold of pore size h, depicted in Figure 6.9, as a simple model for transport in a porous material exposed to rotating fields with no field gradient. Because the channels through the cage are straight, the cage has very low tortuousity and does not look like the model in Figure 6.8 we proposed to derive equation (6.6). However, the cage is simple with a single defining parameter, the pore size h, and allows us to examine the effect of confinement on the transport properties. To observe the dynamics in (6.6), we would need to apply a field gradient and simulate magnetophoresis directly, which is beyond the scope of this work. The cage is composed of beads of the same size as the paramagnetic particles, rigidly constrained together. The cage is fixed in place and its walls interact sterically and hydrodynamically with the particles, with no other cage/particle interactions (*e.g.* magnetic dipole, attractions, *etc.*). A modification to our hydrodynamic model is needed to ensure the particles composing the cage remain rigidly constrained, which is discussed in detail elsewhere.[42,169,171] Like our previous bulk calculations, we computed the long-time self diffusivity from the mean-squared displacement (6.3) and the low-gradient magnetophoretic mobility from equation (6.4), both shown in Figure 6.9.

As expected, both $\widetilde{D}_\parallel$ and $\widetilde{M}^P_\perp$ decrease with decreasing pore size due to steric and hydrodynamic hinderance from the walls. The trends in $\widetilde{D}_\parallel$ and $\widetilde{M}^P_\perp$ with rotation frequency ν remain the same as the bulk trends for all pore sizes. The out-of-plane magnetophoretic mobility decreases with rotation frequency, while the in-plane diffusivity increases with frequency until it reaches a maximum value. $\widetilde{D}_\perp$ and $\widetilde{M}^P_\parallel$ (not shown) also follow the same trends as the bulk for all pore sizes. Because these transport quantities take into account wall effects, they may be the appropriate ones to use in equation (6.6) for porous media with pore size ℓ. Because confinement does not qualitatively change the trends in $\widetilde{D}_i$ and $\widetilde{M}^P_i$, our earlier analysis for the effective porous mobility $\widetilde{M}^P_{i,\mathrm{eff}}$ using bulk values for $\widetilde{D}_i$ and $\widetilde{M}^P_i$ still holds. In particular, the effective magnetophoretic mobility in porous media of low porosity and high tortuousity (large α) is larger in rotating fields than that in steady fields.

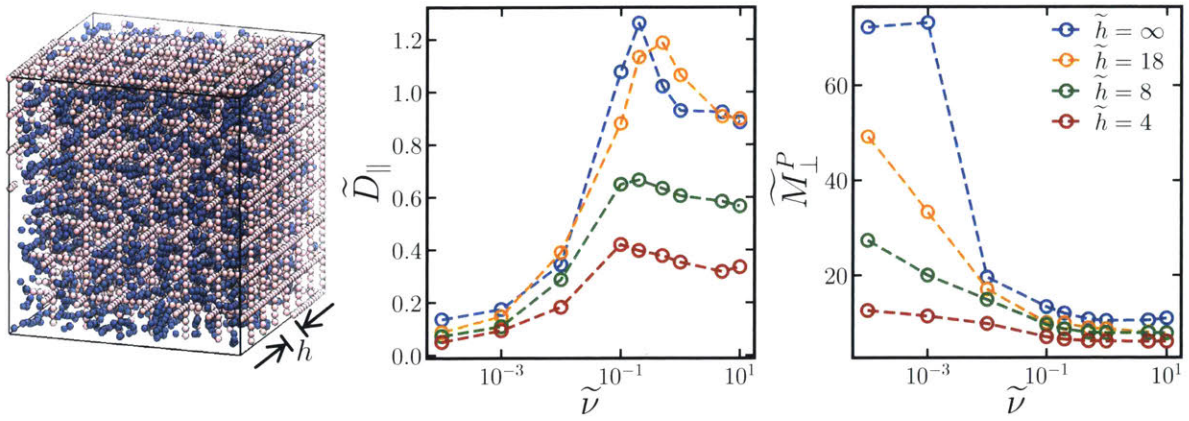

Figure 6.9: (Left) Snapshot of simulation of paramagnetic colloids (blue) in a rigid scaffold (pink) of pore size $\widetilde{h} \equiv h/a$ (measured from the edges of the scaffold particles) exposed to a rotating magnetic field of the same orientation as in Figure 6.2. The long-time, in-plane self-diffusivity $\widetilde{D}_{\parallel}$ (middle) and low-gradient, out-of-plane magnetophoretic mobility $\widetilde{M}_{\perp}^{P}$ (right) as a function of rotation frequency $\widetilde{\nu}$ at a field strength $\widetilde{E}_0 = 1.0$ for different pore sizes (different colors).

Our results for the the steady-state and transport quantities in the bulk and under confinement, along with our simple expressions (6.6) for transport in porous media, can help to optimize particle transport in experimental applications. We investigated how changing three main parameters, the field strength E_0, rotation frequency ν, and volume fraction ϕ, affected particle transport in rotating magnetic fields. For example, increasing E_0 generally increases the magnetophoretic mobility (Figure 6.7). However, if E_0 is too high, particle aggregation cannot be suppressed with rotation and the effective mobility $M_{i,\text{eff}}^{P}$ through porous media is low. This is especially important when considering steric interactions with pore walls, because particles may not enter the pores at all if the aggregate size is larger than the pore size, as in Figure 6.1. The optimal field strength to maximize particle flux through porous materials should lie just below the crystallization boundary, which decreases with ϕ. For small, tortuous pores where transport is diffusion-limited, the flux can be maximized at intermediate ν for which $D_{\parallel}$ has a maximum (Figure 6.4). The frequency at the peak diffusivity scales as $\widetilde{\nu}^* \sim \phi^2$ (Figure 6.5). The larger ϕ, the more particles there are to contribute to the flux, but $D_{\parallel}$ decreases with ϕ. The window of frequencies where enhance diffusion is observed shrinks as ϕ increases, so finding this window experimentally at large ϕ might be challenging. Intermediate field strengths and frequencies, where aggregates have broken up sufficiently to enter pores while retaining enhanced diffusion above D_0 are ideal for magnetophoresis through porous media. The dynamics in this regime are complicated, and experiments have shown transient chaos in particle motion at intermediate frequencies.[261] This time-dependent chaos could have important effects on particle transport that aren't incorporated into our analysis. In any case, the magnetophoretic flux through porous media in rotating fields can be optimized at intermediate $\widetilde{E}_0$, $\widetilde{\nu}$, and ϕ. Such an optimization is predicted in the effective mobility calculations in Figure 6.7. For certain $\alpha\,\text{Pe}$ regimes in porous materials, we have identified some ϕ, $\widetilde{E}_0$, and $\widetilde{\nu}$ that can yield around 2–10-fold increases in the magnetophoretic flux in rotating fields over steady fields. This is consistent with the enhancement observed in experiments.[38]

Conclusion

Because rotating magnetic fields drive paramagnetic colloids and nanoparticles out of equilibrium, they can overcome many of the challenges associated with assembling and transporting particles in steady fields. However, fundamental transport properties of particles in rotating fields, crucial to dictating responses to the time-varying field, had not been characterized in terms of experimental parameters. In this work, we used Brownian dynamics simulations to study dispersions of paramagnetic colloids in rotating magnetic fields. The simulations included both many-bodied long-ranged hydrodynamic interactions as well as many-bodied

mutual polarization among particles. We found that, in the bulk, both the self-diffusivities in plane and out of plane of the rotation increase with rotation frequency as particle aggregation is suppressed. The in-plane diffusivity has a maximum at intermediate frequencies above the Stokes-Einstein diffusivity of an isolated particle. Thus, the rotation frequency can be optimized to enhance self-mixing. Although the magnetophoretic mobility in the bulk is larger for steady fields than in rotating fields, we derived a simple phenomenological model for the effective magnetophoretic mobility in porous media that shows the mobility is larger in rotating fields than in steady fields for porous media of large tortuousity and low porosity. The model requires only bulk transport properties and physical characteristics of the porous geometry and can be used to maximize magnetophoretic transport through porous materials. Finally, we examined the effect of porous confinement on the transport quantities and found no qualitative difference in their trends with respect to rotation frequency. Our results can be leveraged to design and implement efficient transport processes in rotating magnetic fields.

Chapter 7

Nonlinear Electrokinetic Transport of Colloids in Electrolytes

Many technologies take advantage of electrokinetic phenomena for transport at the microscale. Colloidal particles, polymers, cells, and proteins can be moved directly in electric fields *via* electrophoresis if they have a net charge[125,272,273] or in electric field gradients *via* dielectrophresis if they have net dipole moment.[274] Electric fields can also be used to generate electroosmotic flows in electrolyte solutions with dissolved ions, which can become quite large even at modest field strengths.[87,275,276] Typical models of these transport phenomena treat the charges on surfaces as *fixed*, and ions distribute themselves into an electric double layer around the charged surfaces. Electrokinetic formulae have been derived for the electrophoretic velocity of a charged spherical colloid or the electroosmotic velocity of a fluid above a charged wall using this approach.[125,277,278]

Highly conductive particles polarize in the presence of electric fields, acquiring a nonuniform *induced* surface charge distribution in addition to its fixed charge distribution. Positive ions are drawn toward the negative induced charges while negative ions are drawn toward the positive induced charges, so the surrounding ion cloud also polarizes, like in Figure 7.1. As the ions accumulate near the particle surface they induce additional surface charge in the particle (which draws in more ions, *etc.*), and the particle and double layer "charge up", increasing their induced dipole moments over time. This generates a quadrupolar flow field in the surrounding fluid. Squires and Bazant developed an electrokinetic theory to describe the charging dynamics for this "induced-charge electroosmosis" (ICEO) phenomenon.[279,280] If a net charge is added to the particle, the particle translates in the field due to "induced-charge electrophoresis" (ICEP), in addition to charging up due to ICEO. Many experiments have leveraged ICEO and ICEP to generate large flows at micron scales for microfluidic and lab-on-a-chip applications.[87,275,276]

Because of differences in the double layer structure, particles behave differently in ICEO and ICEP than they do in classical electrophoresis. The net dipole moment of the ion cloud is oriented in the opposite direction of the applied electric field. The accumulated negative ions (next to the positive induced charge) want to slip past the particle to travel opposite the field, while the accumulated positive ions (next to the negative induced charge) want to slip past the particle to travel with the field. If the applied electric field is above a critical field strength E_c, the orientation of the polarized double layer becomes unstable, and small fluctuations drive uncharged spherical colloids to break symmetry and spontaneously rotate about a random axis orthogonal to the applied field, a phenomenon called Quincke rotation.[105] A snapshot of a particle undergoing Quincke rotation is shown in Figure 7.1. Quincke rotors have been used to power motors,[281–284] reduce the viscosity of electrorheological fluids,[107,285,286] and generate fluid flows at the micron scale.[287] Particles undergoing Quincke rotation near boundaries roll along them, and Quincke rollers have been used for active matter applications.[288,289]

In this chapter we describe a new mode of electrokinetic transport of colloidal particles. Above E_c, a *charged* particle undergoes both induced-charged electrophoresis and Quincke rotation. We have discovered that these motions couple together to propel the particle in a direction orthogonal to both the driving electric

field and the axis of rotation, shown in Figure 7.1. This is an electrohydrodynamic analogue to the Magnus effect at larger Reynolds number, where a simultaneously translating and rotating object experiences a lift force that pushes it in a direction orthogonal to its main translation direction.[290] Motion orthogonal to a driving field requires some break in symmetry to drive particles off their preferred direction.[291] For example, particles with anisotropic shape can move in complicated paths *via* induced-charge electrophoresis.[104,292] Particles with anisotropic dielectric properties, like Janus particles with both insulating and conducting faces, move orthogonally to an electric field.[293] Particles can roll along walls or in racheted microchannels due to contact-charge electrophoresis.[294,295] In all these cases, anisotropy is specifically engineered into the dispersion to induce orthogonal motion. In contrast, the electrohydrodynamic Magnus effect occurs in the bulk for isotropic spherical particles, with the Quincke rotation instability providing broken symmetry driving orthogonal motion. Because of this the electrohydrodynamic Magnus effect can be leveraged to create bulk, three-dimensional active matter dispersions as well as for particle separation applications.

To utilize the electrohydrodnamic Magnus (EHM) effect in experiments, it is crucial to have a fundamental understanding of the underlying physics governing the phenomenon. In this chapter, we investigate the EHM effect using simulations and continuum theory. First, we recapitulate the theory of Squires and Bazant for induced-charge electrophoresis of a nonrotating particle in an electric field. We extend their model to account for nonlinearities in the description of ions for large zeta potentials and concentrations. Next, we adapt the ICEP model for rotating particles and derive an electrokinetic theory for Quincke rotation. This theory predicts a Magnus velocity for charged particles undergoing Quincke rotation above a critical field. The critical field strength, direction of motion, and magnitude of the Magnus velocity are in reasonable agreement with our simulations. The Magnus velocity persists over many cycles in an alternating-current (AC) electric field. We propose the electrohydrodynamic Magnus effect in AC fields as a mechanism for generating active matter dispersions of isotropic, spherical, polarizable particles in bulk electrolytes. The EHM "swimmers" behave as active Brownian particles, and the field strength and frequency control their activity. We leverage our continuum theory to show how the activity varies as a function of these parameters and predict an effective active diffusion constant that is orders of magnitude larger than the Stokes-Einstein diffusivity.

In this chapter, we consider a single, perfectly conducting particle of radius a and uniform fixed surface charge density q_0 in an electrolyte composed of positive and negative ions of charge $\pm q_i$ and radius a_i, each at number density n_i, dispersed in a fluid of permittivity ε_f and viscosity η.* We choose the ion radius a_i as the hydrodynamic radius of the solvated ion and assume it coincides with a thermodynamic hard sphere radius, which is around 0.4 nm for simple salts.[162] As discussed in Section 2.2, the simulations use a set of dimensionless variables, indicated by tilde. A set of dimensionless units can be constructed by setting the dimensionless versions of the following values to unity: the ion radius a_i, the thermal energy k_BT, the ion drag coefficient $\gamma_i \equiv 6\pi\eta a_i$, and the fluid permittivity ε_f. This sets a_i to be the length scale, k_BT to be the energy scale, the ion diffusion time $\tau_D \equiv k_BT/6\pi\eta a_i^3$ to be the time scale, and $\sqrt{\varepsilon_f a_i k_B T}$ to be the charge scale. With typical values for water at room temperature, $\tau_D \approx 1\,\text{ns}$ and $\sqrt{\varepsilon_f a_i k_B T} \approx 0.2e^-$, where e^- is the charge of an electron. In all of our simulations, we set the total volume fraction of ions (cations + anions) to $\phi_i = 0.10$ and the characteristic ion-ion Coulomb energy at contact,

$$\varepsilon \equiv \frac{q_i^2}{8\pi\varepsilon_f a_i k_B T} = 1 \tag{7.1}$$

which yields a charge of around $\widetilde{q}_i \approx 5$. For typical dimensional values, the salt concentration is around 300 mM and the ion charge is $q_i \approx e^- = 1.60 \times 10^{-19}\,\text{C}$, *i.e.* monovalent ions.

7.1 Induced-Charge Electrophoresis

Consider an uncharged, conducting particle suddenly exposed to an external field $\mathbf{E}_0$. The particle polarizes and acquires an initial induced surface charge distribution $q_{\text{init}}(\theta,\phi) = 3\varepsilon_f E_0 \cos\theta$, corresponding to a dipole

*Here, we use the i subscript to reference quantities pertaining generically to the *ions* (i short for ions). For example, the charge of the positive ions q_+ is $q_+ \equiv q_i$, and the charge of the negative ions q_- is $q_- \equiv -q_i$. i is *not* meant to be a dummy index that can take on the values + or −.

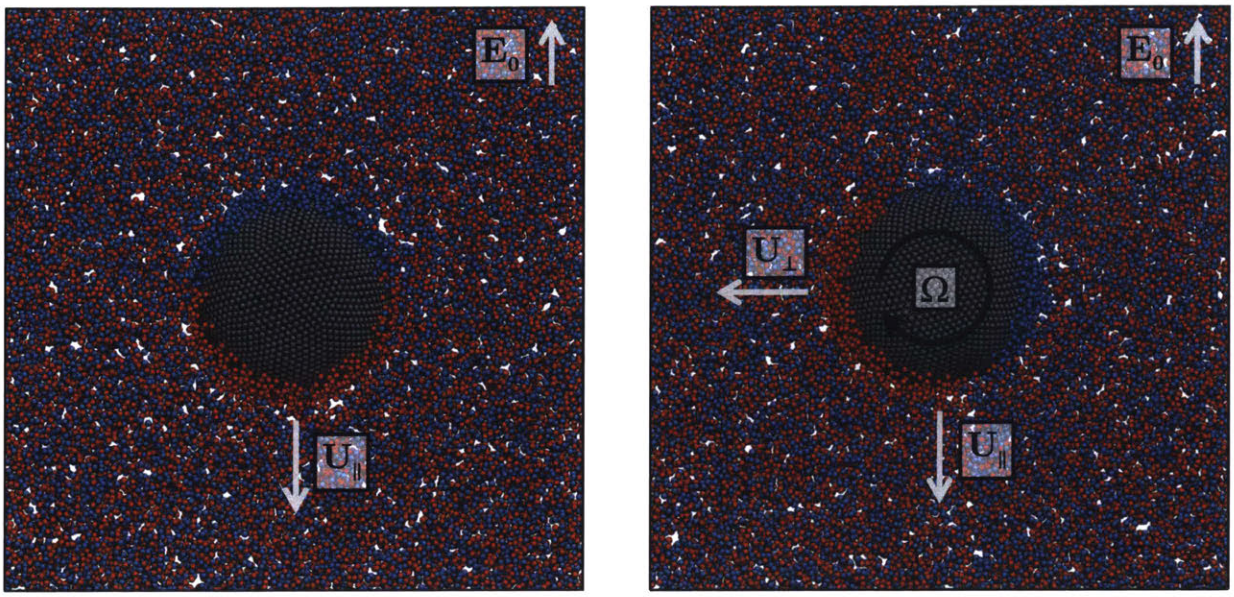

Figure 7.1: Left. A negatively charged colloid in an electrolyte with positive (red) and negative (blue) ions polarizes the surrounding ion cloud in an electric field $\mathbf{E}_0$. The field causes the particle to move downward at velocity $\mathbf{U}_{\parallel}$ *via* induced-charge electrophoresis. **Right.** If the field is above a critical value, the Quincke rotation instability causes the particle to rotate with angular velocity $\boldsymbol{\Omega}$ about an axis orthogonal to the applied field. The coupling between electrophoresis and Quincke rotation drives the particle orthogonally to both the applied field and axis of rotation with velocity $\mathbf{U}_{\perp}$, the electrohydrodynamic Magnus (EHM) effect.

moment $\mathbf{S}_0 \equiv \int_S d\mathbf{r}\, \mathbf{r} q_{\text{init}} = 4\pi a^3 \varepsilon_f E_0$, where $\mathbf{r}$ is the position relative to the colloid center, θ and ϕ are the azimuthal and zenith spherical coordinates relative to the z-axis pointed in the field direction, and the integral is over the particle surface. Positive ions are drawn to the negative induced charges and negative ions are drawn to the positive induced charges, forming a polarized double layer around the particle of thickness $\kappa^{-1} \equiv \sqrt{\varepsilon_f k_B T / 2 n_i q_i^2}$, as in Figure 7.1. As the ions approach the particle surface, their electric field induces additional surface charge in the particle, which pulls in more ions, *etc.*, and the particle and double layer "charge up" over time. An example of the charging dynamics is shown in Figure 7.4A. Squires and Bazant[279,280] showed that if the particle radius a is much larger than the double layer thickness κ^{-1}, there is an inner region close to the particle surface where ions distribute themselves according to the Poisson-Boltzmann equation,

$$\varepsilon_f \nabla^2 \psi' = \rho \tag{7.2}$$

and an outer region where the electrolyte is charge neutral

$$\nabla^2 \psi = 0 \tag{7.3}$$

where $\psi'(\mathbf{r})$ and $\psi(\mathbf{r})$ are the inner and outer potentials and $\rho(\mathbf{r}) = q_i(n_+(\mathbf{r}) - n_-(\mathbf{r}))$ is the charge distribution of the electrolyte in terms of the cation $n_+(\mathbf{r})$ and anion $n_-(\mathbf{r})$ concentrations. If $a \gg \kappa^{-1}$, the angular gradients in (7.2) can be neglected, and the particle surface appears flat in the inner region. At a particular θ and ϕ, ψ' is the solution to the one-dimensional Poisson-Boltzmann equation in a normal coordinate h with a surface charge density $q(\theta, \phi, t)$, the *additional* induced surface charge density of the particle excess of q_{init} from the initial field. The angular dependence of ψ' is due solely to the angular dependence of the boundary condition $q(\theta, \phi, t)$. The solution to the Poisson-Boltzmann equation next to a flat plate is given in Appendix C. Because the particle charges up, q is time-dependent. We assume that the ions in the inner region equilibrate much faster than the time scale on which q varies, so that ψ' always satisfies (7.2) in a pseudosteady sense, with time-dependence coming solely from the time-dependent boundary condition $q(\theta, \phi, t)$.

The potential as $h \to \infty$ in the inner region, $\psi'_p - \zeta$, where ψ'_p is the surface potential of the particle and ζ is

the potential drop across the double layer (*i.e.* the zeta potential), must equal the potential at the particle surface in the outer region, ψ. Because the particle is a conductor with $\psi_p' = 0$,

$$\psi(r = a, \theta, \phi, t) = -\zeta(\theta, \phi, t). \tag{7.4}$$

Therefore, ψ can be expressed as

$$\psi(\mathbf{r}, t) = -\mathbf{E}_0 \cdot \mathbf{r}\left(1 - \frac{a^3}{r^3}\right) + \sum_{\ell m} C_{\ell m}(t) r^{-(\ell+1)} Y_{\ell m}(\theta, \phi), \tag{7.5}$$

where the coefficients are

$$C_{\ell m}(t) = -a^{\ell+1} \int_\Gamma d\Gamma\, \zeta(\theta, \phi, t) Y_{\ell m}(\theta, \phi), \tag{7.6}$$

$Y_{\ell m}$ is the spherical harmonic of degree ℓ and order m, Γ is the unit sphere, and $d\Gamma \equiv \sin\theta\, d\theta\, d\phi$ is the solid angle. Written in this form, ψ satisfies Laplace's equation, approaches the correct value at infinity ($-\nabla\psi \to \mathbf{E}_0$ as $r \to \infty$), and satisfies the initial condition ($\zeta(\theta, \phi, 0) = C_{\ell m}(0) = 0$). For a nonrotating particle, there is no ϕ dependence and only the $m = 0$ coefficients are nonzero. Additionally, symmetry about the particle equator $\theta = \pi/2$ requires all the even ℓ coefficients to vanish. However, we keep the entire expansion for comparison with the rotating particle case in section 7.2. In the bulk electrolyte, there is a local current density $\mathbf{j}(\mathbf{r}, t) = \sigma\mathbf{E}(\mathbf{r}, t)$ from the mobile ions, where $\mathbf{E} \equiv -\nabla\psi$ is the field associated with the outer potential and σ is the electrolyte conductivity, and so there is a current entering the double layer equal to $-\mathbf{j}(a, \theta, \phi, t) \cdot \hat{\mathbf{r}}$. The current induces equal and opposite surface charges $q(\theta, \phi)$ (excess of q_{init}) in the particle to satisfy electroneutrality in the inner region. On the particle surface, $r = a$, we can construct a conservation equation for the induced surface charge

$$\frac{dq(\theta, \phi, t)}{dt} = \sigma\mathbf{E} \cdot \hat{\mathbf{r}} = 3\sigma E_0 \cos\theta + \sigma \sum_{\ell m} (\ell + 1)\, \widetilde{C}_{\ell m}(t) Y_{\ell m}(\theta, \phi). \tag{7.7}$$

where $\widetilde{C}_{\ell m} \equiv C_{\ell m}/a^{\ell+1}$. The induced surface charge is related to the zeta potential through the solution to the Poisson-Boltzmann equation (Appendix C), admitting a relation $q(\zeta)$ as well as the differential capacitance $C(\zeta) \equiv dq/d\zeta$

$$q(\zeta) = \operatorname{sgn}\zeta \sqrt{2\varepsilon_f \int_\zeta^0 d\zeta'\, \rho(\zeta')}, \quad C(\zeta) \equiv \frac{dq}{d\zeta} = -\frac{\varepsilon_f \rho(\zeta)}{q(\zeta)}, \tag{7.8}$$

and the charge balance can be written solely in terms of ζ

$$\frac{d\zeta(\theta, \phi, t)}{dt} = \frac{\sigma}{C(\zeta)}\left(3E_0 \cos\theta + \frac{1}{a}\sum_{\ell m}(\ell + 1)\widetilde{C}_{\ell m} Y_{\ell m}\right). \tag{7.9}$$

We can convert this into an ODE for the coefficients by multiplying the PDE by $Y_{\ell m}$ and integrating over the unit sphere

$$\frac{\partial \widetilde{C}_{\ell m}(t)}{\partial t} = -\int_\Gamma d\Gamma\, \frac{\sigma}{C}\left(3E_0 \cos\theta + \frac{1}{a}\sum_{\ell' m'}(\ell' + 1)\widetilde{C}_{\ell' m'} Y_{\ell' m'}\right) Y_{\ell m} \tag{7.10}$$

The particle dipole moment evolves over time as the particle and double layer charge up,

$$\mathbf{S}(t) = \mathbf{S}_0 + \int_S d\mathbf{r}\, \mathbf{r} q(\theta, \phi, t) \tag{7.11}$$

where the integral is over the particle surface. To solve (7.10), we need $q(\zeta)$ and $C(\zeta)$ from the solution to the Poisson-Boltzmann equation, which requires that we choose a particular model for the ions.

7.1.1 Debye-Huckel Solution

In the Debye-Huckel limit, ions are represented as point charges in the low zeta potential limit $q_i\zeta/k_BT \ll 1$, yielding the a linear relation between q and ζ

$$q = \varepsilon_f \kappa \zeta, \quad C = \varepsilon_f \kappa. \tag{7.12}$$

Because C is independent of ζ, we can easily perform the integration in (7.10) and solve the resulting ODEs analytically. Only $\widetilde{C}_{10}$ has a nontrivial solution,

$$\widetilde{C}_{10}(t) = \sqrt{3\pi} a E_0 \left(e^{-t/\tau_c} - 1\right) \tag{7.13}$$

where $\tau_c \equiv \varepsilon_f \kappa a/2\sigma$ is the charging time. The zeta potential is then,

$$\zeta(\theta, \phi, t) = \frac{3}{2} a E_0 \cos\theta \left(1 - e^{-t/\tau_c}\right), \tag{7.14}$$

and the particle dipole is,

$$\widetilde{S}(t) = 1 + \frac{\kappa a}{2}\left(1 - e^{-t/\tau_c}\right), \tag{7.15}$$

where $\widetilde{S} \equiv S/S_0$ is normalized by the isolated particle dipole $S_0 \equiv 4\pi a^3 \varepsilon_f E_0$. As $t \to \infty$, $C_{10} \to -\sqrt{3\pi} a^3 E_0$, and the zeta potential is equal to that of an insulator, $\zeta \to \frac{3}{2} a E_0 \cos\theta$, corresponding to a final particle dipole of

$$\widetilde{S}(\infty) = 1 + \frac{\kappa a}{2}. \tag{7.16}$$

From (7.7), the dispersion reaches a steady-state when the outer field lines have no normal component, resembling that of an insulator, and ionic current cannot enter the double layer. Because the initial charge distribution goes as $q_{\text{init}} \sim a E_0$, the steady-state zeta potential must also go as $\zeta \sim a E_0$ to bring in enough charge q to counteract q_{init}. This contributes an extra factor of a to the induced dipole $S \sim a^4 E_0$ compared to the isolated particle dipole with no salt $S_0 \sim a^3 E_0$, and the normalized dipole grows as $\widetilde{S} \sim a$. The charging time also grows linearly with particle size $\tau_c \sim a$ and inversely will conductivity $\tau_c \sim \sigma^{-1}$ to bring in this extra charge. In the dilute limit, $\sigma = 2 n_i q_i^2/\gamma_i$, but becomes a complicated function of n_i and E_0 at larger concentrations.[296] Figure 7.6 shows that the conductivity in our simulations is a bit lower than this prediction, likely due to steric hinderance. However, the dependence of the ionic conductivity on system parameters is not the focus here, and we use the dilute estimate so that we may evaluate expressions analytically.

The linear Debye-Huckel theory predicts that both the charging time τ_c and the final normalized particle dipole $\widetilde{S}$ are independent of the field strength E_0. Though the steady-state q grows with E_0, the ionic current also grows with E_0 and these effects cancel out. Figures 7.2 and 7.3 compare these predictions to those from our simulations. At low E_0, the simulations show $\widetilde{S}$ and τ_c are independent of E_0 and grow with a, in agreement with the Debye-Huckel predictions. However, at large field strengths both $\widetilde{S}$ and τ_c decrease with E_0. $\widetilde{S} \to 1$ at large E_0, indicating that polarization from the ion double layer is small compared to the polarization from the external field. The charging time goes as $\tau_c \sim \widetilde{E}_0^{-1}$ at large E_0, and charging is limited only by how fast the external field can electrophoretically shuttle ions to the particle surface. These nonlinear effects indicate a breakdown of the small ζ potential assumption in the Debye-Huckel approximation, $q_i\zeta/k_BT \ll 1$. Because the steady-state zeta potential goes as $\zeta \sim a E_0$, if the particle is large, the induced zeta potential will be large, even for small E_0. For $\tilde{a} = 30$ and $\widetilde{E}_0 = 0.01$, $q_i\zeta/k_BT \approx 2$, and is well outside the linear regime. More sophisticated ion models must be considered to capture nonlinear effects that are important at these large ζ.

7.1.2 Gouy-Chapman Solution

Nonlinearities can be incorporated into the Poisson-Boltzmann equation through the relation between the ionic charge distribution ρ and the inner potential ψ'. This relation is derived by considering the chemical potential $\mu_\pm$ of each ion species. In the Gouy-Chapman model, the ions behave ideally,

$$\mu_\pm = k_BT \ln n_\pm \pm q_i(\psi' + \zeta). \tag{7.17}$$

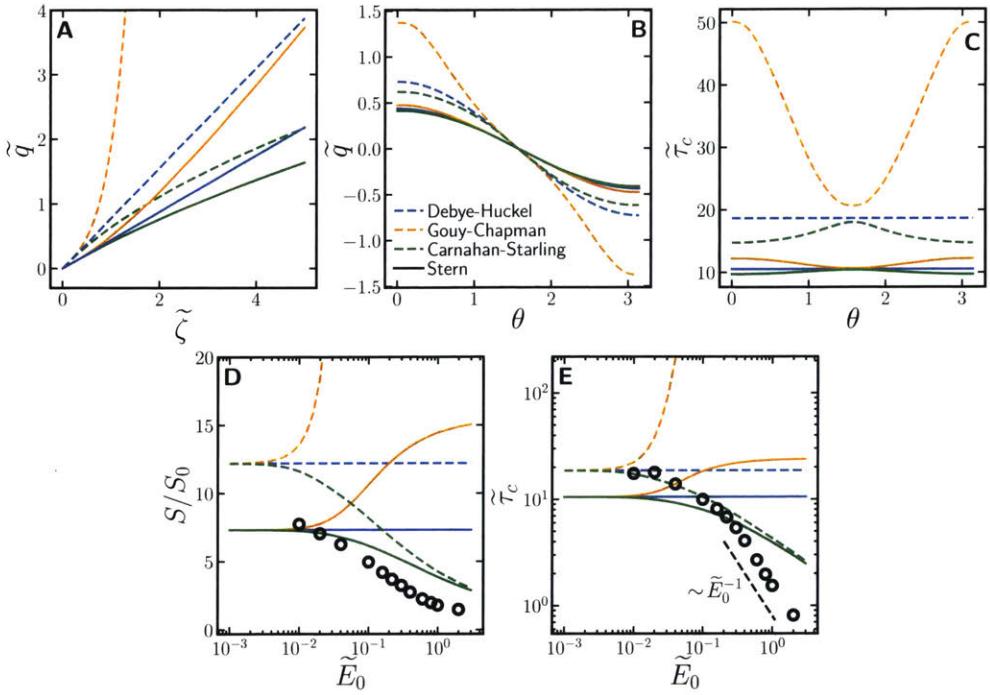

Figure 7.2: Solutions to ICEO of a conducting sphere of radius $\widetilde{a} = 30$ from simulations (points) for several ion models (colored lines). **A.** The surface charge density $\widetilde{q}$ as a function of zeta potential $\widetilde{\zeta}$ from the solution to the one-dimensional Poisson-Boltzmann equation. **B.** and **C.** The steady-state induced surface charge distribution and the charging time distribution $\widetilde{\tau}_c$ as a function of angle θ on the surface for field $\widetilde{E}_0 = 0.02$. **D.** and **E.** Final dipole strength S and overall charging time as a function of field.

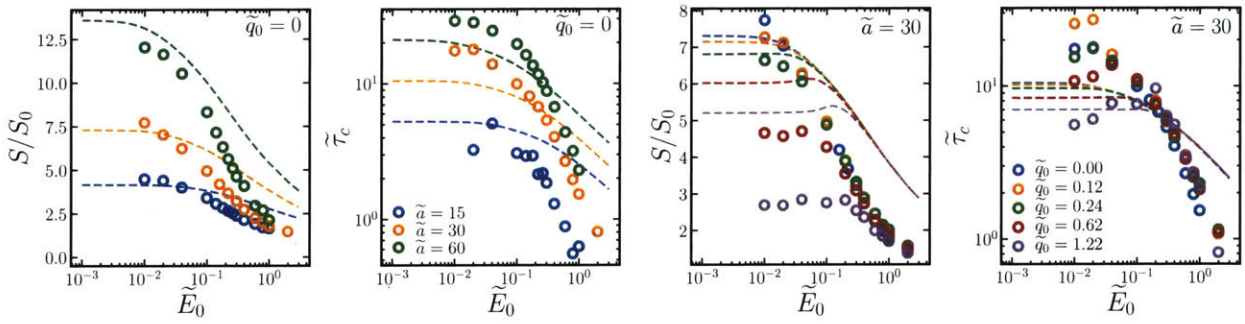

Figure 7.3: Final dipole strength $S\ \widetilde{\tau}_c$ for a nonrotating conducting particle of fixed charge and varying size (left two panels) and of fixed size and varying charge (right two panels) in an electrolyte as a function of field strength $\widetilde{E}_0$ from simulations and for the Carnahan-Starling-Stern ICEO theory (dashed lines) for various particle sizes (different colors).

At equilibrium, the ion chemical potentials must be constant everywhere. In particular, far away from the particle surface, $\psi' \to -\zeta$ and $n_\pm \to n_i$ so this constant value for $\mu_\pm$ is known. Solving for $n_\pm$ allows an expression for the charge density,

$$\rho = -2q_i n_i \sinh \frac{q_i \psi'}{k_B T}. \tag{7.18}$$

From (7.8), the surface charge density and capacitance are

$$q = 4q_i n_i \kappa^{-1} \sinh \frac{q_i \zeta}{2k_B T}, \quad C = \varepsilon_f \kappa \cosh \frac{q_i \zeta}{2k_B T}. \tag{7.19}$$

Note that we recover the Debye-Huckel solution, $q = \varepsilon_f \kappa \zeta$ and $C = \varepsilon_f \kappa$, for $q_i \zeta / k_B T \ll 1$. The Guoy-Chapman solution to the ICEO problem is shown in Figure 7.2.

From (7.9), the nonlinear ion model only affects $C(\zeta)$. This affects the charging dynamics, but the steady-state zeta potential, $\frac{3}{2} a E_0 \cos\theta$, remains the same for any $C(\zeta)$. Because q grows exponentially with ζ and the steady-state ζ goes as aE_0, the particle dipole grows exponentially with E_0,

$$\widetilde{S} = 1 + \frac{4 n_i q_i}{\varepsilon_f \kappa E_0} i_1 \left(\frac{3 q_i a \widetilde{E}_0}{4 k_B T} \right) \tag{7.20}$$

where i_1 is the modified spherical Bessel function of order 1. The nonlinear ODE (7.38) does not have an analytical solution, but we can solve it numerically and fit an exponential to the dipole strength over time to extract the charging time, shown in Figure 7.2E. The charging time grows exponentially with E_0, as it takes a much longer time for the outer field, which only grows as aE_0, to inject the exponetially growing charge in the double layer. Unlike the Debye-Huckel dynamics, where only $\widetilde{C}_{10}$ is nonzero and the particle charges at the same rate everywhere, the Gouy-Chapman dynamics display different rates of charging across the particle surface. The distribution of charging times $\tau_c(\theta)$ is shown in Figure 7.2C and was extracted from an exponential fit over time to the numerical solution $q(\theta, t)$ for each θ. The poles, where the zeta potential and charge are largest, charge much more slowly than the equator, where the zeta potential and charge are small. The overall charging time τ_c determined from the particle dipole is a weighted average of the charging time distribution $\tau_c(\theta)$.

7.1.3 Carnahan-Starling Solution

The Gouy-Chapman solution predicts exponentially growing S and τ_c with increasing E_0, but our simulations show *decreasing* S and τ_c. Because the Gouy-Chapman model treats ions as point charges, they can pack arbitrarily close together, leading to very large, exponentially growing charge distributions. However, real ions have finite size that limit their packing density. At the large induced zeta potentials relevant to ICEO and ICEP, ions are densely packed near the particle surface, and steric interactions become very important. We can treat the ions as hard spheres of radius a_i, and their chemical potential is given by the Carnahan-Starling expression,[234]

$$\mu_\pm = k_B T \left(\ln \phi_\pm + \frac{3 - (\phi_+ + \phi_-)}{(1 - (\phi_+ + \phi_-))^3} - 3 \right) \pm q_i (\psi' + \zeta), \tag{7.21}$$

The ion volume fractions $\phi_\pm$ are found by solving simultaneously,

$$\ln \phi_+ + \frac{3 - (\phi_+ + \phi_-)}{(1 - (\phi_+ + \phi_-))^3} + \frac{q_i(\psi' + \zeta)}{k_B T} = \ln \phi_i + \frac{3 - \phi_i}{(1 - \phi_i)^3} \tag{7.22}$$

$$\ln \phi_- + \frac{3 - (\phi_+ + \phi_-)}{(1 - (\phi_+ + \phi_-))^3} - \frac{q_i(\psi' + \zeta)}{k_B T} = \ln \phi_i + \frac{3 - \phi_i}{(1 - \phi_i)^3}. \tag{7.23}$$

where ϕ_i is the *total* (cation + anion) bulk ion volume fraction. This does not have an analytical solution, but we can solve it numerically and compute q and C with a numerical integration from (7.8). Because there is a maximum sphere packing density where the chemical potential diverges, the charge distribution cannot

exceed a maximum value. As ρ approaches this maximum, an increasingly large ζ is needed to increase ρ, so C decreases with ζ. The Carnahan-Starling solution to the ICEO problem is shown in Figures 7.2 and 7.3.

The steady-state zeta potential is, again, $\frac{3}{2}aE_0\cos\theta$, but the steady-state dipole must be calculated numerically. Because q levels off with increasing ζ, $\widetilde{S}$ decreases with increasing E_0, and the polarization due to the ions becomes small compared to the polarization from the external field. Though q levels off, the outer field injecting charge increases as aE_0, so the charging time decreases with E_0. However, the decrease is not quite as fast as the scaling of $\tau_c \sim E_0^{-1}$ at large E_0 that we observe in our simulations. Like the Gouy-Chapman solution, the particle charges at different rates across its surface. For the Carnahan-Starling solution, the poles charge more quickly than the equator, opposite the trends of the Gouy-Chapman solution. The overall τ_c is limited by the slowest charging modes of $\tau_c(\theta)$. Because the slow modes occur near the equator and the equator contributes more surface area to the overall dipole moment than the poles, the charging time only decreases as $\tau_c \sim E_0^{-1/2}$ in our theoretical model. This is not entirely unexpected, because the theory only allows for ion transport in the radial direction in the double layer. It is likely surface conduction and surface diffusion, which allow for ion transport in tangential directions, play an important role for charging in the simulations, but are not incorporated into the theoretical model.

If the particle has a net charge q_0, it also has a net zeta potential ζ_0 in addition to the induced zeta potential ζ from the ICEO charging, and the ions in the double layer screen both q and q_0. In the linear Debye-Huckel regime, these two situations can be considered separately and their solutions superimposed, so the net charge does not affect the charging dynamics. However, q_0 does change the dynamics in the nonlinear Gouy-Chapman and Carnahan-Starling models. Figure 7.3 shows the particle dipole and charging time for particles with various net charges from simulation and the Carnahan-Starling theory. The capacitance relation in Figure 7.2A shows that the differential capacitance decreases with ζ and q grows slowly. Particles with a net charge, begin with a lower capacitance than a charge-free particle and charge less strongly. Both the dipole strength and the charging time decrease with q_0 at small $\widetilde{E}_0$. In fact, charging is nearly suppressed altogether for the largest net charges we tested. The net charge is important when its associated zeta potential is comparable to or larger than the induced zeta potential, $\zeta_0 \gtrsim a\widetilde{E}_0$. As $\widetilde{E}_0$ gets large, the induced ζ dominates the net ζ_0 and all the net charged particles behave the same.

7.1.4 Stern Layer

The Debye-Huckel, Gouy-Chapman, and Carnahan-Starling models all overpredict the induced dipole observed in the simulations. The steady-state zeta potential is always $\frac{3}{2}aE_0\cos\theta$, so this overestimate implies that the charge and differential capacitance relations, $q(\zeta)$ and $C(\zeta)$, are smaller in the simulations than predicted. As in Appendix C, these relations are derived assuming ions can accumulate arbitrarily close to the particle surface. However, because ions have a finite size a_i, the closest their centers' may approach the surface is a_i. This forms a Stern layer of thickness[†] a_i near the surface where the charge density in the fluid vanishes and the inner potential ψ' is unscreened. The Stern layer has a capacitance $C_S = \varepsilon_f/a_i$ and acts in series with the capacitance C_D of the diffuse region of the double layer given by (7.8), whose reciprocals are additive. The total capacitance is diminished, and the charge and capacitance relations are[162]

$$q(\zeta) = \operatorname{sgn}\zeta\sqrt{2\varepsilon_f\int_{\zeta-qa/\varepsilon_f}^{0} d\zeta'\,\rho(\zeta')}, \quad C(\zeta) = \frac{1}{\dfrac{a_i}{\varepsilon_f} - \dfrac{q}{\varepsilon_f\rho\left(\zeta - qa/\varepsilon_f\right)}} \equiv \frac{1}{1/C_S + 1/C_D}, \tag{7.24}$$

which are implicit functions because q appears on both sides of the equation. This has an analytical form for the Debye-Huckel-Stern model,

$$q = \frac{\varepsilon_f\kappa\zeta}{1+\kappa a_i}, \quad C = \frac{\varepsilon_f\kappa}{1+\kappa a_i}, \tag{7.25}$$

[†]Often the Stern layer thickness is left unspecified and used as a fitting parameter. Because we set the ion size explicitly in our simulations and observe their closest appreoach to the particle surface, we are motivated physically to use a_i as the Stern layer thickness.

which admits analytical solutions for the final dipole and charging time,

$$\widetilde{S} = 1 + \frac{\kappa a}{2(1+\kappa a_i)}, \quad \tau_c = \frac{\varepsilon_f \kappa a}{2\sigma(1++kappaa_i)}, \tag{7.26}$$

but the Gouy-Chapmann-Stern and Carnahan-Starling-Stern relations must be determined numerically. $\zeta_D \equiv \zeta - qa/\varepsilon_f$ is the potential drop across only the diffuse region of the double layer.[‡] Figures 7.2 and 7.3 show that the Stern layer reduces the predicted dipole strengths, which now agree well with our simulation results. Including the Stern layer also decreases the charging time, as the amount of charge in the double layer is smaller. The Stern layer capacitance curbs the exponential growth of the Gouy-Chapman capacitance because $C = 1/(1/C_S + 1/C_D) \approx C_S$ for large C_D, and the Gouy-Chapmann-Stern dipole and charging time level off as $\widetilde{E}_0$ increases. On the other hand, the Carnahan-Starling capacitance becomes small at large $\widetilde{E}_0$, so $C \approx C_D$ and the Carnahan-Starling-Stern predictions approach the Carnahan-Starling predictions at large $\widetilde{E}_0$.

7.1.5 The Electrophoretic Velocity

The fluid velocity outside of the double layer is given by the Helmholtz-Smoluchowski expression[279]

$$\mathbf{u} = -\frac{\varepsilon \zeta_D}{\eta}\mathbf{E}_t, \tag{7.27}$$

where $\mathbf{E}_t$ is the outer field tangent to the particle surface. The particle velocity can then be computed from the integral of the fluid velocity over the surface of the particle[297]

$$\mathbf{U} = -\frac{1}{4\pi a^2}\int_S d\mathbf{r}\,\mathbf{u}. \tag{7.28}$$

For a charge-free particle, the integral in (7.28) vanishes and the induced charge distribution alone cannot result in translation. If the particle has a net surface charge q_0, the net zeta potential ζ_0 in addition to the induced zeta potential ζ_D is included in (7.27), and

$$\mathbf{U} = \frac{1}{4\pi a^2}\int_S d\mathbf{r}\frac{\varepsilon(\zeta_0+\zeta_D)}{\eta}\mathbf{E}_t = \frac{\varepsilon_f \zeta_0}{\eta}\mathbf{E_0}, \tag{7.29}$$

which is the well-known electrophoretic velocity of a charged sphere in the thin double layer limit.[125] This holds for all of the ion models as long as the double layer is sufficiently thin compared to the particle size. Figure 7.7A shows excellent agreement between equation (7.29) and the velocity in our simulations. As q_0 or E_0 become large, particle and double layer convection can play a significant role in the charging dynamics and may be responsible for the large decrease in dipole strength we observe with increasing net charge. Including these effects in the governing equations was not considered here.

7.2 The Electrohydrodynamic Magnus Effect

With an understanding of the induced-charge electrophoresis of a nonrotating particle, we proceed now to our original goal of understanding the induced-charge electrophoresis of a particle undergoing Quincke rotation, which has a translational velocity orthogonal to the applied field due to the electrohydrodynamic Magnus effect. It is crucial to have a fundamental understanding of the underlying physics governing the phenomenon to utilize the electrohydrodnamic Magnus effect in experiments.

Quincke rotation has been well-studied in the context of "electrohydrodynamics" (EH), using the Taylor-Melcher leaky dielectric model.[298,299] In EH models, the fluid and particle phases are assigned electric permittivities ε_f and ε_p, respectively, and electric conductivities σ_f and σ_p, respectively. Because of the conductivity, each phase can conduct an electric current. Though this current is intended to represent a flux

[‡]Sometimes ζ_D is referred to as "the" zeta potential. Here, "zeta potential" refers to ζ.s

of ionic charge, nonuniform ion charge distributions are not incorporated into EH theories. By constructing a charge balance at the particle surface, the angular velocity Ω can be written in terms of the permittivities and conductivities.[241,300] The EH model for Quincke rotation reveals several things. First, Quincke rotation only occurs if the charge relaxation time inside the particle, ε_p/σ_p, is larger than the charge relaxation time inside the fluid, ε_f/σ_f, and so Quincke rotation is usually associated with insulating particles of low conductivity. In this case, the dipole moment induced in the particle is oriented opposite to the applied field. Above a critical field strength,

$$E_c \equiv \sqrt{\frac{2\eta}{\varepsilon_f \tau_{\mathrm{MW}}(\varepsilon_{pf} - \sigma_{pf})}}, \tag{7.30}$$

where the Maxwell-Wagner time is $\tau_{\mathrm{MW}} = (\varepsilon_p + 2\varepsilon_f)/(\sigma_p + 2\sigma_f)$, $\varepsilon_{pf} \equiv (\varepsilon_p - \varepsilon_f)/(\varepsilon_p + 2\varepsilon_f)$, and $\sigma_{pf} \equiv (\sigma_p - \sigma_f)/(\sigma_p + 2\sigma_f)$, this orientation of the dipole becomes unstable, and the particle rotates with angular velocity

$$\Omega = \frac{1}{\tau_{\mathrm{MW}}}\sqrt{\left(\frac{E_0}{E_c}\right)^2 - 1}. \tag{7.31}$$

This scaling of rotation frequency with field strength has been confirmed in numerous experiments.[281,282,285]

While useful to understand the qualitative features of Quincke rotation, the electrohydrodynamic approach has some key weaknesses, especially when applied to conductive colloidal particles in electrolytes.[301] First, the leaky dielectric model is intended for two *fluid* phases. For solid particles, ions cannot penetrate the solid surface and $\sigma_p = 0$. If the particle is highly polarizable, $\varepsilon_p \to \infty$, electrohydrodynamics predicts a vanishing critical field, $E_c \to 0$, and no Quincke rotation, $\Omega \to 0$. This is problematic because we observe Quincke rotation for solid conducting particles, but is only possible with insulators in the EH model. Second, the EH model cannot produce particle translations (other than those due solely to the external field), since electroosmotic flows driving particle motion are not incorporated.[299] This makes EH ineffective in describing electrophoresis or the observed electrohydronamic Magnus effect. Finally, the EH approach contains no information on the structure of the ionic double layer surrounding the particle. There are no predictions for how the critical field should change with experimental parameters like salt concentration or particle size, and there is no systematic way to incorporate nonlinear ionic behavior. Additionally, the double layer structure can have profound impact on the magnitude and direction of electrophoretic motion, even reversing the translation direction in some cases,[302,303] as well the interactions among many particles,[23,62,86] which cannot be elucidated with EH.

In this section, we analyze Quincke rotation and the electrohydrodynamic Magnus effect in the context of "electrokinetics" (EK), where the dynamics of ions are incorporated.[301] With explicit reference to ions, EK approaches can overcome some of the limitations of EH. As we saw in the previous section 7.1, our electrokinetic approach to ICEO and ICEP yielded good agreement with our simulations. We extend our theoretical analysis of induced-charge electrophoresis to a conducting particle that is rotating with angular velocity $\mathbf{\Omega}$, which adds a convection term to (7.7)

$$\frac{\partial q(\theta,\phi,t)}{\partial t} = \sigma \mathbf{E}\cdot\hat{\mathbf{r}} - \nabla_s \cdot (q\mathbf{\Omega}\times\mathbf{r}) \tag{7.32}$$

where ∇_s is the surface gradient. Because particle rotation results from an instability in the polarized ion double layer, we do not know $\mathbf{\Omega}$. Like in Figure 7.1, ions slip pass the particle to travel electrophoretically with the field, with the positive ions traveling in the field direction on one side of the particle and negative ions traveling against the field direction on the other side. The ions drag solvent with them, and their hydrodynamic interactions with the surface generate a torque on the particle $\mathbf{L}^E$ that is sustained by the net ion dipole $\mathbf{S}_i$[144]

$$\mathbf{L}^E = \mathbf{S}_i \times \mathbf{E}_0 = -\int_S dS\, \mathbf{r}q \times \mathbf{E}_0. \tag{7.33}$$

The particle is torque-free, so it rotates at an angular velocity that balances the electric torque driving rotation with the hydrodynamic torque opposing it,[125,126]

$$\mathbf{L}^H = -8\pi\eta a^3 \mathbf{\Omega}. \tag{7.34}$$

Therefore, the angular velocity is

$$\mathbf{\Omega} = -\frac{1}{8\pi\eta a^3}\int_S dS\,\mathbf{r}q \times \mathbf{E}_0. \tag{7.35}$$

In terms of the induced ζ potential,

$$C(\zeta)\frac{\partial \zeta}{\partial t} = \sigma \mathbf{E}\cdot\hat{\mathbf{r}} + \frac{1}{8\pi\eta a^3}\nabla_s \cdot q(\zeta)\left(\int_S dS\,\mathbf{r}q(\zeta)\times\mathbf{E}_0\right)\times\mathbf{r}. \tag{7.36}$$

It is convenient to choose a coordinate system where the z axis points in the direction of $\mathbf{E}_0$ and the y axis points in the direction of $\mathbf{\Omega}$,

$$\frac{\partial\zeta}{\partial t} = \frac{\sigma\mathbf{E}\cdot\hat{\mathbf{r}}}{C(\zeta)} - \frac{aE_0}{8\pi\eta}\left(\int_\Gamma d\Gamma\, q(\zeta)\sin\theta\cos\phi\right)\left(\cos\phi\,\mathbf{E}\cdot\hat{\boldsymbol{\theta}} - \cos\theta\sin\phi\,\mathbf{E}\cdot\hat{\boldsymbol{\phi}}\right),. \tag{7.37}$$

In terms of the coefficients of the spherical harmonic expansion,

$$\begin{aligned}\frac{\partial\widetilde{C}_{\ell m}}{\partial t} = &-\int_\Gamma d\Gamma\,\frac{\sigma}{C(\zeta)}\left(3E_0\cos\theta + \frac{1}{a}\sum_{\ell' m'}(\ell'+1)\widetilde{C}_{\ell' m'}Y_{\ell' m'}\right)Y_{\ell m} - \frac{E_0}{8\pi\eta}\left(\int_\Gamma d\Gamma\, q(\zeta)\sin\theta\cos\phi\right)\\ &\times\left(\frac{1}{2}\sqrt{(\ell+m)(\ell-m+1)}\,\widetilde{C}_{\ell m-1} - \frac{1}{2}\sqrt{(\ell-m)(\ell+m+1)}\,\widetilde{C}_{\ell m+1}\right).\end{aligned} \tag{7.38}$$

If we use the Debye-Huckel solution, $q = \varepsilon_f\kappa\zeta$ and $C = \varepsilon_f\kappa$, we can evaluate the integrals in (7.38)

$$\begin{aligned}\frac{\partial\widetilde{C}_{\ell m}}{\partial t} = &-\frac{2\sqrt{3\pi}\sigma E_0}{\varepsilon_f\kappa}\delta_{lm,10} - \frac{\sigma(\ell+1)\widetilde{C}_{\ell m}}{\varepsilon_f\kappa a} + \frac{\varepsilon_f\kappa E_0(\widetilde{C}_{1,-1}-\widetilde{C}_{11})}{8\sqrt{6\pi}\eta}\\ &\times\left(\sqrt{(\ell+m)(\ell-m+1)}\,\widetilde{C}_{\ell m-1} - \sqrt{(\ell-m)(\ell+m+1)}\,\widetilde{C}_{\ell m+1}\right),\end{aligned} \tag{7.39}$$

At steady-state, all $\partial\widetilde{C}_{\ell m}/\partial t = 0$. For $\ell \geq 2$, (7.38) is linear in $\widetilde{C}_{\ell m}$, and of the form $\mathbf{A}_\ell\cdot\mathbf{C}_\ell = \mathbf{0}$ where $\mathbf{C}_\ell \equiv \left[\widetilde{C}_{\ell,-\ell},\widetilde{C}_{\ell,-\ell+1},\ldots,\widetilde{C}_{\ell,\ell}\right]^T$. $\mathbf{A}_\ell$ is always full rank, so the only solution is $\widetilde{C}_{\ell m} = 0$ for $\ell \geq 2$ and the particle only has a dipole moment. The three equations for $\ell = 1$ admit three steady-state solutions,

$$\widetilde{C}_{10} = -\sqrt{3\pi}aE_0, \quad \widetilde{C}_{1,1} = -\widetilde{C}_{1,-1} = 0 \tag{7.40}$$

$$\widetilde{C}_{10} = -\frac{8\sqrt{3\pi}\eta\sigma}{\varepsilon_f^2\kappa^2 aE_0}, \quad \widetilde{C}_{1,1} = -\widetilde{C}_{1,-1} = \pm\sqrt{\frac{12\pi\eta\sigma}{\varepsilon_f^2\kappa^2}\left(1 - \frac{8\eta\sigma}{\varepsilon_f^2\kappa^2 a^2 E_0^2}\right)} \tag{7.41}$$

The second solution only has real coefficients if

$$E_0 \geq \sqrt{\frac{8\eta\sigma}{\varepsilon_f^2\kappa^2 a^2}} \equiv E_c \tag{7.42}$$

The three possible angular velocities are then

$$\Omega = 0, \pm\frac{1}{\tau_c}\sqrt{\left(\frac{E_0}{E_c}\right)^2 - 1} \tag{7.43}$$

where $\tau_c \equiv \varepsilon_f\kappa a/2\sigma$ is the charging time for a sphere. The Jacobian can be computed analytically and a linear stability analysis about these steady-state solutions reveals that the stationary ($\Omega = 0$) solution is stable below E_c and unstable above E_c, while the rotating solutions are stable for $E_0 > E_c$, *i.e.* a pitchfork bifurcation. The EK expression for Ω (7.43) is similar to the EH expression (7.31), with the charging time τ_c replacing the Maxwell-Wagner time τ_{MW} and the critical field depending on κa rather than τ_{MW}, ε_{pf}, and σ_{pf}. Thus, the EK approach writes predictions for Quincke rotation in terms of experimentally controllable parameters. In particular, the critical field decreases with particle size as $E_c \sim a^{-1}$, unlike the EH equation

(7.30) which is independent of a. Because there is no screening length κ^{-1} in electrohydrodynamics, EH predictions cannot depend on a, as there is no other length scale to compare against. However, for large fields,

$$\Omega \approx E_0\sqrt{\sigma/2\eta}, \quad E_0 \gg E_c, \tag{7.44}$$

and Ω is independent of a, consistent with the EH expectations.[304] The normalized particle dipole is

$$\widetilde{\mathbf{S}} = \begin{cases} (1+\kappa a/2)\,\hat{\mathbf{e}}_z, & E_0 \le E_c \\ \pm\dfrac{\kappa a}{2}\dfrac{E_c}{E_0}\sqrt{1-\left(\dfrac{E_c}{E_0}\right)^2}\,\hat{\mathbf{e}}_x + \left(1+\dfrac{\kappa a}{2}\left(\dfrac{E_c}{E_0}\right)^2\right)\hat{\mathbf{e}}_z, & E_0 > E_c \end{cases} \tag{7.45}$$

with magnitude

$$\widetilde{S} = \begin{cases} 1+\kappa a/2, & E_0 \le E_c \\ \sqrt{1+\kappa a\,(1+\kappa a/4)\,(E_c/E_0)^2}, & E_0 > E_c \end{cases} \tag{7.46}$$

Below the critical frequency when the particle is stationary, the dipole is aligned the field. Above E_c, the dipole breaks symmetry and points off the field axis. $\widetilde{S}$ decreases with E_0 as accumulated ionic charge in the double layer is convected away and $\widetilde{S} \to 1$ at large E_0. The orthogonal component of the *unnormalized* $\mathbf{S}$ reaches a finite value as $E_0 \to \infty$, sustaining the electric torque to drive rotation, even at large E_0.

If the Stern layer is included, the Debye-Huckel capacitance, $\varepsilon_f\kappa$, is replaced with the Deby-Huckel-Stern capacitance, $\varepsilon_f\kappa/(1+\kappa a_i)$, in expressions (7.39)-(7.46), yielding,

$$E_c = \sqrt{\frac{8\eta\sigma(1+\kappa a_i)^2}{\varepsilon_f^2\kappa^2 a^2}} \tag{7.47}$$

$$\tau_c = \frac{\varepsilon_f\kappa a}{2\sigma(1+\kappa a_i)} \tag{7.48}$$

$$\widetilde{\mathbf{S}} = \begin{cases} \left(1+\dfrac{\kappa a}{2(1+\kappa a_i)}\right)\hat{\mathbf{e}}_z, & E_0 \le E_c \\ \pm\dfrac{\kappa a}{2(1+\kappa a_i)}\dfrac{E_c}{E_0}\sqrt{1-\left(\dfrac{E_c}{E_0}\right)^2}\,\hat{\mathbf{e}}_x + \left(1+\dfrac{\kappa a}{2(1+\kappa a_i)}\left(\dfrac{E_c}{E_0}\right)^2\right)\hat{\mathbf{e}}_z, & E_0 > E_c \end{cases} \tag{7.49}$$

$$\widetilde{S} = \begin{cases} 1+\dfrac{\kappa a}{2(1+\kappa a_i)}, & E_0 \le E_c \\ \sqrt{1+\dfrac{\kappa a}{1+\kappa a_i}\left(1+\dfrac{\kappa a}{4(1+\kappa a_i)}\right)\left(\dfrac{E_c}{E_0}\right)^2}, & E_0 > E_c \end{cases} \tag{7.50}$$

Note that the expression for the angular velocity (7.43) remains the same, with the Debye-Huckel-Stern critical field and charging time replacing the Debye-Huckel values.

Figure 7.4 shows the charging kinetics for stationary and rotating particles. Below E_c, the nonrotating branch of (7.43) is stable and the particle dipole in Figure 7.4A charges to its final value over the charging time τ_c. Above E_c, the stationary branch is unstable and the particle undergoes Quincke rotation. From Figures 7.4B-C, the particle is initially nonrotating and charges up like typical ICEO. After an induction time τ_i, the particle spontaneously rotates and Ω sharply increases. The ions accumulated at the poles spill over the sides of the particle, and the particle dipole drops dramatically at τ_i, before settling at a lower S at an angle θ relative to $\mathbf{E}_0$. Figure 7.4D shows that the response of the ions in the double layer lags that of the particle. The lag in these coupled systems leads to oscillations in the dipole and angular velocity that persist at long times. In fact, the ions can be imagined as imparting "inertia" to the colloid's dipole so that the dynamics can become chaotic at large enough field strengths.[305,306]

Figure 7.5 shows further comparisons between the particle and ion dipoles. The electrokinetic theory predicts that the ions in the double layer induce equal and opposite surface charges q in the colloid. The *initial* dipole

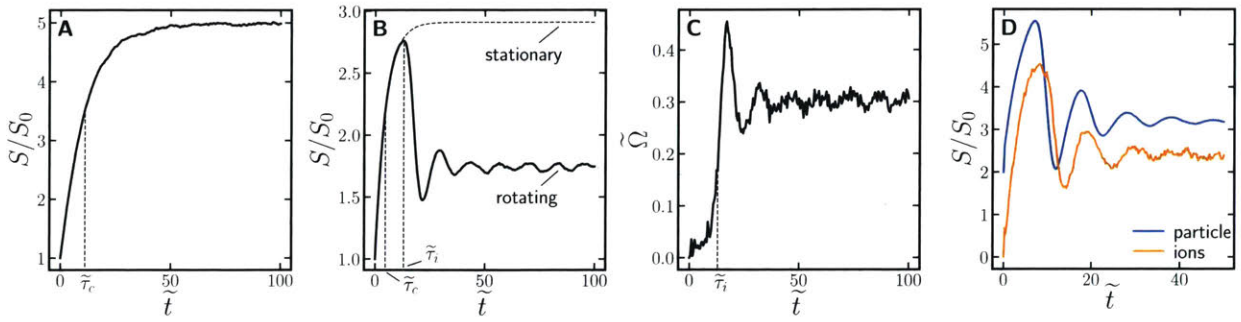

Figure 7.4: **A.** Particle dipole moment charging over time $\widetilde{t}$ from simulation of a nonrotating particle of radius $\widetilde{a} = 30$ at field $\widetilde{E}_0 = 0.1$. The charging time $\widetilde{\tau}_c$ is extracted from an exponential fit the data and is the time for S to reach $(1 - e^{-1})$ of its final value. **B.** and **C.** The particle dipole and angular velocity $\widetilde{\Omega}$ for a rotating particle at $\widetilde{a} = 30$ and $\widetilde{E}_0 = 0.4$. The onset of the Quincke rotation instability occurs at $\widetilde{\tau}_i$, but the stationary solution can be extrapolated from a fit to the stationary region for $t < \widetilde{\tau}_i$. **D.** The particle and ion dipoles for a rotating particle with $\widetilde{a} = 60$ and $\widetilde{E}_0 = 0.3$. The ion dipole lags the particle dipole leading to oscillations, even at steady-state.

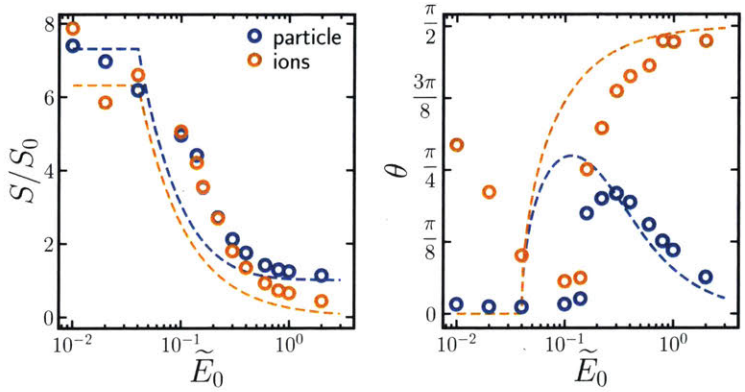

Figure 7.5: Particle and ion dipoles S (left) and deviations angles θ (right) relative to the applied field $\widetilde{E}_0$ for $\widetilde{a} = 30$ and $\widetilde{q}_0 = 0$ from simulations (points) and the Debye-Huckel-Stern theory (lines).

S_0 corresponding to q_{init} induced by the external field is always present for the particle but not the ions, so the ion dipole is predicted to be $\mathbf{S}_i = -(\mathbf{S} - \mathbf{S}_0)$. Below E_c when the particle is stationary, Figure 7.5 shows that the ion dipole matches the *entire* particle dipole, screening both q and q_{init}. Above E_c when the particle rotates, this extra screening vanishes and the ion dipole S_i drops below S and agrees with the predictions. Though the normalized ion dipole $\widetilde{S}_i$ vanishes as $E_0 \to \infty$, the actual dipole S_i is finite and orients at an angle $\theta = \pi/2$, exactly orthogonal to the applied field. This supplies the electric torque to sustain Ω even at large E_0.

By fitting an exponential to the stationary regime $t < \tau_i$, we can extract the charging time and extrapolate the final dipole the particle would have obtained had the rotational instability not occurred. These are shown in Figure 7.6. Because ions are convected away by rotation, the dipole for the rotating state is lower than the dipole for the nonrotating state, where ions accumulate at the poles and increase polarization. The rotation facilitates ion convection and gives rise to an increase in the electrolyte's overall conductivity σ compared to the pure electrolyte. The conductivity increases as the field increases due to the increased angular velocity and depends on the colloid volume fraction (which was not investigated here). This conductivity increase above E_c has also been observed in experiments of Quincke rotation.[307] Both the charging time τ_c and the rotation induction time τ_i decrease with E_0 and decay as $\sim E_0^{-1}$ at large E_0. The induction time always follows the charging time, indicating that the particle has to charge up enough to trip the Quincke rotation instability. As the critical field is approach from above, τ_c begins to level off with decreasing E_0 but the τ_i

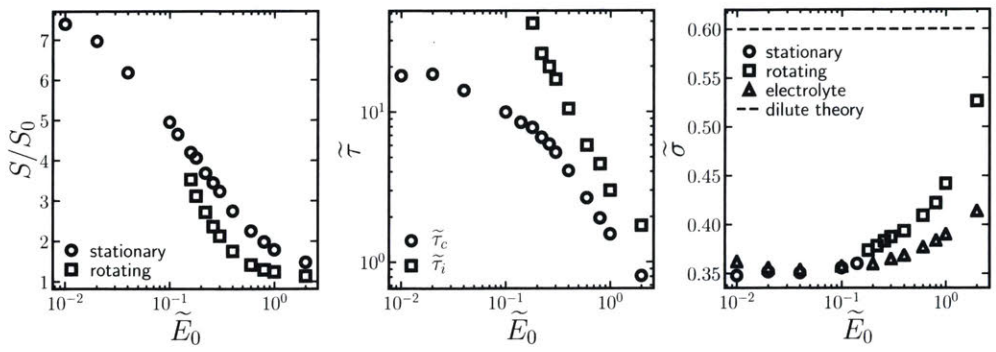

Figure 7.6: Comparison between rotating and nonrotating simulations for $\widetilde{a} = 30$ and $\widetilde{q}_0 = 0$. **Left.** The normalized dipole strength S/S_0. **Middle.** The charging time $\widetilde{\tau}_c$ and onset of rotation time $\widetilde{\tau}_i$. For $E_0 > E_c$, the "stationary" dipole and $\widetilde{\tau}_c$ were extracted from an exponential fit to the stationary regime for $t < \tau_i$. **Right.** The ionic conductivity $\widetilde{\sigma}$ with (circles and squares) and without (triangles) particles.

appears to diverge as $E_0 \to E_c$. Near E_c, the particle completely charges in its nonrotating state and remains metastable for a long time before a fluctuation in the ion dipole drives the Quincke rotation instability. This is similar to nucleation and growth of phase transitions in the metastable region between the binodal and spinodal, where nucleation occurs stochastically after a finite induction time.

If the colloid has a net surface charge density $\widetilde{q}_0$, we can use the Helmholtz-Smoluchowski formula (7.27) to compute the fluid velocity at the particle surface, and integrate over the particle surface (7.28) to compute the translational velocity of the particle. As in ICEO, the integral of $\zeta_D \mathbf{E}_t$ vanishes, and Quincke rotation of an uncharged particle does not produce translation. The integral of $\zeta_0 \mathbf{E}_t$, however, does not vanish,

$$\mathbf{U} = \begin{cases} \dfrac{\varepsilon_f \zeta_0 E_0}{\eta} \hat{\mathbf{e}}_z, & E_0 \leq E_c \\ \dfrac{\varepsilon_f \zeta_0}{\eta} \left(\pm 2 E_c \sqrt{1 - \left(\dfrac{E_c}{E_0} \right)^2} \, \hat{\mathbf{e}}_x + \dfrac{E_c^2}{E_0} \hat{\mathbf{e}}_z \right), & E_0 > E_c \end{cases} \tag{7.51}$$

Below the critical field when the particle is not rotating, the particle moves with its standard electrophoretic velocity. Above the critical field when the particle is rotating, the ionic charge distribution around the particle breaks symmetry and the particle velocity has a component orthogonal to the applied field, *i.e.* the electrohydrodynamic Magnus effect. The Magnus velocity orthogonal to the field increases with increasing field, saturating at a value of $U_{\perp,max} = 2\varepsilon_f \zeta_0 E_c / \eta$. The electrophoretic velocity in the field direction decreases with increasing field. Because accumulated charge in the double layer is swept away by convection as E_0 gets large, the electric field generated from the initial induced charge q_{init} due to $\mathbf{E}_0$ is unscreened. The particle is a conductor, so unscreened field lines are all normal to the particle surface so that $\mathbf{E}_t$ and therefore $U_{\parallel}$ vanish as $E_0 \to \infty$.

Results from simulations of different particle sizes and charges are shown in Figure 7.7 along with the Debye-Huckel-Stern theoretical predictions. The theory slightly underpredicts the value of the critical field, but the predictions agree well with the simulation results. The dipole strength decreases with field as the particle rotates and moves off the field axis with an angle θ to supply the electric torque sustaining rotating. The deviation angle has a maximum at intermediate E_0 but eventually the dipole aligns with the field at large E_0 where polarization from E_0 dominates polarization from the ions. However, there is always a finite component of S (unnormalized) orthogonal to the field, so the angular velocity Ω increases linearly with E_0. S and θ increase as a increases, but Ω is independent of particle size at large E_0, consistent with (7.44). The theory overpredicts the angular velocity a bit, which has also been observed in experiments.[285] For particles with small net charges q_0, the Quincke rotation dynamics and steady-states are identical to that of an uncharged particle. As q_0 increases, the net charge begins to hinder Quincke rotation, suppressing it altogether for sufficiently large charges. Like the net charge effects discussed for ICEP, q_0 hinders charging when nonlinear

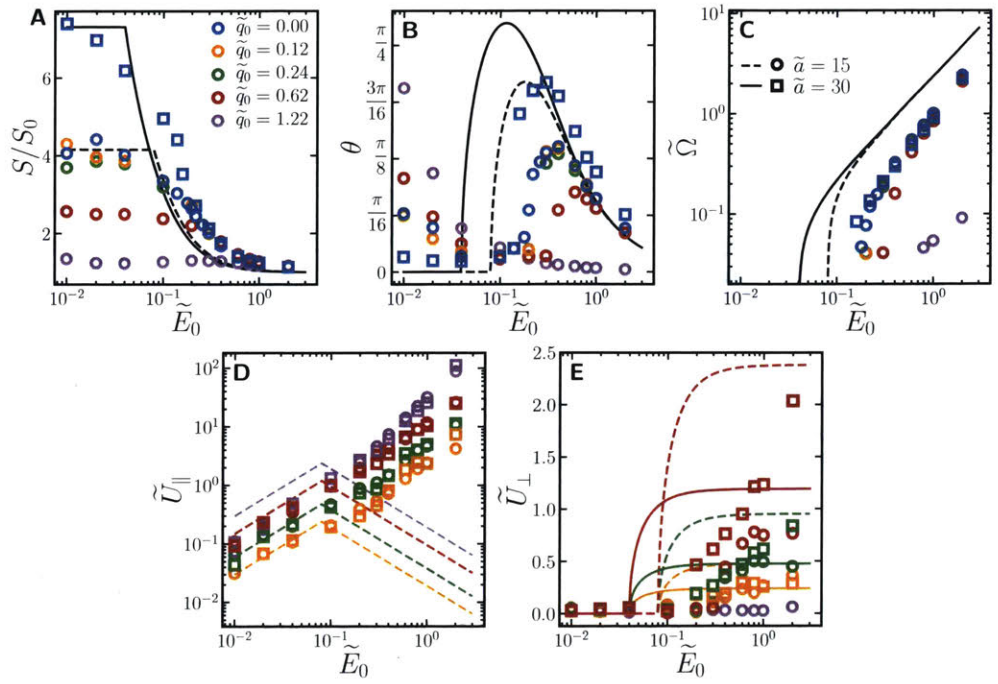

Figure 7.7: The normalized dipole strength S/S_0 (**A**), deviation angle θ relative to the field (**B**), angular velocity $\widetilde{\Omega}$ (**C**), electrophoretic velocity $\widetilde{U}_{\parallel}$ (**D**), and Magnus velocity $\widetilde{U}_{\perp}$ (**E**) for different particle sizes $\widetilde{a}$ (different shapes) and net charges $\widetilde{q}_0$ (different colors) as a function of external field $\widetilde{E}_0$ from simulation (symbols) and Debye-Huckel-Stern theory (lines).

steric interactions occur in the ion double layer or when convection is significant. Because Quincke rotation is coupled to the charging process, it is hindered at large q_0 as well. The Magnus velocity increases with E_0 above E_c until it saturates at a plateau value $U_{\perp,\max}$ at large E_0. For small q_0, the predicted $U_{\perp,\max}$ matches our simulation results very well. Because $U_{\perp,\max} \sim E_c \sim a^{-1}$, the equation (7.51) predicts that the plateau Magnus velocity decreases with particle size, while our simulations show that $U_{\perp,\max}$ generally increases with a. The theory also predicts that the electrophoretic velocity $U_{\parallel}$ above the critical field decreases with increasing E_0 due to the dwindling tangent electric field $\mathbf{E}_t$ as rotation hinders ionic screening in the inner region. However, we observe a linear increase in $U_{\parallel}$ with E_0 and no dependence on a in the simulations, and the classical electrophoretic velocity formula (7.29) seems to hold even while the particle is rotating. This is surprising because if the surface charge is unscreened at large rotation rates, the formula for the fluid velocity (7.27) valid at large κ may break down. An approach that accounts for arbitrary screening lengths may improve the predictions,[125,277] but was not pursued here.

Our continuum theory requires numerous approximations to admit analytic solutions, so there are several ways discrepencies with the simulations can emerge. The charge conservation equation neglects surface conduction, which becomes important at large field strengths.[279] Radial diffusion and translational convection are also neglected. The Debye-Huckel-Stern approximation is used for the description of the ions, which does not offer a good description for concentrated electrolytes, as we saw in Figure 7.2 for ICEO. The analysis assumes a very thin double layer relative to the particle size, but the double layer in our simulations has a finite thickness. Finally, Brownian motion of the particle, fluctuations of the induced surface charge distribution, and fluctuations of the ion cloud are not incorporated in the model (7.32) so that the dynamics are completely deterministic. Even neglecting all these effects, our simple theory seems to be quite accurate.

We can solve (7.38) numerically for the Gouy-Chapman and Carnahan-Starling models to investigate how nonlinearities in the description of the ions affect Quincke rotation. These results are shown in Figure 7.8. The Debye-Huckel solution in the rotating regime $E_0 > E_c$ forms a curve $S(E_0)$ that can be extrapolated

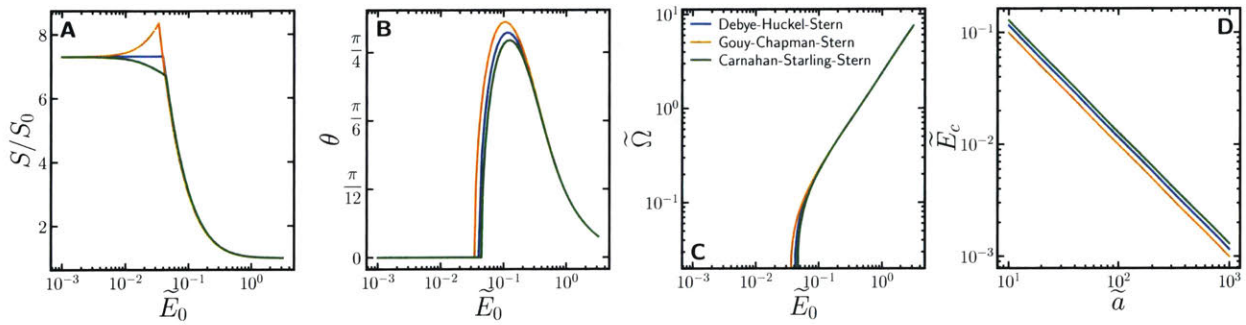

Figure 7.8: Theoretical predictions for the normalized dipole strength S/S_0 (**A**), deviation angle θ relative to the field (**B**), and angular velocity $\widetilde{\Omega}$ (**C**) as a function of external field $\widetilde{E}_0$ for different ion models. **D.** The critical field $\widetilde{E}_c$ as a function of particle size $\widetilde{a}$.

into the nonrotating regime $E_0 < E_c$. This curve acts as a limit of stability for the various ion models. If the ion model predicts a dipole that is smaller than $S(E_0)$, the nonrotating state is stable for that ion model. Quincke rotation occurs once the dipole crosses $S(E_0)$. From Figure 7.2, the Gouy-Chapman model predicts an exponentially growing dipole moment, so the critical field is smaller than that predicted from equation (7.42). Similarly, the Carnahan-Starling model predicts a decreasing dipole moment due to steric hinderance among ions, so the critical field is larger that (7.42). For ICEO and ICEP, the induced zeta potential grew as $\zeta \sim aE_0$ and the Debye-Huckel description failed at large E_0. For Quincke rotation, convection removes ions from the double layer and the induced zeta potential *decreases* with E_0 above E_c. Thus, the Debye-Huckel approximation holds for rotating particles at large E_0. The maximum ζ occurs at E_c, which decreases with $\sim a^{-1}$. Because $\zeta \sim a$ below $E_0 < E_c$, the zeta potential at the critical field is independent of particle size, and the relative predictions for E_c among the models are unchanged for any particle size. This critical ζ appears not to be too large, so that including nonlinearities in the ion model does not significantly alter the predictions for Quincke rotation.

For typical values in water, the critical field (7.42) can be written as a voltage drop across the particle

$$E_c \approx \frac{0.075\,\mathrm{V}}{a}. \tag{7.52}$$

For a 1 µm particle, this corresponds to $E_c \approx 750\,\mathrm{V\,cm^{-1}}$. The plateau value of the Magnus velocity is equal to twice the electrophoretic velocity at the critical field, so for a particle with a net zeta potential $\zeta_0 \approx 50\,\mathrm{mV}$, $U_\perp \approx 5$ mm·s, which is quite fast for a small colloid.

7.3 Active Propulsion of Colloidal Particles *via* the Electrohydrodynamic Magnus Effect in Alternating-Current Electric Fields

Biological systems contain a vast array of entities that consume energy to propel themselves, from the macroscopic scale of animals roaming about to the microscopic scale of swimming bacteria.[15] This has inspired many synthetic variants of dispersions of "active" particles that convert energy into self-locomotion by swimming,[98,103,104] growing,[109] or rotating.[105–108,292] Whether composed of biological or synthetic constituents, this class of materials is called "active matter". Because active particles dissipate energy, they are free from the constraints of equilibrium thermodynamics and dynamically self-assemble into a rich assortment of out-of-equilibrium materials,[110] including flocks,[111,112] nematics,[109] and crystals.[113,114] These phases have useful collective transport properties and have been used to drive microscopic motors,[308,309] significantly increase the translational velocity of flocks of microrollers,[115] understand enhanced mixing in cells,[116,117] and transport passive cargo.[101,118] To utilize active matter for such practical applications on larger scales, we must consider a few engineering challenges. An ideal active matter system should be inexpensive, consist of simple components, allow for robust control over the activity, and retain activity for long periods of time.

Active matter systems constructed with biological components, like swimming bacteria[308–312] or kinesin motors[109,313] can be time-consuming and expensive to grow and/or obtain in purified form and lose activity as they consume their fuel (unless the fuel is continually injected). Janus or asymmetrically-shaped particles have been designed to selectively catalyze a reaction on only a portion of the particle surface, propelling the particle *via* diffusiophoresis[103,113,314] or electromigration.[315,316] However, these particles too lose activity as they consume reactants and synthesizing the complex particle features is not easily scalable,[22] so the particles can be expensive to produce in large quantities.

Particle motion driven by electric fields offers a promising candidate for active matter because particles retain activity as long as the field is on and the activity can easily be controlled with the external field strength and orientation. *Direct* particle transport in electric fields, like electrophoresis of charged particles in a direct-current (DC) field, dielectrophoresis of polarized particles in a field gradient, or electrorotation of asymmetric particles in a rotating field, result in particle motion but not particle activity, as there is no *self*-locomotion. Motion orthogonal to the driving field is decoupled from the field direction and can serve as a form of self-propulsion to provide particles with activity. Polarizable particles that are anisotropic in shape[104,292] or in dielectric properties,[293] move orthogonally to an electric field during ICEP due to asymmetric electroosmotic flows.[279,280,291] However, scalable fabrication of cheap anisotropic particles is challenging.[22] Isotropic particles can move orthogonally to a driving field near a wall[288,289] or in ratched microchannels,[294,295] but this imposes constraints on the dispersion geometry.

In the previous section, we discussed motion orthogonal to a driving electric field for isotropic spheres in the bulk *via* the electrohydrodynamic Magnus effect. In this section, we propose the electrohydrodynamic Magnus effect as a mechanism for generating active matter dispersions of isotropic, spherical, polarizable particles in bulk electrolytes. Such particles are inexpensive and easy to synthesize, easy to control with the external field, do not lose activity as long as the field is sustained, and do not require specific boundary geometries. Thus dispersions of particles with the EHM effect are a possible route to a robust, scalable active matter material.

7.3.1 Electrohydrodynamic Magnus Effect in AC Fields

Above the critical field strength E_c, a conductive colloid in an electrolyte will undergo spontaneous Quincke rotation with angular velocity $\boldsymbol{\Omega}$. The axis of rotation is always orthogonal to the applied field $\mathbf{E}_0$, but the direction is random because the rotation is driven by an instability in the fluctuating dipolar structure of the surrounding ionic double layer. If the rotating particle is also charged, it will translate in the field direction with velocity $\mathbf{U}_{\parallel}$ due to electrophoresis and orthogonally to the field with velocity $\mathbf{U}_{\perp}$ due to the electrohydrodynamic Magnus effect. From (7.51), the EHM velocity $\mathbf{U}_{\perp}$ is orthogonal to both the angular velocity $\boldsymbol{\Omega}$ and the electrophoretic velocity $\mathbf{U}_{\parallel}$, and the directions obey the right-hand rule $\hat{\mathbf{U}}_{\perp} = \hat{\mathbf{U}}_{\parallel} \times \hat{\boldsymbol{\Omega}}$. Because the direction of $\boldsymbol{\Omega}$ is chosen randomly, $\mathbf{U}_{\perp}$ is also oriented in a random direction. $\mathbf{U}_{\perp}$ is not directed by the field and acts as a self-propulsion (*i.e.* the EHM particles "swim"). The particle/double layer assembly undergoes rotational diffusion, so the swim direction wanders over time. Thus, the Magnus swimmers behave like active Brownian particles.

In DC fields, electrophoresis will eventually drive accumulation of ions and particles at the electrodes supplying the field. Not only does this deplete the dispersion of the active particles, but strong interactions with the ions can lead to uncontrolled electroosmotic flows, electrochemical reactions, and dendrite formation at the electrode surfaces. Thus, DC fields are not suited for active matter applications. In AC fields, where the sign of the electric field flips cyclically over time, net electrophoresis is suppressed over many cycles. There are several possible time signals that could be used to vary the field including sinusoid or triangle waves, but here we consider a square wave where the electric field instantaneously flips direction. Within a cycle, if the field is flipped $\mathbf{E}_0 \to -\mathbf{E}_0$, the direction of the electrophoretic velocity flips $\mathbf{U}_{\parallel} \to -\mathbf{U}_{\parallel}$. When the Quincke rotation instability is initially tripped, the structure of the ionic double layer is isotropic in the direction orthogonal to the field, so the direction of $\boldsymbol{\Omega}$ is chosen randomly. This breaks the symmetry of the double layer, and the net dipole of the polarized ion cloud has a component that points orthogonally to the field. Because of this break in symmetry, the particle does not pick a new random axis of rotation when the field is flipped. Instead, the ions all flip their direction of motion and find a preferred dipole orientation

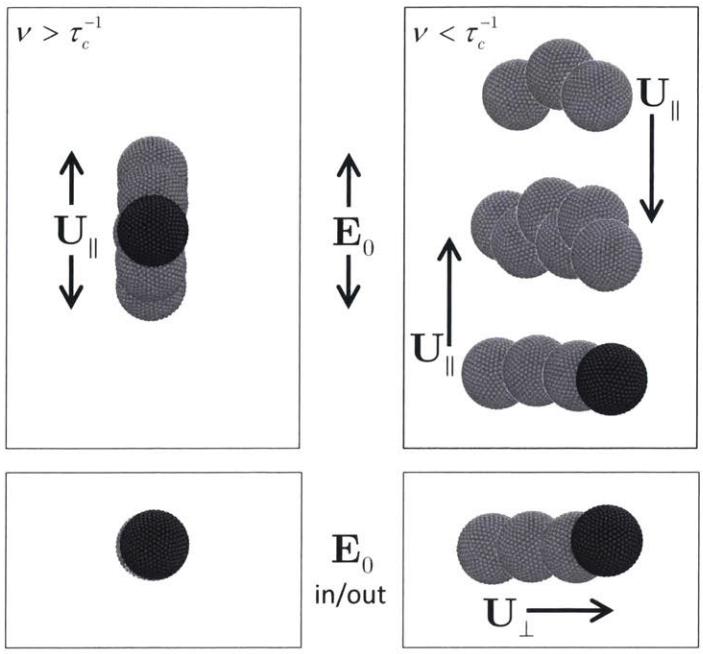

Figure 7.9: Snapshots of a nonrotating (left) and rotating (particle) in an AC field from a side view (top row) and a top-down view (bottom row) with $\widetilde{a} = 15$, and $\widetilde{E}_0 = 1.0$. At large frequencies $\nu > \tau_c^{-1}$ (left), the particle does not have enough time to charge up and has no net angular or translational velocity. At lower frequencies $\nu < \tau_c^{-1}$ (right), that particle has enough time to charge up and trip the Quincke rotation instability, acquiring a net angular velocity $\mathbf{\Omega}$ and Magnus velocity $\mathbf{U}_\perp$ but no net electrophoretic velocity $\mathbf{U}_\parallel$.

that depends on their previous orientation, and so the angular velocity flips sign $\mathbf{\Omega} \to -\mathbf{\Omega}$. Because the direction of the Magnus velocity obeys the right-hand rule $\hat{\mathbf{U}}_\perp = \hat{\mathbf{U}}_\parallel \times \hat{\mathbf{\Omega}}$, the sign flips of $\mathbf{U}_\parallel$ and $\mathbf{\Omega}$ cancel out, and the Magnus direction remains unchanged $\mathbf{U}_\perp \to \mathbf{U}_\perp$ when the field is flipped. Therefore, the Magnus velocity persists over many AC field cycles, as confirmed from our simulations in Figure 7.9. AC fields suppress net particle electrophoresis and net ionic current while maintaining a steady Magnus velocity, making them ideal for active matter applications.

As we reported in section 7.2, Quincke rotation occurs when the orientation of the dipole moment in the polarized ionic double layer (pointed opposite the field) becomes unstable as the dipole strength gets large. When the field is first applied, there is an induction time τ_i for the Quincke rotation instability to occur as the particle and ionic double layer charge up. If the frequency ν of the AC field is small compared to τ_i^{-1}, the particle and double layer have enough time to charge up during a field cycle to trip the Quincke rotation instability and drive orthogonal Magnus motion. However, if ν too large compared to τ_i^{-1}, the particle and double layer do not have enough time to charge up during a field cycle. The Quincke rotation instability is never tripped, and there is no orthogonal Magnus velocity. Thus, the AC frequency serves as a switch that can turn on or off the active Magnus velocity, as shown in Figure 7.9. The critical frequency ν^*, above which the Magnus velocity turns off, is a crucial parameter to understand and predict.

Because Quincke rotation is an instability and is induced by fluctuations of the ion cloud, we cannot predict the induction time τ_i from the deterministic PDE (7.38). However, the larger the induced dipole, the smaller the fluctuation needed to drive the instability, so τ_i is related to the charging time τ_c of the *nonrotating* solution with $\Omega = 0$. Figure 7.6 shows that, at large fields, τ_i is only slightly larger than τ_c. We analyzed the nonrotating charging dynamics in detail in section 7.1. In the Debye-Huckel limit, the charging time is $\tau_c = \varepsilon\kappa a/2\sigma$, predicting no dependence on E_0 and a linear dependence on a. However, nonlinear effects are important at the zeta potentials induced above E_c and Figure 7.2E shows $\tau_c \sim E_0^{-1}$ at large E_0 when steric interactions among ions are considered. In this regime, polarization due to the double layer is small compared to polarization due to the external field and charging is limited only by how quickly the external field can

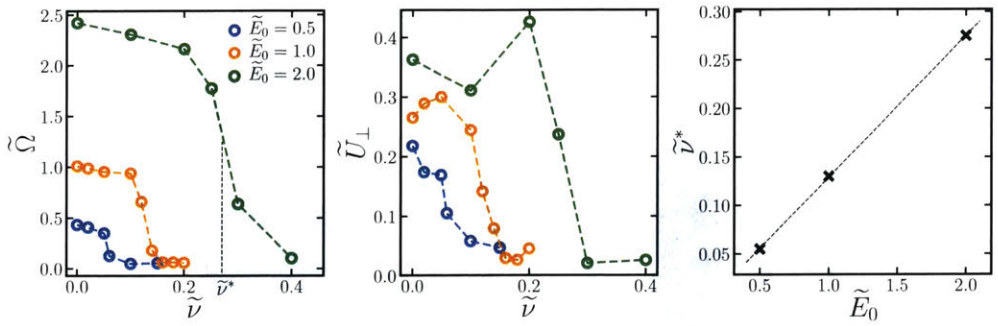

Figure 7.10: The angular velocity $\widetilde{\Omega}$ (left) and Magnus velocity (middle) as a function of AC field frequency $\widetilde{\nu}$ for different field strengths $\widetilde{E}_0$ (different colors) at fixed $\widetilde{a} = 15$ and $\widetilde{q}_0 = 0.12$. The critical frequency $\widetilde{\nu}^*$ where Quincke rotation and the Magnus effect shut off as a function of $\widetilde{E}_0$ is shown on the right along with a linear fit (dashed line).

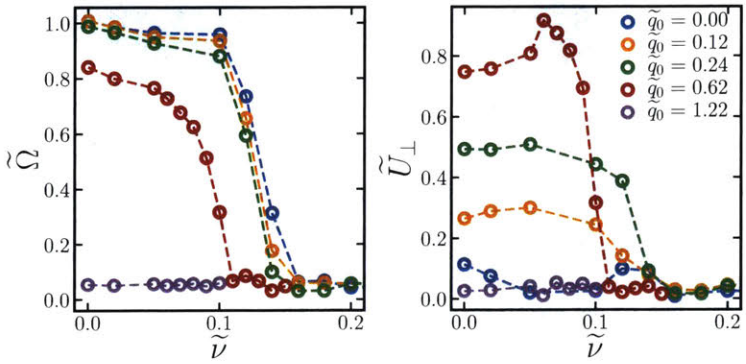

Figure 7.11: The angular velocity $\widetilde{\Omega}$ (left) and Magnus velocity (right) as a function of AC field frequency $\widetilde{\nu}$ for different net charges $\widetilde{q}_0$ (different colors) at fixed $\widetilde{a} = 15$ and $\widetilde{E}_0 = 1.0$.

shuttle ions electrophoretically to the particle surface. Figure 7.6 confirms that the rotation induction time also decreases as $\tau_i \sim E_0^{-1}$ at large E_0. If $\nu^* \sim \tau_c^{-1}$, then the critical frequency should increase as $\nu^* \sim E_0$ at large E_0 and decrease with particle size as $\nu^* \sim a^{-1}$. Figure 7.10 shows the angular velocity and Magnus velocity as a function of AC frequency for different field strengths. The critical frequency ν^* to suppress Quincke rotation and the EHM effect indeed increases as $\nu^* \sim E_0$. The transition from rotating to nonrotating occurs over a narrow region of $\widetilde{\nu}$. Because of the sharp transition, ν really does act as a "switch" to turn on and off the Magnus effect. Figure 7.11 shows the frequency dependence at fixed E_0 and varying net surface charge density q_0. As we saw in Figure 7.7, small $\widetilde{q}_0$ does not affect Ω or $U_\perp$, but larger $\widetilde{q}_0$ hinders charging and rotation and pushes ν^* to smaller values.

The charging time grows linearly with particle size $\tau_c \sim a$, so the critical frequency goes as $\nu^* \sim a^{-1}$. For a 1 µm particle in water, a typical charging time is $\tau_c \sim 10^{-5}$ s.[279] τ_i is a few times larger than τ_c, so the critical frequency is in the 10 – 100 kHz range, which is typical of high frequency experimental setups.[162]

7.3.2 Active Diffusivity

The axis of rotation, and therefore the Magnus direction, is chosen randomly when the rotational instability occurs. Any direction orthogonal to the field is a stable solution to the PDE (7.37) and is equally likely. Over long time scales, the axis of rotation and the Magnus velocity wander as the colloid-double layer assembly undergoes rotational diffusion. This rotational diffusion occurs about the field axis $\hat{\mathbf{E}}_0$, as $\boldsymbol{\Omega}$ and $\mathbf{U}_\perp$ are always oriented orthogonal to $\mathbf{E}_0$. Rotational diffusion is negligible about the axes orthogonal to $\hat{\mathbf{E}}_0$ compared to the angular velocity of Quincke rotation. The associated rotational diffusivity D_r has

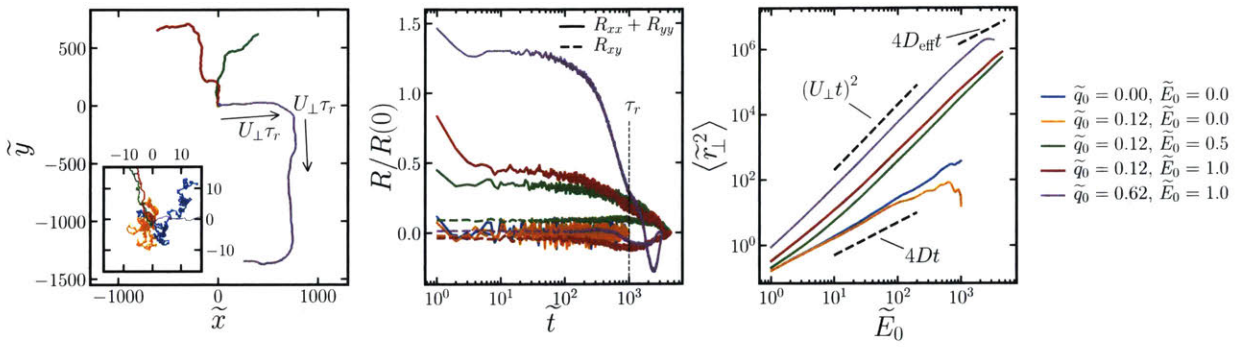

Figure 7.12: Particle trajectories (left), normalized velocity autocorrelation functions(middle), and mean squared displacements (right) for particles of different charge $\widetilde{q}_0$ in AC fields of different strengths $\widetilde{E}_0$ at frequency $\widetilde{\nu} = 0.02$ for rotating and nonrotating particles. Rotating particles run for a length $U_\perp\tau_r$ before reorienting every τ_r, so the long time $t \gg \tau_r$ dynamics are diffusive with an effective diffusivity $D_{\rm eff}$.

dimensions of inverse time, defining a time scale for rotational diffusion as $\tau_r \equiv 1/D_r$.

Figure 7.12 shows trajectories, velocity autocorrelation functions,

$$\mathbf{R}(\tau) \equiv \langle \mathbf{U}_\perp(t)\mathbf{U}_\perp(t+\tau)\rangle, \tag{7.53}$$

and mean-squared displacements (MSD) in the plane orthogonal to $\mathbf{E}_0$,

$$\langle r_\perp^2\rangle(\tau) \equiv \langle (\mathbf{x}_\perp(t+\tau) - \mathbf{x}_\perp(t))\cdot(\mathbf{x}_\perp(t+\tau) - \mathbf{x}_\perp(t))\rangle \tag{7.54}$$

where $\mathbf{x}_\perp \equiv \mathbf{x}\cdot(\mathbf{I} - \hat{\mathbf{E}}_0\hat{\mathbf{E}}_0)$ is the component of the particle position $\mathbf{x}$ orthogonal to the field and the brackets indicate an ensemble average over time. This is similar to viewing the particle along the field axis, as in Figure 7.9, where only motion orthogonal to the field is observable. Nonrotating particles with no Magnus velocity only move orthogonally to the field diffusively, so their velocities are uncorrelated ($R \approx 0$ on the simulation time scales), and the MSD grows linearly with time as $\langle r_\perp^2\rangle \sim Dt$. From the inset to Figure 7.12, this diffusion is slow and particles do not move far over the duration of our simulations. For a rotating particle, on time scales less than τ_r, the orientation of $\mathbf{\Omega}$ is highly correlated in time as is the direction of $\mathbf{U}_\perp$, so R is constant. Because the orientation of the Magnus velocity doesn't change much for $t < \tau_r$, the particle appears to swim in a constant direction with constant velocity $U_\perp$. This ballistic motion yields an MSD that goes as $\langle r_\perp^2\rangle = (U_\perp t)^2$ for $t \ll \tau_r$. On time scales much larger than τ_r, the orientation of $\mathbf{\Omega}$ is uncorrelated in time, as is the direction of $\mathbf{U}_\perp$, due to rotational diffusion, and R drops to zero. Figure 7.12 shows that the particle trajectories wander in different directions over long time scales. Because the particle is traveling in random, uncorrelated directions, the dynamics are diffusive, and the MSD scales as

$$\langle r_\perp^2\rangle(\tau) = 4D_{\rm eff}\tau, \quad t \gg \tau_f, \tag{7.55}$$

where $D_{\rm eff}$ is the effective diffusivity of the Magnus swimmer. The effective diffusivity can equivalently be computed in terms of the integral of the trace of the velocity autocorrelation function,

$$D_{\rm eff} = \frac{1}{2}\mathrm{Tr}\int_0^\infty d\tau\, \mathbf{R}(\tau). \tag{7.56}$$

Because of the particle's activity this effective diffusivity is much larger than the diffusivity of inactive particles, which is close to the Stokes-Einstein value $D_0 = k_BT/6\pi\eta a$.

Because the orientations of $\mathbf{U}_\perp$ are uncorrelated for $t \gg \tau_r$, we can imagine the Magnus swimmer as a "run-and-tumble" active particle. That is, the particle travels at a constant velocity $\mathbf{U}_\perp$ for τ_r and then "tumbles" and chooses a new, random orientation for $\mathbf{U}_\perp$ every τ_r. These run-and-tumble dynamics are

identical to a two-dimensional random walker taking steps of run length $L = U_\perp \tau_r$ every τ_r.[114] Therefore, the effective diffusivity is

$$D_{\text{eff}} = \frac{U_\perp^2 \tau_r}{4}. \tag{7.57}$$

To predict D_{eff}, we need estimates for $U_\perp$ and τ_r. In the Debye-Huckel limit, we derived an expression for $U_\perp$ in equation (7.51) that is in reasonable agreement with our simulations in Figure 7.7. We do not have an analytic expression to derive τ_r for the particle/double layer assembly undergoing Quincke rotation. In the simplest case, we can estimate that the assembly rotates with a diffusivity similar to that of an isotropic sphere, $D_r = k_B T / 8\pi\eta a^3$.[126] Thus, the effective diffusivity is,

$$D_{\text{eff}} = \frac{128\pi a \sigma \zeta_0^2}{\kappa^2 k_B T} \left(1 - \left(\frac{E_c}{E_0}\right)^2\right), \tag{7.58}$$

and is shown in Figure 7.13. Unlike the Stokes-Einstein diffusivity $D_0 \equiv k_B T / 6\pi\eta a$, D_{eff} *increases* linearly with a. Though the Magnus velocity decreases linearly as $U_\perp \sim a^{-1}$, the reorientation time increases more strongly as $\tau_r \sim a^3$. The Magnus swimmer spends more time traveling in the same direction before it tumbles to a new orientation, and the net diffusive motion is enhanced. D_{eff} also depends quadratically on the particle charge as $U_\perp \sim \zeta_0$, though large q_0 can suppress Quincke rotation and reduce D_{eff}. Above E_c, D_{eff} increases with E_0 and saturates to a constant value at large E_0. This allows the diffusivity of the particles to be controlled with the external field strength or turned on and off with the field frequency. Relative to the Stokes-Einstein diffusivity,

$$\frac{D_{\text{eff}}}{D_0} = \frac{728\pi^2 \eta a^2 \sigma \zeta_0^2}{\kappa^2 (k_B T)^2} \left(1 - \left(\frac{E_c}{E_0}\right)^2\right). \tag{7.59}$$

For dilute electrolytes, the conductivity can be estimated as $\sigma = 2 n_i q_i^2 / 6\pi\eta a_i$.[279] At large E_0, the saturation value is

$$\frac{D_{\text{eff}}}{D_0} = \frac{128\pi \varepsilon_f a^2 \zeta_0^2}{a_i k_B T}. \tag{7.60}$$

Therefore, as the particle size grows, the EHM effect yields significantly enhanced diffusion, orders of magnitude larger than D_0. If a Stern-layer is including, the effective diffusivity is

$$\frac{D_{\text{eff}}}{D_0} = \frac{728\pi^2 \eta a^2 \sigma (1 + \kappa a_i) \zeta_0^2}{\kappa^2 (k_B T)^2} \left(1 - \left(\frac{E_c}{E_0}\right)^2\right). \tag{7.61}$$

We compare the diffusivities extracted from the simulations with those predicted from the Debye-Huckel theory:

$\widetilde{q}_0$	$\widetilde{E}_0$	D_{eff}/D_0 (sim.)	D_{eff}/D_0 (Debye-Huckel)
0.12	0.5	700	2100
0.12	1.0	990	2100
0.62	1.0	3500	5.2×10^4

The orders of magnitude are fairly consistent, with the Debye-Huckel predictions overestimating the simulation results by only a factor of 2–3 at small $\widetilde{q}_0$.

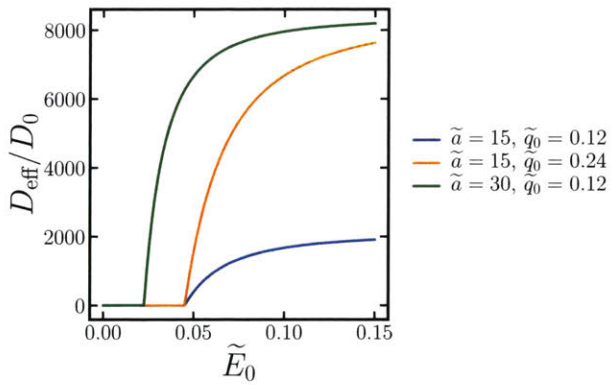

Figure 7.13: The active diffusivity dimensionless on the particle Stokes-Einstein diffusivities for particles of different charge $\widetilde{q}_0$ and radius $\widetilde{a}$ in AC fields $\widetilde{E}_0$.

Chapter 8

Conclusions and Outlooks

Colloidal dispersions have been engineered to self-assemble into a diverse array of functional materials important for society. The types of materials we can manufacture are determined by the kinds of particles we synthesize, which dictate the thermodynamic interactions that drive structure formation, and the fabrication protocol, which affects the assembly kinetics. In Chapter 3, we discussed how electric and magnetic fields are particularly effective for self-assembling dispersions of dielectric and paramagnetic nanoparticles. The particle interactions are *induced* by the field, so the field can be used to control the interparticle potential and change the equilibrium structure. Because the fields are generated *external* to the dispersion, they are easy to control, and one of their promising features is the ability to drive dispersions out of equilibrium by varying the external field in time. Without the constraints of equilibrium thermodynamics, out-of-equilibrium systems assemble into more complicated structures with more robust and useful material and transport properties than their equilibrium counterparts. To leverage these unique properties in real applications, we need fundamental, predictive theories to guide experimental designs. In this thesis, we carried out a systematic investigation of the assembly and dynamics of colloidal dispersions in time-varying external fields using computer simulations, equilibrium and nonequilibrium thermodynamic theories, and electro-/magnetokinetic theory.

Not surprisingly, computational models of electric and magnetic dispersions are difficult to develop. As we discussed in Chapter 2, the particle surfaces impose complicated boundary conditions that preclude analytic solutions to the underlying electro-/magnetostatic PDEs, so various approximate solutions have been proposed. Generally, more severe approximations lead to simpler solutions that are computationally inexpensive, but have limited accuracy. In fact, nearly all computational and theoretical work use the simplest possible model, where each particle in the dispersion behaves a single, isolated particle. In Chapter 3, we showed that this "constant dipole" model leads to predictions that do not agree with experiments. Constant dipole models predict that, at constant volume fraction ϕ, a fluid to BCT transition occurs at a single value of βE_0, for *all* values of the contrast parameters β. However, the experiments in Figure 4.7 show that the value of βE_0 at the fluid/BCT transition *decreases* with β and are not close to the constant dipole predictions. Therefore, a constant dipole description is not satisfactory for studying the assembly of electric and magnetic particles.

More complicated models that accurately represent real dispersions are computationally expensive. Because of this computational burden, higher fidelity models have only been used for small systems of a handful of particles or large systems for a small number of time steps. Neither of these are appropriate for the large length and time scales involved in assembly. We were faced with the challenge of formulating and implementing an efficient numerical scheme for electric/magnetic dispersions that was accurate enough to reproduce experimental results, but fast enough to reach the necessary time and length scales for assembly. Our solution to this challenge is detailed in Chapter 2 and Chapter 4. We constructed a multipole expansion to the electro-/magnetostatic governing equations, where the polarization moments induced in one particle generate fields that affect the polarization moments of all the other particles. Because of this "mutual polarization", the interactions among particles are many-bodied, and depend intimately on the value of β. Though we derived expressions for the moment expansion up to the quadrupole level, we choose to truncate

this at the dipole level in practice, which we refer to as a "mutual dipole model". We developed an efficient numerical scheme for computing the dipole moments and interparticle forces. This scheme involves an iterative solution to the electro-/magnetostatic PDE that leverages a spectrally-accurate Ewald summation method to propogate dipolar interactions among particles. We implemented this numerical method on GPUs in two plugins for the software suite HOOMD-Blue. The `MutualDipole` plugin considers charge-free, polarizable particles of arbitrary β. The `Dielectric` plugin considers charged and polarizable particles of arbitrary β. We also extended our analysis to arbitrarily-shaped conductors in Section 2.4. Here, we used an immersed boundary method to construct conducting bodies out of small beads constrained to move together rigidly. This method can incorporate an arbitrary number of polarization moments at the increased computation cost of resolving the induced charge distribution on the body's surface. An efficient GPU implementation is provided in the `ConductorRigid` plugin and used to study the electrokinetic behavior of colloids dispersed in electrolytes in Chapter 7.

In Chapters 3 and 5, we investigated toggled fields as a means to improve the self-assembly of colloidal crystals. Chapter 3 considered a simple model of toggled depletion attractions, which are isotropic and short-ranged, while Chapter 5 examined the more complicated case of toggled field-directed interactions, which are anisotropic and long-ranged but are easy to implement experimentally. In both cases, particles avoided kinetic arrest and assembled into larger crystals with many fewer defects when the field was toggled compared to fields held steady. Additionally, the crystallization rate was much faster in toggled fields. For assembly in steady fields, there is usually a tradeoff between the quality of the final product and its rate of formation. Toggled fields bypass this tradeoff and are capable of assembling high-quality crystal quickly, making them ideal for inexpensive, scalable synthesis of functional nanomaterials. Both the assembled structures and their assembly mechanism are controlled by the toggling protocol, so the toggle parameters can be optimized for maximum quality and yield.

We proved from first-principles that structures that assemble in toggle fields must satisfy equality of time-averaged chemical potential $\overline{\mu}$ and time-averaged pressure $\overline{P}$ for two phases to coexist at periodic steady-state. This is an out-of-equilibrium analogue to the typical coexistence criteria from equilibrium thermodynamics. The time-averaged equations of state can be constructed from equilibrium equations of state valid for steady fields. This allows a periodic-steady-state diagram to be constructed that predicts coexisting densities and structures as a function of the toggle parameters. By evaluating the time-averaged equations of state, we computed the PSS diagrams for toggled depletion and toggled external field systems. The EoS for equilibrium depletion dispersions was already known,[178] but we developed new EoS for dispersions of mutually polarizable particles in external fields in Chapter 4. The theoretical predictions, which contain no fitting parameters, agree very well with phase coexistence observed in our simulations. The duty cycle $\xi \equiv t_{\text{on}}/(t_{\text{on}}+t_{\text{off}})$ acts as a thermodynamic control variable that can induce phase separation and change the coexisting structures. We also developed phenomenological models to describe the crystallization dynamics for two observed kinetic mechanisms: spinodal-decomposition-like coarsening and nucleation and growth. These theoretical frameworks can be leveraged to guide experimental design of efficient fabrication schemes utilizing toggled fields.

Toggled fields stabilize structures that are only metastable and not observed with steady fields. An interesting example of this is the spontaneous symmetry-breaking and formation of BCO crystal in toggled fields, whereas BCT is the thermodynamically stable crystal structure in steady fields. The lattice parameters of the BCO structure can be continuously transmuted by changing the duty cycle and match the parameters predicted theoretically by minimizing the free energy of a metastable BCO lattice. This is one example where a more complex crystal, BCO, is assembled by toggling between two states that prefer simpler crystals, BCT and HCP/FCC. We believe this idea can be extended to form other exotic crystal structures by changing the two toggle states. For photonic applications, the diamond lattice is predicted to have optimal optical properties, so colloidal diamond is particularly sought after.[317–319] This complex lattice has been formed lithographically,[319] self-assembled using highly anisotopic particles with tetragonal valence,[20] and assembled electrostatically with binary mixtures of nanoparticles with precisely controlled stoichiometry, charge, and size. None of these techniques are particularly scalable, so efficient production of colloidal diamond is not yet possible. One strategy toward scalable diamond synthesis is to use toggled interactions which may allow simpler, inexpensive particles to form diamond. In fact, even isotropic particles can form quite complicated

crystal structures, as long as the interparticle potential can be precisely tuned.[28–30] The goal would be to use the toggle parameters to construct a time-averaged interparticle potential for which the the diamond lattice is at least metastable. Synthesizing colloidal diamond from toggled assembly of inexpensive particles would enable efficient production of high-performance photonic materials.

Toggling the external field is not the only possible form of time-variation. In Chapter 6, we examined dispersions of paramagnetic particles in rotating magnetic fields. Like toggled fields, rotating fields also drive dispersions out of equilibrium, and the structure and dynamics can be tuned using the rotating frequency ν, an extra control knob beyond the normal thermodynamic variables. We showed that the rotating field greatly increases the self-diffusivity compared to steady fields. The diffusivity attains a maximum value well above the Stokes-Einstein diffusivity at intermediate rotation frequencies. This enhanced diffusion is predominately a hydrodynamic effect, as rotating aggregates act as "magnetic stir bars", in agreement with the enhanced tracer diffusion observed in experiments.[93,94] We used our results to develop a simple phenomenological model for magnetophoresis through porous media in rotating field. The model predicts that increased diffusion also enhances the magnetophoretic mobility through porous media in rotating fields compared to steady fields. Experiments with rotating fields have already demonstrated improved magnetophoretic flux through porous media.[38,102] This makes magnetophoresis in rotating fields well-suited for targeted therapeutic applications, where magnetic particle carrying drugs and other cargo must navigate dense porous tissue on their way to a target site. Our analysis shows that the magnetophoretic flux can be optimized at intermediate frequencies, and the model we developed gives predictions for the optimal experimental conditions, *i.e* frequencies, field strengths, concentrations, *etc.*

Toggling and rotating the field are two examples where dispersions are driven out of equilibrium because the time-varying field induced time-varying particle interactions. A different class of out-of-equilibrium material is a dispersion of "active" particles that convert energy into self-locomotion. Like toggled and rotating field dispersions, the dynamics and assembly of active matter systems do not suffer the constraints of equilibrium thermodynamics and have useful collective properties. However, traditional active dispersions are composed of biological material or complicated synthetic particles, which are expensive to produce and tend to loss activity as they consume their fuel. In Chapter 7, we proposed generating active matter from dispersions of conducting colloidal spheres undergoing motion orthogonal to a driving AC electric field *via* the electrohydrodynamic Magnus effect. Above a critical field strength E_c, the orientation of the polarized double layer around the colloids becomes unstable, and small fluctuations drive uncharged spherical particles to break symmetry and spontaneously rotate about an axis orthogonal to the applied field, a phenomenon called Quincke rotation. If the particles are also charged, their electrophoretic motion couples with Quincke rotation to propel the particle in a direction orthogonal to the driving electric field, an electrohydrodynamic analogue to the Magnus effect. Typically, motion orthogonal to the field requires anisotropy in particle shape, dielectric properties, or boundaries to break symmetry. Here, the EHM effect occurs from bulk, isotropic spheres, with the Quincke rotation instability providing broken symmetry driving orthogonal motion. In an AC field, net electophoretic motion in the field direction is suppressed, but the Magnus velocity persists over many field cycles. The particle only has motion that is decoupled from the field, which acts as a self-propulsion and EHM "swimmers" behave like active Brownian particles.

We derived a continuum electrokinetic theory to describe the electrohydrodynamic Magnus effect that is in good agreement with our simulations. The theory allows us to predict the critical field E_c, the charging time τ_c, and the Magnus velocity $U_\perp$ in terms of system parameters like field strength E_0, particle size a, particle charge, and ion concentration. This yields estimates for the critical AC frequency ν^* above which the EHM effect is switched off. Thus the activity can be controlled externally using E_0 or ν. On long time scales, rotational diffusion causes the propulsion direction of EHM particles to wander, and the long time dynamics are diffusive with an effective "active" diffusivity D_{eff}. By casting the transport in terms of run-and-tumble dynamics, we predict D_{eff} in terms of system parameters. Above E_c, D_{eff} increases with E_0, so the field can be used to tune control the diffusivity of the active dispersion. Unlike typical Stokes-Einstein diffusion, D_{eff} *increases* with particle size.

In addition to active matter applications, the scaling of D_{eff} with particle size can be leveraged for particle separation by the EHM effect. This could be especially useful for situations where particles cannot be

separated electrophoretically, since the electrophoretic velocity of a sphere is independent of particle size. One possible particle separation scheme is a field-flow-fractionation setup, with two possible geometries. First, particles can move electrophoretically down a channel in a DC field while diffusing orthogonally from the EHM effect. Second, particle can be flown down a channel and an AC field applied in the flow direction to induce orthogonal EHM diffusion. In both cases, larger particles move more quickly in the orthogonal direction, so collecting particles in radial bins at some point downstream allows separation by particle size.

Toggled fields, rotating fields, and the electrohydrodynamic Magnus effect all drive dispersions out of equilibrium and, in many cases, improve dispersion properties over their equilibrium counterparts. The theoretical analysis of such systems is challenging and limited predictions have prevented driven suspensions from being leveraged in experiments. To address this, I developed a computational and theoretical framework for the assembly and dynamics of colloidal dispersions in steady and time-varying fields. I hope the tools in this thesis will facilitate further theoretical, computational, and experimental investigations of out-of-equilibrium dispersions driven by external fields.

Appendix A

Real Space Contributions to the Electric/Magnetic Ewald Summations

The real space contributions to the Ewald sums in 2.3 require evaluating inverse transforms,

$$\mathbf{P}_i^r(\mathbf{x}_i) = \frac{1}{\lambda_f} \sum_{\mathbf{n}} \sum_j \mathcal{F}^{-1} \left\{ \frac{e^{i\mathbf{k}\cdot(\mathbf{x}_i - \mathbf{x}_j)}}{k^2} (1-h)\, \mathbf{f}_p \right\} \mathbf{f}_m \cdot \mathbf{m}_j. \tag{A.1}$$

We separate out the first exponential term as this transforms to a delta function,

$$e^{i\mathbf{k}\cdot(\mathbf{x}_i - \mathbf{x}_j)} \rightarrow \delta(\mathbf{x} + \mathbf{r}_{ij}), \tag{A.2}$$

where $\mathbf{r}_{ij} \equiv \mathbf{x}_i - \mathbf{x}_j$. This convolves with the remaining portion of the inverse transform, $\int d\mathbf{y} \delta(\mathbf{x}+\mathbf{r}_{ij})\mathbf{u}(\mathbf{n}-\mathbf{x}) = \mathbf{u}(\mathbf{n}+\mathbf{r}_{ij})$. In practice, we truncate the real space sum to contain terms with pair separations much less than the system size. Only nearest image pairs need be considered, and we can always take $\mathbf{n} = 0$. Thus, the relavant spatial variable in the Fourier inversion is $\mathbf{r}_{ij}$,

$$\mathbf{P}_i^r(\mathbf{x}_i) = \frac{1}{\lambda_f} \sum_j \mathbf{m}_j \cdot \frac{1}{(2\pi)^3} \int d\mathbf{r}_{ij} \frac{1}{k^2} (1-h)\, \mathbf{f}_p \mathbf{f}_m e^{i\mathbf{k}\cdot\mathbf{r}_{ij}}. \tag{A.3}$$

This can be a difficult integral to compute, even with symbolic mathematics software like Mathematica and Maple. We begin by first using product-to-sum trigonometric identities to convert products of trigonometric functions to sums of trigonometric functions. This rewrites the integral as a sum of terms like

$$\int_0^\infty dk \frac{(1-h(k))\cos sk}{k^n}, \qquad \int_0^\infty dk \frac{(1-h(k))\sin sk}{k^n}, \tag{A.4}$$

where s is a constant and n is an integer. Mathematica can only integrate these analytically between bounds of 0 and ∞, *i.e* not for arbitrary bounds. However, because $1 - h(k) \rightarrow k^2$ as $k \rightarrow 0$, these terms only converge for certain values of n. Mathematica can evaluate individual terms for $n \leq 2$ with the cosine and $n \leq 3$ with the sine. If the integrand has higher powers of k in the denominator, terms must be grouped so they converge as $k \rightarrow 0$. For example, if the integrand contains cosine and sine terms with k^{-2} and k^{-3}, respectively, these terms must be grouped as,

$$\frac{(1-h(k))}{k^2} \left(\frac{\sin sk}{sk} - \cos sk \right), \tag{A.5}$$

to ensure the integrand is regularized as $k \rightarrow 0$ (as the leading term of $\operatorname{sinc} x - \cos x$ is x^2). With these groupings, Mathematica can integrate in the cases of nonoverlapping, $\mathbf{r}_{ij} \geq 2a$, and overlapping, $\mathbf{r}_{ij} < 2a$, particles separately. The result is of the form

$$\mathbf{P}_i^r(\mathbf{x}_i) = \frac{1}{\lambda_f} \sum_j \mathbf{m}_j \cdot \Big(\mathbf{p}^+ e^{-(r_{ij}+2a)^2\xi^2} + \mathbf{p}^- e^{-(r_{ij}-2a)^2\xi^2} + \mathbf{p}^0 e^{-r_{ij}^2\xi^2} + \mathbf{s}^+ \operatorname{erfc}(r_{ij}+2a)\xi + \mathbf{s}^- \operatorname{erfc}(r_{ij}-2a)\xi + \mathbf{s}^0 \operatorname{erfc} r_{ij}\xi + \mathbf{C} H(2a - r_{ij}) \Big), \tag{A.6}$$

where the $\mathbf{p}$, $\mathbf{s}$, and $\mathbf{C}$ are polynomials of r with directional components depending on $\mathbf{P}$ and $\mathbf{m}$. A few notes: the inclusion of the Heaviside step function H ensures that the last term only applies to overlapping particles; we take the value of the sign function at zero to be $\operatorname{sgn} 0 = 1$; the self contribution is obtained by letting $r \to 0$; and finally, the point particle result is recovered by letting $a \to 0$.

A.1 Potential/Charge Coupling

The potential/charge couplings in $\mathscr{M}^E_{\psi q}$ are,

$$\psi_i(\mathbf{x}_i) - \psi_{i,0}(\mathbf{x}_i) = \frac{1}{\lambda_f V} \sum_{\mathbf{k}\neq 0} j_0(ka) \sum_j \frac{e^{i\mathbf{k}\cdot(\mathbf{x}_i - \mathbf{x}_j)}}{k^2} j_0(ka) q_j. \tag{A.7}$$

The real space contribution is,

$$\psi^r_i(\mathbf{x}_i) - \psi^r_{i,0}(\mathbf{x}_i) = \frac{1}{\lambda_f} \sum_j q_j \frac{1}{(2\pi)^3} \int d\mathbf{k}\, \frac{1}{k^2}(1 - h(k)) j_0(ka) j_0(ka) e^{i\mathbf{k}\cdot\mathbf{r}_{ij}}, \tag{A.8}$$

$$= \frac{1}{\lambda_f} \sum_j q_j \frac{1}{4\pi^2} \int_0^\infty dk \int_0^\pi d\theta\, (1 - h(k)) j_0(ka) j_0(ka) \sin\theta\, e^{ikr_{ij}\cos\theta}, \tag{A.9}$$

$$= \frac{1}{\lambda_f} \sum_j q_j \frac{1}{2\pi^2} \int_0^\infty dk \left(1 - e^{-k^2/4\xi^2}\right) j_0(ka) j_0(ka) j_0(kr_{ij}), \tag{A.10}$$

$$= \frac{1}{\lambda_f} \sum_j q_j \Big(p^+ e^{-(r_{ij}+2a)^2\xi^2} + p^- e^{-(r_{ij}-2a)^2\xi^2} + p^0 e^{-r_{ij}^2\xi^2} + s^+ \operatorname{erfc}(r_{ij} + 2a)\xi$$

$$+ s^- \operatorname{erfc}(r_{ij} - 2a)\,\xi + s^0 \operatorname{erfc} r_{ij}\xi + CH(2a - r_{ij}) \Big), \tag{A.11}$$

where,

$$p^\pm(r) = -\frac{r \pm 2a}{32\pi^{3/2}a^2\xi r}, \tag{A.12}$$

$$p^0(r) = \frac{1}{16\pi^{3/2}a^2\xi}, \tag{A.13}$$

$$s^\pm(r) = \frac{2\xi^2(r \pm 2a)^2 + 1}{64\pi a^2\xi^2 r}, \tag{A.14}$$

$$s^0(r) = -\frac{2\xi^2 r^2 + 1}{32\pi a^2\xi^2 r}, \tag{A.15}$$

$$C(r) = -\frac{1}{4\pi r} + \frac{4a - r}{16\pi a^2}. \tag{A.16}$$

The self term is obtained by letting $r \to 0$,

$$\psi^s_i - \psi^s_{i,0} = \frac{1}{\lambda_f} \left(\frac{1 - e^{-4a^2\xi^2}}{8\pi^{3/2}a^2\xi} + \frac{\operatorname{erfc} 2a\xi}{4\pi a} \right) q_i. \tag{A.17}$$

The point particle result is recovered by letting $a \to 0$,

$$\psi^r_i(\mathbf{x}_i) - \psi^r_{i,0}(\mathbf{x}_i) = \frac{1}{4\pi\lambda_f} \sum_j q_j \frac{\operatorname{erfc} \xi r_{ij}}{r_{ij}}. \tag{A.18}$$

A.2 Potential/Dipole or Field/Charge Coupling

The potential/dipole couplings in $\mathscr{M}^E_{\psi S}$ are,

$$\psi_i(\mathbf{x}_i) - \psi_{i,0}(\mathbf{x}_i) = -\frac{3i}{a\lambda_f V} \sum_{\mathbf{k}\neq 0} j_0(ka) \sum_j \frac{e^{i\mathbf{k}\cdot(\mathbf{x}_i - \mathbf{x}_j)}}{k^2} j_1(ka) \hat{\mathbf{k}} \cdot \mathbf{S}_j, \tag{A.19}$$

with field/charge couplings in $\mathscr{M}^E_{Eq}$ written similarly. The real space contribution is,

$$\psi^r_i(\mathbf{x}_i) - \psi^r_{i,0}(\mathbf{x}_i) = -\frac{1}{\lambda_f}\sum_j \mathbf{S}_j \cdot \frac{3i}{(2\pi)^3 a}\int d\mathbf{k}\,\frac{1}{k^2}(1-h(k))j_0(ka)j_1(ka)\hat{\mathbf{k}}e^{i\mathbf{k}\cdot\mathbf{r}_{ij}}, \tag{A.20}$$

$$= -\frac{1}{\lambda_f}\sum_j \mathbf{S}_j \cdot \frac{3i}{4\pi^2 a}\int_0^\infty dk \int_0^\pi d\theta\,(1-h(k))j_0(ka)j_1(ka)\sin\theta\,\cos\theta\, e^{ikr_{ij}\cos\theta}\hat{\mathbf{r}}, \tag{A.21}$$

$$= \frac{1}{\lambda_f}\sum_j \mathbf{S}_j \cdot \frac{3}{2\pi^2 a}\int_0^\infty dk\,(1-h(k))j_0(ka)j_1(ka)j_1(kr)\hat{\mathbf{r}}, \tag{A.22}$$

$$= \frac{1}{\lambda_f}\sum_j \mathbf{S}_j \cdot \hat{\mathbf{r}}_{ij}\Big(p^+ e^{-(r_{ij}+2a)^2\xi^2} + p^- e^{-(r_{ij}-2a)^2\xi^2} + p^0 e^{-r_{ij}^2\xi^2} + s^+\,\mathrm{erfc}(r_{ij}+2a)\xi$$

$$+ s^-\,\mathrm{erfc}\,(r_{ij}-2a)\,\xi + s^0\,\mathrm{erfc}\,r_{ij}\xi + CH(2a-r_{ij})\Big), \tag{A.23}$$

where,

$$p^\pm(r) = \frac{-6\xi^2 r^3 \mp 4a\xi^2 r^2 + (-3+8a^2\xi^2)r \pm 2a(1-8a^2\xi^2)}{256\pi^{3/2}a^4\xi^3 r^2}, \tag{A.24}$$

$$p^0(r) = \frac{3(2r^2\xi^2+1)}{128\pi^{3/2}a^4\xi^3 r}, \tag{A.25}$$

$$s^\pm(r) = \frac{12\xi^4 r^4 \pm 32a\xi^4 r^3 + 12\xi^2 r^2 - 3 + 64a^4\xi^4}{512\pi a^4\xi^4 r^2}, \tag{A.26}$$

$$s^0(r) = -\frac{3(4\xi^4 r^4 + 4\xi^2 r^2 - 1)}{256\pi a^4\xi^4 r^2}, \tag{A.27}$$

$$C(r) = -\frac{1}{4\pi r^2} + \frac{1}{8\pi a^2}\left(\frac{r}{a} - \frac{3r^2}{8a^2}\right). \tag{A.28}$$

The self term is obtained by letting $r \to 0$,

$$\psi^s_i - \psi^s_{i,0} = 0. \tag{A.29}$$

The point particle result is recovered by letting $a \to 0$,

$$\psi^r_i(\mathbf{x}_i) - \psi^r_{i,0}(\mathbf{x}_i) = \frac{1}{4\pi\lambda_f}\sum_j \mathbf{S}_i \cdot \hat{\mathbf{r}}_{ij}\left(\frac{2\xi e^{-r_{ij}^2\xi^2}}{\sqrt{\pi}r_{ij}} + \frac{\mathrm{erfc}\,\xi r_{ij}}{r_{ij}^2}\right). \tag{A.30}$$

A.3 Field/Dipole Coupling

The field/dipole couplings in $\mathscr{M}^E_{ES}$ are,

$$-\nabla\psi_{i,0}(\mathbf{x}_i) = \frac{9}{a^2\lambda_f V}\sum_{\mathbf{k}\neq 0} j_1(ka)\hat{\mathbf{k}}\sum_j \frac{e^{i\mathbf{k}\cdot(\mathbf{x}_i-\mathbf{x}_j)}}{k^2} j_1(ka)\hat{\mathbf{k}}\cdot\mathbf{S}_j. \tag{A.31}$$

The real space contribution is

$$-\nabla\psi^r_{i,0}(\mathbf{x}_i) = \frac{1}{\lambda_f}\sum_j \mathbf{S}_j \cdot \frac{9}{(2\pi)^3 a^2}\int d\mathbf{k}\,\frac{1}{k^2}\,(1-h(k))\,j_1(ka)j_1(ka)\hat{\mathbf{k}}\hat{\mathbf{k}}e^{i\mathbf{k}\cdot\mathbf{r}_{ij}}, \tag{A.32}$$

$$= \frac{1}{\lambda_f}\sum_j \mathbf{S}_j \cdot \frac{9}{(2\pi)^3 a^2}\int_0^\infty dk\int_0^\pi d\theta\,(1-h(k))j_1(ka)j_1(ka)\sin\theta\, e^{ikr_{ij}\cos\theta}\Big(\pi\sin^2\theta\,(\mathbf{I}-\hat{\mathbf{r}}_{ij}\hat{\mathbf{r}}_{ij}) + 2\pi\cos^2\theta\,\hat{\mathbf{r}}\hat{\mathbf{r}}\Big), \tag{A.33}$$

$$= \frac{1}{\lambda_f}\sum_j \mathbf{S}_j \cdot \frac{9}{2\pi^2 a^2}\int_0^\infty dk\left(1-e^{-k^2/4\xi^2}\right)j_1(ka)j_1(ka)\left(\frac{j_1(kr_{ij})}{kr_{ij}}\,(\mathbf{I}-\hat{\mathbf{r}}_{ij}\hat{\mathbf{r}}_{ij}) + \left(\frac{j_1(kr_{ij})}{kr_{ij}} - j_2(kr_{ij})\right)\hat{\mathbf{r}}_{ij}\hat{\mathbf{r}}_{ij}\right), \tag{A.34}$$

$$= \frac{1}{\lambda_f}\sum_j \mathbf{S}_j \cdot \left(u_\perp\,(\mathbf{I}-\hat{\mathbf{r}}_{ij}\hat{\mathbf{r}}_{ij}) + u_\parallel\hat{\mathbf{r}}_{ij}\hat{\mathbf{r}}_{ij}\right), \tag{A.35}$$

where,

$$u_i = p_i^+ e^{-(r+2a)^2\xi^2} + p_i^- e^{-(r-2a)^2\xi^2} + p_i^0 e^{-r^2\xi^2} + s_i^+\,\mathrm{erfc}(r+2a)\xi + s_i^-\,\mathrm{erfc}(r-2a)\xi + s_i^0\,\mathrm{erfc}\,r\xi + C_i H(2a-r). \tag{A.36}$$

The $\mathbf{I}-\hat{\mathbf{r}}\hat{\mathbf{r}}$ component is

$$p_\perp^\pm(r) = \frac{4\xi^4r^5 \mp 8a\xi^4r^4 + 8\xi^2(2-7a^2\xi^2)r^3 \mp 8a\xi^2(3+2a^2\xi^2)r^2 + r(3-12a^2\xi^2+32a^4\xi^4) \pm 2a(3+4a^2\xi^2-32a^4\xi^4)}{1024\pi^{3/2}a^6\xi^5r^3} \tag{A.37}$$

$$p_\perp^0(r) = \frac{-4\xi^4r^4 - 8\xi^2(2-9a^2\xi^2)r^2 - 3 + 36a^2\xi^2}{512\pi^{3/2}a^6\xi^5r^2}, \tag{A.38}$$

$$s_\perp^\pm(r) = \frac{-8\xi^6r^6 - 36\xi^4(1-4a^2\xi^2)r^4 \pm 256a^3\xi^6r^3 - 18\xi^2(1-8a^2\xi^2)r^2 + 3 - 36a^2\xi^2 + 256a^6\xi^6}{2048\pi a^6\xi^6r^3}, \tag{A.39}$$

$$s_\perp^0(r) = \frac{8\xi^6r^6 + 36\xi^4(1-4a^2\xi^2)r^4 + 18\xi^2(1-8a^2\xi^2)r^2 - 3 + 36a^2\xi^2}{1024\pi a^6\xi^6r^3}, \tag{A.40}$$

$$C_\perp(r) = -\frac{1}{4\pi r^3} + \frac{1}{4\pi a^3}\left(1 - \frac{9r}{16a} + \frac{r^3}{32a^3}\right), \tag{A.41}$$

and the $\hat{\mathbf{r}}\hat{\mathbf{r}}$ component is

$$p_\parallel^\pm(r) = \frac{8\xi^4r^5 \mp 16a\xi^4r^4 + 2\xi^2(7-20a^2\xi^2)r^3 \mp 4a\xi^2(3-4a^2\xi^2)r^2 - (3-12a^2\xi^2+32a^4\xi^4)r \mp 2a(3+4a^2\xi^2-32a^4\xi^4)}{512\pi^{3/2}a^6\xi^5r^3}, \tag{A.42}$$

$$p_\parallel^0(r) = \frac{-8\xi^4r^4 - 2\xi^2(7-36a^2\xi^2)r^2 + 3 - 36a^2\xi^2}{256\pi^{3/2}a^6\xi^5r^2}, \tag{A.43}$$

$$s_\parallel^\pm(r) = \frac{-16\xi^6r^6 - 36\xi^4(1-4a^2\xi^2)r^4 \pm 128a^3\xi^6r^3 - 3 + 36a^2\xi^2 - 256a^6\xi^6}{1024\pi a^6\xi^6r^3}, \tag{A.44}$$

$$s_\parallel^0(r) = \frac{16\xi^6r^6 + 36\xi^4(1-4a^2\xi^2)r^4 + 3 - 36a^2\xi^2}{512\pi a^6\xi^6r^3}, \tag{A.45}$$

$$C_\parallel(r) = \frac{1}{2\pi r^3} + \frac{1}{4\pi a^3}\left(1 - \frac{9r}{8a} + \frac{r^3}{8a^2}\right), \tag{A.46}$$

The self contribution term is obtained by letting $r \to 0$,

$$-\nabla\psi^s_{i,0} = \frac{1}{\lambda_f}\left(\frac{-1+6a^2\xi^2}{16\pi^{3/2}a^6\xi^3} + \frac{(1-2a^2\xi^2)e^{-4a^2\xi^2}}{16\pi^{3/2}a^6\xi^3} + \frac{\mathrm{erfc}\,2a\xi}{4\pi a^3}\right)\mathbf{S}_i. \tag{A.47}$$

The point particle result is recovered by letting $a \to 0$,

$$-\nabla\psi^r_{i,0}(\mathbf{x}_i) = \frac{1}{\lambda_f}\sum_j \left(\left(\frac{\xi e^{-r_{ij}^2\xi^2}}{2\pi^{3/2}r_{ij}^2} + \frac{\operatorname{erfc}\xi r_{ij}}{4\pi r_{ij}^3} \right)(\mathbf{I} - \hat{\mathbf{r}}_{ij}\hat{\mathbf{r}}_{ij}) - \left(\frac{\xi(\xi^2 r_{ij}^2 + 1)e^{-r_{ij}^2\xi^2}}{\pi^{3/2}r_{ij}^2} + \frac{\operatorname{erfc}\xi r_{ij}}{2\pi r_{ij}^3} \right)\hat{\mathbf{r}}_{ij}\hat{\mathbf{r}}_{ij} \right) \tag{A.48}$$

A.4 Potential/Quadrupole or Field Gradient/Charge Coupling

The potential/quadrupole couplings in $\mathscr{M}^E_{\psi Q}$ are,

$$\psi_i(\mathbf{x}_i) - \psi_{i,0}(\mathbf{x}_i) = -\frac{15}{a^2\lambda_f V}\sum_{\mathbf{k}\neq 0} j_0(ka)\sum_j \frac{e^{i\mathbf{k}\cdot(\mathbf{x}_i - \mathbf{x}_j)}}{k^2} j_2(ka)\hat{\mathbf{k}}\hat{\mathbf{k}} : \mathbf{Q}_j, \tag{A.49}$$

with the field gradient/charge couplings in $\mathscr{M}^E_{\nabla q}$ written similarly. The real space contribution is,

$$\begin{aligned}
\psi^r_i(\mathbf{x}_i) - \psi^r_{i,0}(\mathbf{x}_i) &= -\frac{1}{\lambda_f}\sum_j \mathbf{Q}_j : \frac{15}{(2\pi)^3 a^2}\int d\mathbf{k}\,\frac{1}{k^2}(1 - h(k))\, j_0(ka) j_2(ka)\hat{\mathbf{k}}\hat{\mathbf{k}} e^{i\mathbf{k}\cdot\mathbf{r}_{ij}}, && \text{(A.50)}\\
&= -\frac{1}{\lambda_f}\sum_j \mathbf{Q}_j : \frac{15}{(2\pi)^3 a^2}\int_0^\infty dk \int_0^\pi d\theta\,(1 - h(k)) j_0(ka) j_2(ka)\sin\theta\, e^{ikr_{ij}\cos\theta} \\
&\qquad \times \Big(\pi\sin^2\theta\,(\mathbf{I} - \hat{\mathbf{r}}_{ij}\hat{\mathbf{r}}_{ij}) + 2\pi\cos^2\theta\,\hat{\mathbf{r}}_{ij}\hat{\mathbf{r}}_{ij}\Big), && \text{(A.51)}\\
&= \frac{1}{\lambda_f}\sum_j \mathbf{Q}_j : \frac{15}{2\pi^2 a^2}\int_0^\infty dk \left(1 - e^{-k^2/4\xi^2}\right) j_0(ka) j_2(ka) j_2(kr_{ij})\hat{\mathbf{r}}_{ij}\hat{\mathbf{r}}_{ij}, && \text{(A.52)}\\
&= \frac{1}{\lambda_f}\sum_j \mathbf{Q}_j : \hat{\mathbf{r}}_{ij}\hat{\mathbf{r}}_{ij}\Big(p^+ e^{-(r_{ij}+2a)^2\xi^2} + p^- e^{-(r_{ij}-2a)^2\xi^2} + p^0 e^{-r_{ij}^2\xi^2} + s^+\operatorname{erfc}(r_{ij}+2a)\xi \\
&\qquad + \operatorname{sgn}(r_{ij} - 2a)\, s^-\operatorname{erfc}|r_{ij} - 2a|\,\xi + s^0\operatorname{erfc} r_{ij}\xi + CH(2a - r_{ij})\Big), && \text{(A.53)}
\end{aligned}$$

where,

$$\begin{aligned}
p^\pm(r) &= \frac{3}{1024\pi^{3/2}a^6\xi^5 r^3}\Big(20\xi^4 r^5 \pm 24a\xi^4 r^4 + 2\xi^2(10 - 4a^2\xi^2)r^3 \mp 16a\xi^2(2 - a^2\xi^2)r^2 \\
&\qquad - (15 - 12a^2\xi^2 + 32a^4\xi^4)r \pm 2a(9 - 4a^2\xi^2 + 32a^4\xi^4)\Big), && \text{(A.54)}\\
p^0(r) &= \frac{15(4\xi^4 r^4 + 4\xi^2(1 + 2a^2\xi^2)r^2) - 3(1 + 4a^2\xi^2)}{512\pi^{3/2}a^6\xi^5 r^2}, && \text{(A.55)}\\
s^\pm(r) &= \frac{3(40\xi^6 r^6 \pm 128a\xi^6 r^5 + 20\xi^4(3 + 4a^2\xi^2)r^4 - 10\xi^2(3 + 8a^2\xi^2)r^2 + 15 + 60a^2\xi^2 + 256a^6\xi^6)}{2048\pi a^6\xi^6 r^3}, && \text{(A.56)}\\
s^0(r) &= \frac{15(-8\xi^6 r^6 - 4\xi^4(3 + 4a^2\xi^2)r^4 - 2\xi^2(3 + 8a^2\xi^2)r^2 - 3(1 + 4a^2\xi^2))}{1024\pi a^6\xi^6 r^3}, && \text{(A.57)}\\
C(r) &= \frac{15(12\xi^4 r^4 - 2\xi^2(3 + 8a^2\xi^2)r^2 + 3 + 12a^2\xi^2)}{1024\pi a^6\xi^6 r^3}. && \text{(A.58)}
\end{aligned}$$

The self contribution is obtained by letting $r \to 0$,

$$\psi^s_i - \psi^s_{i,0} = 0. \tag{A.59}$$

The point particle result is recovered by letting $a \to 0$,

$$\psi^r_i(\mathbf{x}_i) - \psi^r_{i,0}(\mathbf{x}_i) = \frac{1}{\lambda_f}\sum_j \mathbf{Q}_j : \hat{\mathbf{r}}_{ij}\hat{\mathbf{r}}_{ij}\left(\frac{\xi(\xi^2 r_{ij}^2 + 3)e^{-r_{ij}^2\xi^2}}{2\pi^{3/2}r_{ij}^2} + \frac{\operatorname{erfc}\xi r_{ij}}{4\pi r_{ij}^3} \right). \tag{A.60}$$

A.5 Field/Quadrupole or Field Gradient/Dipole Coupling

The field gradient/dipole couplings in $\mathscr{M}^E_{\nabla S}$ are,

$$-\nabla\nabla\psi_{i,0}(\mathbf{x}_i) = \frac{45i}{a^3\lambda_f V}\sum_{\mathbf{k}\neq 0} j_2(ka)\left(\hat{\mathbf{k}}\hat{\mathbf{k}} - \frac{1}{3}\mathbf{I}\right)\sum_j \frac{e^{i\mathbf{k}\cdot(\mathbf{x}_i-\mathbf{x}_j)}}{k^2} j_1(ka)\hat{\mathbf{k}}\cdot\mathbf{S}_j, \tag{A.61}$$

With the field/quadrupole couplings in $\mathscr{M}^E_{EQ}$ handled similarly. Dropping the ij subscripts for clarity, $\mathbf{r}\equiv\mathbf{r}_{ij}$, the real space contribution is,

$$-\nabla\nabla\psi^r_{i,0}(\mathbf{x}_i) = \frac{1}{\lambda_f}\sum_j \frac{45i}{(2\pi)^3a^3}\int d\mathbf{k}\,\frac{1}{k^2}\,(1-h(k))\,j_2(ka)j_1(ka)\left(\hat{\mathbf{k}}\hat{\mathbf{k}} - \frac{1}{3}\mathbf{I}\right)\hat{\mathbf{k}}e^{i\mathbf{k}\cdot\mathbf{r}}\cdot\mathbf{S}_j, \tag{A.62}$$

$$= \frac{1}{\lambda_f}\sum_j \frac{45i}{(2\pi)^3a^3}\int_0^\infty dk\int_0^\pi d\theta\int_0^{2\pi} d\phi\,(1-h(k))j_2(ka)j_1(ka)\sin\theta\, e^{ikr\cos\theta}\left(\hat{\mathbf{k}}\hat{\mathbf{k}}\hat{\mathbf{k}} - \frac{1}{3}\mathbf{I}\hat{\mathbf{k}}\right)\cdot\mathbf{S}_j, \tag{A.63}$$

$$= \frac{1}{\lambda_f}\sum_j \frac{45i}{8\pi^2a^3}\int_0^\infty dk\int_0^\pi d\theta\,(1-h(k))j_2(ka)j_1(ka)\sin\theta\, e^{ikr\cos\theta} \times\left(\sin^2\theta\cos\theta\,(\mathbf{I}\hat{\mathbf{r}}+\hat{\mathbf{e}}_i\hat{\mathbf{r}}\hat{\mathbf{e}}_i+\hat{\mathbf{r}}\mathbf{I}) + \left(2\cos^3\theta - 3\sin^2\theta\cos\theta\right)\hat{\mathbf{r}}\hat{\mathbf{r}}\hat{\mathbf{r}} - \frac{2}{3}\cos\theta\,\mathbf{I}\hat{\mathbf{r}}\right)\cdot\mathbf{S}_j, \tag{A.64}$$

$$= -\frac{1}{\lambda_f}\sum_j \frac{45}{2\pi^2a^3}\int_0^\infty dk\,(1-h(k))j_2(ka)j_1(ka) \times\left(\frac{j_2(kr)}{kr}(\mathbf{I}\hat{\mathbf{r}}+\hat{\mathbf{e}}_i\hat{\mathbf{r}}\hat{\mathbf{e}}_i+\hat{\mathbf{r}}\mathbf{I}) - j_3(kr)\hat{\mathbf{r}}\hat{\mathbf{r}}\hat{\mathbf{r}} - \frac{j_1(kr)}{3}\mathbf{I}\hat{\mathbf{r}}\right)\cdot\mathbf{S}_j, \tag{A.65}$$

$$= \frac{1}{\lambda_f}\sum_j \frac{45}{2\pi^2a^3}\int_0^\infty dk\,(1-e^{-k^2/4\xi^2})j_2(ka)j_1(ka) \times\left(j_3(kr)\hat{\mathbf{r}}\hat{\mathbf{r}}\hat{\mathbf{r}}\cdot\mathbf{S}_j - \frac{j_2(kr)}{kr}(\mathbf{I}\hat{\mathbf{r}}\cdot\mathbf{S}_j + \mathbf{S}_j\hat{\mathbf{r}} + \hat{\mathbf{r}}\mathbf{S}_j) + \frac{j_1(kr)}{3}\mathbf{I}\hat{\mathbf{r}}\cdot\mathbf{S}_j\right), \tag{A.66}$$

$$= \frac{1}{\lambda_f}\sum_j \Big(u_1(r)\hat{\mathbf{r}}\hat{\mathbf{r}}\hat{\mathbf{r}}\cdot\mathbf{S}_j + u_2(r)(\mathbf{I}\hat{\mathbf{r}}\cdot\mathbf{S}_j + \mathbf{S}_j\hat{\mathbf{r}} + \hat{\mathbf{r}}\mathbf{S}_j) + u_3(r)\mathbf{I}\hat{\mathbf{r}}\cdot\mathbf{S}_j\Big), \tag{A.67}$$

where,

$$u_i = p_i^+ e^{-(r+2a)^2\xi^2} + p_i^- e^{-(r-2a)^2\xi^2} + p_i^0 e^{-r^2\xi^2} + s_i^+\,\mathrm{erfc}(r+2a)\xi + s_i^-\,\mathrm{erfc}(r-2a)\xi + s_i^0\,\mathrm{erfc}\,r\xi + C_iH(2a-r). \tag{A.68}$$

The $\hat{\mathbf{r}}\hat{\mathbf{r}}\hat{\mathbf{r}}\cdot\mathbf{S}_j$ component is

$$p_1^{\pm}(r) = \frac{15}{16384\pi^{3/2}a^8\xi^7r^4}\Big(-24\xi^6r^7 \pm 48a\xi^6r^6 - 4\xi^4(9-8a^2\xi^2)r^5 \pm 8a\xi^4(3-8a^2\xi^2)r^4 + 2\xi^2(21-80a^2\xi^2+64a^4\xi^4)r^3 \mp 4a\xi^2(3-8a^2\xi^2)^2r^2 - (45-120a^2\xi^2+192a^4\xi^4-512a^6\xi^6)r \mp 2a(45+24a^2\xi^2-64a^4\xi^4+512a^6\xi^6)\Big), \tag{A.69}$$

$$p_1^0(r) = \frac{15(24\xi^6r^6+4\xi^4(9-32a^2\xi^2)r^4-2\xi^2(21-128a^2\xi^2)r^2+45-480a^2\xi^2)}{8192\pi^{3/2}a^8\xi^7r^3}, \tag{A.70}$$

$$s_1^{\pm}(r) = \frac{15}{32768\pi a^8\xi^8r^4}\Big(48\xi^8r^8+32\xi^6(3-8a^2\xi^2)r^6-24\xi^4(3-16a^2\xi^2)r^4 + 72\xi^2(1-8a^2\xi^2)r^2-45+480a^2\xi^2+4096\xi^8\Big), \tag{A.71}$$

$$s_1^0(r) = \frac{15(-48\xi^8r^8-32\xi^6(3-8a^2\xi^2)r^6+24\xi^4(3-16a^2\xi^2)r^4-72\xi^2(1-8a^2\xi^2)r^2+45-480a^2\xi^2)}{16384\pi a^8\xi^8r^4}, \tag{A.72}$$

$$C_1(r) = -\frac{15}{4\pi r^4} + \frac{15r^2}{64\pi a^6}\left(1-\frac{3r^2}{16a^2}\right), \tag{A.73}$$

the $\mathbf{I}\hat{\mathbf{r}}\cdot\mathbf{S}_j + \mathbf{S}_j\hat{\mathbf{r}} + \hat{\mathbf{r}}\mathbf{S}_j$ component is

$$p_2^{\pm}(r) = \frac{3}{16384\pi^{3/2}a^8\xi^7r^4}\Big(-40\xi^6r^7 \pm 80a\xi^6r^6 - 20\xi^4(11-24a^2\xi^2)r^5 \pm 8a\xi^4(45+8a^2\xi^2)r^4 - 2\xi^2(45-80a^2\xi^2+64a^4\xi^4)r^3 \mp 4a\xi^2(15+48a^2\xi^2-64a^4\xi^4)r^2 + (45-120a^2\xi^2+192a^4\xi^4-512a^6\xi^6)r \pm 2a(45+24a^2\xi^2-64a^4\xi^4+512a^6\xi^6)\Big), \tag{A.74}$$

$$p_2^0(r) = \frac{15(8\xi^6r^6+4\xi^4(11-32a^2\xi^2)r^4+2\xi^2(9-64a^2\xi^2)r^2-9+96a^2\xi^2)}{8192\pi^{3/2}a^8\xi^7r^3}, \tag{A.75}$$

$$s_2^{\pm}(r) = \frac{3}{32768\pi a^8\xi^8r^4}\Big(80\xi^8r^8+160\xi^6(3-8a^2\xi^2)r^6 \mp 2048a^3\xi^8r^5+120\xi^4(3-16a^2\xi^2)r^4 - 120\xi^2(1-8a^2\xi^2)r^2+45-480a^2\xi^2-4096a^8\xi^8\Big), \tag{A.76}$$

$$s_2^0(r) = \frac{15(-16\xi^8r^8-32\xi^6(3-8a^2\xi^2)r^6-24\xi^4(3-16a^2\xi^2)r^4+24\xi^2(1-8a^2\xi^2)r^2-9+96a^2\xi^2)}{16384\pi a^8\xi^8r^4}, \tag{A.77}$$

$$C_2(r) = \frac{3}{4\pi r^4} - \frac{3r}{8\pi a^5}\left(1-\frac{5r}{8a}+\frac{5r^3}{128a^3}\right), \tag{A.78}$$

and the $\mathbf{I}\hat{\mathbf{r}}\cdot\mathbf{S}_j$ component is,

$$p_3^{\pm}(r) = \frac{5\left(4\xi^4r^5 \mp 8a\xi^4r^4+16\xi^2(1-2a^2\xi^2)r^3 \mp 24a\xi^2r^2+3r\pm 6a\right)}{1024\pi^{3/2}a^8\xi^5r^2}, \tag{A.79}$$

$$p_3^0(r) = \frac{5\left(-4\xi^4r^4-16\xi^2(1-3a^2\xi^2)r^2-3+24a^2\xi^2\right)}{512\pi^{3/2}a^8\xi^5r}, \tag{A.80}$$

$$s_3^{\pm}(r) = \frac{5\left(-8\xi^6r^6-12\xi^4(3-8a^2\xi^2)r^4 \pm 128a^3\xi^6r^3-6\xi^2(3-16a^2\xi^2)r^2+3-24a^2\xi^2\right)}{2048\pi a^8\xi^6r^2}, \tag{A.81}$$

$$s_3^0(r) = \frac{5\left(8\xi^6r^6+12\xi^4(3-8a^2\xi^2)r^4+6\xi^2(3-16a^2\xi^2)r^2-3+24a^2\xi^2\right)}{1024\pi a^8\xi^6r^2}, \tag{A.82}$$

$$C_3(r) = \frac{5r}{8\pi a^5}\left(1-\frac{3r}{4a}+\frac{r^3}{16a^3}\right). \tag{A.83}$$

The self contribution is obtained by letting $r \to 0$,

$$-\nabla\nabla\psi_{i,0}^s = 0. \tag{A.84}$$

The point particle result is recovered by letting $a \to 0$,

$$-\nabla\nabla\psi^r_{i,0}(\mathbf{r}) = \frac{1}{\lambda_f}\sum_j \left(\left(\frac{\xi(4\xi^4 r^4 + 10\xi^2 r^2 + 15)e^{-r^2\xi^2}}{2\pi^{3/2} r^3} + \frac{15\,\mathrm{erfc}\,\xi r}{4\pi r^4} \right) \hat{\mathbf{r}}\hat{\mathbf{r}}\hat{\mathbf{r}} \cdot \mathbf{S}_j \right.$$
$$\left. - \left(\frac{\xi(2\xi^2 r^2 + 3)e^{-r^2\xi^2}}{2\pi^{3/2} r^3} + \frac{3\,\mathrm{erfc}\,\xi r}{4\pi r^4} \right) (\mathbf{I}\hat{\mathbf{r}} \cdot \mathbf{S}_j + \mathbf{S}_j\hat{\mathbf{r}} + \hat{\mathbf{r}}\mathbf{S}_j) - \frac{2\xi^5 r e^{-r^2\xi^2}}{3\pi^{3/2}} \mathbf{I}\hat{\mathbf{r}} \cdot \mathbf{S}_j \right). \quad \text{(A.85)}$$

A.6 Charge/Charge Force

The charge/charge contribution to the force is

$$\mathbf{F}_i = -\sum_j \nabla_{\mathbf{x}_i} \mathbf{M}^E_{\psi q,ij} q_i q.j \quad \text{(A.86)}$$

The real space portion of the charge/charge force is

$$\mathbf{F}^r_i = -\frac{1}{\lambda_f}\sum_j q_i q_j \hat{\mathbf{r}} \Big(p^+ e^{-(r+2a)^2\xi^2} + p^- e^{-(r-2a)^2\xi^2} + p^0 e^{-r^2\xi^2} + s^+ \,\mathrm{erfc}(r+2a)\xi$$
$$+ s^- \,\mathrm{erfc}\,(r-2a)\,\xi + s^0 \,\mathrm{erfc}\, r\xi + CH(2a-r) \Big), \quad \text{(A.87)}$$

where,

$$p^{\pm}(r) = -\frac{r \mp 2a}{32\pi^{3/2} a^2 \xi r^2}, \quad \text{(A.88)}$$

$$p^0(r) = \frac{1}{16\pi^{3/2} a^2 \xi r}, \quad \text{(A.89)}$$

$$s^{\pm}(r) = \frac{2\xi^2 r^2 - 8a^2\xi^2 - 1}{64\pi a^2 \xi^2 r^2}, \quad \text{(A.90)}$$

$$s^0(r) = -\frac{2\xi^2 r^2 - 1}{32\pi a^2 \xi^2 r^2}, \quad \text{(A.91)}$$

$$C(r) = \frac{1}{4\pi r^2} - \frac{1}{16\pi a^2}. \quad \text{(A.92)}$$

A.7 Charge/Dipole Force

The charge/dipole contribution to the force is

$$\mathbf{F}_i = -\sum_j \nabla_{\mathbf{x}_i} \mathbf{M}^E_{\psi S,ij} \cdot q_i \mathbf{S}_j \quad \text{(A.93)}$$

with the charge/dipole force involving $\nabla\mathscr{M}^E_{Eq}$ written similarly. The real space portion is

$$\mathbf{F}^r_i = -\frac{1}{\lambda_f}\sum_j q_i \mathbf{S}_j : \left(u_\perp(\mathbf{I} - \hat{\mathbf{r}}\hat{\mathbf{r}}) + u_\parallel \hat{\mathbf{r}}\hat{\mathbf{r}} \right). \quad \text{(A.94)}$$

Letting $u_{\psi S}$ be the vector coefficient from the potential/dipole or field/charge coupling, we have $u_\perp = u_{\psi S}/r$ and $u_\parallel$ with polynomials

$$p^\pm(r) = \frac{-6\xi^2 r^3 \pm 4a\xi^2 r^2 + (3 - 8a^2\xi^2)r \mp 2a(1 - 8a^2\xi^2)}{128\pi^{3/2}a^4\xi^3 r^3}, \tag{A.95}$$

$$p^0(r) = \frac{3(2r^2\xi^2 - 1)}{64\pi^{3/2}a^4\xi^3 r^2}, \tag{A.96}$$

$$s^\pm(r) = \frac{12\xi^4 r^4 \pm 16a\xi^4 r^3 + 3 - 64a^4\xi^4}{256\pi a^4\xi^4 r^3}, \tag{A.97}$$

$$s^0(r) = -\frac{3(4\xi^4 r^4 + 1)}{128\pi a^4\xi^4 r^3}, \tag{A.98}$$

$$C(r) = \frac{1}{2\pi r^3} + \frac{4a - 3r}{32\pi a^4}. \tag{A.99}$$

A.8 Dipole/Dipole Force

The dipole/dipole contribution to the force is

$$\mathbf{F}_i = -\sum_j \nabla_{\mathbf{x}_i} \mathbf{M}^E_{ES,ij} : \mathbf{S}_i\mathbf{S}_j \tag{A.100}$$

The real space portion is,

$$\mathbf{F}_i^r = -\frac{\partial u_\perp}{\partial r}(\mathbf{S}_i \cdot \mathbf{S}_j)\hat{\mathbf{r}} - \left(\frac{\partial u_\parallel}{\partial r} - \frac{\partial u_\perp}{\partial r}\right)(\mathbf{S}_i \cdot \hat{\mathbf{r}})(\mathbf{S}_j \cdot \hat{\mathbf{r}})\hat{\mathbf{r}} - \frac{u_\parallel - u_\perp}{r}\Big((\mathbf{S}_j \cdot \hat{\mathbf{r}})\mathbf{S}_i + (\mathbf{S}_i \cdot \hat{\mathbf{r}})\mathbf{S}_j - 2(\mathbf{S}_i \cdot \hat{\mathbf{r}})(\mathbf{S}_j \cdot \hat{\mathbf{r}})\hat{\mathbf{r}}\Big), \tag{A.101}$$

with $u_\perp$ and $u_\parallel$ defined above in the field/dipole section. The coefficients of the vector terms are of the same form as the couplings. We have $\partial u_\perp/\partial r = (u_\parallel - u_\perp)/r$ with polynomials,

$$p_1^\pm(r) = \frac{3}{1024\pi^{3/2}a^6\xi^5 r^4}\Big(4\xi^4 r^5 \mp 8a\xi^4 r^4 + 4\xi^2(1 - 2a^2\xi^2)r^3 \pm 16a^3\xi^4 r^2 - (3 - 12a^2\xi^2 + 32a^4\xi^4)r \mp 2a(3 + 4a^2\xi^2 - 32a^4\xi^4)\Big), \tag{A.102}$$

$$p_1^0(r) = \frac{3}{512\pi^{3/2}a^6\xi^5 r^3}\Big(-4\xi^4 r^4 - 4\xi^2(1 - 6a^2\xi^2)r^2 + 3 - 36a^2\xi^2\Big), \tag{A.103}$$

$$s_1^\pm(r) = \frac{3}{2048\pi a^6\xi^6 r^4}\Big(-8\xi^6 r^6 - 12\xi^4(1 - 4a^2\xi^2)r^4 + 6\xi^2(1 - 8a^2\xi^2)r^2 - 3 + 36a^2\xi^2 - 256a^6\xi^6\Big), \tag{A.104}$$

$$s_1^0(r) = \frac{3}{1024\pi a^6\xi^6 r^4}\Big(8\xi^6 r^6 + 12\xi^4(1 - 4a^2\xi^2)r^4 - 6\xi^2(1 - 8a^2\xi^2)r^2 + 3 - 36a^2\xi^2\Big), \tag{A.105}$$

$$C_1(r) = \frac{3}{4\pi r^4} - \frac{3}{64\pi a^4}\left(3 - \frac{r^2}{2a^2}\right), \tag{A.106}$$

and polynomials for $\partial u_{\parallel}/\partial r - \partial u_{\perp}/\partial r$,

$$p_2^{\pm}(r) = \frac{9}{1024\pi^{3/2}a^6\xi^5 r^4}\Big(4\xi^4 r^5 \mp 8a\xi^4 r^4 + 8a^2\xi^4 r^3 \pm 8a\xi^2(1-2a^2\xi^2)r^2 + (3 - 12a^2\xi^2 + 32a^4\xi^4)r \pm 2a(3 + 4a^2\xi^2 - 32a^4\xi^4)\Big), \tag{A.107}$$

$$p_2^0(r) = \frac{9}{512\pi^{3/2}a^6\xi^5 r^3}\Big(-4\xi^4 r^4 + 8a^2\xi^4 r^2 - 3 + 36a^2\xi^2\Big), \tag{A.108}$$

$$s_2^{\pm}(r) = \frac{9}{2048\pi a^6\xi^6 r^4}\Big(-8\xi^6 r^6 - 4\xi^4(1-4a^2\xi^2)r^4 - 2\xi^2(1-8a^2\xi^2)r^2 + 3 - 36a^2\xi^2 + 256a^6\xi^6\Big), \tag{A.109}$$

$$s_2^0(r) = \frac{9}{1024\pi a^6\xi^6 r^4}\Big(8\xi^6 r^6 + 4\xi^4(1-4a^2\xi^2)r^4 + 2\xi^2(1-8a^2\xi^2)r^2 - 3 + 36a^2\xi^2\Big), \tag{A.110}$$

$$C_2(r) = -\frac{9}{4\pi r^4} - \frac{9}{64\pi a^4}\left(1 - \frac{r^2}{2a^2}\right), \tag{A.111}$$

A.9 Point Particle Solution

Our method currently accounts for the finite size of the particles. To compare our results to the known point particle solution, we can take the limit of infinitely small particles $a \to 0$ and then convert the sums to real space. Note that the $i = j, \mathbf{n} = 0$ self contribution must be computed before the limit $a \to 0$. From $\mathbf{k}$ symmetry during inversion and the properties of the moments (*e.g.* traceless quadrupole), there is only a charge self term for the potential, only a dipole self term for the field, *etc.* Extracting the self contribution and keeping the lowest order term in a in each of the blocks of $\mathscr{M}$,

$$\langle\psi\rangle_i - \psi_0(\mathbf{x}_i) = \frac{q_i}{4\pi a\lambda_f} + \frac{1}{\lambda_f}{\sum_{j\mathbf{n}}}' \mathcal{F}^{-1}\left\{\frac{e^{i\mathbf{k}\cdot(\mathbf{x}_i-\mathbf{x}_j)}}{k^2}\left(q_j - \mathbf{S}_j\cdot i\mathbf{k} - \frac{1}{2}\mathbf{Q}_j : \mathbf{kk} + \cdots\right)\right\} \tag{A.112}$$

$$-\nabla\psi_0(\mathbf{x}_i) = \frac{3\mathbf{S}_i}{4\pi a^3(\lambda_p - \lambda_f)} + \frac{\mathbf{S}_i}{4\pi a^3\lambda_f} + \frac{1}{\lambda_f}{\sum_{j\mathbf{n}}}' \mathcal{F}^{-1}\left\{\frac{e^{i\mathbf{k}\cdot(\mathbf{x}_i-\mathbf{x}_j)}}{k^2}\left(q_j i\mathbf{k} + \mathbf{S}_j\cdot\mathbf{kk} - \frac{1}{2}\mathbf{Q}_j : i\mathbf{kkk} + \cdots\right)\right\} \tag{A.113}$$

$$-\nabla\nabla\psi_0(\mathbf{x}_i) = \frac{15\mathbf{Q}_i}{8\pi a^5(\lambda_p - \lambda_f)} + \frac{3\mathbf{Q}_i}{4\pi a^5\lambda_f} + \frac{1}{\lambda_f}{\sum_{j\mathbf{n}}}' \mathscr{F}^{-1}\left\{\frac{e^{i\mathbf{k}\cdot(\mathbf{x}_i-\mathbf{x}_j)}}{k^2}\left(-q_j\left(\mathbf{kk} - \frac{k^2}{3}\mathbf{I}\right) + \mathbf{S}_j\cdot i\mathbf{k}\left(\mathbf{kk} - \frac{k^2}{3}\mathbf{I}\right) + \frac{1}{2}\mathbf{Q}_j : \mathbf{kk}\left(\mathbf{kk} - \frac{k^2}{3}\mathbf{I}\right) + \cdots\right)\right\}, \tag{A.114}$$

where $\mathbf{r} \equiv \mathbf{x}_i - (\mathbf{x}_j + \mathbf{n})$ and the prime $'$ indicates that the sum goes over all j and $\mathbf{n}$ except for $j = i, \mathbf{n} = 0$. Evaluating the inverses,

$$\langle\psi\rangle_i - \psi_0(\mathbf{x}_i) = \frac{q_i}{4\pi a\lambda_f} + \frac{1}{4\pi\lambda_f}{\sum_{j\mathbf{n}}}'\left(q_j\frac{1}{r} - \mathbf{S}_j\cdot\nabla\frac{1}{r} + \frac{1}{2}\mathbf{Q}_j : \nabla\nabla\frac{1}{r} + \cdots\right) \tag{A.115}$$

$$-\nabla\psi_0(\mathbf{x}_i) = \frac{\mathbf{S}_i}{4\pi a^3\lambda_f}\frac{\lambda_p/\lambda_f + 2}{\lambda_p/\lambda_f - 1} + \frac{1}{4\pi\lambda_f}{\sum_{j\mathbf{n}}}'\left(q_j\nabla\frac{1}{r} - \mathbf{S}_j\cdot\nabla\nabla\frac{1}{r} + \frac{1}{2}\mathbf{Q}_j : \nabla\nabla\nabla\frac{1}{r} + \cdots\right) \tag{A.116}$$

$$-\nabla\nabla\psi_0(\mathbf{x}_i) = \frac{3\mathbf{Q}_i}{4\pi a^5\lambda_f}\frac{\lambda_p/\lambda_f + 3/2}{\lambda_p/\lambda_f - 1} + \frac{1}{4\pi\lambda_f}{\sum_{j\mathbf{n}}}'\left(q_j\left(\nabla\nabla - \frac{1}{3}\nabla^2\right)\frac{1}{r} - \mathbf{S}_j\cdot\nabla\left(\nabla\nabla - \frac{1}{3}\nabla^2\right)\frac{1}{r} + \frac{1}{2}\mathbf{Q}_j : \nabla\nabla\left(\nabla\nabla - \frac{1}{3}\nabla^2\right)\frac{1}{r} + \cdots\right). \tag{A.117}$$

Because $\nabla^2(1/r) = \delta(\mathbf{r})$ and the self term is removed from the sum, $\mathbf{r}$ is never zero and the $\delta(\mathbf{r})$ terms vanish.

$$\langle\psi\rangle_i - \psi_0(\mathbf{x}_i) = \frac{q_i}{4\pi a\lambda_f} + \frac{1}{4\pi\lambda_f}\sum_{j\mathbf{n}}{}' \left(q_j \frac{1}{r} - \mathbf{S}_j \cdot \nabla\frac{1}{r} + \frac{1}{2}\mathbf{Q}_j : \nabla\nabla\frac{1}{r} + \cdots \right) \tag{A.118}$$

$$-\nabla\psi_0(\mathbf{x}_i) = \frac{\mathbf{S}_i}{4\pi a^3\lambda_f}\frac{\lambda_p/\lambda_f + 2}{\lambda_p/\lambda_f - 1} + \frac{1}{4\pi\lambda_f}\sum_{j\mathbf{n}}{}' \left(q_j \nabla\frac{1}{r} - \mathbf{S}_j \cdot \nabla\nabla\frac{1}{r} + \frac{1}{2}\mathbf{Q}_j : \nabla\nabla\nabla\frac{1}{r} + \cdots \right) \tag{A.119}$$

$$-\nabla\nabla\psi_0(\mathbf{x}_i) = \frac{3\mathbf{Q}_i}{4\pi a^5\lambda_f}\frac{\lambda_p/\lambda_f + 3/2}{\lambda_p/\lambda_f - 1} + \frac{1}{4\pi\lambda_f}\sum_{j\mathbf{n}}{}' \left(q_j \nabla\nabla\frac{1}{r} - \mathbf{S}_j \cdot \nabla\nabla\nabla\frac{1}{r} + \frac{1}{2}\mathbf{Q}_j : \nabla\nabla\nabla\nabla\frac{1}{r} + \cdots \right). \tag{A.120}$$

This exactly the known point particle solution.

Appendix B

Equations of State

B.1 Hard Sphere Fluid

For hard spheres of radius a at volume fraction ϕ, the pressure can be written in terms of the value of the radial distribution function at contact $g(\phi) \equiv g(r = 2a, \phi)$,[123]

$$\widetilde{P}_{\rm hs} = \frac{3}{4\pi}\left(\phi + 4\phi^2 g(\phi)\right) \tag{B.1}$$

where $\widetilde{P}_{\rm hs} \equiv P_{\rm hs}a^3/k_BT$. The hard sphere chemical potential can be computed from the pressure by integrating the the Gibbs-Duhem relation $\phi d\widetilde{\mu} = (4\pi/3)d\widetilde{P}$,[178]

$$\widetilde{\mu}_{\rm hs} = \frac{4\pi}{3}\int_0^\phi d\phi' \frac{1}{\phi}\frac{d\widetilde{P}}{d\phi'}, \tag{B.2}$$

where $\widetilde{\mu}_{\rm hs} \equiv \mu_{\rm hs}/k_BT$ and we have neglected an additional term, $\ln(\Lambda/a)^3$, containing the DeBroglie wavelength Λ which is not needed for our calculations. The hard sphere Helmholtz energy per volume is then,

$$\widetilde{f}_{\rm hs} = -\widetilde{P}_{\rm hs} + \phi\widetilde{\mu}_{\rm hs}, \tag{B.3}$$

where $\widetilde{f}_{\rm hs} \equiv F_{\rm hs}a^3/Vk_BT$. $g(\phi)$ is given by the piecewise expression for its inverse $h(\phi) \equiv g^{-1}(\phi)$,[36,186,187]

$$h(\phi) = \begin{cases} \dfrac{(1-\phi)^3}{1-\phi/2} & 0 \le \phi \le \phi_f \\ A\dfrac{\phi_{\rm rcp}-\phi}{\phi_{\rm rcp}-\phi_f} + B\left(\dfrac{\phi_{\rm rcp}-\phi}{\phi_{\rm rcp}-\phi_f}\right)^2 + C\left(\dfrac{\phi_{\rm rcp}-\phi}{\phi_{\rm rcp}-\phi_f}\right)^3 & \phi_f < \phi \le \phi_{\rm rcp} \end{cases} \tag{B.4}$$

where $\phi_f = 0.494$ is the hard sphere freezing point and $\phi_{\rm rcp} = 0.64$ is the random close packing limit. The constants A, B and C, are determined by matching h and its first two derivatives at ϕ_f,

$$A = 3h_f + 2h_f'\left(\phi_{\rm rcp}-\phi_f\right) + \frac{1}{2}h_f''\left(\phi_{\rm rcp}-\phi_f\right)^2, \tag{B.5}$$

$$B = -3h_f - 3h_f'\left(\phi_{\rm rcp}-\phi_f\right) - h_f''\left(\phi_{\rm rcp}-\phi_f\right)^2, \tag{B.6}$$

$$C = h_f + h_f'\left(\phi_{\rm rcp}-\phi_f\right) + \frac{1}{2}h_f''\left(\phi_{\rm rcp}-\phi_f\right)^2 \tag{B.7}$$

where,

$$h_f \equiv h(\phi_f) = \frac{(1-\phi_f)^3}{1-\phi_f/2}, \tag{B.8}$$

$$h_f' \equiv \left.\frac{\partial h}{\partial\phi}\right|_{\phi=\phi_f} = \frac{(\phi_f - 5/2)(1-\phi_f)^2}{(1-\phi_f/2)^2}, \tag{B.9}$$

$$h_f'' \equiv \left.\frac{\partial^2 h}{\partial\phi^2}\right|_{\phi=\phi_f} = \frac{(1-\phi_f)\left(7-5\phi_f+\phi_f^2\right)}{2\left(1-\phi_f/2\right)^2}. \tag{B.10}$$

For $\phi \leq \phi_f$, the equations of state are equal to the traditional Carnahan-Starling[234] expressions

$$\widetilde{f}_{\text{hs}} = \frac{3\phi}{4\pi}\left(\ln\phi - 1 + \frac{(3\phi - 3\phi^2)}{(1-\phi)^2}\right), \tag{B.11}$$

$$\widetilde{P}_{\text{hs}} = \frac{3}{4\pi}\frac{\phi + \phi^2 + \phi^3 - \phi^4}{(1-\phi)^3}, \tag{B.12}$$

$$\widetilde{\mu}_{\text{hs}} = \ln\phi + \frac{3-\phi}{(1-\phi)^3} - 3, \tag{B.13}$$

where, again, we have dropped the unnecessary Λ terms in $\widetilde{f}_{\text{hs}}$ and $\widetilde{\mu}_{\text{hs}}$. Above ϕ_f, the equations take a different form. As $\phi \to \phi_{\text{rcp}}$, $h(\phi)$ decays linearly to zero, in agreement with the asymptotic behavior observed in simulations.[320,321] The ϕ^2 and ϕ^3 terms in (B.4) are added to enfore continuity of h and its first two derivatives at ϕ_f. The choice of the freezing transition ϕ_f to be the crossover point, proposed by Torquato,[186,187] is natural because the true equations of state are not analytic at ϕ_f due to the fluid/solid coexistence line.

B.2 Hard Sphere Isotropic Crystal

For isotropic hard spheres crystals, the Lennard-Jones-Devonshire lattice model[178,188] leads to the following analytic equations of state,

$$\widetilde{P}_{\text{hs}} = \frac{9}{4\pi}\frac{\phi}{1-\phi/\phi_{cp}}, \tag{B.14}$$

$$\widetilde{\mu}_{\text{hs}} = \ln\frac{27\Lambda^3}{8v_0} - 3\left(\frac{\phi_{cp}}{\phi} - 1\right) + \frac{3}{1-\phi/\phi_{cp}}, \tag{B.15}$$

where $\phi_{cp} = \sqrt{3}/2 \approx 0.74$ is the volume fraction at closest packing.

B.3 Hard Sphere Anisotropic Crystal

The hard sphere crystal Helmholtz energy per volume is computed using free volume theory,[178] where a single particle moves in the free volume V^* constrained by its neighboring particles fixed to their lattice positions,

$$\widetilde{f}_{\text{hs}} = -\frac{3\phi}{4\pi}\ln V^*, \tag{B.16}$$

where we have dropped the term containing Λ. V^* is estimated using the scheme depicted in Figure B.1.[142] If a particle moves from its lattice position toward a neighbor along the line of centers, the closest the center of the free particle can approach the center of its neighbor is a distance of $2a$. We construct a plane at this contact point, orthogonal to the line of centers of the pair, to approximate the boundary of the free volume near this neighbor. Similar planes are placed at the contact point for each of the free particle's neighbors. If the planes are extended and allowed to intersect, they will form the boundary of a small convex polyhedron centered around the free particle's lattice position. The volume of this polyhedron is an approximation for the true free volume V^*.

B.4 Depletion

The depletion equations of state are derived using free volume and scaled particle theories,[178]

$$\widetilde{P}_{\text{dep}} = \widetilde{P}_{\text{hs}} + \widetilde{\varepsilon} f(\phi), \tag{B.17}$$

$$\widetilde{\mu}_{\text{dep}} = \widetilde{\mu}_{\text{hs}} + \widetilde{\varepsilon} g(\phi), \tag{B.18}$$

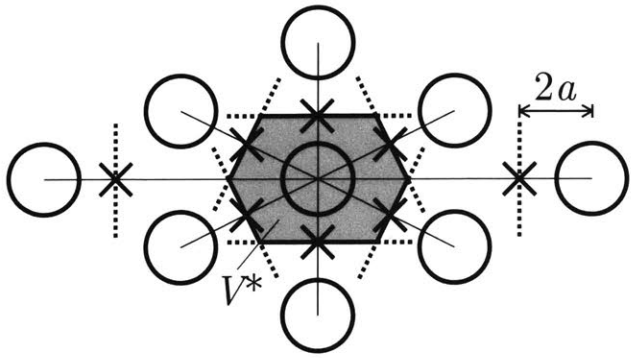

Figure B.1: Two-dimensional sketch for estimating the free volume V^* of the central particle. Boundaries (dashed lines) are placed at the contact points (crosses) of the center particle with its neighbors along the line of centers (thin lines). The boundaries are extended orthogonally to the line of centers. Their intersections bound a small convex region (thick lines) estimating the free volume (shaded region) around the central particle.

where,

$$f = \left(\alpha - \phi\frac{d\alpha}{d\phi}\right), \tag{B.19}$$

$$g = \frac{4\pi a^3}{3}\frac{d\alpha}{d\phi}, \tag{B.20}$$

and

$$\alpha = \frac{1}{\widetilde{\delta}^2(\widetilde{\delta}+3a/2)}\exp\left[\ln(1-\phi) - \frac{3\widetilde{\delta}\phi}{1-\phi} - \frac{1}{2}\left(\frac{6\widetilde{\delta}^2\phi}{1-\phi} + \frac{9\widetilde{\delta}^2\phi^2}{(1-\phi)^2}\right) - \frac{4\pi\widetilde{\delta}^3\widetilde{P}_{\rm hs}}{3}\right]. \tag{B.21}$$

$\widetilde{\varepsilon} \equiv \varepsilon/k_BT$ is the dimensionless depletion strength, $\widetilde{\delta} \equiv \delta/a$ is the dimensionless depletant radius, $\widetilde{P}_{\rm dep} \equiv P_{\rm dep}a^3/k_BT$, and $\widetilde{\mu}_{\rm dep} \equiv \mu_{\rm dep}/k_BT$. Because the depletion interaction is isotropic, the crystals it forms are also isotropic, so we use the isotropic hard sphere crystal expression in the depletion crystal equation of state for Chapter 3.

B.5 Electric/Magnetic Equations of State

The free energy per volume at constant temperature T, volume V, particle number N, and external field $\mathbf{E}_0$ is[142]

$$L\left(T,V,N,\mathbf{E}_0\right) = F_{\rm hs}\left(T,V,N\right) - \frac{N}{2}\mathbf{C}\left(T,V,N,\mathbf{E}_0\right):\mathbf{E}_0\mathbf{E}_0, \tag{B.22}$$

where $F_{\rm hs}$ is the hard sphere Helmholtz energy and $\mathbf{C}$ is the capacitance tensor. The pressure and chemical potentials are computed as derivatives of the free energy,

$$P \equiv -\frac{\partial L}{\partial V}T,N,\mathbf{E}_0 = P_{\rm hs} + \frac{N}{2}\frac{\partial\mathbf{C}}{\partial V}:\mathbf{E}_0\mathbf{E}_0, \tag{B.23}$$

$$\mu \equiv \frac{\partial L}{\partial N}T,V,\mathbf{E}_0 = \mu_{\rm hs} - \frac{1}{2}\left(\mathbf{C} + N\frac{\partial\mathbf{C}}{\partial N}\right):\mathbf{E}_0\mathbf{E}_0, \tag{B.24}$$

In terms of dimensionless quantities,

$$\widetilde{\ell}\left(\phi,\widetilde{\mathbf{E}}_0\right) \equiv \frac{La^3}{Vk_BT} = \widetilde{f}_{\rm hs}\left(\phi\right) - \frac{3\phi}{8\pi}\widetilde{\mathbf{C}}\left(\phi,\widetilde{\mathbf{E}}_0\right):\widetilde{\mathbf{E}}_0\widetilde{\mathbf{E}}_0, \tag{B.25}$$

$$\widetilde{P} \equiv \frac{Pa^3}{k_BT} = \widetilde{P}_{\rm hs} - \frac{3\phi^2}{8\pi}\frac{\partial\widetilde{\mathbf{C}}}{\partial\phi}:\widetilde{\mathbf{E}}_0\widetilde{\mathbf{E}}_0, \tag{B.26}$$

$$\widetilde{\mu} \equiv \frac{\mu}{k_BT} = \widetilde{\mu}_{\rm hs} - \frac{1}{2}\left(\widetilde{\mathbf{C}} + \phi\frac{\partial\widetilde{\mathbf{C}}}{\partial\phi}\right):\widetilde{\mathbf{E}}_0\widetilde{\mathbf{E}}_0, \tag{B.27}$$

where $\widetilde{\mathbf{C}} \equiv \mathbf{C}/a^3\lambda_f$ is the dimensionless capacitance tensor, $\widetilde{\mathbf{E}}_0 \equiv \mathbf{E}_0\sqrt{a^3\lambda_f/k_BT}$ is the dimensionless field, and λ_f is the solvent permittivity/permeability.

B.6 Fluid Capacitance

The simplest expression for the capacitance tensor is derived by assuming that each particle interacts with the mean field of the other particles, which yields the self-consistent mean-field expression,[7,172]

$$\mathbf{C} = \frac{4\pi a^3\lambda_f\beta}{1-\beta\phi}\mathbf{I}, \tag{B.28}$$

where $\beta \equiv (\lambda_p/\lambda_f - 1)/(\lambda_p/\lambda_f + 2)$ is a function of the ratio of particle permittivity/permeability λ_p to solvent permittivity/permeability λ_f. This expression is only accurate to $O(1)$, and therefore only appropriate for very dilute fluids. Jeffrey derived another expression for the capacitance accurate to $O(\phi)$ by considering the exact two-body solution,[172]

$$\mathbf{C} = 4\pi a^3\lambda_f\beta\left(1 + c_1\phi\right)\mathbf{I}, \tag{B.29}$$

where $c_1 = 1.51$ for conductors and $c_1 = -0.392$ for insulators. For other values of β, c_1 is given by the value in Figure 2 of Ref 172 divided by 3β.

B.7 Crystal Capacitance

The capacitance tensor, or rather the average particle dipole $\mathbf{S} = \mathbf{C}\cdot\mathbf{E}_0$, is computed by inverting the potential tensor $\mathscr{M} \equiv \mathscr{M}^E_{ES}$ to solve[142]

$$\mathscr{E}_0 = \mathscr{M}\cdot\mathscr{S}, \tag{B.30}$$

for the particle dipoles $\mathscr{S} \equiv [\mathbf{S}_1, \mathbf{S}_2, \ldots, \mathbf{S}_N]^T$, where $\mathscr{E}_0 \equiv [\mathbf{E}_0, \mathbf{E}_0, \ldots, \mathbf{E}_0]^T$ is the external field repeated N times, the T superscript indicates transposition, and $\mathscr{M}$ has block matrix entries

$$\mathbf{M}_{ij} = \frac{\delta_{ij}\mathbf{I}}{4\pi a^3\left(\lambda_p - \lambda_f\right)} + \frac{1}{\lambda_f V}\sum_{\mathbf{k}\neq 0}\frac{e^{i\mathbf{k}\cdot\mathbf{r}_{ij}}}{k^2}j_1^2(ka)\hat{\mathbf{k}}\hat{\mathbf{k}} \tag{B.31}$$

where $\mathbf{r}_{ij} \equiv \mathbf{x}_i - \mathbf{x}_j$ is the distance vector from particles at lattice positions $\mathbf{x}_i$ and $\mathbf{x}_j$, $\mathbf{k} \in \{(2\pi k_x/L_x, 2\pi k_y/L_y, 2\pi k_z/L_z) : (k_x, k_y, k_z) \in \mathbb{Z}\}$ is the wave vector, $k \equiv |\mathbf{k}|$ is its magnitude, $\hat{\mathbf{k}} \equiv \mathbf{k}/k$ is its unit direction, (L_x, L_y, L_z) are the dimensions of the periodic unit cell, $V \equiv L_xL_yL_z$ is its volume, and j_1 is the spherical Bessel function of degree 1. The average particle dipole is then $\mathbf{S} \equiv \sum_i \mathbf{S}_i/N$.

For crystalline phases, particles fluctuate about a lattice configuration, here BCT, HCP, or BCO. We modify the free energy for a crystalline phase to $\widetilde{\ell}(\phi, \widetilde{\mathbf{E}}_0; A_y, A_z)$, the free energy of a lattice constrained to have aspect ratios $A_y \equiv L_y/L_x$ and $A_z \equiv L_z/L_x$. The combination of ϕ, A_y, and A_z along with the particular lattice type is sufficient to completely specify the crystal structure. We minimize $\widetilde{\ell}(\phi, \widetilde{\mathbf{E}}_0; A_y, A_z)$ over all aspect ratios A_y and A_z to find the equilibrium aspect ratios $A_{y,\mathrm{eq}}$ and $A_{z,\mathrm{eq}}$ and the equilibrium free energy $\widetilde{\ell}(\phi, \widetilde{\mathbf{E}}_0) \equiv \widetilde{\ell}(\phi, \widetilde{\mathbf{E}}_0; A_{y,\mathrm{eq}}, A_{z,\mathrm{eq}})$. Because the crystal can by anisotropic, we use the anisotropic hard sphere crystal procedure for $\widetilde{f}_{\mathrm{hs}}$.

B.8 Electric/Magnetic Phase Coexistence

With explicit functions for $\widetilde{P}$ and $\widetilde{\mu}$ in the fluid phase, we can compute the fluid/fluid binodal by solving

$$P_1\left(\phi_1, \widetilde{\mathbf{E}}_0\right) = P_2\left(\phi_2, \widetilde{\mathbf{E}}_0\right), \qquad \mu_1\left(\phi_1, \widetilde{\mathbf{E}}_0\right) = \mu_2\left(\phi_2, \widetilde{\mathbf{E}}_0\right), \tag{B.32}$$

at each $\widetilde{\mathbf{E}}_0$ for the two fluid volume fractions ϕ_1 and ϕ_2. We choose to use the $O(\phi)$ expression (B.29) for the capacitance for fluid/fluid coexistence which more accurately models the dense fluid phase. For crystals,

we do not have an explicit expression for the equilibrium free energy $\widetilde{\ell}(\phi, \widetilde{\mathbf{E}}_0)$ because we must minimize $\widetilde{\ell}(\phi, \widetilde{\mathbf{E}}_0; A_y, A_z)$ to find the equilibrium aspect ratios. So, it is difficult to compute derivatives of $\widetilde{\ell}$ to find $\widetilde{P}$ and $\widetilde{\mu}$ needed in (B.32). Instead, for fluid/BCT coexistence we compute the free energy per volume for the multiphase dispersion,

$$\widetilde{\ell}\left(\phi, \widetilde{\mathbf{E}}_0\right) = \widetilde{\ell}_1\left(\phi_1, \widetilde{\mathbf{E}}_0\right) \frac{\phi_2 - \phi}{\phi_2 - \phi_1} + \widetilde{\ell}_2\left(\phi_2, \widetilde{\mathbf{E}}_0; A_z\right) \frac{\phi - \phi_1}{\phi_2 - \phi_1}, \tag{B.33}$$

and minimize over the fluid volume fraction ϕ_1, the BCT volume fraction ϕ_2, and the BCT aspect ratio A_z, to find the coexisting values at a particular $\widetilde{\mathbf{E}}_0$. The coexisting volume fractions are independent of the overall ϕ provided it is intermediate the coexisting values, $\phi_1 < \phi < \phi_2$. For fluid/BCT coexistence, we use the $O(1)$ fluid capacitance (B.28) because the coexisting fluid is very dilute (except at small fields, where entropic effects dominate anyway). Note that for BCT, $A_y = 1$ so we do not need to minimize over A_y. Fluid/HCP coexistence is handled the same way as fluid/BCT coexistence, with A_y referring to the HCP aspect ratio. For BCT/HCP coexistence, $\widetilde{\ell}$ is minimized over the volume fraction and aspect ratios of both BCT and HCP structures.

Appendix C

Solutions to the Poisson-Boltzmann Equation for a Charged Plate

Consider a charged, conducting plate at $x = 0$ in a solutions containing a symmetric electrolyte species that dissociates into ions of radius a_i and charges $q_\pm = \pm q_i$. The bulk overall volume fraction is $2\phi_i$, so the bulk species volume fractions are $\phi_{i,+} = \phi_{i,-} = \phi_i/2$. The chemical potential of ionic species i is

$$\mu_\pm(x) = \mu_{0,\pm}(\phi_+(x), \phi_-(x)) \pm q_i\psi(x) \tag{C.1}$$

where $\psi(x)$ is the electric potential, $\phi_\pm(x)$ are the volume fraction distribution of ions, and $\mu_{0,\pm}$ is the chemical potential in the absence of charges. At equilibrium, the force on the ions, which is proportional to $\nabla\mu_\pm$, vanishes so $\mu_\pm(x)$ must equal some constant $\mu_\pm(x) = C_\pm$ everywhere. Far away from the plate, $x \to \infty$, the potential vanishes, $\psi \to 0$, and the ion concentrations approach their bulk values, $\phi_\pm \to \phi_{i,\pm}$, so $C_\pm = \mu_{i,\pm} \equiv \mu_{0,\pm}(\phi_{i,+}, \phi_{i,-})$ and therefore

$$\psi(x) = \pm\frac{1}{q_i}\Big(\mu_{i,\pm} - \mu_{0,\pm}(\phi_+(x), \phi_-(x))\Big). \tag{C.2}$$

The potential obeys the Poisson equation

$$\frac{d^2\psi}{dx^2} = -\frac{\rho}{\varepsilon_f} \tag{C.3}$$

where ε_f is the electric permittivity of the fluid and the charge density is

$$\rho(x) = \frac{3q}{4\pi a^3}\left(\phi_+(x) - \phi_-(x)\right), \tag{C.4}$$

subject to the boundary conditions

$$\psi(0) = \zeta \quad \text{OR} \quad \left.\frac{d\psi}{dx}\right|_{x=0} = -\frac{q}{\varepsilon_f}, \qquad \psi(x \to \infty) \to 0, \tag{C.5}$$

where q is the plate surface charge density. If we knew *both* ψ and $d\psi/dx$ at $x = 0$ (or equivalently, ζ and q), we could numerically integrate the ODE from $x = 0$. We must use the boundary condition on ψ at $x \to \infty$ to infer the missing boundary condition at $x = 0$. Multiplying both sides of the Poisson equation by $2d\psi/dx$,

$$2\left(\frac{\mathrm{d}\psi}{\mathrm{d}x}\right)\frac{d^2\psi}{dx^2} = -2\left(\frac{\mathrm{d}\psi}{\mathrm{d}x}\right)\frac{\rho}{\varepsilon_f} \tag{C.6}$$

$$\frac{\mathrm{d}}{\mathrm{d}x}\left(\frac{\mathrm{d}\psi}{\mathrm{d}x}\right)^2 = -2\left(\frac{\mathrm{d}\psi}{\mathrm{d}x}\right)\frac{\rho}{\varepsilon_f} \tag{C.7}$$

Integrating from $x = 0$ to $x \to \infty$,

$$\left(\frac{\mathrm{d}\psi}{\mathrm{d}x}\right)^2\Bigg|_{x=0}^{x\to\infty} = -\frac{2}{\varepsilon_f}\int_\zeta^0 d\psi\,\rho(\psi), \tag{C.8}$$

where the charge density is known in terms of the potential from (C.2). The gradient in ψ vanishes far from the plate so,

$$\left(\frac{\mathrm{d}\psi}{\mathrm{d}x}\right)_0 = -\operatorname{sgn}\zeta\left(-\frac{2}{\varepsilon_f}\int_0^\zeta d\psi\,\rho(\psi)\right)^{1/2}. \tag{C.9}$$

or in terms of the charge,

$$q = \operatorname{sgn}\zeta\left(-2\varepsilon_f\int_0^\zeta d\psi\,\rho(\psi)\right)^{1/2}. \tag{C.10}$$

The sign of the gradient is chosen so that its magnitude decays away from the plate. If $\zeta > 0$, $(d\psi/dx)_0 < 0$, and if $\zeta < 0$, $(d\psi/dx)_0 > 0$. Equation (C.9) relates the surface potential and surface field, so only one needs to be specified to know both ψ and $d\psi/dx$ at $x = 0$. We can now find the solution to the Poisson equation by a simple numerical integration. The differential capacitance, $C \equiv dq/d\zeta$, can also be computed as

$$C = \frac{1}{2}\sqrt{\frac{1}{-2\varepsilon_f\int_0^\zeta d\psi\,\rho(\phi)}}(-2\varepsilon_f\rho(\zeta)) = -\frac{\varepsilon_f\rho(\zeta)}{q(\zeta)} \tag{C.11}$$

Gouy-Chapman Solution

In the Gouy-Chapman model, the ions behave ideally,

$$\mu_\pm = k_BT\ln n_\pm \pm q_i\psi, \tag{C.12}$$

and so their concentration is

$$n_\pm = n_i e^{\mp q_i\psi/k_BT}. \tag{C.13}$$

The charge density is

$$\rho = q_i n_i\left(e^{-q\psi/k_BT} - e^{q_i\psi/k_BT}\right) = -2q_i n_i\sinh\frac{q_i\psi}{k_BT} \tag{C.14}$$

The surface charge density on the plate is

$$q = \operatorname{sgn}\zeta\left(4\varepsilon_f q_i n_i\int_0^\zeta d\psi\,\sinh\frac{q_i\psi}{k_BT}\right)^{1/2} \tag{C.15}$$

$$= \operatorname{sgn}\zeta\left(4\varepsilon_f n_i k_BT\left(\cosh\frac{q_i\zeta}{k_BT} - 1\right)\right)^{1/2} \tag{C.16}$$

$$= \sqrt{8\varepsilon_f n_i k_BT}\sinh\frac{q_i\zeta}{2k_BT} \equiv 4n_i q_i\lambda\sinh\frac{q_i\zeta}{2k_BT}, \tag{C.17}$$

where $\lambda \equiv \sqrt{\varepsilon_f k_BT/2n_i q_i^2}$ is the Debye length. The differential capacitance is

$$C = \sqrt{\frac{2\varepsilon_f n_\infty q^2}{k_BT}}\cosh\frac{q\zeta}{2k_BT} \equiv \varepsilon\kappa\cosh\frac{q\zeta}{2k_BT}. \tag{C.18}$$

where $\kappa \equiv \lambda^{-1}$ is the inverse Debye length. We can recover the Debye-Huckel solution for $q_i\zeta/k_BT \ll 1$,

$$q = \varepsilon_f\kappa\zeta \tag{C.19}$$

$$C = \varepsilon_f\kappa \tag{C.20}$$

Had we integrated (C.9) from ∞ to x rather than from ∞ to x, we would have obtained,

$$\frac{\mathrm{d}\psi}{\mathrm{d}x} = -\frac{4n_i q_i\lambda}{\varepsilon_f}\sinh\frac{q_i\psi}{2k_BT}$$

$$\Rightarrow \frac{\mathrm{d}\widetilde{\psi}}{\mathrm{d}x} = -2\kappa\sinh\frac{\widetilde{\psi}}{2},$$

where $\widetilde{\psi} \equiv q_i\psi/k_BT$. We can integrate this from 0 to x to obtain the potential,

$$\widetilde{\psi}(x) = 4\tanh^{-1}\left(e^{-\kappa x}\tanh\tfrac{1}{4}\widetilde{\zeta}\right) = 2\ln\frac{1+e^{-\kappa x}\tanh\frac{1}{4}\widetilde{\zeta}}{1-e^{-\kappa x}\tanh\frac{1}{4}\widetilde{\zeta}}. \tag{C.21}$$

Carnahan-Starling Solution

In the Carnahan-Starling model,

$$\mu_\pm = k_BT\left(\ln\phi_\pm + \frac{3-\phi_i}{(1-\phi_i)^3} - 3\right) \pm q_i\psi, \tag{C.22}$$

The ion concentrations are found by solving simultaneously,

$$\ln\phi_+ + \frac{3-(\phi_+ + \phi_-)}{(1-(\phi_+ + \phi_-))^3} + \widetilde{\psi} = \ln\phi_i/2 + \frac{3-\phi_i}{(1-\phi_i)^3} \tag{C.23}$$

$$\ln\phi_- + \frac{3-(\phi_+ + \phi_-)}{(1-(\phi_+ + \phi_-))^3} - \widetilde{\psi} = \ln\phi_i/2 + \frac{3-\phi_i}{(1-\phi_i)^3} \tag{C.24}$$

which does not have an analytical solution. Therefore we can only find ρ, which in turn means we can only find q through a numerical integration. Once ρ and q are found, we can compute C.

Bibliography

[1] Wim Bogaerts, Vincent Wiaux, Dirk Taillaert, Stephan Beckx, Bert Luyssaert, Peter Bienstman, and Roel Baets. Fabrication of photonic crystals in silicon-on-insulator using 248-nm deep uv lithography. *IEEE J. Sel. Top. Quantum Electron.*, 8:928–934, 2002.

[2] J Schilling, R B Wehrspohn, A Birner, F Müller, R Hillebrand, U Gösele, S W Leonard, J P Mondia, F Genereux, H M van Driel, P Kramper, V Sandoghdar, and Busch K. A model system for two-dimensional and three-dimensional photonic crystals: Macroporous silicon. *J. Opt A.*, 3:S121–S132, 2001.

[3] Vicki L. Colvin. From opals to optics: Colloidal photonic crystals. *MRS Bull.*, 26(8):637–641, August 2001.

[4] Xiangdong Meng, Rihab Al-Salman, Jiupeng Zhao, Natalia Borissenko, Yao Li, and Frank Endres. Electrodeposition of 3d ordered macroporous germanium from ionic liquids: A feasible method to make photonic crystals with a high dielectric constant. *Angew. Chem. Int. Ed.*, 48:2703–2707, 2009.

[5] Kiyoshi Kanamura, Nao Akutagawa, and Kaoru Dokko. Three dimensionally ordered composite solid materials for all solid-state rechargeable lithium batteries. *J. Power Sources*, 146:86–89, 2005.

[6] Robert M. Darling, Kevin G. Gallagher, Jeffrey A. Kowalshi, Seungbum Ha, and Fikile R. Brushett. Pathways to low-cost electrochemical energy storage: a comparison of aqueous and nonaqueous flow batteries. *Energy Environ. Sci.*, 7:3459–3477, 2014.

[7] Alice P. Gast and Charles F. Zukoski. Electrorheological fluids as colloidal suspensions. *Adv. Colloid Interface Sci.*, 30:153–202, 1989.

[8] Thomas C. Halsey. Electrorheological fluids. *Science*, 258:761–766, 1992.

[9] Daniel J. Klingenberg. Magnetorheology: Applications and challenges. *AIChE Journal*, 47:246–249, 2001.

[10] Juan de Vicente, Daniel J. Klingenberg, and Roque Hidalgo-Alvarez. Magnetorheological fluids: a review. *Soft Matter*, 7:3701–3710, 2011.

[11] Z. P. Shulman, R. G. Gorodkin, E. V. Korobko, and V. K. Gleb. The electrorheological effect and its possible uses. *J. Non-Newtonian Fluid Mech.*, 8:29–41, 1981.

[12] Costas M. Soukoulis and Martin Wegener. Past achievements and future challenges in the development of three-dimensional photonic metamaterials. *Nat. Photonics*, 5:523–530, 2011.

[13] Xiang Zhang, Cheng Sun, and Nicholas Fang. Manufacturing at nanoscale: Top-down, bottom-up and system engineering. *J. Nanoparticle Res.*, 6:125–130, 2004.

[14] Christian Girard and Erik Dujardin. Near-field optical properties of top-down and bottom-up nanostructures. *J. Opt. A: Pure Appl. Opt.*, 8:S73–S86, 2006.

[15] George M. Whitesides and Bartosz Grzybowski. Self-assembly at all scales. *Science*, 295:2418–2421, March 2002.

[16] Nadrian Seeman and Angela M. Belcher. Emulating biology: Building nanostructures from the bottom up. *Proc. Natl. Acad. Sci.*, 99:6451–6455, 2002.

[17] Sharon C. Glotzer and Michael J. Solomon. Anisotropy of building blocks and their assembly into complex structures. *Nat. Mater.*, 6:557–562, 2007.

[18] Kyle J. M. Bishop, Christopher E. Wilmer, Siowling Soh, and Barotsz A. Grzybowski. Nanoscale forces and their uses in self-assembly. *Small*, 5(14):1600–1630, June 2009.

[19] Herbert B. Callen. *Thermodynamics and an Introduction to Thermostatistics.* John Wiley & Sons, 1985.

[20] Wenyan Liu, Miho Tagawa, Huolin L. Xin, Tong Wang, Hamed Emamy, Huilin Li, Kevin G. Yager, Francis W. Starr, Alexei V. Tkachenko, and Oleg Gang. Diamond family of nanoparticle superlattices. *Science*, 351:582–586, 2016.

[21] Yufeng Wang, Yu Wang, Dana R. Breed, Vinothan N. Manoharan, Lang Feng, Andrew D. Hollingsworth, Marcus Weck, and David J. Pine. Colloids with valance and specific directional bonding. *Nature*, 491:51–55, 2012.

[22] Amar B. Pawar and Ilona Kretzschmar. Fabrication, assembly, and application of patchy particles. *Macromol. Rapid Commun.*, 31:150–168, 2010.

[23] Alexander M. Kalsin, Marcin Fialkowski, Maciej Paszewski, Stoyan K. Smoukov, Kyle J. M. Bishop, and Bartosz A. Grzybowski. Electrostatic self-assembly of binary nanoparticle crystals with a diamond-like lattice. *Science*, 312:420–424, 2006.

[24] Robert J. Macfarlane, Byeongdu Lee, Matthew Jones, Nadine Harris, George C. Schatz, and Chad A. Mirkin. Nanoparticle superlattice engineering with dna. *Science*, 334:204–208, 2011.

[25] Benjamin W. Rogers, William M. Shih, and Vinothan Manoharan. Using dna to program the self-assembly of colloidal nanoparticles and microparticles. *Nat. Rev. Mater.*, 1:1–14, 2016.

[26] Andre V. Pinheiro, Dongran Han, William M. Shih, and Hao Yan. Challenges and opportunities for structural dna nanotechnology. *Nat. Nanotechnol.*, 6:763–772, 2011.

[27] Pablo F. Damasceno, Michael Engel, and Sharon C. Glotzer. Predictive self-assembly of polyhedra into complex structures. *Science*, 337:453–457, 2012.

[28] Beth A. Lindquist, Sayantan Dutta, Ryan B. Jadrich, Delia J. Milliron, and Thomas M. Truskett. Interactions and design rules for assembly of porous colloidal mesophases. *Soft Matter*, 13:1335–1343, 2017.

[29] Beth A. Lindquist, Ryan B. Jadrich, William D. Piñeros, and Thomas M. Truskett. Inverse design of self-assembling frank-kasper phases and insights into emergent quasicrystals. *J. Chem. Phys. B.*, 122:5547–5556, 2018.

[30] Carl S. Adorf, James Antonaglia, Julia Dshemuchadse, and Sharon C. Glotzer. Inverse design of simple pair potentials for the self-assembly of complex structures. *J. Chem. Phys.*, 149:204102, 2018.

[31] Peter G. Bolhuis and David A. Kofke. Monte carlo study of freezing of polydisperse hard spheres. *Phys. Rev. E*, 54:634–643, 1996.

[32] Moreno Fasolo and Peter Sollich. Effects of colloid polydispersity on the phase behavior of colloid-polymer mixtures. *J. Chem. Phys.*, 122:074904, 2005.

[33] Daniel J. C. Herr. Directed block copolymer self-assembly for nanoelectronics fabrication. *J. Mater. Res.*, 26:122–139, 2010.

[34] J. W. Matthews. Defects associated with the accommodation of misfit between crystals. *J. Vac.Sci. Technol.*, 12:126–133, 1975.

[35] Valerie J. Anderson and Henk N. W. Lekkerkerker. Insights into phase transition kinetics from colloid science. *Nature*, 416:811–815, April 2002.

[36] Zachary M. Sherman and James W. Swan. Dynamic, directed self-assembly of nanoparticles *via* toggled interactions. *ACS Nano*, 10:5260–5271, April 2016.

[37] Zachary M. Sherman, Helen Rosenthal, and James W. Swan. Phase separation kinetics of dynamically self-assembling nanoparticles with toggled interactions. *Langmuir*, 34:1029–1041, 2018.

[38] Rasam Soheilian, Young Suk Choi, Allan E. David, Hamed Adbi, Craig E. Maloney, and Randall M. Erb. Toward accumulation of magnetic nanoparticles into tissues of small porosity. *Langmuir*, 31:8267–8274, 2015.

[39] Sonoko Kanai, Jun Liu, Thomas W. Patapoff, and Steven J. Shire. Reversible self-association of a concentrated monoclonal antibody solution mediated by fab-fab interaction that impacts solution viscosity. *J. Pharm. Sci.*, 97:4219–4227, 2008.

[40] Sumit Goswami, Wei Wang, Tsutomu Arakawa, and Satoshi Ohtake. Developments and challenges for mab-based therapeutics. *Antibodies*, 2:452–500, 2013.

[41] V. Burckbuchler, G. Mekhloufi, A. Paillard Giteau, J. L. Grossiord, S. Huille, and F. Agnely. Rheological and syringeability properties of highly concentrated human polyclonal immunoglobulin solutions. *Eur. J. Pharm. Biopharm.*, 76:351–356, 2010.

[42] Gang Wang, Zsigmond Varga, Jennifer Hofmann, Isidro E. Zarraga, and James W. Swan. Structure and relaxation in solutions of monoclonal antibodies. *J. Phys. Chem. B*, 122:2867–2880, 2018.

[43] Yingying Lu, Shyamal K. Das, Surya S. Moganty, and Lynden A. Archer. Ionic liquid-nanoparticle hybrid electrolytes and their application in secondary lithium-metal batteries. *Adv. Mater.*, 24:2012, 4430–4435.

[44] Zhengyuan Tu, Yu Kambe, Yingying Lu, and Lynden A. Archer. Nanoporous polymer-ceramic composite electrolytes for lithium metal batteries. *Adv. Energy Mater.*, 4:1300654, 2014.

[45] A. Manuel Stephan. Review on gel polymer electrolytes for lithiium batteries. *Eur. Polym. J.*, 42:21–42, 2006.

[46] Marek Grzelczak, Jan Vermant, Eric M. Furst, and Luis M. Liz-Marzàn. Directed self-assembly of nanoparticles. *ACS Nano*, 4(7):3591–3605, June 2010.

[47] Rafal Klajn, Kyle J. M. Bishop, and Bartosz A. Grzybowski. Light-controlled self-assembly of reversible and irreversible nanoparticle suprastructures. *Proc. Natl. Acad. Sci.*, 104(25):10305–10309, June 2007.

[48] Maria-Melanie Russew and Stefan Hecht. Photoswitches: From molecules to materials. *Adv. Mater.*, 22:3348–3360, 2010.

[49] Immanuel Willerich and Franziska Gröhn. Photoswitchable nanoassemblies by electrostatic self-assembly. *Angew. Chem. Int. Ed.*, 49:8101–8108, 2010.

[50] Yuming Cheng, Jinfeng Dong, and Xuefeng Li. Light-switchable self-assembly of non-photoresponsive gold nanoparticles. *Langmuir*, 34:6117–6124, 2018.

[51] Matthew E. Helgeson, Shannon E. Moran, Harry Z. An, and Patrick S. Doyle. Mesoporous organohydrogels from thermogelling photocrosslinkable nanoemulsions. *Nat. Mater.*, 11:344–352, 2012.

[52] Lilian C. Hsiao and Patrick S. Doyle. Celebrating *Soft Matter's* 10th anniversary: Sequential phase transitions in thermoresponsive nanoemulsions. *Soft Matter*, 11:8426–8431, 2015.

[53] Li-Chiun Cheng, P. Douglas Godfrin, James W. Swan, and Patrick S. Doyle. Thermal processing of thermogelling nanoemulsions as a route to tune material properties. *Soft Matter*, 14:5604–5614, 2018.

[54] Li-Chiun Cheng, Zachary M. Sherman, James W. Swan, and Patrick S. Doyle. Colloidal gelation through thermally-triggered surfactant displacement. *Langmuir*, 2019. Submitted.

[55] Lorenzo Di Michele, Francesco Varrato, Jurij Kotar, Simon H. Nathan, Giuseppe Foffi, and Erika Eiser. Multistep kinetic self-assembly of dna-coated colloids. *Nat. Commun.*, 4(2007):2007, 2013.

[56] Sara C. Wagner, Meike Roskamp, Helmut Cölfen, Christoph Böttcher, Sabine Schlecht, and Beate Koksch. Switchable electrostatic interactions between gold nanoparticles and coiled coil peptides direct colloid assembly. *Org. Biomol. Chem.*, 7:46–51, 2009.

[57] S. R. Johnson, S. D. Evans, and R. Brydson. Influence of a terminal functionality on the physical properties of surfactant-stabilized gold nanoparticles. *Langmuir*, 14:6639–6647, 1998.

[58] K. George Thomas, Said Barazzouk, Binil Itty Ipe, S. T. Shibu Joseph, and Prashant Kamat. Uniaxial plasmon coupling through longitudinal self-assembly of gold nanorods. *J. Phys. Chem.*, 108:13066–13068, 2004.

[59] Zhenhua Sun, Weihai Ni, Zhi Yang, Xiaoshan Kou, Li Li, and Jianfang Wang. ph-controlled reversible assembly and disassembly of gold nanorods. *Small*, 4:1287–1292, 2008.

[60] Seth Fraden, Alan J. Hurd, and Robert B. Meyer. Electric-field-induced association of colloidal particles. *Phys. Rev. Lett.*, 63(21):2373–2376, November 1989.

[61] Anand Yethiraj and Alfons van Blaaderen. A colloidal model system with an interaction tunable from hard sphere to soft and dipolar. *Nature*, 421:513–517, 2003.

[62] Simon O. Lumsdon, Eric W. Kaler, and Orlin D. Velev. Two-dimensional crystallization of microspheres by a coplanar ac electric field. *Langmuir*, 20:2108–2116, 2004.

[63] Ronald Pethig, Ying Huang, Xiao-Bo Wang, and Julian P. H. Burt. Positive and negative dielectrophoretic collection of colloidal particles using interdigitated castellated microelectrodes. *J. Phys. D: Appl. Phys.*, 25:881–888, 1992.

[64] Joanne H. E. Promislow and Alice P. Gast. Magnetorheological fluid structure in a pulsed magnetic field. *Langmuir*, 12(17):4095–4102, August 1996.

[65] Joanne H. E. Promislow and Alice P. Gast. Low-energy suspension structure of a magnetorheological fluid. *Phys. Rev. E*, 56(1):642–651, July 1997.

[66] Randall M. Erb, Hui S. Son, Bappaditya Samanta, Vincent M. Rotello, and Benjamin B. Yellen. Magnetic assembly of colloidal superstructures with multipole symmetry. *Nature*, 457:999–1002, 2009.

[67] James W. Swan, Paula A. Vasquez, Peggy A. Whitson, E. Michael Fincke, Koichi Wakata, Sandra H. Magnus, Frank De Winne, Michael R. Barratt, Juan H. Agui, Robert D. Green, Nancy R. Hall, Donna Y. Bohman, Charles T. Bunnell, Alice P. Gast, and Eric M. Furst. Multi-scale kinetics of a field-directed colloidal phase transition. *Proc. Natl. Acad. Sci.*, 109(40):16023–16028, October 2012.

[68] James W. Swan, Jonathan L. Bauer, Yifei Liu, and Eric M. Furst. Directed colloidal self-assembly in toggled magnetic fields. *Soft Matter*, 10(8):1102–1109, February 2014.

[69] Jaakko V. I. Timonen, Mika Latikka, Ludwik Leibler, Robin H. A. Ras, and Olli Ikkala. Switchable static and dynamic self-assembly of magnetic droplets on superhydrophobic surfaces. *Science*, 341:253–257, 2013.

[70] T. H. Besseling, M. Hermes, A. Fortini, M. Dijkstra, A. Imhof, and A. van Blaaderen. Oscillatory shear-induced 3d crystalline order in colloidal hard-sphere fluids. *Soft Matter*, 8:6931–6939, 2012.

[71] J. Vermant and M. J. Solomon. Flow-induced structure in colloidal suspensions. *J. Phys.: Condens. Matter*, 17:R187–R216, 2005.

[72] Xiang Cheng, Xinliang Xu, Stuart A. Rice, Aaron R. Dinner, and Itai Cohen. Assembly of vorticity-aligned hard-sphere colloidal strings in a simple shear flow. *PNAS*, 109:63–67, 2012.

[73] James W. Swan, Paula A. Vasquez, and Eric M. Furst. Buckling instability of self-assembled colloidal columns. *Phys. Rev. Lett.*, 113:138301, 2014.

[74] Jonathan L. Bauer, Yifei Liu, Martin J. Kurian, James W. Swan, and Eric M. Furst. Coarsening mechanics of a colloidal suspension in toggled fields. *J. Chem. Phys.*, 143:074901, 2015.

[75] Jonathan L. Bauer, Martin J. Kurian, Johnathan Stauffer, and Eric M. Furst. Suppressing the rayleigh-plateau instability in field-directed colloidal assembly. *Langmuir*, 32:6618–6623, 2016.

[76] Xun Tang, Bradley Rupp, Yuguang Yang, Tara D. Edwards, Martha A. Grover, and Michael A. Bevan. Optimal feedback controlled assembly of perfect crystals. *ACS Nano*, 10:6791–6798, 2016.

[77] Xun Tang, Jianli Zhang, Michael A. Bevan, and Martha A. Grover. A comparison of open-loop and closed-loop strategies in colloidal self-assembly. *J. Process Control*, 60:141–151, 2017.

[78] Prateek K. Jha, Vladimir Kuzovkov, Bartosz A. Grzybowski, and Monica Olvera de la Cruz. Dynamic self-assembly of photo-switchable nanoparticles. *Soft Matter*, 8:227–234, 2012.

[79] Rui Zhang, David A. Walker, Bartosz A. Grzybowski, and Monica Olvera de la Cruz. Accelerated self-replication under non-equilibrium, periodic energy delivery. *Angew. Chem.*, 126:177–181, 2014.

[80] Rui Zhang, Joshua M. Dempster, and Monica Olvera de la Cruz. Self-replication in colloids with asymmetric interactions. *Soft Matter*, 10:1315–1319, 2014.

[81] Mario Tagliazucchi, Emily A. Weiss, and Igal Szleifer. Dissipative self-assembly of particles interacting through time-oscillatory potentials. *Proc. Natl. Acad. Sci.*, 111(27):9751–9756, July 2014.

[82] Sumedh R. Risbud and James W. Swan. Dynamic self-assembly of colloids through periodic variation of inter-particle potentials. *Soft Matter*, 11(16):3232–3240, February 2015.

[83] M. Tagliazucchi and I. Szleifer. Dynamics of dissipative self-assembly of particles interacting through oscillatory forces. *Farad. Discuss.*, 2016.

[84] Chen Long, Qun-li Lei, Chun-lai Ren, and Yu-qiang Ma. Three-dimensional non-close-packed structures of oppositely charged colloids driven by ph oscillation. *J. Phys. Chem. B*, 122:3196–3201, 2018.

[85] Peter Reimann. Brownian motors: Noisy transport far from equilibrium. *Phys. Rep.*, 361:57–265, 2002.

[86] Manish Mittal, Pushkar P. Lele, Eric W. Kaler, and Eric W. Furst. Polarization and interactions of colloidal particles in ac electric fields. *J. Chem. Phys.*, 129:064513, 2008.

[87] Martin Z. Bazant. Induced-charge electrokinetic phenomena. In A. Ramos, editor, *Electrokinetics and Electrohydrodynamics of Microsystems*. Springer, 2011.

[88] Faiz Ul Amin, Ali Kafash Hoshiar, Ton Duc Do, Yeongil Noh, Shahid Ali Shah, Muhammad Sohail Khan, Jungwon Yoon, and Myeong Ok Kim. Osmotin-loaded magnetic nanoparticles with electromagnetic guidance for the treatment of alzheimer's disease. *Nanoscale*, 9:10619–10632, 2017.

[89] Mirjam E. Leunissen, Hanumantha Rao Vutukuri, and Alfons van Blaaderen. Directing colloidal self-assembly with biaxial electric fields. *Adv. Mater.*, 21:3116–3120, 2009.

[90] Frank Smallenburg and Marjolein Dijkstra. Phase diagram of colloidal spheres in a biaxial electric or magnetic field. *J. Chem. Phys.*, 132:204508, 2010.

[91] James E. Martin and Alexey Snezhko. Driving self-assembly and emergent dynamics in colloidal suspensions by time-dependent magnetic fields. *Rep. Prog. Phys.*, 76:126601, 2013.

[92] Di Du, Dichuan Li, Maghuri Thakur, and Sibani Lisa Biswal. Generating an *In Situ* tunable interaction potential for probing 2-d colloidal phase behavior. *Soft Matter*, 9:6867–6875, 2013.

[93] Sibani Lisa Biswal and Alice P. Gast. Micromixing with linked chains of paramagnetic particles. *Anal. Chem.*, 76:6448–6455, 2004.

[94] Thomas Franke, Lothar Schmid, David A. Weitz, and Achim Wixforth. Magneto-mechanical mixing and manipulation of picoliter volumes in vesicles. *Lab Chip*, 9:2831–2835, 2009.

[95] Anil K. Vuppu, Antonio a. Garcia, Mark A. Hayes, Karl Booksh, Patrick E. Phelan, Ronald Calhoun, and Sanjoy K. Saha. Phase sensitive enhancement for biochemical detection using rotating paramagnetic particle chains. *J. Appl. Phys.*, 96:6831–6838, 2004.

[96] McNaughton. Brandon H., Rodney R. Agayan, Roy Clarke, Ron G. Smith, and Raoul Kopelman. Single bacterial cell detection with nonlinear rotational frequency shifts of driven magnetic microspheres. *Appl. Phys. Lett.*, 91:224105, 2007.

[97] Sang Yooh Park, Hiroshi Handa, and Adarsh Sandu. Magneto-optical biosensing platform based on light scattering from self-assembled chains of functionalized rotating magnetic beads. *Nano Lett.*, 10:446–451, 2010.

[98] Rémi Dreyfus, Jean Baudry, Marcus L. Roper, Marc Fermigier, Howard A. Stone, and Jérôme Bibette. Microscopic artificial swimmers. *Nature*, 437:862–865, 2005.

[99] Famin Qiu, Satoshi Fujita, Rami Mhanna, Li Zhang, Benjamin R. Simona, and Bradley J. Nelson. Magnetic helical microswimmers functionalized with lipoplexes for targeted gene delivery. *Adv. Funct. Mater.*, 25:1666–1671, 2015.

[100] Di Du, Elaa Hilou, and Sibani Lisa Biswal. Reconfigurable paramagnetic microswimmers: Brownian motion affects non-reciprocal actuation. *Soft Matter*, 14:3463–3470, 2018.

[101] Fernando Martinez-Pedrero and Pietro Tierno. Magnetic propulsion of self-assembled colloidal carpets: Efficient cargo transport via a conveyor-belt effect. *Phys. Rev. Appl.*, 3:051003, 2015.

[102] Sung-Yon Kim, Jae Hun Cho, Evan Murray, Naveed Bakh, Heejin Choi, Kimberly Ohn, Luzdary Ruelas, Austin Hubbert, Meg McCue, Sara L. Vassallo, Philipp J. Keller, and Kwanghun Chung. Stochastic electrotransport selectively enhances the transport of highly electromobile molecules. *Proc. Natl. Acad. Sci.*, 46:E6274–E6283, 2015.

[103] Stephen J. Ebbens and Jonathan R. Howse. Direct observation of the direction of motion for spherical catalytic swimmers. *Langmuir*, 27:12293–12296, 2011.

[104] Allan M. Brooks, Syeda Sabrina, and Kyle J. M. Bishop. Shape-directed dynamics of active colloids powered by induced-charge electrophoresis. *Proc. Natl. Acad. Sci.*, 115:1090–1099, 2018.

[105] Thomas B. Jones. Quincke rotation of spheres. *IEEE Trans. Ind. Appl.*, IA-20:845–849, 1984.

[106] Bartosz A. Grzybowski, Howard A. Stone, and George M. Whitesides. Dynamic self-assembly of magnetized, millimetre-sized objects rotating at a liquid-air interface. *Nature*, 405:1033–1036, 2000.

[107] E. Lemaire, L. Lobry, N. Pannacci, and F. Peters. Viscosity of an electro-rheological suspension with internal rotations. *J. Rheol.*, 52:769–783, 2008.

[108] Nguyen H. P. Nguyen, Daphne Klotsa, Michael Engel, and Sharon C. Glotzer. Emergent collective phenomena in a mixture of hard shaped through active rotation. *PRL*, 112:075701, 2014.

[109] Tim Sanchez, Daniel T. N. Chen, Stephen J. DeCamp, Michael Heymann, and Zvonimir Dogic. Spontaneous motion in hierarchically assembled active matter. *Nature*, 491:431–435, 2012.

[110] M. C. Marchetti, J. F. Joanny, S. Ramaswamy, T. B. Liverpool, J. Prost, Madan Rao, and R. Aditi Simha. Hydrodynamics of soft active matter. *Rev. Mod. Phys.*, 85:1143–1189, 2013.

[111] John Toner, Yuhai Tu, and Sriram Ramaswamy. Hydrodynamics and phases of flocks. *Ann. Phys.*, 318:2170–244, 2005.

[112] Joakim Stenhammer, Davide Marenduzzo, Rosalind J. Allen, and Michael E. Cates. Phase behavior of active brownian particles: the role of dimensionality. *Soft Matter*, 10:1489–1499, 2014.

[113] Jeremie Palacci, Stefano Sacanna, Asher Preska Steinberg, David J. Pine, and Paul M. Chaikin. Living crystals of light-activated colloidal surfers. *Science*, 339:936–940, February 2013.

[114] S. C. Takatori and J. F. Brady. Towards a thermodynamics of active matter. *Phys. Rev. E*, 91:032117, 2005.

[115] Michelle Driscoll, Blaise Delmotte, Mena Youssef, Stefano Sacanna, Aleksander Donev, and Paul Chaikin. Unstable fronts and motile structures formed by microrollers. *Nat. Phys.*, 13:375–379, 2017.

[116] Alexandra Zidovska, David A. Weitz, and Timothy J. Mitchison. Micro-scale coherence in interphase chromatin dynamics. *Proc. Natl. Acad. Sci.*, 110:15555–15560, 2013.

[117] David Saintillan, Michael J. Shelley, and Alexandra Zidovska. Extensile motor activity drives coherent motions in a model of interphase chromatin. *Proc. Natl. Acad. Sci.*, 115:11442–11447, 2018.

[118] Arnold Mathijssen, Francisca Guzmán-Lastra, Andreas Kaiser, and Hartmut Löwen. Nutrient transport driven by microbial active carpets. *Phys. Rev. Lett.*, 121:248101, 2018.

[119] Bruce J. Ackerson and Schätzel. Classical growth of hard-sphere colloidal ccrystals. *Phys. Rev. E*, 52:6448–6460, 1995.

[120] Pablo. G. Debenedetti. *Metastable Liquids: Concepts and Principles.* Princeton University Press, 1996.

[121] John W. Cahn and John E. Hilliard. Free energy of a nonuniform system. i. interfacial free energy. *J. Chem. Phys.*, 28(2):258–267, February 1958.

[122] John W. Cahn. On spinodal decomposition. *Acta. Metall.*, 9:795–801, 1961.

[123] Donald A. McQuarrie. *Statistical Mechanics.* University Science Books, 2000.

[124] W. B. Russel, P. M. Chaikin, J. Zhu, W. V. Meyer, and R. Rogers. Dendritic growth of hard sphere crystals. *Langmuir*, 13:3871–3881, 1997.

[125] W. B. Russel, D. A. Saville, and W. R. Schowalter. *Colloidal Dispersions.* Cambridge University Press, 1989.

[126] Sangtae Kim and Seppo J. Karrila. *Microhydrodynamics: Principles and Selected Applications.* Dover Publications, 2005.

[127] Jens Rotne and Stephen Prager. Variational treatment of hydrodynamic interactions in polymers. *J. Chem. Phys.*, 50:4831, 1969.

[128] Andrew M. Fiore, Florencio Balboa Usabiaga, Aleksander Donev, and James W. Swan. Rapid sampling of stochastic displacements in brownian dynamics simulations. *J. Chem. Phys.*, 146:124116, 2017.

[129] Andrew Fiore and James Swan. Rapid sampling of stochastic displacements in brownian dynamics simulations with stresslet constraints. *J. Chem. Phys.*, 148:044114, 2018.

[130] John F. Brady and Georges Bossis. Stokesian dynamics. *Annu. Rev. Fluid Mech.*, 20:111–157, 1988.

[131] Asimina Sierou and John F. Brady. Accelerated stokesian dynamics simulations. *J. Fluid Mech.*, 448:115–146, 2001.

[132] Donald L. Ermak and J. A. McCammon. Brownian dynamics with hydrodynamic interactions. *J. Chem. Phys.*, 69(4):1352–1360, August 1978.

[133] W. B. Russel. Review of the role of colloidal forces in the rheology of suspensions. *J. Rheol.*, 24:287–317, 1980.

[134] C. Patrick Royall, Wilson C. K. Poon, and Eric R. Weeks. In search of colloidal hard spheres. *Soft Matter*, 9:17–27, 2013.

[135] David M. Heyes and Paul J. Mitchell. Self-diffusion and viscoelasticity of dense hard-sphere colloids. *J. Chem. Soc. Faraday Trans.*, 90(13):1931–1940, 1994.

[136] D. M. Heyes and J. R. Melrose. Brownian dynamics simulations of model hard-sphere suspensions. *J. Non-Newtonian Fluid Mech.*, 46(1):1–28, January 1993.

[137] Zsigmond Varga, Gang Wang, and James Swan. The hydrodynamics of colloidal gelation. *Soft Matter*, 11:9009–9019, September 2015.

[138] Andrew M. Fiore, Gang Wang, and James W. Swan. From hindered to promoted settling in dispersions of attractive colloids: Simulation, modeling, and application to macromolecular characterization. *Phys. Rev. Fluids*, 3:063302, 2018.

[139] Joshua A. Anderson, Chris D. Lorenz, and A. Travessat. General purpose molecular dynamics simulations fully implemented on graphics processing units. *J. Comput. Phys.*, 227(10):5342–5359, May 2008.

[140] Carolyn L. Phillips, Joshua A. Anderson, and Sharon C. Glotzer. Pseudo-random number generation for Brownian dynamics and dissipative particle dynamics simulations on GPU devices. *J. Comput. Phys.*, 230(19):7191–7201, August 2011.

[141] Jens Glaser, Trung Dac Nguyen, Joshua A. Anderson, Pak Lui, Filippo Spiga, Jaime A. Millan, David C. Morse, and Sharon C. Glotzer. Strong scaling of general-purpose molecular dynamics simulations on gpus. *Comput. Phys. Commum.*, 192:97–107, 2015.

[142] Zachary M. Sherman, Dipanjan Ghosh, and James W. Swan. Field-directed self-assembly of mutually polarizable nanoparticles. *Langmuir*, 34:7117–7134, 2018.

[143] L. D. Landau and E. M. Lifshitz. *Electrodynamics of Continuous Media.* Pergamon Press, 1960.

[144] John David Jackson. *Classical Electrodynamics.* John Wiley & Sons, 1998.

[145] R. T. Bonnecaze and J. F. Brady. A method for determining the effective conductivity of dispersions of particles. *Proc. R. Soc. A*, 430:285–313, 1990.

[146] Eric E. Keaveny and Martin R. Maxey. Modeling the magnetic interactions between paramagnetic beads in magnetorheological fluids. *J. Comput. Phys.*, 227:9554–9571, 2008.

[147] Pietro Tierno, Ramanathan Muruganathan, and Thomas M. Fischer. Viscoelasticity of dynamically self-assembled paramagnetic colloidal clusters. *Phys. Rev. Lett.*, 98:028301, 2007.

[148] J.-F. Berret, O. Sandre, and A. Mauger. Size distribution of superparamagnetic particles determined by magnetic sedimentation. *Langmuir*, 23:2993–2999, 2007.

[149] Jose Ramos, Juan de Vicente, and Hidalgo-Álvarez. Small-amplitude oscillatory shear magnetorheology of inverse ferrofluids. *Langmuir*, 26:9334–9341, 2010.

[150] J. Ramos, D. J. Klingenberg, R. Hidalgo-Alvarez, and J. de Vicente. Steady shear magnetorheology of inverse ferrofluids. *J. Rheol.*, 55:127–152, 2011.

[151] B. Cichocki, R. B. Jones, Ramzi Kutteh, and E. Wajnryb. Friction and mobility for colloid spheres in stokes flow near a boundary: The multipole method and applications. *J. Chem. Phys.*, 112:2548–2561, 2000.

[152] Eligiusz Wajnryb, Krzysztof A. Mizerski, Pawel J. Zuk, and Piotr Szymczak. Generalization of the rotne-prager-yamakawa mobility and shear disturbance tensors. *J. Fluid Mech.*, 731:R3, 2013.

[153] Roland Freund, Gene H. Golud, and Noël M. Nachtigal. Iterative solution of linear systems. *Acta Numer.*, 1:57–100, 1991.

[154] R. T. Bonnecaze and J. F. Brady. Dynamic simulation of an electrorheological fluid. *J. Chem. Phys.*, 96:2183–2202, 1992.

[155] Dag Lindbo and Anna-Karin Tornberg. Spectral accuracy in fast ewald-based methods for particle simulations. *J. of Comput. Phys.*, 230:8744–8761, 2011.

[156] Andrew M. Fiore. *Fast Simulation Methods for Soft Matter Hydrodynamics.* PhD thesis, Massachusetts Institute of Technology, February 2019.

[157] Nvidia. cufft. `developer.nvidia.com/cufft`.

[158] Kipton Barros and Erik Luijten. Dielectric effects in the self-assembly of binary colloidal aggregates. *Phys. Rev. Lett.*, 113:017801, 2014.

[159] Sandeep Yadav, Thomas M. Laue, Devendra S. Kalonia, Shubhadra N. Singh, and Steven J. Shire. The influence of charge distribution on self-association and viscosity behavios of monoclonal antibody solutions. *Mol. Pharmaceutics*, 9:791–802, 2012.

[160] Eric J. Yearley, Isidro E. Zarraga, Steven J. Shire, Thomas Scherer, Yatin Gokarn, Norman J. Wagner, and Yun Liu. Small-angle neutron scattering characterization of monoclonal antibody conformations and interactions at high concentrations. *Biophys. J.*, 105:720–731, 2013.

[161] Eric J. Yearley, Paul D. Godfrin, Tatiana Perevozchikova, Hailiang Zhang, Peter Falus, Lionel Porcar, Michihiro Nagao, Joseph E. Curtis, Pradad Gawande, Rosalynn Taing, Isidro E. Zarraga, Norman J. Wagner, and Yun Liu. Observation of small cluster formation in concentrated monoclonal antibody solutions and its implications to solution viscosity. *Biophys. J.*, 106:1763–1770, 2014.

[162] Martin Z. Bazant, Mustafa Sabri Kilic, Brian D. Storey, and Armand Ajdari. Towards an understanding of induced-charge electrokinetics at large applied voltages in concentrated solutions. *Adv. Colloid Interface Sci.*, 152:48–88, 2009.

[163] M. Mittal and E. M. Furst. Electric field-directed convective assembly of ellipsoidal colloidal particles to create optically and mechanically anisotropic thin films. *Adv. Funct. Mater.*, 19:3271–3278, 2009.

[164] Anke Kuijk, Thomas Troppenz, Laura Filion, Arnout Imhof, René Roji, Marjolein Dijkstra, and Alfons van Blaaderen. Effect of external electric fields on the phase behavior of colloidal silia rods. *Soft Matter*, 10:6249–6255, 2014.

[165] Thomas Troppenz, Laura Filion, René van Roji, and Marjolein Dijkstra. Phase behaviour of polarizable colloidal hard rods in an external electric field: A simulation study. *J. Chem. Phys.*, 141:154903, 2014.

[166] Arash Azari, Jérôme J. Crassous, Adriana M. Mihut, Erik Bialik, Peter Schurtenberger, Joakim Stenhammar, and Per Linse. Directed self-assembly of polarizable ellipoids in an external electric field. *Langmuir*, 33:13834–13840, 2017.

[167] Kyung-Sang Cho, Dmitri V. Talapin, Wolfgang Gaschler, and Christopher B. Murray. Designing pbse nanowires and nanorings through oriented attachment of nanoparticles. *J. Am. Chem. Soc.*, 127:7140–7147, 2005.

[168] Xi Zhang, Zhenli Zhang, and Sharon C. Glotzer. Simulation study of dipole-induced self-assembly of nanocubes. *J. Phys. Chem. C*, 111:4132–4137, 2007.

[169] James W. Swan and Gang Wang. Rapid calculation of hydrodynamic and transport properties in concentrated solutions of colloidal particles and macromolecules. *Phys. Fluids*, 28:011902, 2016.

[170] Michele Benzi, Gene H. Golub, and Jörg Liesen. Numerical solution of saddle point problems. *Acta Numer.*, 14:1–137, 2005.

[171] Gang Wang, Andrew M. Fiore, and James W. Swan. On the viscosity of adhesive hard sphere dispersions – critical scaling and the role of rigid contacts. *J. Rheol.*, 63:229–245, 2019.

[172] D. J. Jeffrey. Conduction through a random suspension of spheres. *Proc. R. Soc. A.*, 335:355–367, 1973.

[173] A. S. Sangani and A. Acrivos. The effective conductivity of a periodic array of spheres. *Proc. R. Soc. Lond. A.*, 386:263–275, 1983.

[174] H. A. Kramers. Brownian motion in a field of force and the diffusion model of chemical reactions. *Physica*, 7:284–304, 1940.

[175] Peter Hänggi, Peter Talkner, and Michal Borkovec. Reaction-rate theory: Fifty years after kramer. *Rev. Mod. Phys.*, 62:251–341, 1990.

[176] R. J. Baxter. Percus-yevick equation for hard spheres with surface adhesion. *J. Chem. Phys.*, 49:2770–2774, 1968.

[177] Massimo G. Noro and Daan Frenkel. Extended corresponding-states behavior for particles with variable range attractions. *J. Chem. Phys.*, 113(8):2941–2944, August 2000.

[178] Henk N. W. Lekkerkerker and Remco Tuinier. *Colloids and the Depletion Interaction.* Springer, 2011.

[179] Sho Asakura and Fumio Oosawa. On interaction between two bodies immersed in a solution of macromolecules. *J. Chem. Phys.*, 22:1255–1256, June 1954.

[180] C. Haas and J. Drenth. Understanding protein crystallization on the basis of the phase diagram. *J. Cryst. Growth*, 196:388–394, 1999.

[181] C. Haas and J. Drenth. The interface between a protein crystal and an aqueous solution and its effects on nucleation and crystal growth. *J. Phys. Chem. B*, 104:368–377, 2000.

[182] Deniz Erdemir, Alfred Y. Lee, and Allan S. Myerson. Nucleation of crystals from solution: Classical and two-step models. *Acc. of Chem. Res.*, 42(5):621–629, May 2009.

[183] Thierry Biben, Jean-Pierre Hansen, and Jean-Louis Barrat. Density profiles of concentrated colloidal suspensions in sedimentation equilibrium. *J. Chem. Phys.*, 98(9):7330, May 1993.

[184] M. A. Rutgers, J. H. Dunsmuir, J. Z. Xue, W. B. Russel, and P. M. Chaikin. Measurement of the hard-sphere equation of state using screened polystyrene colloids. *Phys. Rev. B*, 53(9):5043–5046, March 1996.

[185] Daniel J. Beltran-Villega, Benjamin A. Schultz, Nguyen H. P. Nguyen, Sharon C. Glotzer, and Ronald G. Larson. Phase behavior of Janus colloids determined by sedimentation equilibrium. *Soft Matter*, 10(26):4593–4602, July 2014.

[186] S. Torquato. Mean nearest-neighbor distance in random packings of hard d-dimensional spheres. *Phys. Rev. Lett.*, 74(12):2156–2159, March 1995.

[187] S. Torquato. Nearest-neighbor statistics for packings of hard spheres and disks. *Phys. Rev. E*, 51(4):3170–3182, April 1995.

[188] J. E. Lennard-Jones and A. F. Devonshire. Critical phenomena in gases–i. *Proc. R. Soc. A*, 163(912):53–70, November 1937.

[189] F. A. Lindemann. The calculation ofmolecularvibration frequencies. *Phys. Z.*, 11:609–612, 1910.

[190] F. H. Stillinger and T. A. Wber. Lindemann melting criterion and the gaussian core model. *Phys. Rev. B*, 22:3790–3794, 1980.

[191] James Sethna. *Statistical Mechanics: Entropy, Order Parameters, and Complexity.* Oxford University Press, 2011.

[192] Peter J. Lu, Emanuela Zaccarelli, Fabio Ciulla, Andrew B. Schofield, Francesco Sciortino, and David A. Weitz. Gelation of particles with short-range attraction. *Nature*, 453:499–503, 2008.

[193] G. A. Vliegenthart and H. N. W. Lekkerkerker. Measurement of the interfacial tension of demixed colloid-polymer suspensions. *Progr. Colloid Polym. Sci.*, 105:27–30, 1997.

[194] Paul van der Schoot. Remarks on the interfacial tension in colloidal systems. *J. Phys. Chem. B.*, 103:8804–8808, 1999.

[195] R. Tuinier, J. Rieger, and C. G. Kruif. Depletion-induced phase separation in colloid-polymer mixtures. *Adv. Colloid Interface Sci.*, 103:1–31, 2003.

[196] Michael Dean Bybee. *Hydrodynamic Simulations of Colloidal Gels: Microstructure, Dynamics, and Rheology.* ProQuest, 2009.

[197] Hojin Kim, Jonathan L. Bauer, Paula A. Vasquez, and Eric M. Furst. Structural coarsening of magnetic ellipsoid particle suspensions driven in toggled fields. *J. Phys. D: Appl. Phys.*, 52:184002, 2019.

[198] Jianping Ge and Yadong Yin. Responsive photonic crystals. *Angew. Chem., Int. Ed.*, 50:1492–1522, 2011.

[199] Kevin D. Hermanson, Simon O. Lumsdon, Jacob P. Williams, Eric W. Kaler, and Orlin D. Velev. Dielectrophoretic assembly of electrically functional microwires from nanoparticle suspensions. *Science*, 294:1082–1086, November 2001.

[200] Jason M. McMullan and Norman J. Wagner. Directed self-assembly of colloidal crystals by dielectrophoretic ordering. *Langmuir*, 28:4123–4130, 2012.

[201] A. T. Skjeltorp. One- and two- dimensional crystallization of magnetic holes. *Phys. Rev. Lett.*, 51:2306–2309, 1983.

[202] T. Gong, D. T. Wu, and D. W. M. Marr. Electric field-reversible three-dimensional colloidal crystals. *Langmuir*, 19:5967–5970, 2003.

[203] Anand Yethiraj, Alan Wouterse, Benito Groh, and Alfons van Blaaderen. Nature of an electric-field-induced colloidal martensitic transition. *Phys. Rev. Lett.*, 92:058301, 2004.

[204] T. Ding, K. Song, K. Clays, and C. Tung. Fabrication of 3d photonic crystals of ellipsoids: Convective self-assembly in magnetic field. *Adv. Mater.*, 21:1936–1940, 2009.

[205] Tomaž Mohorič, Gašper Kokot, Natan Osterman, Alexey Snezhko, Andrej Vilfan, Dušan Babič, and Jure Dobnikar. Dynamic assembly of magnetic colloidal vortices. *Langmuir*, 32:5094–5101, 2016.

[206] Antti-Pekka Hynninen and Marjolein Dijkstra. Phase diagram of dipolar hard and soft spheres: Manipulation of colloidal crystal structures by an external field. *Phys. Rev. Lett.*, 94(13):138303, April 2005.

[207] Antti-Pekka Hynninen and Marjolein Dijkstra. Phase behavior of dipolar hard and soft spheres. *Phys. Rev. E*, 72:051402, 2005.

[208] Amit Goyal, Carol K. Hall, and Orlin D. Velev. Phase diagram for stimulus-responsive materials containing dipole colloidal particles. *Phys. Rev. E*, 77:031401, 2008.

[209] K. Han, Y. T. Feng, and D. R. J. Owen. Three-dimensional modelling and simulation of magnetorheological fluids. *Int. J. Numer. Meth. Engng.*, 84:1273–1302, 2010.

[210] Eric. Climent, Martin R. Maxey, and George Em Karniadakis. Dynamics of self-assembled chaining in magnetorheological fluids. *Langmuir*, 20:507–513, 2004.

[211] D. J. Klingenberg, C. F. Zukoski, and J. C. Hill. Kinetics of structure formation in electrorheological suspensions. *J. Appl. Phys.*, 73:4644–4648, 1993.

[212] J. C. Fernández-Toledano, J. A. Ruiz-López, R. Hidalgo-Álvarez, and J. de Vicente. Simulations of polydisperse magnetorheological fluids: A structural and kinetic investigation. *J. Rheol.*, 59:475–498, 2015.

[213] José Antonio Ruiz-López, Juan Carlos Fernández-Toledano, Daniel J. Klingenberg, Roque Hidalgo-Alvarez, and Juan de Vincente. Model magnetorheology: A direct comparative study between theories, particle-level simulations and experiments, in steady and dynamic oscillatory shear. *J. Rheol.*, 60:61–74, 2016.

[214] Hanna G. Lagger, Thomas Greinlinger, Jan G. Korvink, Michael Moseler, Alberto Di Renzo, Francesco Di Mai, and Claas Bierwisch. Influence of hydrodynamic drag model on shear stress in the simulation of magnetorheological fluids. *J. Non-Newtonian Fluid Mech.*, 218:16–26, 2015.

[215] R. Tao and Qi Jiang. Simulation of structure formation in an electrorheological fluid. *Phys. Rev. Lett.*, 73:205–208, 1994.

[216] G. L. Gulley and R. Tao. Structures of an electrorheological fluid. *Phys. Rev. E*, 56:4328–4336, 1997.

[217] Jordi Faraudo, Jordi S. Andreu, Carles Calero, and Juan Camacho. Predicting the self-assembly of superparamagnetic colloids under magnetic fields. *Adv. Funct. Mater.*, 26:3837–3858, 2016.

[218] G. Bossis, P. Lançon, A. Meunier, L. Iskakova, V. Kostenko, and A. Zubarev. Kinetics of internal structures growth in magnetic suspensions. *Phys. A*, 392:1567–1576, 2013.

[219] Di Du and Sibani Lisa Biswal. Micro-mutual-dipolar model for rapid calculation of forces between paramagnetic colloids. *Phys. Rev. E*, 90:033310, 2014.

[220] Tae Gon Kang, Martien A. Hulsen, Jaap M. J. den Toonder, Patrick D. Anderson, and Han E. H. Meijer. A direct simulation method for flows with suspended paramagnetic particles. *J. Comput. Phys.*, 227:4441–4458, 2008.

[221] Bas W. Kwaadgras, René Roij, and Marjolein Dijkstra. Self-consistent electric field-induced dipole interaction of colloidal spheres, cubes, rods, and dumbbells. *J. Chem. Phys.*, 140:154901, 2014.

[222] Eric. M. Furst and Alice P. Gast. Dynamics and lateral interactions of dipolar chains. *Phys. Rev. E*, 62:6916–6925, 2000.

[223] Y. Chen, A. F. Sprecher, and H. Conrad. Electrostatic particle-particle interactions in electrorheological fluids. *J. Appl. Phys.*, 70:6796–6803, 1991.

[224] L. C. Davis. Polarization forces and conductivity effects in electrorheological fluids. *J. Appl. Phys.*, 72:1334–1340, 1992.

[225] H. Zhang and M. Widom. Field-induced forces in colloidal particle chains. *Phys. Rev. E*, 51:2099–2103, 1995.

[226] L. C. Davis. Ground state of an electrorheological fluid. *Phys. Rev. A*, 46:R719–R721, 1992.

[227] H. J. H. Clercx and G. Bossis. Many-body electrostatic interactions in electrorheological fluids. *Phys. Rev. E*, 48:2721–2738, 1993.

[228] A. S. Sangani and A. Acrivos. The effective conductivity of a periodic array of spheres. *Proc. R. Soc. A*, 386:263–275, 1983.

[229] H. V. Ly, F. Reitich, M. R. Jolly, H. T. Banks, and K. Ito. Simulations of particle dynamics in magnetorheological fluids. *J. Comput. Phys.*, 155:160–177, 1999.

[230] R. Tao. Super-strong magnetorheological fluids. *J. Phys. Condens. Matter*, 13:R979–R999, 2001.

[231] L. V. Woodcock. Entropy difference between the face-centered cubic and hexagonal close-packed crystal structures. *Nature*, 385:141–143, 1997.

[232] Philip C. Brandt, Alexei V. Ivlev, and Gregor E. Morfill. Solid phases in electro- and magnetorheological systems. *J. Chem. Phys.*, 130:204513, 2009.

[233] R. J. Buehler, W. G. Wentorf, J. O. Hirschfelder, and C. F. Curtis. The free volume for rigid sphere molecules. *J. Chem. Phys.*, 19(1):61–71, January 1951.

[234] Norman F. Carnahan and Kenneth E. Starling. Equation of state for nonattracting rigid spheres. *J. Chem. Phys.*, 51(2):635–636, July 1969.

[235] G. R. Smith and A. D. Bruce. Multicanonical monte carlo study of solid-solid phase coexistence in a model colloid. *Phys. Rev. E*, 53:6530–6543, 1996.

[236] Marjolein Dijkstra. Phase behavior of hard spheres with a short-range yukawa attraction. *Phys. Rev. E.*, 66:021402, 2002.

[237] Mark Ivey, Jing Liu, Yun Zhu, and Serge Cutillas. Magnetic-field-induced structural transitions in a ferrofluid emulsion. *Phys. Rev. E*, 63:011403, 2000.

[238] Weijiaa Wen, Xianxiang Huang, and Ping Shend. Particle size scaling of the giant electrorheological effect. *Appl. Phys. Lett.*, 85:299–301, 2004.

[239] Weijia Wen, Xianxiang Huang, Shihe Yang, Kunquan Lu, and Ping Sheng. The giant electrorheological effect in suspensions of nanoparticles. *Nat. Mater.*, 2:727–730, 2003.

[240] Thomas C. Halsey and Will Toor. Fluctuation-induced couplings between defect lines or particle chains. *J. Stat. Phys.*, 61:1257–1281, 1990.

[241] T. B. Jones, R. D. Miller, K. S. Robinson, and W. Y. Fowlkes. Multipolar interactions of dielectric spheres. *J. Electrost.*, 22:231–244, 1989.

[242] Lu Yao, Nima Sharifi-Mood, Iris B. Liu, and Kathleen J. Stebe. Capillary migration of microdisks on curved interfaces. *J. Colloid Interface Sci.*, 449:436–442, 2015.

[243] Nima Sharifi-Mood, Iris B. Liu, and Kathleen J. Stebe. Curvature capillary migration of microspheres. *Soft Matter*, 11:6768–6779, 2015.

[244] Zachary M. Sherman and James W. Swan. Transmutable colloidal crystals and active phase separation *via* dynamic, directed self-assembly in toggled external fields. *ACS Nano*, 13:764–771, 2019.

[245] Kyoung Ah Min, Meong Cheol Shin, Faquan Yu, Meizhu Yang, Allan E. David, Victor C. Yang, and Gus R. Rosania. Pulsed magnetic field improves the transport of iron oxide nanoparticles through cell barriers. *ACS Nano*, 7:2161–2171, 2013.

[246] Randall M. Erb, Joshua J. Martin, Rasam Soheilian, Chunzhou Pan, and Jabulani R. Barber. Actuating soft matter with magnetic torque. *Adv. Funct. Mater.*, 26:3859–3880, 2016.

[247] Feng Li, Weidong Nie, Fan Zhang, Guihong Lu, Chengliang Lv, Yanlin Lv, Weier Bao, Lijun Zhang, Shuang Wang, Xiaoyong Gao, Wei Wei, and Hai-Yan Xie. Engineering magnetosomes for high-performance cancer vaccination. *ACS Cent. Sci.*, XXX:XXX–XXX, 2019.

[248] Sonia Melle, Gerald G. Fuller, and Miguel A. Rubio. Struture and dynamics of magnetorheological fluids in rotating magnetic fields. *Phys. Rev. E*, 61:4111–4117, 2000.

[249] Sonia Melle, Oscar G. Calderón, Miguel A. Rubio, and Gerald G. Fuller. Rotational dynamics in dipolar colloidal suspensions: Video microscopy experiments and simulations results. *J. Non-Newtonian Fluid Mech.*, 102:135–148, 2002.

[250] Sonia Melle, Oscar G. Calderón, Gerald G. Fuller, and Miguel A. Rubio. Polarizable particle aggregation under rotating magnetic fields using scattering dichroism. *J. Colloid Interface Sci.*, 247:200–209, 2002.

[251] Sonia Melle, Oscar G. Calderón, Miguel A. Rubio, and Gerald G. Fuller. Microstructure evolution in magnetorheological suspensions governed by mason number. *Phys. Rev. E*, 68:041503, 2003.

[252] Sibani Lisa Biswal and Alice P. Gast. Rotational dynamics of semiflexible paramagnetic particle chains. *Phys. Rev. E*, 69:041406, 2004.

[253] Ioannis Petousis, Erik Homburg, Roy Derks, and Andreas Dietzel. Transient behavior of magnetic mirobead chains rotating in a fluid by external fields. *Lab Chip*, 7:1746–1751, 2007.

[254] S. Krishnamurthy, A. Yadav, P. E. Phelan, R. Calhoun, A. K. Vuppu, A. A. Garcia, and M. A. Hayes. Dynamics of rotating paramagnetic particle chains simulated by particle dynamics, stokesian dynamics, and lattice boltzmann methods. *Microfluid. Nanofluid.*, 5:33–41, 2008.

[255] Y. Gao, M. A. Hulsen, T. G. Kang, and J. M. J. den Toonder. Numerical and experimental study of a rotation magnetic particle chain in a visous fluid. *Phys. Rev. E*, 86:041503, 2012.

[256] A. Vázquez-Quesada, T. Franke, and M. Ellero. Theory and simulation of the dynamics, deformation, and breakup of a chain of superparamagnetic beads under a rotating magnetic field. *Phys. Fluids*, 29:032006, 2017.

[257] Anil K. Vuppu, Antonio A. Garcia, and Mark A. Hayes. Video microscopy of dynamically aggregated paramagnetic particlce chains in an applied rotating magnetic field. *Langmuir*, 19:8646–8653, 2003.

[258] Geir Helgesen, Piotr Pieranski, and Arne T. Skjeltorp. Nonlinear phenomena in systems of magnetic holes. *Phys. Rev. Lett.*, 64:1425–1428, 1990.

[259] Anna C. H. Coughlan and Michael A. Bevan. Rotating colloids in rotating magnetic fields – dipolar relaxation and hydrodynamic coupling. *Phys. Rev. E*, 94:042613, 2016.

[260] Anna C. H. Coughlan and Michael A. Bevan. Effective colloidal interactions in rotating magnetic fields. *J. Chem. Phys.*, 147:074903, 2017.

[261] Hamed Abdi, Rasam Soheilian, Randall M. Erb, and Craig E. Maloney. Paramagnetic colloids: Chaotic routes to clusters and molecules. *Phys. Rev. E*, 97:032601, 2018.

[262] Thomas C. Halsey, Robert A. Anderson, and James E. Martin. The rotary electrorheological effect. *Int. J. Mod. Phys. B*, 10:3019–3027, 1996.

[263] James E. Martin, Robert A. Anderson, and Chris P. Tigges. Simulation of the athermal coarsening of composites structred by a biaxial field. *J. Chem. Phys.*, 108:7887–7900, 1998.

[264] James E. Martin, Eugene Venturini, Judy Odinek, and Robert A. Anderson. Anisotropic magnetism in field-structured composites. *Phys. Rev. E*, 61:2818–2830, 2000.

[265] D. J. Jeffrey. The temperature field or electric potential around two almost touching spheres. *J. Inst. Maths Applics.*, 22:337–351, 1978.

[266] Sebastian Jäger and Sabine H. L. Klapp. Pattern formation of dipolar colloids in rotating fields: Layering and synchronization. *Soft Matter*, 7:6606–6616, 2011.

[267] Zsigmond Varga and James Swan. Hydrodynamic interactions enhance gelation in dispersions of colloids with short-ranged attraction and long-ranged repulsion. *Soft Matter*, 12:7670–7681, 2016.

[268] G. K. Batchelor. Diffusion in a dilute polydisperse system of interacting spheres. *J. Fluid. Mech.*, 131:155–175, 1983.

[269] John F. Brady. The long-time self-diffusivity in concentrated colloidal dispersions. *J. Fluid. Mech.*, 272:109–133, 1994.

[270] James Swan and John F. Brady. Particle motion between parallel walls: Hydrodynamics and simulation. *Phys. Fluids*, 22:103301, 2010.

[271] James W. Swan and John F. Brady. The hydrodynamics of confined dispersions. *J. Fluid Mech.*, 687:254–299, 2011.

[272] C. F. Zukoski and D. A. Saville. An experimental test of electrokinetic theory using measurements of electrophoretic mobility and electrical conductivity. *J. Colloid Inteface Sci.r*, 107:322–333, 1985.

[273] C. F. Zukoski and D. A. Saville. Electrokinetic properties of particles in concentrated suspensions. *J. Colloid Interface Sci.*, 115:422–436, 1987.

[274] Orlin D Velev and Ketan H. Bhatt. On-chip micromanipulation and assembly of colloidal particles by electric fields. *Soft Matter*, 2:738–750, June 2006.

[275] A. B. D. Brown, C. G. Smith, and A. R. Rennie. Pumping of water with ac electric fields applied to asymmetric pairs of microelectrodes. *Phys. Rev. E*, 63:016305, 2000.

[276] Chien-Chih Huang, Martin Z. Bazant, and Todd Thorsen. Ultrafast high-pressure ac electro-osmotic pumps for portable biomedical microfluidics. *Lab Chip*, 10:80–85, 2010.

[277] D. C. Henry. The cataphoresis of suspended particles. part i. – the equation of cataporesis. *Proc. R. Soc. A*, 133:106–129, 1831.

[278] Richard W. O'Brien and Lee R. White. Electrophoretic mobility of a spherical colloidal particle. *J. Chem. Soc. Faraday Trans.*, 74:1607–1626, 1978.

[279] Todd M. Squires and Martin Z. Bazant. Induced-charge electro-osmosis. *J. Fluid Mech.*, 509:217–252, 2004.

[280] Martin Z. Bazant and Todd M. Squires. Induced-charge electrokinetic phenomena: Theory and microfluidic applications. *Phys. Rev. Lett.*, 92:066101, 2004.

[281] P. E. Secker and I. N. Scialom. A simple liquid-immersed dielectric motor. *J. Appl. Phys.*, 39:2957–2961, 1968.

[282] T. Coddington, A. F. Pollard, and H. House. Operation of a dielectric motor with a low conductivity liquid. *J. Phys. D: Appl. Phys.*, 3:1212–1218, 1970.

[283] P. Simpson and R. J. Taylor. Characteristic rotor speed variations of a dielectric motor with a low-conductivity liquid. *J. Phys. D: Appl. Phys.*, 4:1893–1897, 1971.

[284] Wolfgang Benecke, Berhhard Wagner, Gunter Fuhr, Rolf Hagedorn, Ronald Glaser, and Jan Gimsa. Dielectric motor, 1989.

[285] L. Lobry and E. Lemaire. Viscosity decrease induced by a dc electric field in a suspension. *J. Electrostat.*, 47:61–69, 1999.

[286] Nicolas Pannacci, Elisabeth Lemaire, and Laurent Lobry. Rheology and structure of a suspension of particles subjected to quincke rotation. *Rheol. Acta.*, 46:899–904, 2007.

[287] Paul Salipante and Petia M. Vlahovska. Electrohydrodynamic rotations of a viscous droplet. *Phys. Rev. E*, 88:043003, 2013.

[288] Antoine Bricard, Jean-Baptiste Caussin, Nicolas Desreumaux, Olivier Dauchot, and Denis Bartolo. Emergence of macroscopic directed motion in populations of motile colloids. *Nature*, 503:95–98, 2013.

[289] Antoine Bricard, Jean-Baptiste Caussin, Debasish Das, Charles Savoie, Vijayakumar Chikkadi, Kyohei Shitara, Oleksandr Chepizhko, Fernando Peruani, David Saintillan, and Denis Bartolo. Emergent vortices in populations of colloidal rollers. *Nat. Commun.*, 6:7470, 2015.

[290] Lyman Briggs. Effect of spin and speed on the lateral deflection (curve) of a baseball; and the magnus effect for smooth spheres. *Am. J. Phys.*, 27:589–596, 1959.

[291] Todd M. Squires and Martin Z. Bazant. Breaking symmetries in induced-charge electro-osmosis and electrophoresis. *J. Fluid Mech.*, 560:65–101, 2006.

[292] Fuduo Ma, Sijia Wang, David T. Wu, and Ning Wu. Electric-field-induced assembly and propulsion of chiral clusters. *Proc. Natl. Acad. Sci.*, 112:6307–6312, 2015.

[293] Sumit Gangwal, Olivier J. Cayre, Martin Z. Bazant, and Orlin D. Velev. Induced-charge electrophoresis of metallodielectric particles. *Phys. Rev. Lett.*, 100:058302, 2008.

[294] Aaron M. Drews, Hee-Young Lee, and Kyle J. M. Bishop. Ratcheted electrophoresis for rapid particle transport. *Lab Chip*, 13:4295–4298, 2013.

[295] Kyle J. M. Bishop, Aaron M. Drews, Charles A. Cartier, Shashank Pandey, and Yong Dou. Contact charge electrophoresis: Fundamentals and microfluidic applications. *Langmuir*, 34:6315–6327, 2018.

[296] Margaret Robson Wright. *An Introduction to Aqueous Electrolyte Solutions.* Joh Wiley & Sons, 2007.

[297] Howard A. Stone and Aravinthan D. T. Samuel. Propulsion of microorganisms by surface distortions. *Phys. Rev. Lett.*, 77:4102–4104, 1996.

[298] J. R. Melcher and G. I. Taylor. Electrohydrodynamics: A review of the role of interfacial shear stresses. *Annu. Rev. Fluid Mech.*, 1:111–146, 1969.

[299] D. A. Saville. Electrohydrodynamics: The taylor-melcher leaky dielectric model. *Annu. Rev. Fluid Mech.*, 29:27–64, 1997.

[300] Debasish Das and David Saintillan. Electrohydrodynamic interaction of spherical particles under quincke rotation. *Phys. Rev. E*, 87:043014, 2013.

[301] Martin Z. Bazant. Electrokinetics meets electrohydrodynamics. *J. Fluid. Mech.*, 782:1–4, 2015.

[302] Ilya Semenov, Shervin Raafatnia, Marcello Sega, Vladimir Lobaskin, Christian Holm, and Friedrich Kremer. Electrophoretic mobility and charge inversion of a colloidal particle studied by single-colloid electrophoresis and molecular dynamics simulations. *Phys. Rev. E*, 87:022302, 2013.

[303] Robert F. Stout and Aditya S. Khair. A continuum approach to predicting electrophoretic mobility reversals. *J. Fluid Mech.*, 752:R1, 2014.

[304] F. Peters, l. Lobry, A. Khayari, and E. Lemaire. Size effect in quincke rotation: A numerical study. *J. Chem. Phys.*, 130:194905, 2009.

[305] François Peters, Laurent Lobry, and Elsabeth Lemaire. Experimental observation of lorenz chaos in the quincke rotor dynamics. *Chaos*, 15:013102, 2005.

[306] E. Lemaire and L. Lobry. Chaotic behavior in electro-rotation. *Physica A*, 314:663–671, 2002.

[307] N. Pannacci, L. Lobry, and E. Lemaire. How insulating particles increase the conductivity of a suspension. *Phys. Rev. Lett.*, 99:094503, 2007.

[308] R. Di Leonardo, L. Angelani, D. Dell'Arciprete, G. Ruocco, V. Iebba, S. Schippa, M. P. Conte, F. Mecarini, F. De Angelis, and E. Di Fabrizio. Bacterial ratchet motors. *Proc. Natl. Acad. Sci.*, 107:9541–9545, 2010.

[309] Gaszton Vizsnyiczai, Giacomo Frangipane, Claudio Maggi, Filippo Saglimbeni, Silvio Bianchi, and Roberto Di Leonardo. Light controlled 3d micromotors powered by bacteria. *Nat. Commun.*, 8:15974, 2017.

[310] Christopher Dombrowski, Luis Cisneros, Sunita Chatkaew, Raymond E. Goldstein, and John O. Kessler. Self-concentration and large-scale coherence in bacterial dynamics. *Phys. Rev. Lett.*, 93:098103, 2004.

[311] H. P. Zhang, Avraham Be'er, E.-L. Florin, and Harry L. Swinney. Collective motion and density fluctuations in bacterial colonies. *Proc. Natl. Acad. Sci.*, 107:13626–13630, 2010.

[312] Eric Lauga. Bacterial hydrodynamics. *Annu. Rev. Fluid Mech.*, 48:105–130, 2016.

[313] Thomas Surrey, François Nédélec, Stanislas Leibler, and Eric Karsenti. Physical properties determining self-organization of motors and microtubules. *Science*, 292:1167–1171, 2001.

[314] Walter F. Paxton, Kevin C. Kistler, Christine C. Olmeda, Ayusman Sen, Sarah K. St. Angelo, Yanyan Cao, Thomas E. Mallouk, Paul E. Lammert, and Vincent H. Crespi. Catalytic nanomotors: Autonomous movement of striped nanorods. *J. Am. Chem. Soc.*, 126:13424–13231, 2004.

[315] Charles Wyatt Shields IV, Koohee Han, Fuduo Ma, Touvia Miloh, Gilad Yossifon, and Orlin D. Velev. Supercolloidal spinners: Complex active particles for electrically powered and switchable rotation. *Adv. Funct. Mater.*, 28:1803465, 2018.

[316] Allan M. Brooks, Mykola Tasinkevych, Syeda Sabrina, Darrell Velegol, Ayusman Sen, and Kyle J. M. Bishop. Shape-directed rotation of homogeneous micromotors via catalytic self-electrophoresis. *Nat. Commun.*, 10:495, 2019.

[317] K. M. Ho, C. T. Chan, and C. M. Soukoulis. Existence of a photonic gap in periodic dielectric structures. *Phys. Rev. lett.*, 65:3152–3155, 1990.

[318] E. Yablonovitch. Photonic band-gap structures. *J. Opt. Soc. Am. B*, 10:283–295, 1993.

[319] Martin Maldovan and Edwin Thomas. Diamond-structures photonic crystals. *Nat. Mater.*, 3:593–600, 2004.

[320] Jan Tobochnik and Phillip M. Chapin. Monte carlo simulation of hard spheres near random closest packing using spherical boundary conditions. *J. Chem. Phys.*, 88(9):5824–5830, January 1988.

[321] Leslie V. Woodcock. Glass transition in the hard-sphere model and kauzmann's paradox. *Ann. N. Y. Acad. Sci.*, 371:274–298, October 1981.